

High-order methods in fully general-relativistic hydrodynamics & magnetohydrodynamics

Dissertation zur Erlangung des
Doktorgrades der Naturwissenschaften

vorgelegt beim Fachbereich Physik der
Johann Wolfgang Goethe-Universität in Frankfurt am Main

von
SVEN KÖPPEL
aus
KÖNIGSTEIN IM TAUNUS

Frankfurt am Main, März 2019
(D30)



Geschrieben am

INSTITUT FÜR THEORETISCHE PHYSIK (ITP)
Max-von-Laue-Straße 1
60431 Frankfurt am Main

und am

FRANKFURT INSTITUTE FOR ADVANCED STUDIES (FIAS)
Ruth-Moufang-Straße 1
60431 Frankfurt am Main

vom Fachbereich Physik der
Goethe-Universität als Dissertation angenommen.

Dekan: Prof. Dr. Michael Lang

Gutachter: Prof. Dr. Luciano Rezzolla
Prof. Dr. Piero Nicolini
Prof. Dr. David Radice (Princeton University/IAS)

Datum der Disputation:

Abstract

This thesis is a summary of existing and upcoming publications [168, 194, 204, 274, 275, 276, 290, 406], with a focus on high order methods in numerical relativity and general relativistic flows. The text is structured in five chapters. In the first three ones, the ADER-DG technique and its application to the Einstein-Euler equations is introduced. Novel formulations for both the Einstein equations in the 3+1 split as well as the general relativistic magnetohydrodynamics (GRMHD) had to be derived. The first order conformal and covariant Z4 formulation of Einstein equations (FO-CCZ4) is proposed and proven to be strongly hyperbolic. Together with the fluid equations of general relativistic magnetohydrodynamics (GRMHD), a number of benchmark scenarios is presented to show both the correctness of the PDEs as well as the applicability of the numerical scheme.

As an application in astrophysics, a general-relativistic study of the threshold mass for a prompt-collapse of a binary neutron star merger with realistic nuclear equation of states has been carried out. A nonlinear universal relation between the threshold mass and the maximum compactness is found. Furthermore, by taking recent measurements of GW170817 into account, lower limits on the stellar radii for any mass can be given.

Furthermore, an (unpaired) work in quantum mechanical black hole engineering is presented. Higher dimensional extensions of generalized Heisenberg's uncertainty principle (GUP) are studied. A number of new phenomenology is found, such as the existence of a conical singularity which mimics the effect of a gravitational monopole on short scale and that of a Schwarzschild black hole at a large scale, as well as oscillating Hawking temperatures which we call "lighthouse effect". All results are consistent with the self complete paradigm and a cold evaporation endpoint remnant.

This document is written with \LaTeX and a style inspired by the books of the data visualization pioneer EDWARD TUFTE. In physics, his style was first adopted in the textbooks of RICHARD FEYNMAN. It is characterized by the large margin column and the flat structure, among others. I chose this format to include a lot of illustrating figures and supplementary comments. Deeply nested hierarchies are omitted.

The text and figures (see page 136 for a list) in this work are licensed under a Creative Commons Attribution-ShareAlike license ([CC BY-SA](#)).

Contents

	German summary (Zusammenfassung)	7
Chapter 0	Introduction	12
	Numerical schemes for the Exascale era, A novel hyperbolic formulation of Einsteins Equations, General relativistic Magnetohydrodynamics within the new framework, A general-relativistic criterion to seperate prompt from delayed collapse in a binary neutron star merger, Quantum modified Schwarzschild solutions.	
Chapter I	Evolution equations on the computer	17
1	Motivation: Hamiltonian time evolution	17
2	Conservation laws The non-conservative product, Quasi-linear PDEs, The Riemann problem.	18
3	Solving PDEs with machines Symbolic computing, Analog computing.	21
4	Time and Space discretizations Semi temporal discretization, ADER time integration, CFL factor, Methods for spatial discretization, Finite-difference schemes.	22
5	Finite-volume schemes Godunov's scheme, Higher order finite volume, Riemann solvers and the non-conservative product, MUSCL-Hancock, WENO.	26
6	Discontinuous Galerkin schemes Subcell structure in nodal DG schemes, A path-conservative ADER-DG scheme, Local spacetime predictor, Finite-volume subcell limiter.	29
7	Grid meshing Block regular grids, Mesh refinement, Parallelization, ADER-DG <i>hp</i> -refinement.	36
8	Aspects of input and output on AMR and DG In-situ initial data, In-situ postprocessing, Visualization of ADER-DG simulations.	40
9	Summary	42
Chapter II	General Relativity	43
10	Motivation: The two body problem of GR	43
11	The Cauchy Initial value formulation of GR Foliation of spacetime, ADM equations, Gauge fixing.	44
12	The BSSNOK equations Covariance of the BSSNOK formulation, Definitions for the conformal factor, Evolution equations.	48

13	The Z4 family and CCZ4 Z4c, SO-CCZ4.	50
14	The first order CCZ4 equations (FO-CCZ4) Auxilliary variables, ordering constraints, The FO-CCZ4 PDE system in the differential/algebraic split, Eigenstructure of the FO-CCZ4 system.	52
15	Implementation of the FO-CCZ4 equations About the PDE system's costs, Choosing the right language.	61
16	Benchmarks for solving FO-CCZ4 with ADER-DG Linearized gravitational-wave test, Gauge-wave test, Robust stability test, Convergence tests on three-dimensional black-hole spacetimes, Evolution of a single puncture black hole, Preliminary results for moving punctures.	63
17	Summary	71
Chapter III	Hydrodynamics	72
18	Motivation: An effective theory for dense and hot matter	72
19	Introduction of Hydrodynamics Classical Hydrodynamics, Special relativistic hydrodynamics (SRHD), The primitive recovery in relativistic hydrodynamics.	73
20	General relativistic hydrodynamics (GRHD) 3+1 split of special relativistic hydrodynamics, Conformal factor, Sources for curved spacetimes, Cowling approximation.	75
21	General relativistic magnetohydrodynamics (GRMHD) Magnetodynamics, The GRMHD coupling, Fluxes and sources, Divergence cleaning.	78
22	Benchmarks and GRMHD codes Benchmark description.	80
23	Smooth special-relativistic benchmarks Michel accretion onto a Schwarzschild black hole in 2D, Torus interior around a Schwarzschild black hole in 2D, 3D Michel accretion with radial magnetic field.	81
24	Non-smooth special-relativistic benchmarks Riemann problems, Advection of a 2D magnetic field loop, 2D blast wave, Orszag-Tang vortex.	86
25	Non-smooth general-relativistic benchmarks 2D torus around a Schwarzschild black hole, 3D torus around a Schwarzschild black hole, Preliminary results on a TOV star.	91
26	Summary	94
Chapter IV	Binary Neutron Star lifetimes	95
27	Motivation: Nuclear equation of state	95
28	Methods	96
29	Definition of merger and collapse time Definition of merger time, The lapse as indicator, The free fall timescale, Angular momentum.	97
30	Initial data and EOS Nuclear equations of state taken into account.	99
31	Results on the treshold mass	100

32	Constraining Neutron Star radii	103
33	Convergence and error budget	105
34	Summary	105
Chapter V	Models for Quantum Black Holes	107
35	Motivation: Higher dimensional Black Hole spacetimes	107
36	A brief introduction into the Generalized Uncertainty principle	108
37	Review of GUP Black Holes in the KMM measure 3+1 Dimensional GUP inspired Black Holes.	109
38	Higher Dimensional KMM Black Holes Extremal configuration, Thermodynamics.	111
39	Ambiguity of GUP in higher dimensional spacetimes	114
40	Revised GUP in higher dimensions Calculation of the energy density.	116
41	Summary	120
Chapter VI	Conclusions	121
Chapter A	Appendix	123
A1	Notation and conventions Units, Symbols, Symbols with canonical physical meaning.	123
A2	Convergence, consistency and stability of PDEs	125
A3	ADER vs. Runge-Kutta for time integration	127
A4	FO-FCCZ4: a first-order fully covariant Z4 formulation	129
A5	Boundary conditions for Einstein Equations Sommerfeld boundary conditions, Exact wave-absorbing Riemann Solver .	131
A6	Extracting gravitational waves	133
A7	Adjusted GUP profiles	135
Chapter B	References	136
B1	List of figures	136
B2	List of tables	138
B3	List of computer codes and libraries Initial data codes, Time evolution codes.	138
B4	List of co-authored papers Bibliography Acknowledgement Curriculum Vitae	139 140 168 169

Zusammenfassung

Schwarze Löcher und Gravitationswellen gehören zu den faszinierenden Vorhersagen der allgemeinen Relativitätstheorie. Schwarze Löcher gibt es auf fast jeder Längenskala und seit einigen Jahren gibt es mehr und mehr Möglichkeiten, sie zu messen. Die größten schwarzen Löcher werden supermassereich genannt, Millionen von Sonnenmassen schwer werden sie im Zentrum von jeder Galaxie vermutet. Das Event Horizon Telescope hat zum Ziel, die Photonensphäre des Objekts Sagittarius A* zu messen, welches als supermassreiches schwarzes Loch im Zentrum der Milchstraße vermutet wird. Das Laser-Interferometer-Gravitationswellen-Observatorium (LIGO) wiederum konnte bereits 2016 zum ersten mal Gravitationswellen direkt beobachten, die durch den Kollaps zweier stellarer schwarzer Löcher (jeweils ca 20-30 Sonnenmassen schwer) entstanden. Dafür erhielten drei LIGO-Physiker 2017 den Nobelpreis.

Ebenfalls wurden von LIGO und dem europäischen Pendant Virgo die Gravitationswellen von der Verschmelzung zweier Neutronensterne gemessen. Neutronensterne gehören zu den kompaktesten astrophysikalischen Objekten, mit einer Ausdehnung von wenigen Kilometern und einer mit der Sonne vergleichbaren Masse. Die zentrale Massendichte in Neutronensternen erreicht ein Vielfaches der nuklearen Sättigungsdichte. Damit sind Neutronensterne ein Ort in der Natur, in dem sich außergewöhnliche Materiezustände vorfinden lassen, wie etwa das Quark-Gluon-Plasma. Mit der Beobachtung von Kollisionen solcher Sterne, insbesondere über mehrere Kanäle (Radiowellen verschiedener Spektren sowie Gravitationswellen) können erstmals präzise Aussagen über die Beschaffenheit dieser Sterne gemacht werden.

Die Messung dieser Gravitationswellen ist nicht nur eine experimentelle Meisterleistung, sondern unter anderem auch dem Fortschritt der computerbasierten Lösung von Einsteins nichtlinearen Feldgleichungen zu verdanken. Die numerische Relativitätstheorie hat in den letzten 15 Jahren gewaltige Fortschritte gemacht, die nicht bloß einer allgemein gestiegenen verfügbaren Rechenleistung zu verdanken sind, sondern vor allem dem besseren Verständnis der wesentlichen Freiheitsgrade der allgemeinen Relativitätstheorie, der trickreichen Reformulierung der Feldgleichungen als hyperbolische partielle Differentialgleichungen im Rahmen eines wohldefinierten klassischen Anfangs-Randwertproblems, dem Verständnis ihrer Eigenstruktur sowie nicht zuletzt besser konvergierenden numerischen Methoden, welche allgemein unter dem engl. Stichwort "high order methods" zusammengefasst werden. Erst seit 2005 ist es nach Jahrzehntelanger Forschung möglich, schwarze Löcher in Doppelsystemen in einer Computersimulation stabil in der Zeit zu entwickeln und dabei die Abstrahlung von Gravitationswellen zu beobachten. Auf ganzen Datenbanken solcher Wellenvorhersagen fußt die experimentelle Messung von Gravitationswellen, denn ohne diesen wäre dem verrauschten Signal nichts zu entnehmen.

Methoden zur kommunikationsvermeidende Zeitentwicklung

Daher entsteht ein enormer Bedarf an einer weiteren Verbesserung der Vorhersagekraft von Computersimulationen. Informatiker stehen vor einem Problem: Es steht zwar immer mehr Rechenleistung für die Wissenschaft zur Verfügung – die Rede ist von einem Exaskalencomputer, also einem Rechner, der 10^{18} Grundrechenarten pro Sekunde bewältigt – allerdings werden bestehende Simulationspro-

gramme gnadenlos scheitern, diese neue Rechnergeneration, die rein rechnerisch in der Lage sein soll, ein menschliches Gehirn zu simulieren, dabei allerdings aus hunderten Millionen Prozessorkernen bestehen, voll auszuschöpfen. Im Rahmen dieser Dissertation wurden daher neuartige Methoden zum Lösen der hyperbolischen Zeitentwicklung, die von Anfang an die Kommunikation innerhalb eines Supercomputers auf ein Minimum beschränkt, auf astrophysikalische Probleme angewandt. Diese so genannten diskontinuierliche Galerkin-Verfahren versprechen darüber hinaus eine hohe Konvergenzordnung bei, verglichen mit herkömmlichen Methoden, niedrigem Stromverbrauch. Im Gegenteil zu herkömmlichen Finite Volumen-Verfahren wird die räumliche Simulationsdomäne dabei in eine Anzahl von unabhängig voneinander (daher "diskontinuierlich") zeitentwickelten Zellen unterteilt, welche ihrerseits Polynome beherbergen, die die physikalischen Felder beschreiben.

Um das Gibbs'sche Phänomen bei physikalischen Unstetigkeitsstellen (etwa Singularitäten der Raumzeit oder hydrodynamischen Schocks) zu verhindern, fällt das Schema als Prädiktor-Korrektor-Verfahren bei Unstetigkeit lokal auf ein klassisches robustes Finite Volumen-Verfahren zurück. Es verbindet damit die Erprobtheit herkömmlicher Methoden mit den Vorteilen von diskontinuierlichen Galerkin-Verfahren. Im Rahmen dieser Dissertation wurden unter anderem diese numerischen Methoden in den neuartigen "ExaHyPE"-Code (engl., für "an Exascale Hyperbolic PDE Engine") eingebaut, einem Computerprogramm zur Lösung beliebig vieler gekoppelter hyperbolischen Differentialgleichungen, welches den hohen Anforderungen der zukünftigen Exaskalencomputer gerecht werden soll. Mit Beispielanwendungen aus der Seismologie (Erdbebenvorhersagen) und der Astrophysik (Neutronensternverschmelzungen) soll ExaHyPE ab Ende 2019 der Öffentlichkeit zugänglich sein.

Die konform kovariante Formulierung der Einsteingleichungen in erster Ordnung

Im Rahmen dieser Arbeit wurde eine neue Formulierung der Einsteingleichungen hergeleitet, die aus 59 gekoppelten nichtlinearen Differentialgleichungen besteht. Das partielle Differentialgleichungssystem ist erste Ordnung in Zeit *und* Raum. Die Motivation war dabei, eine streng hyperbolische Formulierung der Einsteingleichungen zu finden, die für eine numerische Zeitentwicklung mit den oben vorgestellten diskontinuierlichen Galerkin-Verfahren geeignet ist.

Diese neue Formulierung, die den Namen "FO-CCZ4" trägt, geht als Umschreibung der CCZ4-Gleichungen zurück, der konform kovarianten Z4-Formulierung (engl. "conformally covariant Z4") der Einsteingleichungen. Diese erhält man, in dem die vier Eichfreiheitsgrade der Einsteingleichungen im Rahmen der Cauchy-Anfangswert-Formulierung (ADM-Split) separiert und fixiert werden. Die erstmals 2010 formulierte Z4-Variante stellt die Kovarianz dieser Eichtheorie sicher, in dem sie die Hamiltonschen Zwangsbedingungen zusätzlich als dynamische Zustandsgröße entwickelt. Auf diese Weise wird die Formulierung um ein selbstheilendes Element ergänzt, welches numerische Fehler korrigiert und den Zustandsvektor des Gleichungssystems zu einem physikalischen Zustand konvergieren lässt.

Im Zuge weiterer Umschreibungen werden die konformen Freiheitsgrade separiert und transversal-spurlose Tensordichten zeitentwickelt, welche zu einer weiteren Stabilisierung des Systems beitragen. Sie erlauben es, hyperbolische (also insbesondere zeitabhängige) singularitätsvermeidende Eichfixierungen vorzunehmen, die die Variation des räumlichen Koordinatenvolumens minimal halten (diese bewährten Eichfixierungen heißen "Bona-Massó Slicing" und "Gamma Driver"). Die auf diese Weise beschriebene konforme und kovariante Z4-Formulierung der Einsteingleichungen wurden anschließend in ein Differentialgleichungssystem erster Ordnung umgeschrieben. Dabei wurde eine approximative Symmetrisierung der dünnbesetzten Systemmatrix erreicht, in dem der Satz von Schwarz zur Symmetrisierung von Ableitungen (Ordering Constraints) rigoros angewendet wurde, ohne dabei das Entstehen von Jordan-Blöcken zu erlauben. Es konnte gezeigt werden, dass das konform-kovariante Z4-System in den üblichen Eichfixierungen nicht nur streng hyperbolisch ist, sondern sogar die Dynamik der vierdimensionalen Metrik (in der konformen ADM-Formulierung zusammengesetzt aus dem sogenannten Lapse-Skalar, Shift-Vektor, der räumlichen Metrik und dem konformen Faktor) als

gewöhnliche Differentialgleichungen entkoppeln. Ferner sind alle Felder linear degeneriert, was zur Folge hat, dass das System keine “gravitativen Schockwellen” entwickeln kann. Bis auf Orte unendlicher Krümmung (Singularitäten) sind die in dieser Formulierung zeitentwickelten Felder, welch die Raumzeit beschreiben, also immer kontinuierlich.

Die konform kovarianten Z4-Formulierung in erster Ordnung (*engl. first order conformally covariant Z4, FO-CCZ4*) ist mit ihren 59 gekoppelten nichtlinearen Differentialgleichungen erheblich komplexer als die Einsteingleichungen (üblicherweise geschrieben als 16 gekoppelte Differentialgleichungen, aber nur 10 Freiheitsgrade beschreibend). Trotzdem ist ihr Einsatz ökonomisch, da die Formulierung in erster Ordnung erlaubt, das Gleichungssystem räumlich diskret mit pfadkonservativen Methoden zu integrieren. Ähnlich wie in der Flüssigkeitsdynamik werden dabei alle charakteristischen Wellen des Systems vom numerischen Schema “erfasst”. Dies äußert sich bei der Zeitentwicklung stationärer Raumzeiten etwa dadurch, dass die Lösung besser erhalten wird als mit herkömmlichen Methoden.

Zur Demonstration der Korrektheit der Formulierung sowie ihrer Lösbarkeit mit den dargestellten numerischen Schemata wurden einige Standardtests der numerischen Relativitätstheorie erfolgreich demonstriert, darunter linearisierte Gravitationswellen-Tests, Stabilitätstests einer gestörten Minkowskimetrik, Zeitentwicklung nichtlinearer “Eichwellen”, Konvergenztests zur Demonstration der Konvergenzordnung bei der Zeitentwicklung der statischen Schwarzschild-Raumzeit und der stationären Kerr-Raumzeit, sowie zuletzt die numerische Lösung des Zweikörperproblems (Verschmelzung zweier schwarzer Löcher mithilfe der Punkturmethode).

Relativistische Magnetohydrodynamik im nichtkonservativen Split

Die relativistische Hydrodynamik ist eine erfolgreiche Theorie, um die Materie (ausgedehnter) kompakter Objekte zu beschreiben. Zur Beschreibung von Effekten, in denen elektrodynamische Wechselwirkungen eine wichtige Rolle spielen, ist zudem die allgemein relativistische Magnetohydrodynamik (*engl. GRMHD, für “general relativistic magnetohydrodynamics”*) eine anerkannte effektive Theorie. In ihrer idealen Näherung beschreibt diese Gleichung die relativistische Dynamik eines Fluides, welches durch seine Bewegung ein Magnetfeld induziert und mit diesem auch wechselwirkt. Auf diese Weise lassen sich eine Vielzahl astrophysikalischer Phänomene beschreiben, etwa Jets, Pulsare und Gammastrahlenblitze.

Neben den Einsteingleichungen wurden auch die Gleichungen der allgemein relativistischen Magnetohydrodynamik in eine flusskonservative Form gebracht, in der Erhaltungsterme und nichtkonservative Flüsse getrennt werden. Auf diese Weise ist eine pfadkonservative Integration aller Flüsse möglich, was zu einer wesentlich exakteren Beschreibung des diskretisierten Problems führt als herkömmliche Methoden.

In Standard-Benchmarks wurde die neue Formulierung der allgemein relativistischen Magnetohydrodynamik auf stationären gekrümmten Hintergrundräumen (Cowling-Näherung) mithilfe der oben eingeführten diskontinuierlichen Galerkin-Verfahren demonstriert. Dabei wurden als kontinuierliche Flüsse in der Schwarzschild-Raumzeit separat die Dynamik im Inneren eines Torus, die Akkretion eines elektrisch neutralen sowie die Akkretion eines magnetohydrodynamisch wechselwirkenden Fluides demonstriert. Als nichtkontinuierliche speziell-relativistische Flüsse wurden einige akademische Beispiele präsentiert, etwa die Lösung eindimensionaler Riemannprobleme in gekrümmten Hintergrundräumen, die Zeitentwicklung einer zweidimensionalen magnetischen Schleife, einer magnetischen Druckwelle, sowie des Orszag-Tang-Vortexes. Als nichtkontinuierliche allgemein-relativistische Flüsse werden Raumzeiten einer Torus-Schwarzes Loch-Konfiguration simuliert und ferner vorläufige Ergebnisse auf die Zeitentwicklung eines Neutronensterns (TOV-Lösung, nach Tolmann-Oppenheimer-Volkhoff) präsentiert.

Wie lange überlebt ein hypermassiver Neutronenstern?

Ein weiteres Projekt, welches in der vorliegenden Dissertation beschrieben wird, ist eine Anwendung obiger Methoden, also der numerischen Zeitintegration des gekoppelten Einstein-Euler-Systems. Dabei wurde das Szenario eines “verzögerten Kollapses” bei der Vereinigung zweier Neutronensterne untersucht. Es wurden quantitative Kriterien entwickelt, um einen sofortigen Kollaps zu einem schwarzen Loch von der Entstehung eines metastabilen hypermassiven Neutronensternes zu unterscheiden. Als Unterscheidungskriterium für das Szenario des “verzögerten Kollapses” kommt dabei die Masse der Raumzeit bzw. der Konstituenten zum Tragen. Oberhalb einer kritischen Masse kommt es zum prompten Kollaps zu einem schwarzen Loch und unterhalb zu einem verzögerten Kollaps. Dazu wurde eine Parameterstudie durchgeführt, bei der für eine Vielzahl an realistischen nuklearen Zustandsgleichungen eine Menge an Anfangswertprobleme gebildet wurden, die sich durch die Masse ihrer Konstituenten unterscheiden. Um Anfangswerte für die Einstein-Euler-Gleichungen zu erhalten, die die Raumzeit eines Doppelsternsystems im stark wechselwirkenden Endstadium beschreiben, müssen elliptische Gleichungen gelöst werden. Iterative Anfangswertcodes finden dazu zunächst die Lösung der TOV-Gleichungen und fügen diesen dann schrittweise Drehmoment hinzu, während der Abstand der Sterne verringert wird. Die erzeugten Anfangswerte werden dann mit den obengenannten hyperbolischen Methoden zeitentwickelt bis sich ein schwarzes Loch gebildet hat.

Die Überlebenszeit des Kollisionsproduktes ist definiert als die Koordinatenzeit, die zwischen Verschmelzung und Kollaps zum schwarzen Loch verstrichen ist. Anhang der Simulationsdaten können eine Vielzahl an Kriterien herangezogen werden, um Verschmelzung und Kollaps zu definieren, so zum Beispiel über den Koordinatenabstand der Neutronensterne, den Peak des Gravitationswellensignals, einem kritischen Wert für das globale Maximum der Ruhemassendichte oder das globale Minimum des effektiven Potentials. Im Rahmen der Untersuchung stellte sich heraus, dass die dynamische Eichfixierung dank ihrer Eigenschaft, die Koordinaten aus dem Gravitationspotential (her)rauszutreiben, sowohl für die Definition des Zeitpunkts der Verschmelzung als auch des Kollapses am besten geeignet ist.

Die Überlebenszeiten, die nun jedem einzelnen Computerexperiment (einem Doppelneutronensternsystem mit gewisser Masse und Zustandsgleichung) zugewiesen werden konnte, wurden für jede Zustandsgleichung die Systemmassen zu einer charakteristischen Zeit extrapoliert, die der Eigenzeit beim freien Kollaps eines TOV-Sternes bis zur Entstehung eines schwarzen Loches entspricht. Die auf diese Weise definierten kritischen Massen zeigen eine Korrelation zu den TOV-Massen der Zustandsgleichung. Vor allem lassen sich aber Zusammenhänge zwischen den kritischen Massen aller untersuchten Zustandsgleichungen herstellen, welche erlauben für eine neue Zustandsgleichung die kritische Masse anhand ihrer TOV-Eigenschaften vorherzusagen. Zuguterletzt lassen sich die Zahlen auch unter Zuhilfenahme von echten Gravitationswellenmessungen benutzen, um den minimalen Radius eines Neutronensterns einzuschränken. Mithilfe der Experimentellen Daten von GW170817 wurde der minimale Radius $R = 9.74(\pm 0.1)\text{km}$ ermittelt.

Die Raumzeit eines quantenmechanischen schwarzen Loches

Als letztes Projekt ist dieser Monographie ein Projekt aus dem Bereich der Quantengravitation beigelegt, welches die Eingangs aufgelisteten Skalen von schwarzen Löchern komplettieren: Die Modellierung der Metriken von mikro-schwarzen Löchern. Es wird dabei eine stringtheoretisch motivierte impulsabhängige Modifikation der Heisenbergschen Unschärferelation eingeführt, welche als effektive Theorie die erste Ordnung einer quantenmechanischen Gravitationstheorie beschreiben kann. Die neuen Kommutatorrelationen erlauben exakte Impulsoperatoren, aber erzwingen eine minimale Länge im Ortsraum. Die Dirac-Deltaquelle der Schwarzschild-Metrik lässt sich somit als Fouriertransformierte der ebenen Welle (im Impulsraum) nicht mehr exakt (im Ortsraum) darstellen und bewirkt damit eine Verschmierung / Delokalisierung des gravitativen Potentials. Berechnet man die Hawking-

Temperatur dieses quantenmechanisch modifizierten schwarzen Loches, findet man einen kalten Evaporationsendpunkt, welcher sich im selbstvollständigen Paradigma mit der Planck-Skala in Verbindung setzen lässt. Dieses stabile “kleinstmögliche” schwarze Loch ist dabei lediglich das Ergebnis der Tatsache, dass kleine schwarze Löcher signifikant viel Energie durch Hawkingstrahlung verlieren. Das stabile Überbleibsel eignet sich etwa als Kandidat zur Beschreibung von dunkler Materie.

Im Rahmen der Dissertation wurden mögliche Erweiterungen der Theorie der modifizierten Heisenbergschen Unschärferelation auf große Extradimensionen untersucht. Ein solches “Extradimensions”-Szenario könnte das schwache Hierarchieproblem des Standardmodells lösen und birgt die einzige Chance, dass schwarze Löcher im Teilchenbeschleuniger gemessen werden können. Gedankenexperimente suggerieren allerdings verschiedene Möglichkeiten, welche algebraische Form die Unschärferelation in höheren Dimensionen haben sollte. Zwei Formulierungen stechen dabei heraus: Zum einen eine, welche in einer Extradimension (also 4+1-dimensional Raumzeit) eine konische Singularität aufweist. Dies ist die erste exakte Lösung einer Raumzeit, welche auf kurzen Skalen wie ein gravitativer Monopol aussieht und auf großen Skalen wie ein schwarzes Loch.

Eine weitere, modifizierte Unschärferelation wiederum reproduziert in jeder Dimension die gleiche Impulsraum-Regularisierung, verfügt darüber hinaus aber über einen neuen komplexeren thermodynamischen Zustandsraum. Dabei handelt es sich um das Phänomen, dass das schwarze Loch kurz vor seiner Verdampfung auf der Planck-Skala Temperaturoszillationen aufweist, welche mit wiederholten Phasenübergängen zwischen negativer und positiver Wärmekapazität einhergehen. Die damit verbundene stetig veränderte Luminosität verleiht zur Prägung des Begriffes “Leuchtturm-Effekt”. Darüberhinaus gibt es mehrere stabile Evaporationsendpunkte, welche für kleine schwarze Löcher (enstanden aus dem quantenmechanischen Regime) unterschiedliche minimale Längen vorhersagen als für große schwarze Löcher (entstanden aus dem semiklassischen Regime).

Introduction

CHAPTER

0

Shortly after the beginning of my PhD position in theoretical astrophysics end of 2015, the first direct observation of gravitational waves was made, where the merger of $36M_{\odot}$ and $29M_{\odot}$ black holes to a single $62M_{\odot}$ black hole was measured. This remarkable event identified as GW150914 [1] prove the existence of gravitational waves, of stellar mass binary black hole systems and heralded a new era of gravitational wave multimessenger astronomy. The breakthrough gained international attention due to the 2017 Nobel prize awarding to Weiss, Barish and Thorne “for decisive contributions to the LIGO detector and the observation of gravitational waves”.

In 2017 the first direct observation of two merging neutron stars was made, with constituent neutron star masses up to $1.6M_{\odot}$ and a merger mass of $2.74M_{\odot}$. This event, identified as GW170817 [437], was followed by a short gamma-ray burst and a number of other observations in the electromagnetic spectrum.

Due to their bad signal to noise ratio, gravitational wave interferometry depends on precomputed gravitational wave-forms. These wave-forms are computed by large scale perturbative but especially numerical approaches to general relativity. Numerical relativity had emerged as a powerful tool for the study of astrophysical systems, following the breakthrough calculations of the merger of binary “moving puncture” black holes in mid-2000 [45, 46, 104, 117, 233, 365].

0.1 Numerical schemes for the Exascale era

The interest for high accuracy simulations of general-relativistic spacetimes has only been strengthened by the observational breakthrough. There is a need for stable and accurate methods which can exploit the computational ressources available. Chapter I on page 17 is a mathematical one which purely concentrates on numerical aspects in hyperbolic partial differential equations and introduces a sophisticated numerical scheme with arbitrary convergence order in time and space. At the same time, it is communication avoiding and therefore suitable for the upcoming generation of exascale computers — machines which can compute 10^{18} basic arithmetic operations per second. The scheme was used in the coauthored publications [168, 194] as well as in [135, 406]. Particular challenges in computer science/high performance computing (HPC) are discussed and the ExaHyPE code is introduced, a dynamical adaptive mesh refinement (AMR) code which uses finite state machines for determining the control flow and take off the control from the user. ExaHyPE can solve a specific class of hyperbolic partial differential equations (PDEs) and will be open sourced end of 2019.

Discontinuous Galerkin methods belong to the family of finite-element methods which consider the numerical approximation of a weak formulation of the governing system of partial differential equations over a set of non-overlapping elements. The discrete solution space is restricted to the space of piecewise polynomials of maximum degree $N \geq 0$ and the degrees of freedom (i.e., the expansion coefficients) of the chosen polynomial basis are directly evolved in time. In particular, in the DG formulation the numerical solution is allowed to be discontinuous at element interfaces. In the last twenty years, DG methods became increasingly popular mainly because of four attractive properties:

- (i) nonlinear L_2 stability (See Appendix A1.2 for standard definitions such as “ L_2 ”) has been proven for general nonlinear scalar conservation laws [257];
- (ii) arbitrary high order of accuracy can be easily achieved for smooth solutions by simply increasing the polyno-

mial degree N of the chosen basis functions;

- (iii) high parallel scalability makes DG methods better suited for large-scale simulations even on general unstructured meshes when compared with high-order finite-difference or finite-volume methods;
- (iv) high-order DG methods are not very dissipative and dispersive, even when compared with high-order finite-volume and finite-difference schemes and are thus essential for accurate long-term simulations.

0.2 A novel hyperbolic formulation of Einsteins Equations

Chapter II on page 43 concentrates on general relativity and casts these equations in the mathematical framework proposed in the the previous chapter. In fact, the development of hyperbolic formulations of the Einstein equations that allow for long-term simulations of generic spacetimes, including the ones encompassing the physical singularities arising in the presence of black holes, has been of great importance in numerical relativity. The first step in this direction has been the derivation of the Arnowitt-Deser-Misner (ADM) formulation. While this formulation splits time and space and presents general relativity as an initial boundary-value problem, suitable for numerical implementation, it is known to be not hyperbolic, and therefore unstable in numerical applications.

Subsequently, a lot of effort has been devoted to find hyperbolic formulations of the Einstein equations. These efforts have lead to the derivation of the Baumgarte-Shapiro-Shibata-Nakamura-Oohara-Kojima (BSSNOK) formulation [63, 100, 338, 413], which achieves hyperbolicity via a conformal transformation of the 3-metric and the promotion of some contractions of the Christoffel symbols to independently evolved variables and, most importantly, by inserting the momentum and Hamiltonian constraint expressions in the evolution system. A general-covariant alternative is the Z4 formulation of [11, 85, 86], which has been presented both in first- and second-order form in the spatial derivatives. More successful have been formulations based on the Z4 one that include a conformal transformation of the metric. These are the Z4c formulation, that removes some source terms in the Einstein equations in order to bring the evolution equations into a form which is closer to the BSSNOK system [75], and the CCZ4 formulation [12, 13], which also includes a mechanism to damp constraint violations as they arise during the evolution (see also [78, 398] for some recent and slight variants).

Parallel to the quest for better formulations of the equations, the development and implementation of better numerical methods has been a main priority of ongoing research. While most general-relativistic codes use finite-differences (e.g., [99, 328, 375, 377, 473]) or spectral methods (e.g., [427]) for the spacetime evolution, increasing interests is being focused towards DG methods, which are very attractive due to their excellent scalability and wave-propagation properties. The latter allow the propagation of smooth linear and nonlinear waves over long distances with little dissipation and dispersion errors, and turn out to be well suited for the solution of the Einstein equations, where (apart from physical singularities in black holes) the fields are smooth and high accuracy can be achieved.

So far, however, only a rather limited number of attempts have been made to solve Einstein equations with DG methods. Field et al. [200] tested a second-order BSSNOK formulation, while Brown et al. [101] developed a first-order formulation of BSSNOK, however both works were limited to spherical symmetry and vacuum spacetimes. The first DG implementation in non-vacuum spacetimes was published by Radice & Rezzolla [374], but was still restricted to spherical symmetry. The first three-dimensional (3D) implementation, albeit in a fixed spacetime and focused on hydrodynamics was developed by Bugner et al. [107, 108]. Miller and Schnetter [329] proposed an operator-based DG method suitable also for second-order systems and applied it to the BSSNOK system, while Kidder et al. [268] developed a task based relativistic magnetohydrodynamics code.

Within theis thesis, a novel first-order (FO) form of the CCZ4 system is presented, refered to as FO-CCZ4. The system's eigenstructure is studied and strong hyperbolicity is shown for a particular choice of gauges. Subsequently, different numerical implementations of this PDE system are discussed. The scheme is solved with the three dimensional code proposed in the previous chapter, using an ADER-DG algorithm with adaptive mesh refinement (AMR) and local time-stepping (LTS), supplemented with a high order ADER-WENO [234, 258, 307] finite-volume subcell limiter [166, 169, 174] to deal with singularities in black-hole spacetimes.

A series of standard tests for general-relativistic codes [8, 40] are adopted to demonstrate the stability and accu-

racy of both the PDE itself and its ADER-DG discretization. Verifications for the expected convergence order are given and long-time robustness and stability is proven. Finally, the scheme is applied at a long-term evolution of single black-hole spacetimes, showing that the new code is able to stably evolve a puncture black-hole spacetime for a time scale of $\sim 1000 M$ (M being the mass of the black hole). Preliminary results for the head-on collisions of two black holes are presented.

While the equations are given in a general way including matter terms, they are vanishing in the presented tests and Einstein field equations are only presented “in vacuum”. Scientific results of this chapter have been published in [168], as well as in [135, 274].

0.3 General relativistic Magnetohydrodynamics within the new framework

Chapter III on page 72 discusses relativistic hydrodynamics. It is the complementary topic compared to the previous chapter, concentrating solely on the right hand side of Einsteins equations.

In fact, electromagnetism plays an important role in many astrophysical processes such as compact objects and binaries consisting of black holes and neutron stars. The general-relativistic theory of magnetohydrodynamics (GRMHD) is a successful theory to describe these systems, combining the fluid description of matter with a simplified theory for electromagnetic fields in the absence of free charge carriers. Similar to general-relativistic hydrodynamics (GRHD), first successful (lower-dimensional) simulations of the GRMHD system date back to the pioneering work of [462] more than 40 years ago (See [202, 319] for recent reviews in the progress of GRMHD simulations).

In the past years, several groups started to recast the system of GRMHD equations into a conservative form in order to make use of conservative Godunov-type finite-volume schemes based on approximate Riemann solvers and high-resolution shock-capturing schemes (HRSC). Many GRHD and GRMHD codes have been developed over the last decade (for instance [23, 29, 31, 42, 105, 157, 161, 214, 270, 310, 364, 375, 377, 461]) and applied to various topics in astrophysics. Some codes also evolve the spacetime by feeding back the fluid and magnetic energy-momentum tensor in the Einstein field equations, which govern the time evolution of the metric tensor; some codes even incorporate radiation transfer like the one proposed by [428], or include the full Maxwell theory in a resistive relativistic MHD formulation [14, 22, 106, 157, 175, 358].

DG methods have attracted the interest of the computational-astrophysics community only over the last few years. In particular, the first DG-based method for general-relativistic hydrodynamics has been developed by [374], but it was limited to spherically symmetric spacetimes. The first three dimensional implementation of a DG method for relativistic flows on curved but fixed background spacetimes has been recently presented by [107], but without considering the magnetic field interaction. Recently, [268] provided a DG implementation within a task-based parallelism model for GRMHD, while [27] presented also a DG code with hp-refinement.

In this work, the previously introduced new numerical scheme is proposed for the solution of the GRMHD equations. Its shock capturing properties and high-order accuracy on spacetime adaptive meshes (AMR), supplemented by a high-order a posteriori subcell 2nd order TVD finite-volume limiter (adopted for shocks and discontinuities) make it well suited for the evolution of the MHD flow on curved background spacetimes. In fact, this method was already successfully applied on special-relativistic MHD equations (SRMHD) in [470].

An important and novel aspect of this approach is the interpretation of the source terms in the GRMHD equations that account for the gravitational field in curved spacetimes as separate nonconservative products. In other words, while the GRMHD equations are normally written in a flux-conservative form with a generic source term which holds derivatives stemming from the spacetime curvature, in the presented framework, it is written without an algebraic source but with a differential nonconservative term which is part of the system eigenstructure. This is a simple rewrite of the equations which neither changes its hyperbolic nature [25, 272] nor the fact that it is already first order, suitable for a large number of finite volume methods.

After the presentation of the modified PDE system, the solution of number of smooth and non-smooth (i.e., shocks and large gradients including) benchmark situations are provided which demonstrate the correctness of the PDE and the quality of its numerical solution.

The results of this chapter have been published in [194] and also in [135, 277, 406].

0.4 A general-relativistic criterion to separate prompt from delayed collapse in a binary neutron star merger

Chapter IV on page 95 is the first chapter discussing a purely astrophysically driven research topic where all the techniques developed in the previous chapters serve as a tool for modeling four dimensional spacetimes of astrophysical phenomena. The chapter presents research done in respect to the issue of lifetimes of binary neutron star collision remnants. Thanks to the first neutron star binary merger observations [437] which offers new insight into the nature of neutron stars, constraints in the properties of nuclear matter can be probed [26, 70, 112, 333, 336, 361, 373].

When two neutron stars merge, they will produce an object that either collapses promptly to a black hole, or does not [41]. In the latter case, the remnant may be a metastable object, e.g., a hypermassive neutron star (HMNS), eventually collapsing to a black hole on a secular timescale, or survive for much longer times, either as a rotating or a nonrotating star (see e.g., [43] for a review). In the case of the first detection of merging neutron stars, GW170817 [437], the precise fate of the merger remnant is presently unknown, although the formation of a black hole naturally matches the simultaneous observation of a short gamma-ray burst [186, 385], and has been the working hypothesis to set new limits on the maximum mass of neutron stars [316, 386, 395, 411].

Determining the time of collapse of the merger remnant is particularly challenging as there are a number of physical processes that either determine or undermine the stability of merger remnant. These include: the ejection of matter [95, 155, 289, 302, 372, 392], the angular-momentum transfer via magnetic fields [264, 269, 415], the evolution of the degree of differential rotation [232, 262], and possible viscous effects mediated either by neutrinos or magnetic fields [10, 160, 370, 412].

As already said, observationally, the two scenarios can be clearly kept apart by both the gravitational wave and electromagnetic spectra which are much richer in the case of the delayed collapse. A first attempt to separate prompt to delayed collapse can be made by the mass of the system M . It is simple to separate the two scenarios by a critical (threshold) mass M_{th} which distinguishes prompt collapses ($M > M_{\text{th}}$) from delayed ones ($M < M_{\text{th}}$), although it still poses numerical and conceptual challenges. Bauswein et. al. [68] have been the first to explore this problem by employing a smooth-particle approximation for the hydrodynamics and a conformally flat approximation to general relativity. In this way, they were able to find a linear universal relationship between M_{th} and the compactness of the maximum-mass model, $\mathcal{C}_{\text{TOV}} := M_{\text{TOV}}/R_{\text{TOV}}$, where M_{TOV} and R_{TOV} are respectively the mass and radius of the maximum-mass nonrotating star. Here, we improve on this result by using a fully general-relativistic approach, a wider range of compactnesses, and a rigorous definition of the threshold mass. As a result, we find a nonlinear relation between M_{th} and \mathcal{C}_{TOV} , which offers a better match to the numerical-relativity results. Furthermore, exploiting the information from GW170817, we use the new relation to set more stringent lower bounds on the radii of neutron stars [68, 70, 96]. The results presented in this chapter have been published in [275].

0.5 Quantum modified Schwarzschild solutions

Chapter V on page 107 discussed black hole spacetimes at the smallest scales. The Schwarzschild solution is only characterized by its mass M which can have any value. When it comes to quantum size black holes, a natural mass scale is given by the Planck scale, $M_{\text{Pl}} = \sqrt{\hbar c/G} \sim 2.1 \times 10^{-8} \text{ kg} \sim 5.6 \times 10^{27} \text{ eV}/c^2$, which is tiny compared to astrophysical scales but nevertheless huge when compared to the masses of the standard model particles. The theory of quantum mechanical black holes is called quantum gravity (QG), and its theoretical description is a long-standing problem, experimentally it also remains inaccessible. Quantum field theory on curved space (QFTCS) is an approximating theory to describe quantum matter on classical curved background space, and Hawking's famous result that quantum black holes are actually black bodies that emit thermal radiation at a temperature proportional to their surface gravity [238] belongs to this class of first order quantum gravity effects. As soon as the Hawking temperature comes in the regime of the Planckian black hole mass itself, this thermodynamical description breaks down.

Black holes also question the understanding of quantum mechanics itself. Conventionally the Compton wavelength is thought to assume arbitrarily small values, provided one smashes particles at higher enough energies. This way of reasoning, however, breaks down at the Planck scale. A Planckian black hole is expected to form

due to the collapse of particles at such extreme energies [3]. This is equivalent to saying that gravity is ultraviolet self-complete, *i.e.*, there are no propagating quantum degrees of freedom in the trans-Planckian regime and length scales below the Planck length are inaccessible [39, 123, 125, 178, 179, 180, 181, 182, 183, 204, 337, 348, 420]. Such features are effectively captured by a modification of commutation relations known as generalized uncertainty principle (GUP) [19, 21, 266, 312, 454], resulting in a modification of Heisenberg's uncertainty principle $\Delta x \Delta p \leq \hbar/2(1 + \beta(\Delta p)^2)$, where $\sqrt{\beta} \sim \ell_{\text{Pl}}$ and ℓ_{Pl} the Planck length. For $\Delta p \ll \ell_{\text{Pl}}$, length scales become proportional to Δp , as expected from the presence of a black hole in the trans-Planckian regime. For reviews see [249, 421, 434].

The GUP has been invoked to improve the scenario of black hole evaporation, that is customarily affected by a divergent profile of the Hawking temperature T in the terminal phase. With $\Delta p \sim T$ and $\Delta x \sim GM$, the temperature profile is no longer divergent and a Planckian black hole remnant forms as an evaporation endpoint [4, 5]. Such a remnant has also been considered as a candidate for cold dark matter component [136]. There are, however, potential problems at the basis of such results. Planckian remnants have Planckian temperatures. The surface gravity description of the temperature no longer holds.

To amend the above limitations, a new approach has been proposed in order to implement GUP effects in gravitational systems [254]. As a start, one can notice that the GUP introduces nonlocality by preventing infinitesimal resolution. Therefore one might be led to consider a nonlocal version of Einstein equations [60, 284, 331, 443], where nonlocal spacetime (*i.e.*, a nonlocal Einstein tensor, smeared by a operator-valued gravitational coupling constant) is coupled to classical spacetime (*i.e.*, the Schwarzschild source term). Such a theory can be either used to described large scale degravitating effects [34, 61, 62, 184] or short scale modified gravity theories [115, 204, 210, 332, 342]. One can select a specific smeared gravitational coupling constant $G_N^{-1}(L^2 \square)$ to reproduce the GUP momentum space deformation for the static potential due to virtual particle exchange. The resulting non-rotating black hole metric allows for horizon extremisation with consequent formation of a zero temperature black hole remnant at the end of the evaporation [254]. Such a black hole solution not only supersedes the aforementioned limitations of the scenario proposed in [4, 5], but offers additional interesting properties: it removes the scale ambiguity of the Schwarzschild metric and fulfills the gravity ultraviolet self completeness by preventing black hole radii smaller than the Planck length; it allows for a semiclassical description of the whole evaporation process and for the presence of a final heating phase (SCRAM phase [343]) before the remnant formation.

Within this thesis, the case of GUP effects in higher dimensional black hole metrics is studied. It should be noted that there is no unique prescription for the GUP in the presence of extra dimensions [290]. As a result, an analysis of the existing proposals [122, 123, 126, 159, 291, 292, 293, 320, 321, 322, 400] for the GUP in higher dimensions will be given.

The results presented in this chapter have been published in [290], while other are going to be published in an upcoming publication [276].

CHAPTER

I

Evolution equations on the computer

This chapter introduces techniques of solving evolution equations for physical systems with the help of a computer. After an introduction, a basic review of the literature, standard definitions and techniques is given. The focus is then turned to the codes used or developed within this work. Note that this chapter is with a slight focus on relativistic theories (in astrophysics), but kept technical and general. In contrast, chapter II is devoted to the Einstein equations and chapter III to hydrodynamics, where the actual equations are discussed in detail.

The results of this chapter have been published in [135, 168, 194, 274] and texts in this chapter are partially based on these publications.

1 Motivation: Hamiltonian time evolution

The broad class of “evolution equations” can be motivated by Hamiltonian dynamics: Given a Hamiltonian system, the Hamiltonian H allows to predict the value of any function $f = f(q, p, t)$ of canonical coordinates q, p and time t , once $f_0 = f(q, p, t_0)$ is known at an initial time t_0 . This can be written as

$$\frac{\partial f}{\partial t} = \{f, H\} = \frac{\partial f}{\partial q} \frac{\partial H}{\partial p} - \frac{\partial f}{\partial p} \frac{\partial H}{\partial q} \quad (1.1)$$

where the curly brackets indicate the Poisson bracket and the equation itself is a way to write Liouville’s theorem which holds for a broad class of physical theories such as classical mechanics and quantum mechanics, where at the latter, the Poisson brackets are replaced by the canonical commutator and equation (1.1) gets an abstract Schrödinger equation $\partial_f = [f, H]$ ¹.

The Hamiltonian equations of motion $\{\dot{q} = \partial_p H, \dot{p} = -\partial_q H\}$ can be written as a flux conservative evolution law²

$$\partial_t Q^k = \partial_i F^{ik}(Q) \quad (1.2)$$

for the two-dimensional phase space coordinate $\vec{Q} = (p, q)$ with gradient vector $\vec{\partial} = (\partial_p, \partial_q)$ and 2×2 flux matrix $F^{ik} = \epsilon^{ik} H(Q)$ determined by the Hamiltonian $H = H(q, p, t)$ of the system³.

The Hamilton-Jacobi equation (1.1) can be written as $\partial_t f = \dot{Q}_i \partial^i f = \partial_i \dot{Q}^i f$ since $\partial_i Q^i = 0$. This gives rise to also write it in flux conservative form (1.2), with an extended

$$\text{solution vector } \tilde{Q} = (\dot{Q}, f) \text{ and fluxes } \tilde{F} = \begin{pmatrix} F^{ik} & 0 \\ 0 & \dot{Q} f \end{pmatrix}. \quad (1.3)$$

¹ In fact, Chapter V on page 107 deals with modifying this commutator in order to introduce quantum effects into GR without doing canonical quantization.

² We use Einstein sum convention, repeated indices are summed over.

³ With ϵ^{ik} the Levi civita symbol in two dimensions (Appendix A1.2 on page 124). Note that in this chapter, the position of indices has no physical meaning (no covariant/contravariant tensors involved).

This conservation law rewrite exposes the conservation of f in phase space and gives rise to a probability distribution interpretation of f .

It is worth mentioning that in the mathematical initial value boundary problem, *time* is a name for the evolution direction and gets its semantic meaning only in physics ⁴. Ultimately, a “time evolution” is an *extension* from the boundary t_0 of a known domain, characterized by $t < t_0$, into an unknown domain $t > t_0$. An example where the evolution direction is not called time is the adoption of the Cauchy-Riemann equations, ⁵

$$\partial_x u = \partial_y v, \quad \partial_y u = -\partial_x v, \quad (1.4)$$

to perform an analytic continuation of a complex function $f(x, y) = u(x, y) + i v(x, y)$, with $z = x + iy$, from the real numbers to the complex domain. Then one can recast the imaginary axis as time, $t = y$, and write the PDE in flux conservative form $\partial_t Q_k = \partial_x F_k$ as a time evolution of Q_k in one-dimensional space (x), with state $Q = (u, v)$ and fluxes $F = (-v, u)$. As both the flux F and the function f are linear in Q , a holomorphic function (i.e., a solution to (1.4)) is conserved within analytic continuation.

⁴ Section 11 on page 44 provides another discussion of *time* in the Cauchy initial value formulation of general relativity.

⁵ an introductory example from [444]

2 Conservation laws

A general definition of a conservation law is

$$\partial_t u_k + \partial_i F_k^i(u) = 0 \quad (2.1)$$

and we call $\vec{u} = \vec{u}(t, \vec{x}) \in \mathbb{R}^n$ the conserved quantity or (system) state, $\vec{\partial} \in \mathbb{R}^d$ is the vector differential operator (Nabla operator) in d spatial dimensions. \vec{F}_k is called the *flux* for u_k , all fluxes $F_k^i \in \mathbb{R}^{d \times n}$ together encode the physical evolution law ⁶.

\vec{u} is frequently referred to as *state vector*, but in general no transformation properties as for a vector in physics are required within this chapter, and for the theories presented in this work, \vec{u} will not transform as a vector in physics. Instead, this object should be referred to as the *state tuple* of length $n \in \mathbb{N}$. While for conservation laws the distributional interpretation of \vec{u} suggests $u_i \in \mathbb{R}$, in general there is nothing prohibiting one from using alternative spaces, such as a complex state vector $u_i \in \mathbb{C}$, as well as elements u_i following any other transformation rule ⁷. In these cases, the state vector should collect all *degrees of freedom* of the mathematical objects it holds. Sometimes, (2.1) is written compactly in spacetime as $\partial_u F_k^\mu(u) = 0$, and $F_k^0(u)$ then allows to map u to the mathematical objects of interest.

⁶ All quantities introduced here should be understood as *fields* $\phi = \phi(t, \vec{x})$, and therefore $F(u)$ only has an implicit dependence on time and location. However, one can trivially make this dependence explicit by including the coordinates \vec{x} itself into the state vector.

⁷ For instance a state vector holding square matrix elements $u_i = m_{kj} \in M^{N \times N}(\mathbb{R})$, with the row-major sequentialization rule $i = f(k, j) = Ni + j$.

2.1 The non-conservative product

If one allows an arbitrary (differential) source term $\vec{\mathcal{S}} = \vec{\mathcal{S}}(u, \partial_i u)$ ⁸ to add sinks and sources for \vec{u} , the resulting modification of (2.1) is called a *balance law*,

$$\partial_t u_k + \partial_i F_k^i(u) = \mathcal{S}_k(u, \partial_i u). \quad (2.2)$$

Sources are a convenient way to formalize the coupling to other theories, however if a source term depends on derivatives of u , the differential separability of the balance law and an external theory is questionable. In order to formalize the differential structure of the PDE in question, the arbitrary source term \mathcal{S}_k shall be restricted to an *purely algebraic source term*

⁸ In this section, we restrict on first order theories, so any higher order derivatives of u are neglected.

$S_k = S_k(u)$. Instead, derivatives shall be collected in another in an explicit quasi-linear nonconservative term which couples to the gradient field of u , giving rise to a modified balance law

$$\partial_t u_k + \partial_i F_k^i(u) + B_k^{ij}(u) \partial_i u_j = S_k(u) \quad (2.3)$$

We refer to $B_k^j \in \mathbb{R}^{n \times n}$ as the non-conservative matrices ⁹ and to $B^i(u) \partial_i u$ as the non-conservative product (NCP) or the non-conservative flux (in contrast to the conservative flux).

The advantage of introducing the non-conservative product is that it can be straightforwardly included in the quasi-linear formulation (next section) and in numerical methods (Section 5.3 goes into detail about the inclusion in a Riemann solver).

2.2 Quasi-linear PDEs and their eigensystem

All evolution laws presented so far are first order partial differential equations (PDEs). There is a rich theory of this class of PDEs, based on casting the PDE as a quasi linear system

$$\partial_t u_k + A_k^{ij}(u) \partial_i u_j = S_k(u) \quad (2.4)$$

with the d system matrices $A^i \in \mathbb{R}^{n \times n}$ given by

$$A^i = A_k^{ij}(u) = \partial F_k^i(u) / \partial u_k + B_k^{ij}(u) \quad (2.5)$$

and sometimes also called velocity matrices. The theory of hyperbolic PDEs investigates the system matrixes A^i in an eigenvalue analysis. Therefore, the *differential* contributions to (2.4) are recognized as part of a *differentially* linear system ¹⁰. In the eigenbasis, the system decouples to n advection equations of type $\partial_t \phi_k + \lambda_k \partial_i \phi_k = 0$, where ϕ_k are called the characteristic fields. The eigenvalues λ_k are recognized as the fundamental propagation speeds of waves in a hyperbolic system. ¹¹

Higher order PDEs have to be rewritten to first order to reveal their characteristic structure. A classic example is the one dimensional wave equation [444]

$$\partial_t^2 \phi - c^2 \partial_x^2 \phi = 0 \quad (2.6)$$

which is trivially rewritten as two first order equations, by means of factorizing the differential operator

$$(\partial_t - c \partial_x) \underbrace{(\partial_t + c \partial_x)}_{:=\psi} \phi = 0, \quad (2.7)$$

where the auxilliary field ψ was introduced and a set of two couple PDEs is obtained,

$$\partial_t \psi - c \partial_x \psi = 0, \quad \partial_t \phi + c \partial_x \phi = \psi. \quad (2.8)$$

The first order in time and space formulation of the wave equation (2.8) can then be brought into quasi-linear form (2.4) and then immediately exposes the wave speeds $\pm c$, since A^x is diagonal,

$$\partial_t \begin{pmatrix} \psi \\ \phi \end{pmatrix} + \underbrace{\begin{pmatrix} -c & 0 \\ 0 & +c \end{pmatrix}}_{A^x} \partial_x \begin{pmatrix} \psi \\ \phi \end{pmatrix} = \begin{pmatrix} 0 \\ \psi \end{pmatrix}. \quad (2.9)$$

⁹ To avoid confusion, all indices are given in equation (2.3). However, again, the index position has *no* meaning in terms of contra/covariant. In three dimensions, $B = (B_b^{1a}, B_b^{2a}, B_b^{3a})$ is a vector of three $\mathbb{R}^{n \times n}$ matrices. The same applies for the system matrices A^i introduced in (2.4).

¹⁰ That means especially that the purely algebraic sources S do not contribute to the characteristic form.

¹¹ see for instance classical textbooks about hyperbolic systems [303, 444]

Depending on the eigenvalues of A^i , the PDE system is called elliptic (not a single real eigenvalue, an example is the Poisson equation $\partial_i \partial^i u = f$ where the wave speeds are unlimited), parabolic (an example is the heat equation $\partial_t u - \alpha \partial_i \partial^i u = 0$) or hyperbolic (n real eigenvalues, as the presented wave equation (2.8)). Weak hyperbolicity is given if the set of eigenvectors is not complete (i.e., A^i not diagonalizable), while strong hyperbolicity is given with a complete set of eigenvectors (and real eigenvalues). Strict hyperbolicity is given with n distinct eigenvalues. Symmetric hyperbolicity is given when A^i is symmetric and thus diagonalizable (see Figure 2.1 for a diagram). In one spatial dimension, all strongly hyperbolic systems are also symmetric hyperbolic.

Weakly hyperbolic PDEs suffer from well-posedness, i.e., small perturbations in the initial data can change the solution dramatically (Appendix A2). In contrast, strongly hyperbolic systems can be decomposed into independent advection equations (characteristics) with the help of a symmetrizer matrix which is composed by the (right) eigenvectors. The different finite wave speeds of the characteristics are given by the eigenvalues of the system matrix, which accounts for the wave-like nature associated with hyperbolic systems.

Stiffness is another feature which can be derived from the eigenstructure: PDEs which describe phenomena on very different timescales. Stiffness is defined by the ratio $R = \lambda_{\max}/\lambda_{\min}$ between the largest and the smallest eigenvalue (wave speed), and a large stiffness $R \gg 1$ can be challenging for a computer-aided solution.

For linear PDEs, where $A^i(u) = A^i$ does not depend on the state u and thus the quasi-linear form is also algebraically linear, any PDE can be reduced to ordinary differential equations (ODEs) by separation of variables. For nonlinear systems, fundamental definitions of existence and uniqueness of a solution to the PDE must be solved. A popular example are the harmonic solutions of Laplace's equation which are obviously non-unique in the vicinity of boundary conditions. Appendix A2 contains a couple of standard mathematical definitions of convergence, consistency and stability.

2.3 The Riemann problem

The Riemann problem is a general initial value problem with initial data

$$u_0(x) = u(t_0, x) = u_L \Theta(x - x_0) + u_R \Theta(x_0 - x) \quad (2.10)$$

separating a left state u_L from a right state u_R at x_0 with the Heavyside step function $\Theta(x)$ ¹². Within fluid dynamics, there is a straightforward interpretation of the problem: It models a tube with a membrane that separates two different fluid states (for instance with different densities). The membrane is removed at $t = 0$. The system equilibrates, and due to the discontinuity, the different wave speeds of the system can be recognized [303, 444]. The resulting waves have a physical and mathematical meaning. Mathematically, the waves expose the characteristics of the system. Physically, the three different eigenvalues of hydrodynamics¹³ manifest in three different types of shock waves: Contact discontinuities (an equilibrium surface

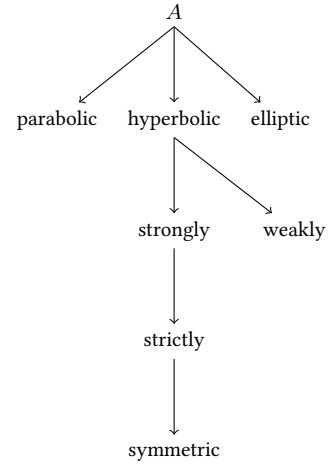


Figure 2.1: Standard classification of (first order) PDE systems depending on the system matrix A . The relationship $x \rightarrow y$ means that each y has also all properties of x (i.e. each y is a x), but not the other way around.

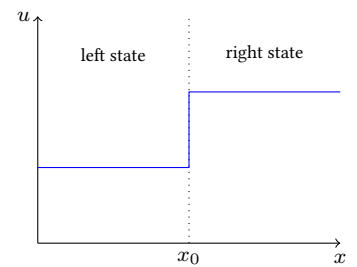


Figure 2.2: Initial value cartoon for the generic one dimensional Riemann problem (2.10).

¹² See symbol definitions at Appendix A1.2 on page 124.

¹³ Chapter III is devoted to hydrodynamics. Classical Euler equations and its eigenvalues are discussed in Section 19.1 on page 74.

seperating the two states), shock waves (accompanying compression) and rarefaction waves (accompanying expansion).

Nonlinear systems (such as Euler equations) can develop shocks in finite time even in the case of smooth initial data, this makes the Riemann problem as the formalization of discontinous (initial) data especially interesting. In numerical schemes for nonlinear systems, the occurence of shock waves introduces one of the most challenging problems. Shock waves have a number of undesirable features, such as the reduction to first order around the shock wave and complete loss of convergence at the discontinuity, as well as the introduction of persistent artificial oscillations around the discontinuity.

The Riemann problem is a key part of Godunov's method (Section 5). Due to its relevance in hydrodynamics, part of the demonstration of the correctness of a fluid dynamics code are the numerical solutions to one dimensional Riemann problems. The exact reference solution is not known analytically, but iterative solutions are possible. [14](#)

3 Solving PDEs with machines

When it comes to solving partial differential equations, numerical methods are a powerful tool for evolving equation systems without approximations (simplifications) [15](#). Numerical mathematics (also referred to as numerical analysis) is the discipline which studies the effects of numerical approximations of continous theories. It is worthwhile to say that while efforts are to *reduce* the discretization errors in practice, it is much more important to understand and *control* them in the first place. [16](#)

Nowadays, the term “computer” usually refers to a register machine which excels at doing basic arithmetic operations on lists and tables of numbers, typically with the IEEE 754 floating point arithmetic operations (FLOP). Clearly the engineering efforts in the last decades demonstrated the power of this technology, nowadays a consumer-grade laptop (notebook) can compute up to $\sim 10^{11.5}$ FLOP/second while a supercomputer is capable of roughly $\sim 10^{17.5}$ FLOP/sec. Furthermore, the contemporary meaning of a “supercomputer” is a cluster of up-to-date processors, i.e., causally speaking, a network of $\sim 10^6$ consumer-grade laptops. Therefore, the central topic of computer engineering a modern PDE code is *parallelization*. The remaining sections of this chapter are dedicated to schemes which satisfy concurrency challenges of the upcoming generation of supercomputers.

However, the way computers represent numbers and implement arithmetics is neither self-evident nor unique. In the following, two non-numeric approaches to computationally backed up PDE time evolution shall be given.

3.1 Symbolic computing

In the 1950s it was a widespread belief that scientific computers would *only* be capable of doing numerics [93]. Mainly driven by the young research branch of artificial intelligence, new programming languages were developed (the family of functional languages, such as LISP [323]) or formally specified (based on the Lambda calculus model of computation) which demonstrated that von-Neumann register machines are well capable of do-

[14](#) Riemann problems for the GRMHD equations are discussed in Section 24.1 on page 86, where their exact solution was for instance explored in [215].

[15](#) for a particular discussion of approximations to the equations vs. approximations to space and time see Section 10 on page 43 about solution attempts in general relativity.

[16](#) Any method which promises “neglectable” errors fails to comply the central scientific claim of numerical mathematics, namely quantitatively understanding errors.

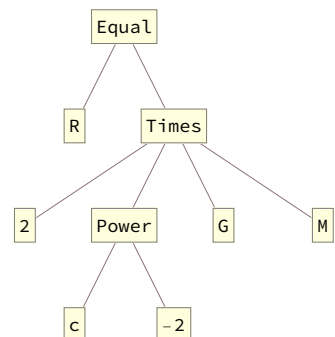


Figure 3.1: An exemplaric representation of $R = 2GM/c^2$ as an expression tree, produced by the Mathematica expression `TreeForm[R==2GM/c^2]`.

ing *symbolic* mathematics (instead of *numeric* mathematics). In the modern scientific computing landscape, these approaches are bundled in Computer Algebra Systems (CAS) which provide an orthogonal approach to numerical computations. For instance, all modern computer-driven perturbative approaches (in the weak-field regime of field theories) are ultimately based on this symbolic machinery. An exemplaric code in quantum field theories is `xloops` (based on `giNaC`) for evaluating Feynman diagrams up to thousands of orders [102, 416]. In fact, computer algebra is also very prominent in general relativity (see [311] for a review). An example for a popular CAS package is `SageManifolds` (based on `Mathematica`) [81, 223, 224], as well as the `Mathematica` based `Kranc` code for generating tensorial evolution equations [252, 301].

Symbolic computing has an abstract syntax tree as fundamental data structure (Figure 3.1). In contrast, numerical computing uses tables of numbers as fundamental data structure. Delayed evaluation has no relevance in numerical schemes. In practice, the CAS frequently serves as a preprocessor to generate numerical code or as a general tool in the daily work of a data scientist to manipulate and study lengthy expressions ¹⁷.

3.2 Analog computing

Another example is in the domain of *analog computing*, a form of building computing machines especially popular in the 1950s. Analog computers excelled at solving differential equations. Such a computer was “programmed” by modeling the physical problem with an electrical analog (therefore the name), i.e., connecting inductors, capacities and ohmic resistors in a way that the currents or voltages in the electric circuit are determined by the same PDE as the actualy problem which shall be solved. Figure 3.2 shows a simple example which already shows an abstraction layer, as the electrical circuit components are high level building blocks such as integrators and summers.

While analog computers disappeared from the frontline of computing in favour of digital computers, even today there is active research stating that analog computers could solve PDEs in a parallel and energy-efficient way, as it is out of reach for digital processors [451]. It is likely that analog computing will enjoy a similar revival as vector computing did, in terms of an integration in modern computer generations. Analog parts could be casted as coprocessors or accelerator units in the same way as graphic cards and dedicated computing cards are used today.

In fact, analog models of gravity is a research field on its own [49, 58], where modern attempts date back to 1980s proposals of Unruh about accessing black hole evaporation in fluid flows determined by analog laws [452]. However, general relativity was not solved on analog computers yet, and this remains a research program for the future.

¹⁷ The first order CCZ4 system in Section 14 on page 52 is in fact derived and manipulated with several CAS (`Mathematica`, `Maple`, `sympy`).

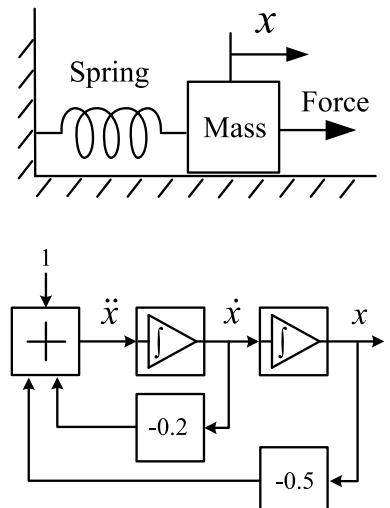


Figure 3.2: Sketch of a damped oscillation as a toy problem from classical mechanics, described by the ODE IVP $\ddot{x} = -0.2\dot{x} - 0.5x + 1$ with ID $x(0), \dot{x}(0)$. The lower panel shows the electrical circuit to solve the *analogue* problem. Adopted from [230].

4 Time and Space discretizations

After the excursion of section 3, for the rest of this work, all PDEs are subject to a *numerical* solution (if not mentioned otherwise). This requires to discretize the continuum problem in a suitable way. The classical literature

distinguishes between temporal and spatial discretization ¹⁸. This section is a short survey in basic grid based methods with focus on “semi-discrete” time integration techniques in order to solve PDEs such as (2.3). In contrast, the subsequent Sections 5 on page 26 and 6 on page 29 cover fully discrete techniques, i.e., approaches which allow for the PDE solution in a single (uniform) spatial and temporal discretization procedure.

¹⁸ Where the “temporal” direction (dimension) is characterized by the (volatile) evolution direction while the “spatial” directions (dimensions) define the spatial simulation domain which is hold in memory.

4.1 Semi temporal discretization

A scheme with spatial discretization, but without a similar (explicit) temporal one is called *semi discrete*. Semi discretization is a popular term in literature and may be misleading: In a numerical attempt to solve PDEs, eventually both the spatial and the temporal dimensions must be discretized. However, the different treatment of the temporal and spatial differential operators as well as the non-discretization in temporal direction between discrete timesteps (Figure 4.1) is a motivation to adopt the term “semi discrete”.

The *method of lines* (MoL) is a particular example of a semi temporal method. The idea in MoL is to recast the PDE describing $u_k(x_i, t)$ into $n \times N$ ordinary differential equations (ODEs), with n the state vector length and N the number of points x_i covering the spatial domain Ω ¹⁹. That is, the MoL solves one ODE in time (from initial data t_0 to t_1) for every (discretized) spatial point and field, that could be denoted as

$$\partial_t u_k(x_i, t) = \mathcal{R}(x_i, u_k(t_0), \partial_j u_k(t_0)) \quad (4.1)$$

where the spatial differential operator \mathcal{R} collects all PDE terms of (2.3). Popular ODE time integrators are Euler’s method or the higher order nonlinear total-variation diminishing (TVD) or strong stability preserving (SSP) Runge-Kutta (RK) methods (see Appendix A2 for details). These are explicit (dependency at time t only on $t_0 < t$, not $t_1 > t$) single-step (no dependence on $t < t_0$) methods and easy to implement. Another popular example for ODE integration are linear multistep high order integrators, such as the Adams-Basforth (AB) method which represents the field with polynomials in time. The cost to pay for high order methods is the need for repeatedly evaluate/update the right hand side (RHS) in (4.1), which requires evaluating spatial derivatives, which implies communication.

Implicit or backward methods such as the Crank-Nicholson are popular for stiff PDEs due to their small domain of dependency (i.e., the spatial region which influences the solution at a given point due to causality / characteristic speeds) or for when the timestep size is constrained by a spatial discretization method (such as in the Discontinuous Galerkin method, see below). Implicit methods allow larger timesteps compared to explicit methods. On the other hand, the solution for a time t has to be found by solving an implicit equation (e.g., iterative root finding).

For special problems, sophisticated time integrators beyond the MoL exist which take particular problem properties into account. For instance, a symplectic integrator scheme conserves the momentum space volume $dp dq$ during the integration of Hamilton’s equations by evolving the coupled canonical coordinates p and q .

¹⁹ Note that the MoL approach is invariant under the spatial discretization. It does not require any particular grid.

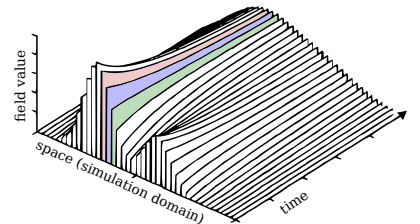


Figure 4.1: Motivation for the naming *Method of Lines* (4.1): The lines are the individual solutions at certain positions within the spatial domain, over the simulation time. This figure illustrates that space is discretized but time is not. The three coloured lines (“slices” in the height-elevated plot) are neighboured: In order to determine the time evolution of the blue slice, information from the green and red slice have to be taken into account.

The example shows a scalar diffusion equation $\partial_t \phi = \kappa \partial_x^2 \phi$ with arbitrary κ and initial field $\phi_0 = \frac{1}{2} \exp\{-(x-1)^2 + \exp(-(x+1)^2)\}$. It is modified and colorized from [402].

4.2 ADER time integration

The ADER technique (from Arbitrary high order DERivatives) was pioneered by Toro and Titarev [438, 439, 447] in the context of Finite volume schemes (Section 5). It bases on the idea of tayloring the time evolution in (4.1),

$$\partial_t u_k(x_i, t) = \sum_{l=0}^N \frac{t^l}{l!} \partial_t^l u_k(x_i, t_0), \quad (4.2)$$

so that $\Delta t = t - t_0$, and then expressing the l th order temporal derivative with spatial derivatives which are obtained by the PDE weak form and partial integration with a N th order test function, similar as it will be presented in Section 6. This way, the time update relies on the N th order spatial discretization and can be computed analytically to N th order.

The ADER approach leads to arbitrary high-order accurate fully discrete one-step schemes in space and time. The arbitrariness here is just represented by the fact that $N \in \mathbb{N}$ can be chosen freely (with bigger N resulting in higher computational cost, of course). *one-step* effectively means no repeated evaluation of the (4.2) RHS. This is the communication-avoiding property of the ADER approach which pays off on massively parallel grids. ²⁰

²⁰ Appendix A3 on page 127 compares the ADER time evolution with the Runge-Kutta one.

4.3 CFL factor

In hyperbolic systems, the temporal discretization is limited by the spatial discretization. The formalization for limiting the timestep size $\Delta t = t_1 - t_0$ is known as the Courant-Friedrichs-Lowy (CFL) condition. The argument can easily be derived by the classical kinematic law $s = v \cdot t$, with s the traveled distance of a particle moving with constant velocity v over time t . Given the distance $\Delta x = \Lambda_i \Delta t$ traveled by a system's wave with characteristic (eigenvalue) λ_i , the maximum timestep is therefore constrained from above,

$$\Delta t \leq \Delta x / \Lambda, \quad (4.3)$$

with Λ the maximum of the systems eigenvalues λ_i . In practice, the inequality (4.3) is replaced by $\Delta t = C \Delta x / \Lambda$ with $0 < C \leq 1$, where the arbitrarily chosen C is called the CFL or Courant factor.

4.4 Methods for spatial discretization

For spatial discretization, there exist a couple of standard classes with different attempts. While adopting a somewhat regular grid (Figure 4.2) is probably obvious (Section 7 discusses grid meshing in detail), there is a whole class of *meshfree* methods. A particular example is smoothed-particle hydrodynamics (here coordinates move with the fluid), which is in particular popular in astrophysics, since it easily allows to cover several orders of magnitude in length scales. Hybrid attempts exist, such as Particle-in-cell (PIC) approaches which combines particle methods with grid based ones.

Another general class of methods are *spectral* methods where the simulation domain Ω is covered by a function basis [241]. This is typically used for smooth problems where Fourier series can be used to eliminate differential operators. Formally, spectral methods belong to *finite element* methods (FEM) which first subdivides the computational domain Ω by a

finite number of (typically) nonoverlapping elements Ω_i where the spectral methods are then applied within (see also Section 6.1). Finite-element methods are known also under the name of variational-difference or projection-difference methods [211, 390].

Finite volume methods (FVM or just FV) share some features with FEM, and these two terms can be used in some respect synonymously, whereas “FEM” has a slight focus on meshing topologies and embedding of methods within single cells, while “FVM” has to some extend a focus on the integral formulation and interfacing of cells (Godunov’s method, Riemann problem), typically implemented around a grid with small volumes around spatial points.

A clear distinction however can be made between FV and *finite differences* (FD) methods. In the later method, the PDE is solved by employing the finite difference quotient between certain connected points in a grid, while a FV scheme works on volume and surface integrals, applying Gauss’ theorem.

4.5 Finite-difference schemes

Finite differencing is probably the most straightforward way of solving differential equations on a computer. The starting point and origin of the name is to undo the infinite limit $h \rightarrow \infty$ of the difference quotient

$$\frac{df(x)}{dx} \approx \frac{f(x+h) - f(x)}{(x+h) - x} \quad (4.4)$$

By choosing a finite but small h , the spatial differential operator in the Method of Lines (4.1) can be computed. The most simple way to implement this is to discretize space on a finite number of grid points $x_i = i\Delta x$, store the function values $f(x_i) = f_i$ and set $h = \Delta x$.

The concept is easily extended to generic finite differencing stencils (Figure 4.2), higher dimensions and arbitrary order derivatives ($df/d^n x$). Finite differencing techniques are popular for being computationally cheap and easy to implement. For instance, there is no need to cast a PDE system into a particular form (such the nonconservative form (2.3)) and rectangular regular grids as well as differential stencils can be represented by (continuous storage) arrays.

A major drawback of obtaining high order in a large simulation is the appearance of *ghost points* outside the simulation domain. In a naive cartesian domain decomposition for the parallel evaluation of the differential operator, the “ghost halo” fraction can quickly make a substantial part of the simulation domain on the computer which is especially costly when it comes to data exchange in the boundary (Figure 4.3).

A numerical drawback of high order finite differencing schemes is the unsuitability for discontinuous solutions where the large stencil will generate spurious solutions. This makes them unattractive for nonlinear conservation laws. On the other hand, such problems do not occur in linear and linearly degenerate systems ²¹ where no shocks can be generated if the initial data is not discontinuous itself.

Finite difference methods can be “fortified” with a number of methods such as *artificial dissipation* for stabilisation [285]. Another typical choice

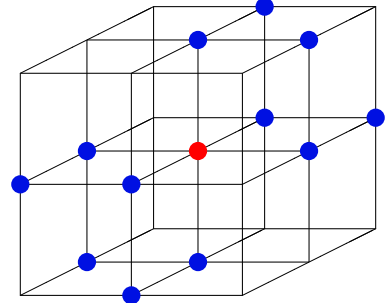


Figure 4.2: Example of an arbitrary three dimensional finite differencing stencil. Dependent points (blue) are neighbouring the evaluation point (red). In order to compute the derivative of a field on this grid at the red point, all dependent points in a certain direction projection are taken into account. (coloured from [217])

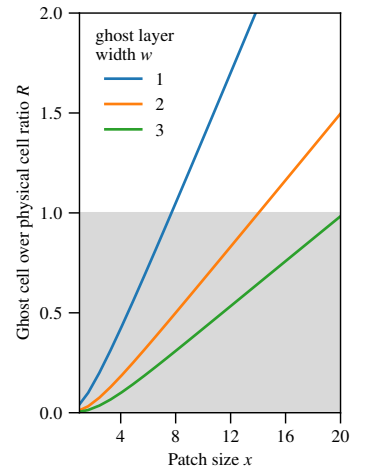


Figure 4.3: Ghost cell volume $G = 12xw^2 + 6x^2w + 8w^3$ to actual physical domain $V = x^3$ ratio $R = G/V$ in three dimensions for different ghost layer widths w (i.e., half the stencil sizes in FD context). On the abscissa, the width x of a cuboid (domain or patch) is given in number of cells. These small patches are realistic in the ExaHyPE AMR code, while traditional codes such as Cactus have an order of magnitude larger cells.

²¹ In section 14 on page 52 it will be shown that parts of a particular formulation of Einstein equations, the CCZ4 equations, can be written in a linear degenerate way.

for hyperbolic conservation laws are special *upwinding* stencils to correctly track the system characteristics. Both topics are typically covered by Riemann solvers in FV schemes and implementing them explicitly in FD schemes can be seen as a hardening of the simple FD schemes in order to gain robustness by maintaining a computationally and logically cheap scheme. In the same way, FD can also be used empowered with high resolution shock capturing (HRSC) techniques.

5 Finite-volume schemes

Finite-Volume schemes discretize the simulation domain Ω into cells Ω_i which shall hold *cell averaged* or *piecewise constant* solutions. It was the insight of Godunov in 1959 [218] to solve then the Riemann problem (Section 2.3) at these interfaces in order to solve the PDE. Godunov's method itself is fully discrete in time and space, but its time update can easily be replaced by the method of lines (Section 4.1). For recent reviews for FV in relativistic astrophysics, see [202, 318].

5.1 Godunov's scheme

A finite volume scheme works on the average value $\bar{\mathbf{u}}_i^n$ of the state vector within a spacetime-cell $[t^n, t^{n+1}] \times \Omega_i$, and for simplicity we work in one dimensions in this subsection, so $\Omega_i = [x_i, x_{i+1}]$, $\Delta t = t^{n+1} - t^n$ and $\Delta x = |\Omega_i| = x_{i+1} - x_i$. The cell barycenter is located at $x_{i+1/2} = x_i + \Delta x/2$ and the cell average given by

$$\bar{\mathbf{u}}_i^n := \frac{1}{|\Omega_i|} \int_{\Omega_i} \mathbf{u}(t^n, x) \, dx. \quad (5.1)$$

Godunov's scheme can be derived by integrating the PDE (2.3) in time and applying the piecewise constant assumption $\mathbf{u}(t, x) \equiv \bar{\mathbf{u}}_i^n$ for $t \in [t^n, t^{n+1}]$. The time integral collapses and allows to write

$$\mathbf{u}_i^{n+1} = \mathbf{u}_i^n - \frac{\Delta t}{\Delta x} (\mathbf{f}_{i+1/2} - \mathbf{f}_{i-1/2}) + \frac{\Delta t}{\Delta x} \mathbf{B} \cdot (\mathbf{u}_{i+1/2}^n - \mathbf{u}_{i-1/2}^n) + \Delta t \mathbf{S}(\mathbf{u}_i^n). \quad (5.2)$$

Here, a couple of remarks are necessary: First, this scheme is obviously fully discrete in space and time, as well as explicit in time. The conserved flux was replaced by a numerical flux which is thanks to the piecewise constant assumption just given as

$$\begin{aligned} \mathbf{f}_{i-1/2} &= \frac{1}{2} (\mathbf{F}(\mathbf{u}_{i-1/2}^-) + \mathbf{F}(\mathbf{u}_{i-1/2}^+)) = \frac{1}{2} (\mathbf{F}(\mathbf{u}_{i-1}^n) + \mathbf{F}(\mathbf{u}_i^n)), \\ \mathbf{f}_{i+1/2} &= \frac{1}{2} (\mathbf{F}(\mathbf{u}_{i+1/2}^-) + \mathbf{F}(\mathbf{u}_{i+1/2}^+)) = \frac{1}{2} (\mathbf{F}(\mathbf{u}_{i+1}^n) + \mathbf{F}(\mathbf{u}_i^n)). \end{aligned} \quad (5.3)$$

Second, since Godunov's method is first order, the nonconservative contribution vanishes as the boundary extrapolated data are equal, $\mathbf{u}_{i+1/2}^n - \mathbf{u}_{i-1/2}^n = 0$. The nonconservative source term \mathbf{B} therefore vanishes.

The essential idea of Godunov is now that with the piecewise constant assumption, a Riemann problem can be solved at each cell interface. The initial data for the Riemann problem between x_i and x_{i+1} is then given by the two cell values

$$\mathbf{u}(t^n, x) = \mathbf{u}_i^n \theta(x - x_{i+1/2}) + \mathbf{u}_{i+1}^n \theta(x_{i+1/2} - x) \quad (5.4)$$

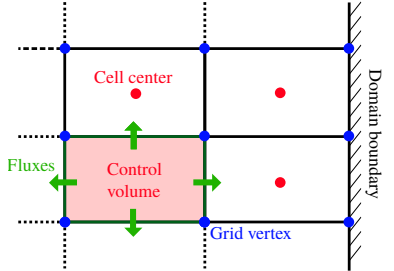


Figure 5.1: Finite volume simulation domain and terminology in an exemplaric simple two-dimensional Cartesian grid with rectangular cells. Shown are the cell barycenters, the cell corners, a domain boundary, the fluxes/waves which are described by the Riemann problem for a single highlighted demonstrator cell.

with Heaviside step function $\theta(z)$. Once the Riemann problem is solved, also the time update (5.2) is given [22]. We call equations of type (5.3) Riemann solvers and in fact this simple one is already sufficient for first order Godunov. However, there are more sophisticated Riemann solvers which do not make the piecewise constant assumption. Popular choices are the Roe solver and HLLE solver (see next Sections).

5.2 Higher order finite volume

Higher order FV is achieved by improving description of the interface state values \mathbf{u}^\pm by taking next-to-neighbour cells into account. The simplest possibility is to switch to a piecewise linear 2nd order description where $\mathbf{u}_i(x) = \mathbf{u}_i + v_i(x - x_i)$ within a cell (Figure 5.2).

TVD conditions lead to non-linear limiting of slopes, such as the minmod limiter. In general, a k th order reconstruction operator

$$\mathcal{R}[\mathbf{q}_i] = \lim_{y \rightarrow x_i} \mathbf{q}(y) + \mathcal{O}(\Delta x^k) \quad (5.5)$$

applied at a cell average at position x_i reconstructs the continuous field \mathbf{q} locally around x_i . Successful methods used in the literature are for instance the piecewise parabolic method (PPM), the essentially non-oscillatory (ENO), the weighted essentially non-oscillatory (WENO) and the monotonicity-preserving (MP) [376]. All of them are high resolution shock capturing, i.e., they preserve a good resolution at discontinuities and do not introduce spurious oscillations.

Similar as to FD methods, for a k th order reconstruction, the domain of dependency includes k neighbouring cells per dimension. Reconstruction operators can also be formulated in stencils which look like FD stencils.

5.3 Riemann solvers and the nonconservative product

The generic integral form for solving (2.3) with FV introduces a space and time integral,

$$\mathbf{u}_i^{n+1} - \mathbf{u}_i^n - \iint_{T^n \partial \Omega_i} \mathcal{F}(\mathbf{q}^-, \mathbf{q}^+) d^d x dt = \iint_{T^n \Omega_i} [\mathbf{S}(\mathbf{q}) - \mathbf{B}(\mathbf{q}) \cdot \nabla \mathbf{q}] d^d x dt. \quad (5.6)$$

Here, \mathcal{F} is the numerical flux at the element interface. If not mentioned otherwise, a simple Rusanov Riemann solver is used [397],

$$\mathcal{F}(\mathbf{q}_h^-, \mathbf{q}_h^+) \cdot \mathbf{n} = \frac{1}{2} (\mathbf{F}(\mathbf{q}^+) + \mathbf{F}(\mathbf{q}^-)) \cdot \mathbf{n} - \frac{1}{2} |\Lambda_i| (\mathbf{q}^+ - \mathbf{q}^-) \pm \frac{1}{2} \mathbf{B} \left(\frac{\mathbf{q}^+ + \mathbf{q}^-}{2} \right) \cdot \mathbf{n} (\mathbf{q}^+ - \mathbf{q}^-). \quad (5.7)$$

Note that for the piecewise constant approximation (Godunov's first order scheme), $\mathbf{q}^+ = \mathbf{q}^-$ and (5.7) reduces to (5.3).

It should be stressed that the use of the nonconservative product within the Riemann solver/path conservative integration is *not* required per-se. It would have been equally possible to integrate a differential source in a non-path conservative way. However, the special treatment allows it to formulate well-balanced numerical methods [74].

The inspiration to use path-conservative schemes for nonconservative products has been taken from successful developments in the context of

²² The CFL conditions (4.3) must be fulfilled and the scheme can be easily extended to higher dimensions in a dimension-by-dimension fashion.

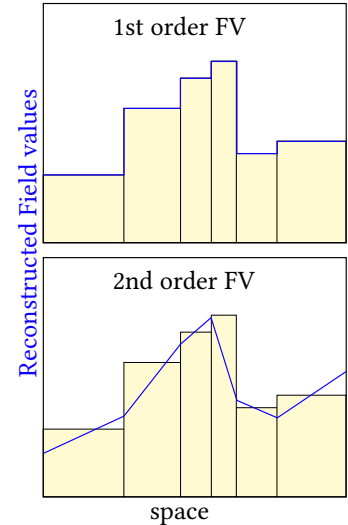


Figure 5.2: Cartoon which demonstrates how higher order reconstruction of the field works: While a first order reconstruction method assumes cells to have an average value (cells in this one-dimensional example are non-uniformly sized), in a second order reconstruction (think of a Taylor expansion in each cell, with a linear term) the field is approximated by taking neighbouring cells into account. In general, requirements such as a continuity condition do not necessarily have to be fulfilled, while they typically are desirable in schemes.

well-balanced numerical methods for the solution of the shallow-water equations [129, 130, 359], where the bottom-slope term (which is the gradient of a known function and accounts for gravitational forces in shallow-water models) is discretized as a nonconservative product in the principal part of the system rather than as a classical algebraic source term. In the shallow water context, the family of path-conservative schemes allows to preserve certain stationary equilibrium solutions exactly up to machine precision also on the discrete level, including nontrivial equilibria [208, 209].

5.4 MUSCL-Hancock

The second-order accurate MUSCL-Hancock TVD finite-volume scheme [448] is the second-order FV scheme available in ExaHyPE. It has proven robustness in the presence of shock waves and low density atmospheres. Formally, the second-order MUSCL-Hancock scheme can be derived from the PDE (2.3) as in (5.6).

High order in space, together with non-oscillatory properties, are achieved via a nonlinear reconstruction of piecewise polynomials from the known cell averages $\bar{v}_{i,s}^n$ using a TVD reconstruction. In order to preserve high resolution shock capturing properties, high order reconstruction requires slope limiting (also referred to as flux limiting). Such a limiter allows to restrict the order of the scheme at discontinuities. In ExaHyPE, different slope limiters were implemented, such as the *minmod* [391] or the *Koren* limiter [282].

Particularly relevant for ExaHyPE is the fact that in this code, the reconstruction stencils at patch boundaries lack isentropy (Figure 5.3). In ExaHyPE, corner cells are not synchronized for performance reasons (especially because it is primarily a DG code and DG does not require the knowledge of corner values). This requires the FV reconstruction in $d \geq 2$ dimensions to stick to a + shaped stencil at the corner (domain $A \cup B$ or $a \cup b$ in Figure 5.3), i.e., the field information c is not available, while B and b is. For slope limiting, a conservative estimate (guess) on the slopes has to be made. The problem does not occur in a first order scheme where no reconstruction takes place.

5.5 WENO

As an alternative to the MUSCL scheme, an arbitrarily accurate ADER-WENO finite-volume schemes can be used in the ExaHyPE prototype. The weighted essentially non-oscillatory (WENO) approach does not clip local extrema, in contrast to the second-order TVD method. For fluid dynamics (Chapter III) the TVD scheme was found to be more robust than the WENO scheme.

The (ADER-) WENO scheme shares many aspects of the (ADER-) DG schemes presented in the subsequent Section 6. The spacetime predictor solution q_h is however computed from an initial condition given by a WENO reconstruction polynomial $w_h(x, t^n)$ computed from the cell averages $\bar{u}_{i,s}^n$ via a multi-dimensional WENO reconstruction operator detailed in [167, 176, 258]. The values at the cell interfaces q_h^- and q_h^+ are computed as the boundary extrapolated values from the left and the right subcell adjacent to the interface.

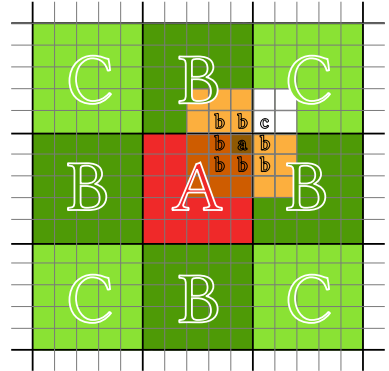


Figure 5.3: Cartoon of the ghost cell optimization in ExaHyPE: Patches are denoted with upper case letters (A, B, C), while embedded FV subcells are denoted with lower-case letters (a, b, c). The letter a refers to the patch/cell which solution shall be computed. The letters b refer to their direct neighbours (sharing a face), while the letters c refer to the corners (sharing an edge). Two ghost layers are drawn. Here, the information in the domain $C \cap c$ is not available.

The nonlinear WENO reconstruction works as follows: for each subcell $\Omega_{i,s}$ we compute several reconstruction polynomials $\mathbf{w}_h^k(\mathbf{x}, t^n)$ requiring integral conservation of \mathbf{w}_h^k on a set of different reconstruction stencils $\mathcal{S}_{i,s}^k$,

$$\frac{1}{|\Omega_{i,j}|} \int_{\Omega_{i,j}} \mathbf{w}_h^k(\mathbf{x}, t^n) d\mathbf{x} = \bar{\mathbf{u}}_{i,j}^n \quad \forall \Omega_{i,j} \in \mathcal{S}_{i,s}^k. \quad (5.8)$$

This system is solved via a constrained least-squares algorithm requiring at least exact conservation in the cell $\Omega_{i,s}$ itself [171]. From the set of reconstruction polynomials \mathbf{w}_h^k , the final WENO reconstruction polynomial \mathbf{w}_h is obtained by using a classical nonlinear weighted combination of the polynomials [171, 258]

$$\mathbf{w}_h(\mathbf{x}, t^n) = \sum_k \omega_k \mathbf{w}_h^k(\mathbf{x}, t^n), \quad \text{with } \omega_k = \frac{\tilde{\omega}_k}{\sum_l \tilde{\omega}_l} \quad \text{and } \tilde{\omega}_k = \frac{\lambda_k}{(\sigma_k + \epsilon)^r}, \quad (5.9)$$

where the oscillation indicators σ_k are computed from

$$\sigma_k := \sum_{l \geq 1} \int_{\Omega_{i,s}} \Delta \mathbf{x}_{i,s}^{2l-1} \left(\frac{\partial^l}{\partial \mathbf{x}^l} \mathbf{w}_h^k(\mathbf{x}, t^n) \right)^2 d\mathbf{x}. \quad (5.10)$$

The small parameter ϵ in (5.9), which is only needed to avoid division by zero, is typically set to $\epsilon = 10^{-14}$ and the exponent in the denominator is chosen as $r = 8$. The linear weights are $\lambda_1 = 10^5$ for the central stencil (i.e., $k = 1$), while all other stencils (i.e., $k > 1$) have linear weight $\lambda_k = 1$. This choice corresponds also to the one made in [171].

In a practical implementation it is convenient to write also the WENO reconstruction polynomials in terms of some reconstruction basis functions $\psi_l(\mathbf{x})$ as $\mathbf{w}_h(\mathbf{x}, t^n) = \Psi_l(\mathbf{x}) \hat{\mathbf{w}}_l^n$. Here, following [167], the basis functions Ψ_l are defined in the same way as the Φ_l in Section 6.1, i.e., as tensor products of Lagrange interpolation polynomials through the Gauss-Legendre quadrature nodes.

6 Discontinuous Galerkin schemes

Galerkin methods (developed independently by Boris Galerkin and Walther Ritz, but named only after Galerkin) are another method to discretize a PDE, by casting it in a weak (integral) formulation where test function and solution are part of a Hilbert space. A finite discretization is then achieved by the approximative projection to a finite-dimensional Hilbert space; a matrix representation instead is achieved by finding an orthogonal basis in this function vector space. Formally this class of methods bear resemblance to spectral methods and can share the same properties such as exponential convergence. Thus Galerkin methods are formally finite element methods which combine the advantages of spectral methods with grid-based methods.

Discontinuous Galerkin (DG) schemes then again combine Galerkin methods with Finite Volume paradigms (Godunovs methods). DG methods can be motivated as an extension to FV methods where a single cell average is replaced by more degrees of freedom, such as a linear or quadratic approximation of the real solution. As the particular feature, the approximations

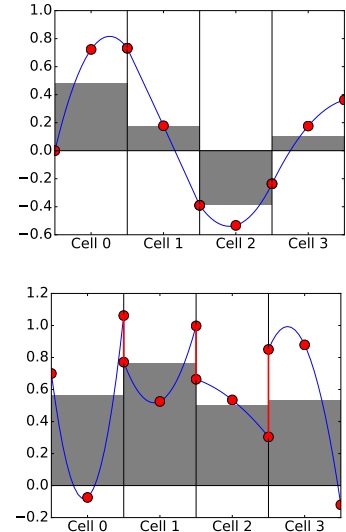


Figure 6.1: A motivational cartoon of DG in one dimensions: A $N = 2$ polynomial with $N + 1$ DOF ($a + bx + cx^2$) is embedded in each cell. The cell sizes and nodal basis points (red) are arbitrary in this plot and in general. The shading indicates the single cell averages (one DOF). The upper panel shows a continuous function while the lower panel shows an example with jumps/discontinuities at the cell interfaces, yielding in a double valued function at the cell interface. In contrast to high order FV, the DOF really live within a single cell and no reconstruction takes place which averages over multiple cells.

between the cells don't have to be smooth/continuous but can exhibit jumps (Figure 6.1). Of course, in the continuum limit where the cell size goes to zero while the number of cells goes to infinity, these discontinuities are as well defined as the discontinuity of Godunov's piecewise constant method itself.

Given the concept of embedding information within a cell (or patch), DG methods exhibit *hp*-adaptivity: Meshes can be refined both in terms of cells (*h*-refinement) or in terms of subcell degrees of freedoms (*p*-refinement). For classical grid *h*-refinement, DG methods exhibit polynomial accuracy (similar to FV/FD), while for subcell *p*-refinement they exhibit spectral accuracy.

In DG methods, the number of degrees of freedom *p* is naturally associated to the order of the scheme. A major benefit of DG schemes is the need of only one ghost layer ²³ at any order, due to the functional basis within one cell. That provides optimal scalability and makes DG attractive for large parallel problems, in fact explains the spreading of DG methods in the Exascale era. The price which has to be paid (in comparison to a FV scheme) is primarily the complexity of an implementation which cannot be underestimated. The DG method will get intertwined with the way how the grid is managed and how communication works. Arguable disadvantages of the DG method (compared to a FV method) are its apparently larger memory footprint, coming from the larger amounts of degrees of freedom and, for explicit DG methods, the limitation on the timestep size (a penalty of $\sim 1/2N$ where *N* is the degrees of freedom, compared to a FV method). However, this criticism disregards the high order spectral convergence which allows to describe smooth problems with orders of magnitudes less cells than any high order FV method would allow to. A way to alleviate the severe CFL timestep restriction is the use of semi-implicit DG schemes, as those proposed, for instance by [193, 432].

DG methods have been proven to be non-linearly stable at all orders and can be formulated covariantly [324]. Similar as Godunov's method, the mathematical foundations are only well defined for first order PDEs, but DG has been applied to second order PDEs.

It has taken nearly two decades for the DG methods to be extended to general nonlinear hyperbolic systems, thanks to the groundbreaking works of [140, 142, 143]. DG methods are reviewed in [139, 141, 144, 241, 242, 414] whereas [163, 164, 175] provide the fundaments for the path-conservative nodal semi-discrete ADER-DG methods which are presented in the following.

6.1 Subcell structure in nodal DG schemes

In order to mathematically describe the DG structure, a couple of symbols shall be introduced. The computational domain Ω is fully covered by a finite number N_e of non-overlapping elements Ω_i , also referred to as *patches* or *cells* [267]. Especially the usage of the term *cells* stresses the close relationship to FV methods. In *d* spatial dimensions, the cells are characterized by their individual size $\Delta\vec{x}_i \in \mathbb{R}^d$ and barycenter $\vec{x}_i \in \mathbb{R}^d$. The discrete solution (state vector of the PDE) is denoted by \mathbf{u}_h and is defined in the space of tensor

²³ Since DG uses a polynomial basis, the concept of an integral number of "layer cells" (as in FD/FV) makes no sense. One ghost layer means, that the field values on the lower-dimensional surface of the computational domain need to be exchanged within the corrector phase of the scheme presented in Section 6.2. In a two dimensional simulation on square elements, the one dimensional polynomials on four element border lines have to be exchanged. In a three dimensional simulation on cuboid elements, the two dimensional polynomials on six element surfaces have to be exchanged. No particular treatment is necessary for the edges/corners of the squares/cuboids.

products of piecewise polynomials of degree N in each spatial direction, [24](#)

$$\mathbf{u}_h(\mathbf{x}, t^n) = \sum_l \hat{\mathbf{u}}_{i,l} \Phi_l(\mathbf{x}) := \hat{\mathbf{u}}_{i,l}^n \Phi_l(\mathbf{x}). \quad (6.1)$$

Here, obviously the spatial basis functions $\Phi_l(\mathbf{x})$ spawn the orthogonal N^d -dimensional function vector space \mathcal{U}_h^N . In \mathcal{U}_h^N , \mathbf{u} has the components $\hat{\mathbf{u}}_l$ in each direction $l \in \mathbb{N}^d$. $\hat{\mathbf{u}}_l$ are the discrete components/degrees of freedom of the solution which have to be stored.

The spatial basis functions $\Phi_l(\mathbf{x}) = \prod_{i=1}^d \varphi_{l_i}(\xi_i)$ are generated by the one-dimensional basis functions $\varphi_k(\xi)$ on a one-dimensional reference element with normal extend $\xi \in [0, 1]$. The physical coordinates $\mathbf{x} \in \Omega_i$ are mapped to the reference coordinates $\xi \in [0, 1]^d$ by

$$\mathbf{x} = \mathbf{x}_i - \frac{1}{2} \Delta \mathbf{x}_i + \xi \cdot \Delta \mathbf{x}. \quad (6.2)$$

In order to apply Gaussian quadrature, typically Legendre polynomials are used for the basis functions $\varphi_k(\psi)$ and ξ_i shall be the quadrature nodes of the $(N+1)$ point Gauss quadrature formula. The Gauss-Legendre quadrature has the advantage of a diagonal mass matrix [25](#). The cost to pay is a non-uniform nodal basis (subcell grid structure), especially there is no nodal point at the cell boundary [26](#). In our implementation we also support the Gauss-Lobatto quadrature with its uniformly distributed nodal points. In this basis, there are always points on the cell boundary (Figure 6.2). The actual nodal basis is a pure technical decision and (except for the quadrature rule) has no impact on the mathematical structure of the scheme, therefore we assume the Legendre nodes in the following exposition whenever in doubt. [27](#)

The orthogonal polynomials satisfy the interpolation property $\varphi_k(\xi_j) = \delta_{kj}$. Thanks to this nodal tensor product basis, the entire subsequent scheme can be written *dimension for dimension*, all higher-dimensional integrals decompose in a multiplication of one-dimensional integrals which can be evaluated on $N+1$ DOF in each dimension.

To summarize, note again that the total number of quadrature points $\{\mathbf{x}_{GP}^m\}$ in Ω_i , as well as the total number of basis elements $\{\varphi_k\}$, is $(N+1)^d$.

6.2 A path-conservative ADER-DG scheme

The weak formulation of a first order PDE system (2.4) is recast as integral equation by integrating over the control volume $\Omega_i \times [t^n, t^{n+1}]$,

$$\int_{t^n}^{t^{n+1}} \int_{\Omega_i} \Phi_k [\partial_t \mathbf{Q} + \mathbf{A}(\mathbf{Q}) \cdot \nabla \mathbf{Q} - \mathbf{S}(\mathbf{Q})] \, d^d x \, dt = 0, \quad (6.3)$$

where $\Phi_k \in \mathcal{U}_h^N$ is a generic basis element out of the piecewise polynomials of maximum degree N which are by definition allowed to be discontinuous across the element interfaces $\partial\Omega_i$. The resulting jump terms have to be properly taken into account. This is done in our numerical scheme with the aid of the path-conservative approach, first developed by Castro and Parés in the finite-volume framework [[129](#), [359](#)] and later extended also to the DG finite-element framework in [[166](#), [169](#), [388](#)]. In this ADER-DG framework,

[24](#) To clarify: \mathbf{u} is the analytic solution while \mathbf{u}_h is an approximation within the restricted space of solutions which can be represented by piecewise polynomials.

Furthermore, for the sake of a readable notation, vector indices are now neglected in favour of discrete indices and flags.

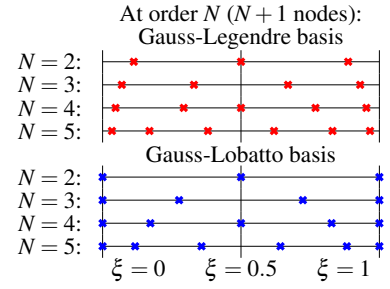


Figure 6.2: Some Gaussian quadrature nodal basis on the one-dimensional reference cell. These two examples have been implemented in the ExaHyPE code.

[25](#) The mass matrix is defined as $M_{ij} = \int \Phi_i(x) \Phi_j(x) dx$. An extensive discussion of the consequences of a non-diagonal Mass matrix and especially of Gauss Legendre vs. Gauss Lobatto in AMR codes is given in [[435](#)].

[26](#) This hides the double valued character of the field value at the patch boundary at the first glance, for instance when no polynomial reconstruction is done in a naive (Gauss-Legendre) vertex-interpolating visualization, as typically done when visualizing DG results.

[27](#) See also [[424](#)] for a detailed discussion of multidimensional quadrature.

higher order in time is achieved with the use of an element-local space-time predictor, denoted by $\mathbf{q}_h(\mathbf{x}, t)$, which is subject to later discussion. At this point of the deviation, the solution Q will just be replaced by the local predictor solution $\mathbf{q}_h = \Phi_k(\mathbf{x})\hat{\mathbf{u}}_k^n$. By integration of the first part in time, and adding a surface flux integral for the integral over system matrix \mathbf{A} ²⁸, thus taking jumps between elements into account, the approximation to the weak form solution (6.3) can be written as

$$\left(\hat{\mathbf{u}}_{i,l}^{n+1} - \hat{\mathbf{u}}_{i,l}^n \right) \int_{\Omega_i} \Phi_k \Phi_l \, d^d x + \iint_{T^n \Omega_i^\circ} \Phi_k (\mathbf{A}(\mathbf{q}_h) \cdot \nabla \mathbf{q}_h) \, d^d x \, dt + \iint_{T^n \partial \Omega_i} \Phi_k \mathcal{A}(\mathbf{q}_h^-, \mathbf{q}_h^+) \cdot \mathbf{n} \, d^{d-1} x \, dt = \iint_{T^n \Omega_i^\circ} \Phi_k \mathbf{S}(\mathbf{q}_h) \, d^d x \, dt, \quad (6.4)$$

where the first integral is a scalar product between two basis elements (called “element mass matrix”, diagonal for the Legendre basis nodes), the second integral collects the smooth part of the discrete solution in the interior $\Omega_i^\circ = \Omega_i \setminus \partial \Omega_i$ ²⁹, the third integral collects the unsteady solution across element interfaces on the surface $\partial \Omega$ and the fourth integral is the source term volume integral which underwent no special treatment thanks to the purely algebraic nature of the source terms (lack of derivatives).

In order to distinguish the conservative and nonconservative fluxes, the weak form (6.3) shall be expanded again, this time by using the PDE functions F_j^i and B_k^{ij} in $\mathbf{A} = \partial \mathbf{F} / \partial \mathbf{Q} + \mathbf{B}$,

$$\begin{aligned} \left(\hat{\mathbf{u}}_{i,l}^{n+1} - \hat{\mathbf{u}}_{i,l}^n \right) \int_{\Omega_i} \Phi_k \Phi_l \, d^d x - \iint_{T^n \Omega_i^\circ} (\nabla \Phi_k) \cdot \mathbf{F}(\mathbf{q}_h) \, d^d x \, dt &+ \iint_{T^n \partial \Omega_i} \Phi_k \mathcal{G}(\mathbf{q}_h^-, \mathbf{q}_h^+) \cdot \mathbf{n} \, d^{d-1} x \, dt \\ &+ \iint_{T^n \Omega_i^\circ} \Phi_k (\mathbf{B}(\mathbf{q}_h) \cdot \nabla \mathbf{q}_h) \, d^d x \, dt + \iint_{T^n \partial \Omega_i} \Phi_k \mathcal{D}(\mathbf{q}_h^-, \mathbf{q}_h^+) \cdot \mathbf{n} \, d^{d-1} x \, dt = \iint_{T^n \Omega_i^\circ} \Phi_k \mathbf{S}(\mathbf{q}_h) \, d^d x \, dt. \end{aligned} \quad (6.5)$$

Note that the integrals in (6.5) for the nonconservative matrix \mathbf{B} are the same as for the system matrix \mathbf{A} in (6.4). Here, the surface integral over \mathcal{G} was derived rigorously by partial integration of the volume integral over $\nabla \cdot \mathbf{F}$ and mathematically, $\mathcal{G} = \mathbf{F}$. Similarly, $\mathcal{D} = \mathbf{B} \cdot \nabla Q$ and $\mathcal{A} = \mathcal{G} + \mathcal{D}$. The curly symbols indicate approximate Riemann solvers which depend on the boundary extrapolated states on the left \mathbf{q}_h^- and right \mathbf{q}_h^+ of the interface³⁰. In this work we mainly use the simple Rusanov flux [397]

$$\mathcal{G}(\mathbf{q}_h^-, \mathbf{q}_h^+) \cdot \mathbf{n} = \frac{1}{2} (\mathbf{F}(\mathbf{q}_h^+) + \mathbf{F}(\mathbf{q}_h^-)) \cdot \mathbf{n} - \frac{1}{2} |\Lambda_i| (\mathbf{q}_h^+ - \mathbf{q}_h^-), \quad (6.6)$$

where $|\Lambda_i| = \max\{\max(\Lambda_i(\mathbf{q}_h^+)), \max(\Lambda_i(\mathbf{q}_h^-))\}$ denotes the maximum wave speed (eigenvalue) computed from both sides³¹. In contrast, the jump term \mathcal{D} of the nonconservative product follows the path-conservative approach [129, 149, 174, 359], the jump terms are defined via a path integral (line/curve integral) in phase space (state vector space) between the boundary extrapolated interface states

$$\mathcal{D}^-(\mathbf{q}_h^-, \mathbf{q}_h^+) \cdot \mathbf{n} = \frac{1}{2} \left(\int_0^1 \mathbf{A}(\psi) \cdot \mathbf{n} \, ds \right) (\mathbf{q}_h^+ - \mathbf{q}_h^-) - \frac{1}{2} |\Lambda_i| (\mathbf{q}_h^+ - \mathbf{q}_h^-), \quad (6.7)$$

²⁸ A similar flux is not even possible for the source \mathbf{S} because it is by construction purely algebraic and must lack derivatives.

²⁹ The volume integrals $\int_{\Omega_i^\circ}$ can be evaluated exactly in N th order with Gaussian quadrature, since all functions under the integral are written on the $(N+1)$ th nodal basis.

³⁰ Here the discontinuous nature manifests, where the system state is really double valued (at a single coordinate).

³¹ Any other monotone numerical flux function could be used equally well, see for instance [448] for an overview of different Riemann solvers

with a simple segment path $\psi = q_h^- + s(q_h^+ - q_h^-)$. Again, the line integral can be solved on Gaussian quadrature points. Note the similarity between the conserved (6.6) and nonconserved flux approximation (6.7). It represents the extension of the Rusanov (or local Lax-Friedrichs) flux to the nonconservative case. Indeed, other more sophisticated schemes may be used with the aim of reducing the numerical dissipation ³².

Several notes shall be made at this point. First, the explicit formalization of source terms containing derivatives as “nonconservative terms” (Section 2.1) allows to take both contributions—the algebraic and differential sources—into account in a Riemann solver, resulting in a more exact and balanced scheme at computationally little extra cost. The main advantage of these path-conservative schemes is that they allow at least in principle the construction of well-balanced numerical schemes that are able to preserve particular steady-state solutions of the governing partial differential equations exactly ³³. Second, it should be noted that the overall ADER-DG scheme presented here is $(N + 1)$ th order accurate for smooth solutions. Since the final algorithm is a purely explicit DG scheme, a CFL-type stability condition on the time step holds in the form

$$\Delta t_{\text{DG}} < C \frac{\Delta x}{d(2N + 1)} \frac{1}{|\Lambda_i|}, \quad (6.8)$$

with spatial patch size Δx in d spatial dimensions, $|\Lambda_i|$ the maximal wave speed of the system, and $0 < C < 1$ the CFL factor, which can be chosen as large as $C = 0.9$. ³⁴

6.3 Local spacetime predictor

The element-local spacetime predictor solution $\mathbf{q}_h(\mathbf{x}, t)$ is computed from the known discrete solution $\mathbf{u}_h(\mathbf{x}, t^n)$ at time t^n using a solution of the Cauchy problem “in the small”, i.e., within a single cell, without considering the interaction with the neighbouring cell. For linear systems, the Cauchy-Kovalewski procedure [172, 234, 438, 439, 447] is suitable, it avoids a quadrature in time in favour of an iterative Taylor series (for which the PDE system has to undergo an algebraic manipulation, this makes its application very hard for complex systems). For nonlinear systems, a fixed-point Picard iteration is more suitable. ³⁵ In the following, the solution is written in a spacetime basis $\mathbf{q}_h = \Theta_k(t, \mathbf{x}) \hat{\mathbf{u}}_k^n$ with $\Theta_k(t, \mathbf{x}) = \phi_{k_0}(\tau) \Phi(\xi)$ the same nodal basis as before, but including time (which is mapped to a reference time $\tau = (t - t^n)/\Delta t \in [0, 1]$). Formally the procedure of multiplying the PDE (2.4) by the new test functions Θ_k and integrating over $\Omega_i \times T^n$ yields ³⁶

$$\iint_{T^n \Omega_i} \Theta_k(t, \mathbf{x}) [\partial_t \mathbf{q}_h + \mathbf{A}(\mathbf{q}_h) \cdot \nabla \mathbf{q}_h - \mathbf{S}(\mathbf{q}_h)] d^d x dt = 0, \quad (6.9)$$

Again, an integration by parts of the temporal derivative part is done, but in contrast to (6.4) or (6.5), no surface integrals are introduced since jumps are not taken into account in this element-local prediction,

³² see e.g., the HLLEM-type version of [165], which is an extension of the HLLEM flux of [187, 235], or the path-conservative Osher schemes forwarded in [174].

³³ This is applied in Section III on page 72 to the GRMHD PDE for the first time.

³⁴ For the results of a numerical von Neumann stability analysis of ADER-DG schemes, see e.g., [162, 167, 367].

³⁵ Picard's method for solving an ODE is based on the Picard-Lindelöf theorem, better known as Cauchy-Lipschitz theorem [16]. It is a simple iterative procedure which is especially suitable in DG due to the function base.

³⁶ (6.9) is (6.3) with Θ_k in place of Φ_k and (anticipating) \mathbf{q}_h in place of \mathbf{Q} .

$$\begin{aligned} \int_{\Omega_i} \Theta_k(\mathbf{x}, t^{n+1}) \mathbf{q}_h(\mathbf{x}, t^{n+1}) d^d x - \int_{\Omega_i} \Theta_k(\mathbf{x}, t^n) \mathbf{u}_h(\mathbf{x}, t^n) d^d x - \iint_{T^n \Omega_i} \frac{\partial \Theta_k(\mathbf{x}, t)}{\partial t} \mathbf{q}_h(\mathbf{x}, t) d^d x dt \\ = \iint_{T^n \Omega_i} \Theta_k(\mathbf{x}, t) (\mathbf{S}(\mathbf{q}_h) - \mathbf{A}(\mathbf{q}_h) \cdot \nabla \mathbf{q}_h) d^d x dt. \quad (6.10) \end{aligned}$$

(6.10) is now a system of N independent element-local equation systems (with N the number of elements covering the simulation domain Ω). Each of these equations can now be solved with a (discrete) fixed-point Picard iteration, without needing any communication with neighbour elements [166, 167, 170, 446].

It should be stressed that the choice of an appropriate initial guess $\mathbf{q}_h^0(\mathbf{x}, t)$ for $\mathbf{q}_h(\mathbf{x}, t)$ is crucial to obtain a computationally efficient scheme. One can either use an extrapolation of \mathbf{q}_h from the previous time interval $[t^{n-1}, t^n]$, as suggested in [469], or a second-order accurate MUSCL-Hancock method, as suggested in [243]. For the initial guess, one can write a Taylor series expansion in time and then only needs to compute approximations to the time derivatives of \mathbf{q}_h at time t^n . A second-order accurate MUSCL-type initial guess for $\mathbf{q}_h(\mathbf{x}, t)$ is given by ³⁷

$$\mathbf{q}_h^0(\mathbf{x}, t) = \mathbf{u}_h(\mathbf{x}, t^n) + (t - t^n) \mathcal{L}(\mathbf{u}_h(\mathbf{x}, t^n)), \quad (6.11)$$

while a third-order accurate initial guess for $\mathbf{q}_h(\mathbf{x}, t)$ reads

$$\mathbf{q}_h^0(\mathbf{x}, t) = \mathbf{u}_h(\mathbf{x}, t^n) + (t - t^n) \mathbf{k}_1 + \frac{1}{2} (t - t^n)^2 \frac{(\mathbf{k}_2 - \mathbf{k}_1)}{\Delta t}, \quad (6.12)$$

where $\mathbf{k}_1 := \mathcal{L}(\mathbf{u}_h(\mathbf{x}, t^n))$ and $\mathbf{k}_2 := \mathcal{L}(\mathbf{u}_h(\mathbf{x}, t^n) + \Delta t \mathbf{k}_1)$. For an even higher-order accurate initial guess, continuous extension Runge-Kutta (CERK) schemes as proposed in [357] were adopted ³⁸. Having an initial guess of the order N chosen, it is sufficient to use *one single* Picard iteration in order to solve (6.10) ³⁹.

It should be remarked again that one-step ADER schemes, in contrast to classical Runge-Kutta time stepping, is particularly well suited for AMR with time-accurate local-timestepping (LTS), requiring only one communication with neighbouring cells per timestep.

³⁷ Here $\partial_t u = \mathcal{L}(u, \partial_t u)$ is the right hand side of the PDE, as in (4.1).

³⁸ For the use of CERK schemes as time integrators of explicit discontinuous Galerkin schemes, see [213].

³⁹ In fact within the ExaHyPE code it was found that the N th order CERK guess could dramatically improve the parallelizability of the code. This is because a variable-length fixed point iteration is hardly vectorizable.

6.4 Finite-volume subcell limiter

The ADER-DG scheme (6.5) is formally of order $N + 1$ for smooth solutions, hence the method must be oscillatory for $N > 0$ in the presence of discontinuities, since the scheme is linear in the sense of Godunov [218], thus inevitably generating spurious oscillations (also known as the “Gibbs phenomenon”). In order to cope with this problem, several attempts have been made, e.g., artificial viscosity [134, 236, 363], filtering [374], hybridisation with finite-volume/finite-difference schemes for the selected “troubled cells” adopting some sort of high-order slope-limiting procedures [51, 138, 246, 255, 286, 368, 369, 474].

In this section, a finite volume subcell limiter technique shall be presented (first proposed in [170]), which is based on the multi-dimensional optimal order detection (MOOD) [137, 158]. The main advantage of this approach is that the high-resolution properties of unlimited DG methods

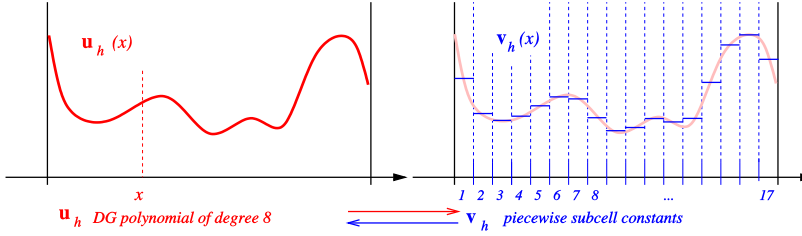


Figure 6.3: A cartoon which demonstrates how a high order Discontinuous Galerkin solution/polynomial u_h within a single patch (red) is projected onto $2N + 1$ finite volume subcell averages (blue). The projection works in both ways, whereas the one from the higher amount of degrees of freedom (FV limiter) is called *restriction*. Figure modified from [170, 406].

are preserved thanks to the introduction of a subgrid level, which is used for integrating the partial differential equations in troubled cells by means of a more robust high-order accurate finite-volume scheme. In the present scheme, limiting is implemented on a *per cell* basis, i.e., either the whole cell Ω_i undergoes a treatment or no point within it. In order to encounter this problem, adaptive mesh refinement (Section 7.2) is necessary to localize the limited cells sharply around the problematic spatial region. ⁴⁰

Limiting criteria

Limiting can be applied *a-priori* (before an ADER-DG time step) or *a-posteriori* (after an ADER-DG time step, as an *predictor-corrector* approach). In both cases, criteria are necessary to decide whether limiting is necessary. A-priori criteria can be geometry-based ⁴¹ or depend on the state vector. ⁴²

A-posteriori criteria test the computed *candidate solution* $u_h(t^{n+1}, \mathbf{x})$ on mathematical and physical admissibility criteria. Mathematical scenarios that may violate the admissibility are the vicinity of steep-gradients or discontinuities, under-resolved flow features or the presence of floating point errors ⁴³. Physical admissible criteria go along with the PDE properties and can be for instance low pressure and density conditions ⁴⁴, superluminal velocities, failure of recovering primitive variables from conserved ones (examples taken from the GRMHD, Chapter III) or closeness to a singularity, indicated by a certain steepness of the curvature (example from the CCZ4, Chapter II). Furthermore, the ExaHyPE code applies a relaxed discrete maximum principle (DMP), which checks for an unphysical steepening and reads

$$\min_{\mathbf{y} \in \mathcal{V}_i} (\mathbf{u}_h(\mathbf{y}, t^n)) - \delta \leq \mathbf{u}_h(\mathbf{x}, t^{n+1}) \leq \max_{\mathbf{y} \in \mathcal{V}_i} (\mathbf{u}_h(\mathbf{y}, t^n)) + \delta, \quad (6.13)$$

where \mathcal{V}_i is the set containing the space-element Ω_i and its neighbours that share a common node with Ω_i . In [168, 194], we choose the parameter δ in (6.13) as as

$$\delta = \max \left(\delta_0, \epsilon \times \left(\max_{\mathbf{y} \in \mathcal{V}_i} (\mathbf{u}_h(\mathbf{y}, t^n)) - \min_{\mathbf{y} \in \mathcal{V}_i} (\mathbf{u}_h(\mathbf{y}, t^n)) \right) \right), \quad (6.14)$$

with typical values $\delta_0 = 10^{-8}$ and $\epsilon = 10^{-7}$.

The coupled limiting ADER-DG scheme

In practice, each computational cell Ω_i that has been marked for limiting is split into $(2N + 1)^3$ finite-volume subcells, which are denoted by $\Omega_{i,s}$ and

⁴⁰ For alternative subcell DG limiters, see also [128, 198, 325, 417, 418].

⁴¹ for instance: limit in the vicinity of a spacetime singularity in a stationary spacetime, within the context of Einstein field equations, Section II.

⁴² for instance, having reached a critical value within an element Ω_i .

⁴³ Floating point errors result in NaNs (Not-a-number), a special number state within the IEEE754 number representation which for instance occurs after dividing by zero or after taking the root of a negative number. Clearly, the user PDE has to be sensitive on such events to generate NaNs.

⁴⁴ This particular example suggests that vacuum regions in fluid dynamics should be limited, which is in fact not favorable at all.

that satisfy $\Omega_i = \bigcup_s \Omega_{i,s}$ (see Fig. 6.3). Note that this very fine division of a DG element into finite-volume subcells does *not* reduce the timestep of the overall ADER-DG scheme, since the Courant-Friedrichs-Lowy (CFL) coefficient of explicit DG schemes scales with $1/(2N + 1)$, while the CFL of finite-volume schemes (used on the subgrid) is of the order of unity [170, 195, 470, 472, 472]. The discrete solution in the subcells $\Omega_{i,s}$ is represented at time t^n in terms of *piecewise constant* subcell averages $\bar{u}_{i,s}^n$, i.e., ⁴⁵

$$\bar{u}_{i,s}^n := \frac{1}{|\Omega_{i,s}|} \int_{\Omega_{i,s}} \mathbf{Q}(\mathbf{x}, t^n) d\mathbf{x}. \quad (6.15)$$

These subcell averages are evolved in time with any suitable finite-volume scheme. ⁴⁶

In fact, the limiting ADER-DG (or: hybrid) scheme can be understood as a DG solver coupled to a FV solver, acting on the same grid. To do so, on a limited patch, the “embedded” DG quadrature points are replaced by an equally embedded finite volume grid. The resulting limited finite volume patch has a block-regular structure of $(2N + 1)$ cells (see Section 7.1 about block regular grids).

From the finite volume scheme, a new piecewise constant solution $v_h(\mathbf{x}, t^{n+1})$ given by the cell averages $\bar{v}_{i,s}^{n+1}$ is obtained, from which the final, limited DG polynomial as $\mathbf{u}_h(\mathbf{x}, t^{n+1}) = \mathcal{R}(v_h(\mathbf{x}, t^n))$ is reconstructed, where \mathcal{R} is the reconstruction operator associated with the projector \mathcal{P} , so that $\mathcal{R} \circ \mathcal{P} = \mathcal{I}$, with \mathcal{I} the identity operator [170]. For the subcell finite-volume scheme a different CFL stability condition applies and takes the form

$$\Delta t_{\text{FV}} < \text{CFL} \frac{h_{\min}}{d N_s} \frac{1}{|\lambda_{\max}|}, \quad (6.16)$$

with h_{\min} the minimum cell size referred to the DG control volumes Ω_i and $\lambda_{\max} = |\Lambda_i|$ the maximal wave speed of the system. Choosing $N_s \geq N + 1$ is a natural requirement that allows to reconstruct the of degrees of freedom of \mathbf{u}_h from the piecewise constant solution v_h via \mathcal{R} . Following [170] we choose $N_s = 2N + 1$ so that $\Delta t_{\text{FV}} = \Delta t_{\text{DG}}$. This choice allows us to maximise the resolution properties of the chosen subcell finite-volume scheme and to run it at its maximum possible CFL number.

When considering time integration, in ADER schemes for nonlinear hyperbolic PDE, limiters need to be applied only once per time step, while in Runge-Kutta based MoL schemes, the limiter needs to be applied in each Runge-Kutta stage again ⁴⁷.

7 Grid meshing

The issue of storing the data necessary for the presented numerical schemes is tightly coupled to the representation of the numerical grid on the computer. This is a technical challenge continuously addressed by computer scientists, since computer architectures are evolving in time and different aspects get important.

In this section, a couple of aspects are presented in a generic fashion, i.e., there is no particular focus on FD, FV or DG methods and it is left open what the grid actually holds (point/vertex data, cell averages or cells with a subcell structure).

⁴⁵ as in Godunov’s scheme, eq. (5.1)

⁴⁶ See Section 5 for a presentation of finite volume schemes. The ExaHyPE paradigm to decide *suitability* is to assume that robust finite volume methods for a given problem are understood and can be used as a safe *fallback* in case of problematic DG solutions which require limiting.

⁴⁷ For a detailed comparison of Runge-Kutta and ADER finite-volume schemes, see [173] and [53], while Runge-Kutta DG and Lax-Wendroff DG schemes (the latter are very similar to ADER-DG schemes) have been compared in [367], also concerning computational performance. Detailed computational performance comparison between ADER-DG schemes and RKDG schemes are also given in Appendix A3 on page 127.

7.1 Block regular grids

The simplest grids are *regular* (or *uniform*, also referred to as *unigrid*), that means each grid coordinate

$$\vec{x} = \sum_{i=0}^d x_i \Delta x^i \quad (7.1)$$

can be described by the constant vector of grid spacings $\Delta \vec{x} \in \mathbb{R}^d$ and integer position indices $\vec{x} \in \mathbb{N}^d$. Therefore, a finite domain grid is fully characterized by the grid spacings $\Delta \vec{x}$ and a description of the domain, for instance $\vec{x} = \vec{x}_0 + x_i \Delta x^i$ with offset x_0 and $x_i \in [0, N]^d$ with N being the number of points.

Uniform grids can be Cartesian (unit squares, $\Delta x^i = \Delta x \forall i \in [1, d]$) or rectilinear (all Δx^i may be different from each other). They also may be curvilinear, for instance in a cylindrical or spherical coordinates mapping. In contrast, irregular grids are called *unstructured* and a priori a list of all grid points must be stored.

Figure 7.1 shows the grid structure in an exemplary setup how it is used by the Carpet code, which is part of the EinsteinToolkit ⁴⁸. Carpet implements block regular grids, i.e., each of the displayed three blocks is a regular grid. In practice, different blocks are evolved in time by different processors/computers. For the implementation of the particular FD/FV scheme, exchange of information at the boundaries of each block is necessary, which is facilitated by a small overlap of the patches. Cells within the overlapping region are called *ghost cells*. Figure 7.1 shows one layer of ghost cells around each block.

7.2 Mesh refinement

Grid codes implement mesh refinement in order to resolve local features while being able to evolve a large spatial domain. As refinement layers are supposed to have smaller cells, they also have smaller maximum timestep sizes (due to the CFL condition). A code with *global time stepping* evolves all refinement levels with the maximum timestep size of the finest layer, this typically leads to numerical dissipation in the coarser layers and is very slow, as the coarser layers allow bigger timesteps. Therefore, a proper refinement code implements *local time stepping* where each refinement level is evolved with the maximum time step possible locally. Depending on the scheme and implementation, this requires prolongation (projection of field values from the finer to the coarser levels) and restriction (projection of field values from the coarser to the finer levels) in order to make use of the finer resolved data at the different time levels.

The Carpet code implements *Fixed Mesh Refinement* (FMR), also referred to as *moving boxes* or *boxes in boxes*. The concept is visualized in Figure 7.2 where three refinement levels are displayed (here without ghost zones). Refinement layers can be ordered by their resolution, this motivates to collect them in tree-structures [267]. Typically, codes restrict to a single refinement factor k . Given a numerical scheme with convergence order α , the convergence (refinement) factor of the overall code will be $k\alpha$.

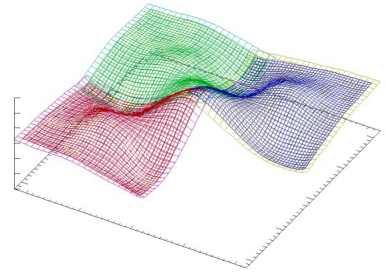


Figure 7.1: A height-elevated plot of a scalar field on a two-dimensional domain. The displayed grid structure reveals a unigrid layout. Multiple patches are shown which cover the physical domain, each having the same resolution $\Delta \vec{x}$. Color is used to distinguish the patches. Furthermore, the overlapping ghost zones are displayed in a different colour. Figure modified from [121].

⁴⁸ See appendix B3 on page 138 for details about the codes referenced in the main text.

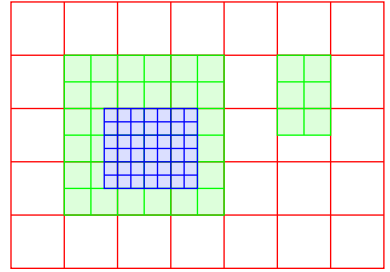


Figure 7.2: Multiple Fixed Mesh Refinement layers (FMR) in Carpet, from [403]

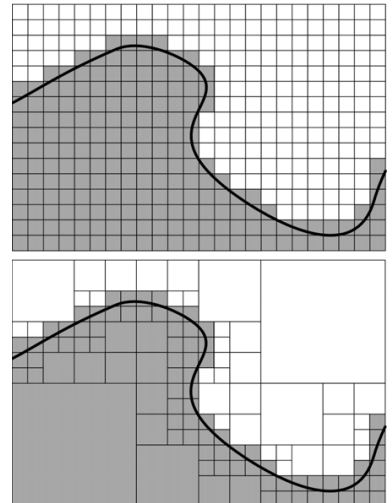


Figure 7.3: Resolving a curve in a unigrid ($16 \cdot 24 = 384$ elements) vs. a local mesh refinement (quadtree, $6 + 12 + 48 + 96 = 166$ elements) with the same resolution, but only 43% storage. Adopted from [419].

The dynamical version of FMR is Adaptive Mesh Refinement (AMR), where the refined areas are created, moved and destroyed by a criterion such as a threshold on a degree of freedom (Figure 7.3).

Dynamical load-balancing (of a dynamical AMR grid) is an open research problem in computer science. A difficulty is to detect load inequalities, moving load between nodes and assessing the effectiveness of such an expensive operation. A code with *static* load balancing (of a static AMR problem) can circumvent this in advance by hand-crafted distribution of work.

Further aspects of mesh refinement are the starting paradigm: For instance, being a sane Octree code, the ExaHyPE code refines from a *single cell*, that is, it is an AMR code by heart (Figure 7.4). In contrast, the ExaHyPE prototype codes as well as Cactus start with an already refined unigrid. At startup, this allows for Cartesian slicing which minimizes the surface of the blocks right at the beginning but postpones the load balancing problem to later refinement steps.

7.3 Parallelization

Hyperbolic laws with finite wave speeds invite to parallelize on the spatial domain. Modern codes need to exploit parallelism on several hierarchies. On the programming level, the HPC landscape is dominated by shared and distributed memory parallelization (MIMD, multiple instruction, multiple data) as well as vectorization (SIMD, single instruction, multiple data).

The Cactus framework manages the distributed memory parallelization internally by splitting up the simulation domain. The split follows a traditional Cartesian domain composition. In Cactus, program modules (*thorns*) allow for random read and write access to the grid, have to describe the numerical schemes and the physics (PDEs). They need to implement shared memory parallelization as well as vectorization. In contrast, the ExaHyPE framework manages both distributed and shared memory parallelization, so that users are only confronted with providing their PDE in a vectorizable way ⁴⁹. Being an active research code for AMR, ExaHyPE implements a number of state-of-the-art domain decomposition paradigms, for instance it dimensionally reduces the computational domain by *domain filling curves*, thus mapping physical locality to memory locality. This is useful for hyperbolic conservation laws where causality implies that significantly separated spatial regions do not influence each other. The mesh code in ExaHyPE is called Peano (like the spacefilling curve) and uses two coupled state machines (finite automata) to couple a numerical scheme to the grid traversal (Figure 7.6). This formalization allows to optimize the code in numerous ways (such as doing research on task based graphs, Figure 7.5) but locks down the scheme to the predefined actions, prohibiting random access and attempts done in classical codes [459]. This paradigm is called “principle of loosing control” (or “Hollywood principle”, “inversion of control”) and is typical for application frameworks.

7.4 *hp*-refinement with ADER-DG and subcell limiter

The ADER-DG algorithms with subcell finite-volume limiter described above has been here implemented on spacetime adaptive Cartesian meshes. De-

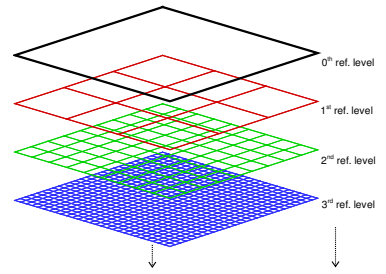


Figure 7.4: The *space-tree* structure of the refinement levels for a single element at the coarsest level ℓ_0 is shown, corresponding to the choice $\mathcal{R} = 3$. Figure published in [196].

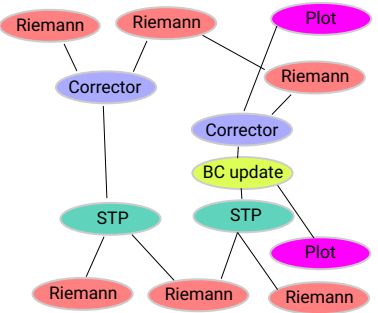


Figure 7.5: Idealized parallel task graph in ExaHyPE. Modified from [135].

⁴⁹ Section 15 provides a discussion of vectorized implementations of the CCZ4 formulation of Einsteins Equations.

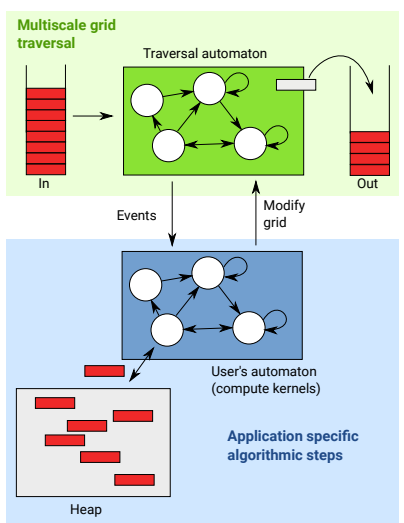


Figure 7.6: Cartoon of the Peano/ExaHyPE architecture. Figure modified from [459].

tails on the used AMR algorithm are described in [177, 195, 470, 472, 472]. The AMR strategy adopted is named *cell-by-cell* refinement and consists in providing a space-tree data structure [109, 177, 267, 458], whose *leaves* correspond to the spatial elements Ω_i used by the numerical scheme described before. The main alternative to a space-tree data structure is the use of *patches*, [71, 72, 73], where a set of independent overlaying Cartesian sub-grid domains (or patches) is introduced and activated when necessary. In the AMR approach used in ExaHyPE, the numerical solution is checked independently along every single space-element for an eventual recursive refining or recoarsening process. In practice, starting from an initial Cartesian grid of refinement level $\ell = \ell_0 = 0$, which is the basic mesh without refinement, the tree-type infrastructure of finer refinement levels is made accessible. The refinement levels $\ell > 0$ are built according to the so called refinement factor \mathcal{R} , which is the number of smaller space-elements per space-direction in which a coarser element is broken in a refinement process, or which are merged in a recoarsening stage. Note that choosing a refinement factor $\mathcal{R} = 2$ would generate the well known *quadtree*s in two-dimensional (2D) meshes and *octree*s in 3D meshes. For an arbitrary refinement factor \mathcal{R} , general space-trees are obtained [109, 458].

For practical purposes, a finite number of refinement levels is provided, i.e., from the coarser $\ell = \ell_0$ to a finest possible refinement level $\ell = \ell_{\max} \in \mathbb{N}_0^+$. The refinement/recoarsening process is driven by the standard *Loehner scheme* [309], i.e., a prescribed refinement-estimator function

$$\chi(\varphi) = \sqrt{\frac{\sum_{k,l} (\partial_l \partial_k \varphi)^2}{\sum_{k,l} \left(\frac{|\partial_k \varphi|_{i+1} + |\partial_k \varphi|_i}{\Delta x_i} + \epsilon |\partial_k \partial_l | \varphi | \right)^2}} \quad (7.2)$$

which is a function of discrete gradients and second derivatives of a scalar *indicator function* $\varphi = \varphi(\mathbf{u}_h(\mathbf{x}, t^n))$ and by two thresholds χ^+ and χ^- [195, 309, 470]. Elements are marked for refinement whenever $\chi > \chi^+$ and for recoarsening whenever $\chi < \chi^-$. Examples for the indicator function φ in hydrodynamics are the rest mass density ($\varphi = \rho$), production of entropy [147, 366, 407], the Lorentz factor, as well as geometric criteria ($\varphi = \varphi(\vec{x})$).

To simplify the AMR algorithm, two neighbour elements are allowed to belong either to the same level ℓ or to an adjacent refinement level $\ell \pm 1$. To each element in the tree we assign a basic element status which is

$$\sigma_i = \begin{cases} -1, & \text{for the } \textit{parent cells} \\ 0, & \text{for } \textit{active elements} \\ +1, & \text{for the } \textit{virtual children} \end{cases} \quad (7.3)$$

$$i = 1, \dots, N_{\text{tot}}$$

where N_{tot} is the total number of space-elements present in the tree. Note that N_{tot} should be distinguished from the total number of active elements N_E , which are the leaves of the tree that define the Ω_i used in the numerical scheme, and for which $N_{\text{tot}} > N_E$ holds in general. The parent cells ($\sigma_i = -1$) are those tree elements which contain active elements on a higher level and finally a virtual child cell ($\sigma_i = +1$) is a tree element which is contained within an active cell that belongs to a lower and adjacent refinement level $\ell - 1$.

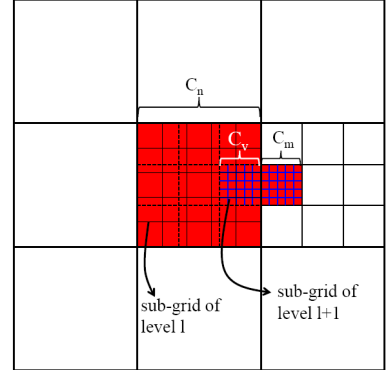


Figure 7.7: An example of combination of AMR and DG subcell reconstruction is shown. The limited cells ($\beta = 1$) C_n and C_m are highlighted in red. The simplest way for the polynomial reconstruction between C_n and C_m elements is: (i) project the piecewise constant solution from C_n to the virtual child-element C_v (see Fig. 7.8); (ii) do polynomial reconstruction along the same refinement level, between C_v and C_m . Figure published in [196].

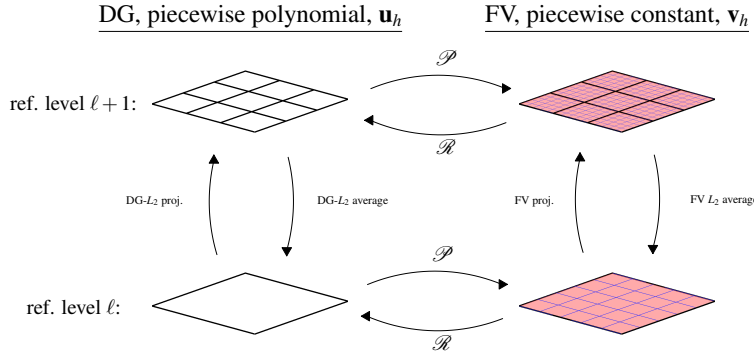


Figure 7.8: Mapping of the numerical solution between the piecewise polynomials \mathbf{u}_h of the DG scheme and the piecewise constant data \mathbf{v}_h of the finite-volume scheme as well as between two different AMR-levels ℓ and $\ell + 1$. Figure published in [196].

Apart from the storage of flux contributions from neighbour cells within our high-order time-accurate local time stepping (LTS) algorithm [177], virtual cells are also needed for high-order finite-volume schemes to provide the necessary data for polynomial reconstructions (TVD, WENO) on a given refinement level if two adjacent active cells belong to different refinement levels; this is illustrated schematically in Fig. 7.7. This strategy produces a locally uniform grid around each cell and greatly simplifies reconstruction. Our strategy of generating a locally uniform grid around each cell is very different from the approach based on genuinely multidimensional CWENO reconstructions proposed by [407].

The dynamics of the numerical solution on virtual elements is given by standard L_2 projection (for virtual children) or averaging (for parent cells), as depicted in Fig. 7.8, where the mapping between the chosen solution spaces, piecewise polynomial (unlimited) or piecewise constant (limited), and between two adjacent refinement levels ℓ and $\ell + 1$ is depicted.

Due to the possibility of handling a large range of spatial scales within the same domain, corresponding to very different CFL time restrictions, a time-accurate and fully conservative local time stepping (LTS) has been implemented in order to use the smallest admitted timestep only where necessary, and a large timestep where it is allowed [177].

Within the ExaHyPE code, the adaptive mesh refinement can further be triggered by the finite volume subcell limiter, which is always applied at the finest AMR level of the simulation. In such a case, a padding is applied around the limited regions [135, 406].

8 Aspects of input and output on adaptive meshes and discontinuous Galerkin methods

For completeness, this section presents a few aspects of input and output in a numerical time evolution code, especially in the context of dynamical AMR and DG. These features were implemented for the ExaHyPE code.

8.1 In-situ initial data

Reading initial data on an AMR grid is more challenging than on a predefined grid, as local features in the initial data shall already be resolved, not only features which appear after certain time during the evolution. In order

to setup an AMR grid hierarchy which adaptively adopts to non-analytical initial data, an AMR grid code needs to evaluate the refinement criterion on the ID.

One way to do this is to evaluate the initial state $Q_0(\vec{x})$ on subsequent grid levels until the required accuracy is gained. At the same time, in the context of parallelism, an AMR code has to load balance the spawned space-tree over the available processors.

The paradigm shift from a classical block-regular code (such as Carpet) towards an AMR code (such as ExaHyPE) shall be demonstrated on an example: As per definition, a-priori there is no grid, the evaluation of an initial data (ID) subroutine has to happen locally for a given spatial point \vec{x} . Typically, within this thesis, initial data itself are the numerical solution of an elliptic PDE and therefore present on a certain grid. Reading in the data from the ID code to the time evolution code typically results in interpolating between two grids.

As soon as non-local computations are necessary, this attempt fails. An example are initial data available as solution of a second order elliptic PDE but to be evolved with a first order formulation of that PDE (as with the formulation of Einstein field equations presented in section 14). In this case, auxiliary fields $a_i = \partial_i \phi$ for some field ϕ have to be computed, and the derivative operator is nonlocal by definition.

The two solutions are either to precompute the auxiliary field also on the initial data code grid, or to compute them on-demand (in-situ). The latter option is preferable to have point-wise access to the initial data in the time evolution at any time. For computing derivatives, in ExaHyPE we chose two approaches (Figure 8.1): Patchwise, using the DG derivatives (which can be thought of a semi-local attempt) or off-grid with finite differences.

8.2 In-situ postprocessing

Within the time evolution codes presented so far, it is common practice to write out the system state also during the time evolution (and not only at its arbitrary end). This outputting is done repeatedly by a time or iteration criterion (formulated for instance as “write every N th iteration” or “write every Δt ”), but any other kind of *query based plotting* can be imagined.

⁵⁰ The concept of a writeout is to store the current *snapshot* $u(t, \mathbf{x})$ for a given time t permanently, while it is necessarily erased at one point in an evolution scheme which thrives to have a constant memory need during time evolution.

When it comes to the writeout phase, any kind of *postprocessing* can be done. This term shall be defined by a local mapping $f : \Omega^n \rightarrow \Omega^m$ which maps the solution vector $\mathbf{u}(\mathbf{x})$ at a fixed given time t to a vector of written quantities $\mathbf{w}(\mathbf{x})$ on the spatial d -dimensional simulation domain Ω ⁵¹. One can imagine that $\mathbf{w} = f(\mathbf{u})$ is computed either during the time evolution (“online”), in order to write out *only* the mapped state vector, or afterwards, so \mathbf{u} is written and $f(\mathbf{u})$ is computed in an offline postprocessing step. Online post processing might save a lot of computing resources if $m \ll n$ and f is computationally cheap.

Reductions or volume/surface integrals can be modeled with a mapping

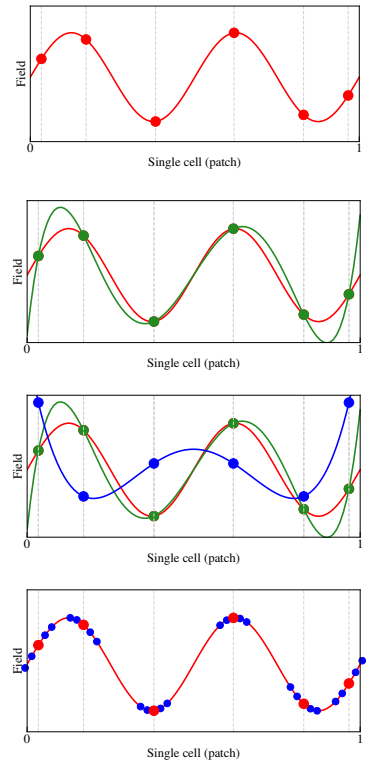


Figure 8.1: Cartoon of FD vs. DG derivatives for initial data in one dimension. Each panel shows the same exemplaric patch, where a fifth order DG polynomial is embedded on a Euler-Legendre nodal basis (i.e., the filled circles indicate the spatial positions where the field values are stored). First panel: The exemplaric field solution which is subsequently projected onto the DG polynomial (green, second panel) and subsequently differentiated (blue, third panel). In contrast, the last panel shows the cartoon of a finite differencing stencil for off-grid computation of the initial data around a requested point. Here, the initial data have to be provided at each bullet, i.e., have to be provided five times as much as in the DG derivative case.

⁵⁰ We use the terms *plotting*, *writing*, *dumping* of data synonymously.

⁵¹ This mapping can be non-locally extended to allow for derivatives, such as $\mathbf{w}(\mathbf{x}) = f(\mathbf{u}(\mathbf{x}), \partial_i \mathbf{u}(\mathbf{x}), \dots)$.

$g : \mathbf{R}^{d \times n} \rightarrow \mathbf{R}^{e \times m}$, where $e < d$ is the dimensional reduction and again $m < n$ stands for a lossy mapping of the solution vector to less degrees of freedom. For the highly symmetric spacetimes of compact objects, as presented in the next chapters, simple 1D and 2D cuts of the Cartesian coordinate systems on the axis are typical dimensional reductions, while L_1 , L_2 and L_∞ (volume) integrals are evaluated on the whole space and provide “0D” scalar output. Surface integrals over an arbitrary surface (defined by its normal vector field S^i) are technically more complex to implement but nevertheless fall into the class of mappings g .

8.3 Visualization of ADER-DG simulations

When simulation data should be stored permanently, a well-defined file format provides interoperability between different (possibly postprocessing) codes. The ExaHyPE grid structure can be casted as *block regular*: The DG polynomials in each patch can be sampled on a unigrid, without loss of accuracy (i.e., by keeping the number of nodal points the same). This is the basic idea of the implementation of the CarpetHDF5 file format within ExaHyPE, which was originally developed for Carpet [382].

While the CarpetHDF5 ⁵² file format is tailored to the memory layout of Carpet, where block regular *components* are sized in order to match one parallel rank (i.e., a MPI process), in ExaHyPE the patches are kept intentionally small to hold a single DG polynomial. Therefore, the number of patches per dimension is typically one to two orders of magnitude larger in Carpet grids compared to ExaHyPE grids, and the amount of *meta data* in the CarpetHDF5 file format dominates over the *payload data*. In this context, the term “meta data” refers to the description of the grid structure and component geometry, while “payload data” are the actual field values. This property makes the CarpetHDF5 format especially inattractive in ExaHyPE as a volumetric file format (i.e., in three spatial dimensions). ⁵³

9 Summary

In Chapter I, all the ingredients for a new code developed within this thesis were proposed. At the very heart, it is a coupled evolution scheme which uses a local ADER-DG scheme which is by construction communication avoiding and thus suitable for the next generation of machines, in contrast to traditional schemes, as well as an undemanding traditional Finite Volume scheme, which is however time variation diminishing and suitable to evolve a solution at low order. The infrastructure for running three-dimensional astrophysical simulations was presented, and it will be brought to life in the subsequent chapters II on the facing page (with general relativity) and chapter III on page 72 (with hydrodynamics).

⁵² HDF is short for “Hierarchical Data Format” and is a container file format for scientific data, especially multidimensional arrays. In principle, the proposed discussion is independent of the container file format. See [406] for details about the file formats.

In contrast to the formats discussed in the main text, VTK (“Visualization Toolkit”) is a widely supported standarized format for describing higher dimensional geometries. ExaHyPE can write VTK files, but these files are only optimized for interoperability.

⁵³ The structure-of-array/array-of-structure representation of fields is the underlying difference between Carpet (basically storing $(Q_0(\vec{x}), Q_1(\vec{x}), \dots)$) and ExaHyPE (storing $\vec{Q}(\vec{x}_0), \vec{Q}(\vec{x}_1), \dots$). This is also the main difference between the Carpet file format and the tailored Peano block regular file format [406].

General Relativity

A first-order formulation of the Einstein equations and its solution with DG schemes

CHAPTER

II

This chapter summarizes the efforts of writing Einstein Field equations (EFE) [188, 189] in a way specially suitable for high (convergence) order numerical integration, with the numerical schemes presented in chapter I. For an introduction into the problem and a review of previous work, see Section 0.2 on page 13. This chapter relies partially on the coauthored publications [168] as well as [274].

10 Motivation: The two body problem of GR

Exact solutions of Einstein Field equations are “rare” [148] and well known solutions are highly symmetric spacetimes. Two astrophysically relevant examples are the stationary Kerr black hole (two Killing vectors: rotational / azimuthal and in time direction) and the static TOV solution of an isotropic fluid in equilibrium (spherically symmetric, thus three orthogonal spacelike Killing vectors) ¹.

Being a nonlinear theory where the superposition principle no longer holds (in contrast to classical and quantum mechanics), the two body problem in (full) general relativity (GR) is nontrivial. That is, there is no way of analytically solving Einstein field equations exactly for a spacetime holding two compact objects (black holes or neutron stars). Instead, all attempts to find such spacetimes are using approximations which however can be subsequently refined to converge to the real solution. The two major approximation scales are (1) the mass ratio M_1/M_2 of the two objects and (2) the compactness $C = M/R$ of the system, with R the object separation and $M = M_1 + M_2$ the total spacetime mass [111, 330, 455]. Due to the virial theorem, this scale is similar to v^2/c^2 with the characteristic velocity v of an object in the binary system.

It is popular to inspect the two-dimensional space spanned by these two parameters in a diagram (Figure 11.1): Two perturbation theories cover either the small compactness or the high mass ratio regime. The first one is the Post Newtonian (PN) expansion of EFE where the velocity ratio is small compared to the speed of light. The second one are gravitational self-force corrections [456] which correct around an infinite mass ratio (static approximation of the heavier object / test particle on a geodesic in an external metric). Being analytic theories which approximate Einstein equations, for a given order of approximation, these theories fail to describe a binary system with high mass, finite extend, rapid rotation. In order to describe this

¹ The TOV solution is referred here synonymously to as TOV star or neutron star.

Particular spacetimes are introduced in the benchmark sections, for instance the Kerr(-Schild) solution in Section 16.4 on page 67 and the TOV solution in Section 25.3 on page 93.

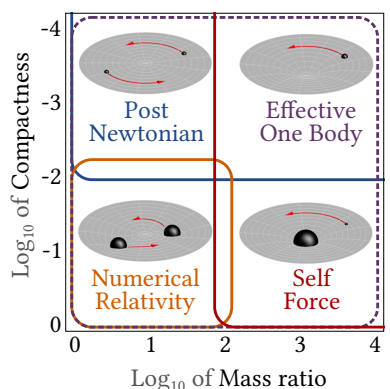


Figure 10.1: Practicability/availability diagram of the two body problem in GR with the parameter range achievable with approximations.

strong gravity regime correctly, Einstein equations must be solved without simplifying approximations. The answer from numerical relativity (NR) is to approximate the spacetime itself instead of the field equations. The mathematical approach is no more analytic but numerical, working on discretized fields, whereas the “full” Lagrangian is solved, without the (computational/mathematical) need for a simplification.² In practice, however, it is a long way to recast the Einstein field equations in a hyperbolic way, suitable for “time” integration, and the following Sections will provide an insight into the approach used within this work.

This broad-brush motivation for numerical approaches in field theory disregards many successful attempts of covering the whole parameter space of Figure 11.1 analytically. In case of GR, there is the effective one body formalism which is able of an analytic treatment of the strong gravity regime of two body spacetimes by taking into account results from PN and NR [110, 150]. In contrast, numerical relativity is the only approach to arbitrary strong gravity spacetimes which works from first principles, i.e., without any external input, and that can in principle cover the whole space.

11 The Cauchy Initial value formulation of GR

General relativity is invariant under the Lorentz (Lie) group, that makes it a gauge theory. The four degrees of freedom (DOF) from Lorentz group can be cast in general smooth coordinate transformations $x'_\mu = f_\mu(x)$ and this invariance is known as general or diffeomorphism covariance. From the $4 \times 4 = 16$ components of Einstein equations, only 10 are independent, and the gauge freedom removes another 4 DOF, thus 6 physical DOF remain.

The ADM formulation (dating back to 1959 by Arnowitt, Deser, Misner [37]) is an Hamiltonian formulation of Einstein field equations.³ It allows to define a time coordinate and thus to perform a time evolution on the orthogonal spatial coordinates (cf. Section 1 on Hamiltonian time evolution). The ADM formulation is one way to identify/fix the gauge degrees of gravity by dimensional reduction and restricting Einstein field equations on the lower-dimensional hyperspaces (e.g., $D = 4$ -dimensional spacetime is restricted on 3-dimensional hypersurfaces)⁴. Arbitrarily embedding ($D-1$)-manifolds within a D -manifold can be described by a vector field N_μ with $D - 1$ degrees of freedom, thus this is a suitable method for gauge fixing.

The D -dimensional spacetime remains now as a gauge orbit. If the vector N_μ collects the gauge connections, one can arbitrarily select a direction (for instance the first component of the vector N_μ) and call it “time”.

² It is interesting to do an excursion to the other popular nonlinear theory in high energy physics, since there are similar approximations done: Quantum chromodynamics (QCD), the special relativistic quantum theory of the strong force, part of the Standard Model of elementary particles and suitable for describing, for instance, fundamental baryonic and mesonic particles hold together by the strong force. The two body problem in QCD in the context of heavy quarks has a similar parameter space with similar solutions: Instead of Post Newtonian expansion, there is non-relativistic QCD, while the heavy quark effective theory is renowned for describing dynamic quarks in the presence of infinitely heavy quarks. However, in the relativistic regime of two quarks with similar mass, the full QCD Lagrangian must be solved to predict correct observables. A successful theory to do so discretizes spacetime (with periodic boundary conditions, therefore referred to as a “lattice”) where a QCD Lagrangian (not necessarily describing all flavours) is solved numerically. This research field is called Lattice QCD. At the present, numerical relativity and lattice QCD are the two major challenging applications in high energy computational physics.

³ We will refer to the ADM formulation synonymously to as the (Cauchy) initial value problem formulation or the canonical formulation of EFE.

⁴ The ADM split, or rather the ADM canonical coordinates, are not a unique choice. The Ashtekar variables [38], which rewrite three-dimensional slices into SU(2) gauge fields, are an example of a popular different choice which is actually the foundation of loop quantum gravity [393].

11.1 Foliation of spacetime

The way to the classic 3+1 formulation of Einstein equations is typically two-part: First, the geometry of foliations is specified by introducing a number of tensors suitable for projecting four dimensional tensors onto the submanifolds. Second, the projections are applied on Einstein's equations and the resulting PDE system is discussed. This approach is proven and part of modern numerical relativity books such as Alcubierre [7], Bona and Palenzuela [91], Baumgarte and Shapiro [64], Gourgoulhon [222], Rezzolla and Zanotti [387] or Shibata [410].

Given arbitrary gauge connections $N^\mu = (\alpha, \beta^\mu)$, time shall be defined to advance along the vector $t^\mu = \alpha n^\mu + \beta^\mu$. This motivates to define the normal vector to the spatial hypersurfaces Ω as $n^\mu = (1/\alpha, -\beta^i/\alpha)$ ⁵.

The line element shall commonly read $dl^2 = \gamma_{ij} dx^i dx^j$, the proper time along the normal vector (Eulerian observer) $d\tau = \alpha dt$. The induced three metric is identified as $\gamma_{\mu\nu} = g_{\mu\nu} + n_\mu n_\nu$ and the line element thus $ds^2 = \alpha^2 dt^2 + \gamma_{ij}(dx^i + \beta^i dt)(dx^j + \beta^j dt)$.

The extrinsic curvature describes how the submanifold is embedded in the outer space and can be derived as $K_{\mu\nu} = -1/2 \mathcal{L}_n \gamma_{\mu\nu}$ wie Lie derivative along the normal direction n , which evaluates on purely spatial tensors as

$$\mathcal{L}_n = (\mathcal{L}_t - \mathcal{L}_\beta)/\alpha = (\partial_t - \beta^\mu \partial_\mu)/\alpha. \quad (11.1)$$

It is worth mentioning that the original ADM group had a fairly different notation [222], they derive the canonical conjugate momenta π_{ij} instead of the extrinsic curvature $K_{ij} = -1/\sqrt{\gamma}(\pi_{ij} - 1/2\gamma_{ij}\pi_m^m)$. The way 3+1 gravity is presented in modern literature basically follows York [467].

3+1 split of the Energy momentum tensor

The normal vector n_μ as well as the spatial metric γ_{ij} are suitable for projecting four dimensional tensors into purely spatial or purely temporal objects. Before this “split” is applied to Einstein equations (Section 11.2), it shall be applied to the Einstein source, i.e., the energy momentum tensor $T_{\mu\nu}$. Following the standard definitions, the following four quantities, all measured by the Eulerian observer, shall be defined:

$$E = n^\alpha n^\beta T_{\alpha\beta} \quad \text{the energy (momentum) density}, \quad (11.2)$$

$$S_\alpha = -\gamma_\alpha^\mu n^\nu T_{\mu\nu} \quad \text{the energy (momentum) flux}, \quad (11.3)$$

$$S_{\alpha\beta} = \gamma_\alpha^\mu \gamma_\beta^\nu T_{\mu\nu} \quad \text{the spatial energy momentum tensor and} \quad (11.4)$$

$$S = S_i^i \quad \text{its trace}. \quad (11.5)$$

11.2 3+1 split of Einstein Equations: ADM equations

The ADM split of Einsteins field equations is most readily obtained by projection operators applied on EFE written as $G_{\mu\nu} - 8\pi T_{\mu\nu} = 0$ with the Einstein tensor $G_{\mu\nu} = R_{\mu\nu} + 1/2Rg_{\mu\nu}$ and the Energy-Momentum-Tensor $T_{\mu\nu}$. Then, a full projection onto the normal direction yields the Hamiltonian constraint equation

$$0 = n_\mu n_\nu (G_{\mu\nu} - 8\pi T_{\mu\nu}) = R - \text{tr}(K^2) + (\text{tr}K)^2 - 16\pi E := H \quad (11.6)$$

Similarly, the three momentum constraints are derived by the mixed projection: ⁶

$$0 = \gamma_{\alpha\beta} n_\gamma (G_{\alpha\gamma} - 8\pi T_{\alpha\gamma}) = (0, \nabla_k K_a^k - \nabla_a \text{tr} K - 8\pi S_a) := M_a \quad (11.7)$$

$H = 0$ and $M_a = 0$ are the Hamiltonian and Momentum constraints, respectively, and their deviation from zero (due to numerically introduced errors) is a measure to assess the physicality of a system state.

The full projection onto the spatial hypersurface gives an evolution equation for the extrinsic curvature,

$$\gamma_{\alpha\beta} G^{\alpha\gamma} = \gamma_{\alpha\beta} 8\pi T^{\alpha\gamma} \Leftrightarrow \mathcal{L}_n K_{ij} = \mathcal{E}_{ij}, \quad (11.8)$$

⁵ Actually t^μ does *not* need to be timelike, the only requirement is not to be tangential to the spatial hypersurfaces [7].

This is because the gauge choices are arbitrary ($N_\mu \in \mathbb{R}$) and i.e., a superluminal shift does not violate causality by principle.

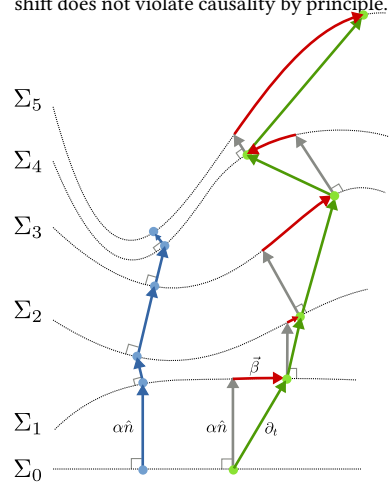


Figure 11.1: Cartoon for demonstrating the slicing (foliation) of 1+1 spacetime. The fixing of gauge freedoms is arbitrary and the shown example follows by intention no standard gauge fixing choice in NR. The foliation geometry is defined in continuum, this cartoon shows a number of different spatial hypersurfaces Σ_i , an exemplary normal vector fieldline (blue) as well as an exemplary coordinate fieldline (green), determined by the time vector, which decomposes into spatial (shift) and temporal (lapse) direction. The lapse is the only spatial vector (“living on Σ_i ”), while the other shown vectors are temporal. Since the vectors are shown non-bended, they shall be understood as infinitesimal.

⁶ The notation $v_\alpha = (0, w_a)$ shall indicate that the left hand side is four dimensional, while the right hand side is a purely spatial vector.

$$\text{with } \mathcal{E}_{ij} = -1/\alpha \nabla_i \nabla_j \alpha + R_{ij} - 2K_{ij}K_j^k + KK_{ij} - 8\pi \left(S_{ij} - \frac{1}{2}\gamma_{ij}(S-E) \right).$$

The definition $K_{\mu\nu} = -1/2\mathcal{L}_n\gamma_{\mu\nu}$ is already the evolution equation for γ_{ij} ,

$$\mathcal{L}_n\gamma_{ij} = -2K_{ij}. \quad (11.9)$$

The two evolution equations in n^μ direction can be transformed to evolution equations using the “time” introduced in the previous section, i.e., (11.1).

The four equations (11.6–11.9) are generally known as ADM equations. With their 1+3 constraint equations and 6 evolution equations [7], they have the same 10 DOF as Einstein field equations.

It is worthwhile to emphasize at this point that the constraint equations can be used as Lagrangian Multipliers, for instance was H already introduced as Lagrangian multiplier in $\mathcal{L}_n K_{ij} = \mathcal{E}_{ij} - \gamma_{ij}H$ by York [467]. Obviously this does not change (continuum) physics, but the PDE structure (system matrix) is a different one.

The ADM evolution equations are only weakly hyperbolic. This can be seen by rewriting them as a first order formulation, fixing the gauges and showing that parts of the system are not diagonalizable [7]. As discussed in Section 2.2, weakly hyperbolic PDEs are not suitable for numerical integration since they are not well-posed.

[7] γ_{ij} and K_{ij} are symmetric 3-tensors with 6 DOF each, however they are conjugate variables and therefore hold the same information.

11.3 Gauge fixing

In numerical relativity, gauge terms *have* to be fixed since they appear in the ADM system (11.8) and a numerical treatment requires every variable to be represented by a number.

Physically, the effect of gauge fixing in the ADM split is equivalent to choose a reference frame in GR (as it fixes the same four DOF). Fixing the lapse α determines the foliation and time coordinates (“slicing conditions”) while fixing the shift β^i chooses the spatial coordinates. The gauge freedom can be used to move coordinates in a desirable way through the simulation domain which itself can make the three-dimensional evolution equations more hyperbolic or more elliptic [222], but they can even be (dynamically) evolved by a PDE and thus extend the overall evolution system [8].

Slicing conditions

Slicing conditions can be time-locally defined by constraining ADM quantities, for instance the maximal slicing condition where $K_i^i = 0$. This maximises the volume of the spatial hypersurface (hence the name) and has singularity avoiding features, i.e., $\alpha \rightarrow 0$ when $t \rightarrow \infty$. It yields an elliptic equation for the lapse α which makes it unsuitable for time evolutions [9]. Being maximal sliced is a property of a single hypersurface. In contrast, slicing conditions which are defined via the lapse (or coordinates) characterize a series of hypersurfaces and are not meaningful for single hypersurfaces [222], because in general the lapse has no meaning on a single hypersurface [10]

There is also the class of algebraic slicing conditions which directly determine the lapse function and do not require to solve a (differential) equation

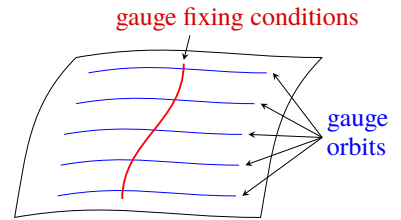


Figure 11.2: Gauge fixing conditions must cut every gauge orbit once. Every gauge orbit represents one physical solution which is similar to another one. This generic sketch and language from gauge theory can be mapped to GR/ADM language, a physical solution is a particular coordinate system/slicing of spacetime. Colored from [326].

[8] That means their PDEs necessarily have to be taken into account when making an eigenanalysis of the particular 3+1 formulation of Einsteins equation (referring to modification of ADM equations, as presented in the subsequent sections).

[9] This is because the elliptic equation (which has no time derivatives) has to be solved at every timestep. There are however approximations by parabolic laws [409, 410].

[10] However, given a prescribed gauge-fixing law, the lapse can be given meaning even on a single hypersurface.

(at least not for constructing the initial data/initial slice). The most simple example of this class is geodesic slicing, where $\alpha := 1$. It got its name from the worldlines of Eulerian observers, which can be shown to be geodesic. Their eigentime $\tau = t$ is equivalent to coordinate time.

Harmonic slicing is the most likely a gauge which is comparable to Lorentz gauge ($\partial_\mu A^\mu = 0$ with gauge field A^μ in electrodynamics and related field theories). It can be defined as imposing the gauge $\nabla_\mu \nabla^\mu x^\alpha = 0$ on the coordinates. This translates the Laplace equation $\nabla_\mu \nabla^\mu t = 0$ in 3+1 formalism, i.e., the time coordinate has a harmonic solution. It is a special case of 1 + log/Bona Masso slicing, which is given by [88]

$$(\partial_t - \mathcal{L}_\beta)\alpha = -(K - K_0)\alpha^2 f(\alpha) \quad (11.10)$$

where $f(\alpha) = 0$ gives geodesic slicing, $f(\alpha) = 1$ gives harmonic slicing and $f(\alpha) = 2/\alpha$ gives “1+log”-slicing, which gets it name from the special case $\beta = 0$ where (11.10) reduces to $\partial_t \alpha = \partial_t \ln |\gamma|$ which has the solution $\alpha = 1 + \ln |\gamma|$. 1+log slicing has even better singularity avoidance properties than harmonic slicing but can penetrate horizons (in Schwarzschild spacetime), furthermore it mimics maximal slicing. Here, a formulation with $K_0 = K(t_0)$ the extrinsic curvature trace at beginning of the simulation is given, which can help to preserve maximally sliced initial data. Most worth mentioning, (11.10) is a hyperbolic conservation law for the lapse, which makes it an interesting addition to a 3+1 evolution system.

Spatial gauges

Fixing the temporal gauge freedom α determines the arrow of time at any spatial hypersurface, since time is defined differentially between spatial hypersurfaces. Instead, fixing the three gauge freedoms β^i determines only the propagations of coordinates between the hypersurfaces but leaves the choice of coordinates for instance at the initial data hypersurface undetermined. This is because the gauge connections (α, β^i) are only meaningful quantities *inbetween* two spatial hypersurfaces ¹¹.

Similar to the geodesic slicing, there is the Eulerian gauge $\beta^i = 0$ as then $x^i = \text{const}$ are the worldlines of an Eulerian observer. As soon as the spacetime is non-static, better more tailored spatial coordinates might be wanted. One example are minimal distortion gauges which try to minimize the change of the (conformal) 3-metric. They yield in an elliptic equation for the shift. However, minimal distortion gauges are interesting for the wave zone in a merger event, basically because they are adapted to the way how gravitational waves are defined and extracted (Appendix A6).

Most interesting for this monograph are the Gamma freezing and Gamma driver shift conditions. The first one is a simplification of approximative (pseudo) minimal distortion gauges and can be formulated as ¹²

$$\partial_t \tilde{\Gamma}^i = 0, \quad \text{with } \tilde{\Gamma}^i := \tilde{\gamma}^{jk} \left(\tilde{\Gamma}^i_{jk} - \tilde{\Gamma}^i_{jk} \right) \quad (11.11)$$

An elliptic equation for the shift can be derived which must be fulfilled. By further modifying the minimal distortion law, a parabolic [9] and eventually a hyperbolic [6, 87, 306] alternative has been found, which reads in first

¹¹ In fact, there exist also *full* spatial coordinate-fixing choices but they are not discussed here.

¹² Here, the tilde in $\tilde{\gamma}$ and $\tilde{\Gamma}$ indicate *conformal* quantities as introduced in Section 12 on the next page. Especially, the contracted Christoffel symbol is an evolution quantity in the BSSNOK system.

order formulation

$$\partial_t \beta^i = \frac{3}{4} b^i + \beta^k \partial_k \beta^i \quad \text{and} \quad \partial_t b^i = \partial_t \tilde{\Gamma}^i - \eta b^i + \beta^k \partial_k b^i \quad (11.12)$$

with a positive function k , a dissipation/damping coefficient η and b^i the auxilliary field required for the first order rewrite [103, 453]. Typical values are $k = 3/4$ and $\eta = 1$ or $\eta \sim M/M_0$ with M the ADM mass measured in multiples of the unit mass M_0 (i.e., $M_0 = M_\odot$ in astrophysical spacetimes).

The gamma driver shift condition turned out to be very successful for moving puncture solutions and is, as part of the BSSNOK equations as presented in the next section, an “industry standard” for stable general relativistic evolutions of compact object mergers.

12 The BSSNOK equations

The Baumgarte-Shapiro-Shibata-Nakamura-Oohara-Kojima (BSSNOK) formulation [63, 100, 338, 413], is a hyperbolic formulation of Einsteins Equations in the 3+1 split. Hyperbolicity is archived with several “tricks” added to the ADM system. These are primarily a conformal transformation of the ADM state variabels $\gamma_{ij}, K_{ij} \rightarrow \tilde{\gamma}_{ij}, \tilde{A}_{ij}$, the addition of the constraint equations $H = M_i = 0$ to the evolution equations, the addition of slicing conditions and Gamma driver to the evolved equations and the seperate evolution of several quantities such as the extrinsic curvature trace K , a contracted Christoffel symbol and the conformal factor. The evolved variables of the BSSNOK system are therefore

$$\begin{aligned} \tilde{\gamma}_{ij} &:= e^{-4\phi} \gamma_{ij}, & \tilde{A}_{ij} &:= e^{-4\phi} [K_{ij}]^{\text{TF}} := e^{-4\phi} \left(K_{ij} - \frac{1}{3} \gamma_{ij} K \right), \\ \Phi &:= \frac{1}{12} \ln(\gamma), & K &:= \gamma^{ij} K_{ij} \quad \text{and} \quad \tilde{\Gamma}^i &:= \tilde{\gamma}^{jk} \tilde{\Gamma}_{jk}^i, \end{aligned} \quad (12.1)$$

where $\tilde{\gamma}_{ij}$ is the conformal 3-metric,

$$\tilde{\Gamma}_{jk}^i := \frac{1}{2} \tilde{\gamma}^{ab} (\partial_j \tilde{\gamma}_{kb} + \partial_k \tilde{\gamma}_{jb} - \partial_b \tilde{\gamma}_{jk}) \quad (12.2)$$

are the Christoffel symbols associated with this metric and $\tilde{\Gamma}^i$ the freely evolved contraction of this symbol. Φ is the conformal factor (see Section 12.2) split off the metric. \tilde{A}_{ij} is the conformal trace-free extrinsic curvature tensor which is evolved in place of K_{ij} . Furthermore, with suitable slicing conditions and the Gamma driver, lapse α , shift β^i and an auxillary field b^i is evolved.

12.1 Covariance of the BSSNOK formulation

All new evolution fields $\Psi, K, \tilde{\Gamma}^i$ are pure gauge quantities [63]. The scalars Ψ and K are derived from tensors, however $\tilde{\Gamma}^i$ does not transform like a vector, since the connection coefficients $\tilde{\Gamma}_{jk}^i$ do not. Therefore, the BSSNOK equations are not (fully) covariant. However, the difference between two Christoffel symbols in a coordinate change transforms like a tensor field [222]. That is, if one introduces a background metric $\dot{\gamma}_{ij}$ and a new metric $\epsilon_{ij} = \tilde{\gamma}_{ij} - \dot{\gamma}_{ij}$, then the Christoffel symbols of the new metric, $\Delta_{kl}^i = \tilde{\Gamma}_{kl}^i - \dot{\gamma}_{kl}^i$ and the derived $\hat{\tilde{\Gamma}}^i$ does so, too. For BSSNOK, a system like this was

introduced in [394] in order to evolve Einstein field equations on spherical and singular coordinate systems. ¹³

¹³ Appendix A4 deepens this issue for the presented FO-CCZ4 formulation in this chapter.

12.2 Definitions for the conformal factor

A key concept in BSSNOK is splitting off a conformal factor, recognizing that the three-metric γ_{ij} and three-extrinsic curvature K_{ij} are part of a conformal equivalence class. Evolving a fundamental representation does not only have an advantage in conformally flat spacetimes but in fact it was shown by York [465, 466] that a traceless and transverse tensor carries the true degrees of freedom of the gravitational field [222]. Therefore, the concept was picked up by various other formulations of Einsteins equations and especially by various technical implementations, sometimes with subtle differences in the definition, usually due to technical reasons (like positivity preserving techniques) which promise better numerical stability. In order to clarify the definitions, some intermediate symbols shall be defined. First of all, any (rank 2) tensor, for instance the 3-metric γ_{ij} , has a corresponding tensor density $\tilde{\gamma}_{ij} = \gamma^{n/2} \gamma_{ij}$ with weight $n \in \mathbb{R}$ and determinant $\gamma = \det(\gamma_{ij})$ [222]. The weight of the three metric is $n = 2/3$ and therefore, the conformal factor Ω can be introduced as

$$\Omega = \gamma^{1/3} \quad \text{so that} \quad \gamma_{ij} = \Omega \tilde{\gamma}_{ij} \quad (12.3)$$

In literature, the notation $\psi^4 \equiv \Omega$ is more widespread ¹⁴, thus $\gamma = \psi^{12}$. The following three popular but different choices are widespread in literature ¹⁵, formalized by a function $f(\Omega)$, or $f(\psi^4)$, respectively. It is then $\gamma_{ij} = f^{-1} \tilde{\gamma}_{ij}$. The three choices $f \in \{\xi, \Phi, W\}$ are ¹⁶

$$\xi(\Omega) = \Omega^{-1} = \psi^{-4} = \gamma^{-1/3}, \quad \text{then} \quad \gamma_{ij} = \xi^{-1} \tilde{\gamma}_{ij} \quad (12.4)$$

$$\Phi(\Omega) = \log \Omega^3 = \log \psi = \frac{1}{12} \log \gamma, \quad \text{then} \quad \gamma_{ij} = e^{4\Phi} \tilde{\gamma}_{ij} \quad (12.5)$$

$$W(\Omega) = \Omega^{-1/2} = \psi^{-2} = \gamma^{-1/6}, \quad \text{then} \quad \gamma_{ij} = W^{-2} \tilde{\gamma}_{ij} \quad (12.6)$$

¹⁴ to be explicit, in ψ^4 , the 4 is an exponent, not an index. This symbol should not be mixed up with the Weyl scalar ψ_4 , where the $\cdot 4$ is really an index.

¹⁵ This choice is motivated due to the implementation of all three variants in the Antelope code (see Section 15 on page 61).

¹⁶ Within the BSSNOK community, the choice $f = \Phi$ is popular (and was made here in the text), while for instance [410] uses $f = W$ and [244] uses $f = \xi$.

However, the choice of a particular f does not necessarily mean that this quantity is evolved. In fact, the notation used for the FO-CCZ4 system (Section 14) uses choice (12.6) but calls $W(\Omega) =: \phi$. However, ϕ is treated as a *primitive* variable which is converted to a *conserved* variable where $\log \phi = \log W = -1/6 \log \gamma$, which however does not meet any standard definitions of (12.4-12.6)

12.3 The BSSNOK evolution equations

The BSSNOK equations are given by (see [100] for a derivation)

$$(\partial_t - \mathcal{L}_\beta) \Phi = \frac{1}{6} \partial_k \beta^k - \frac{1}{6} \alpha K \quad (12.7)$$

$$(\partial_t - \mathcal{L}_\beta) \tilde{\gamma}_{ij} = -2\alpha \tilde{A}_{ij} - \frac{2}{3} \tilde{\gamma}_{ij} \partial_k \beta^k \quad (12.8)$$

$$(\partial_t - \mathcal{L}_\beta) K = \alpha \left(\tilde{A}_{ij} \tilde{A}^{ij} + \frac{1}{3} K^2 \right) - \gamma^{ij} \nabla_i \nabla_j \alpha + 4\pi (S_k^k + E) \quad (12.9)$$

$$(\partial_t - \mathcal{L}_\beta) \tilde{A}_{ij} = e^{-4\Phi} [\alpha(R_{ij} - 8\pi S_{ij}) - \nabla_i \nabla_j \alpha]^{\text{TF}} - \frac{2}{3} \tilde{A}_{ij} \partial_k \beta^k + \alpha \left(K \tilde{A}_{ij} - 2 \tilde{A}_{ik} \tilde{A}_j^k \right) \quad (12.10)$$

$$(\partial_t - \mathcal{L}_\beta) \tilde{\Gamma}^i = \tilde{\gamma}^{kl} \partial_k \partial_l \beta^i + \frac{2}{3} \tilde{\gamma}^{jk} \tilde{\Gamma}_{jk}^i \partial_l \beta^l + \frac{1}{3} \nabla^i \partial_k \beta^k - 2 \tilde{A}^{ik} \partial_k \alpha + 2\alpha \tilde{A}^{kl} \tilde{\Gamma}_{kl}^i + 12\alpha \tilde{A}^{ik} \partial_k \phi - \frac{4}{3} \alpha \tilde{\nabla}^i K - 16\pi \alpha \tilde{\gamma}^{ij} S_j \quad (12.11)$$

$$(\partial_t - \mathcal{L}_\beta) \alpha = -2\alpha K \quad (12.12)$$

$$(\partial_t - \mathcal{L}_\beta) \beta^i = \frac{3}{4} b^i \quad (12.13)$$

$$(\partial_t - \mathcal{L}_\beta) b^i = \partial_t \tilde{\Gamma}^i - \eta b^i \quad (12.14)$$

with the covariant derivative $\tilde{\nabla}$ with respect to $\tilde{\gamma}_{ij}$ ¹⁷, Lie derivative $\mathcal{L}_\beta = \beta^k \partial_k$ ¹⁸, the trace-free operator $[T_{ij}]^{\text{TF}}$ defined as in (12.1), and (E, S_i, S_{ij}) being the spatial parts of the energy momentum tensor as defined in (11.2-11.4). In this equation system, there are especially two very lengthy abbreviations used: First, the 3-Ricci tensor in (12.10) which is defined with the conformal decomposition $R_{ij} := \tilde{R}_{ij}^\Phi + \tilde{R}_{ij}$ as¹⁹

$$\tilde{R}_{ij}^\Phi = \Phi^{-2} \left[\Phi \left(\tilde{\nabla}_i \tilde{\nabla}_j \Phi + \tilde{\gamma}_{ij} \tilde{\nabla}^k \tilde{\nabla}_k \Phi \right) - 2\tilde{\gamma}_{ij} \tilde{\nabla}^k \tilde{\nabla}_k \Phi \right], \quad (12.15)$$

$$\tilde{R}_{ij} = -\frac{1}{2} \tilde{\gamma}^{lm} \partial_l \partial_m \tilde{\gamma}_{ij} + \tilde{\gamma}_{k(i} \partial_{j)} \tilde{\Gamma}^k + \tilde{\Gamma}^k \tilde{\Gamma}_{(ij)k} + \tilde{\gamma}^{lm} \left[2\tilde{\Gamma}_{l(i}^k \tilde{\Gamma}_{j)km} + \tilde{\Gamma}_{im}^k \tilde{\Gamma}_{kj} \right],$$

and second, the time-derivative of $\tilde{\Gamma}^i$ in (12.14) which refers to (12.11).

The evolution system also contains PDEs for the lapse α and shift vector β^i , in this particular case the famous Bona-Masso type slicing conditions.

For the numerical intergration, a partly constrained approach is used at every time step to impose that²⁰

$$\det(\tilde{\gamma}_{ij}) = 1 \quad \text{and} \quad \text{tr}(\tilde{A}_{ij}) = 0 \quad (12.16)$$

Similiar to ADM equations, the BSSNOK system is first order in time and second in space, for a proof of hyperbolicity it must be brought into first order in time and space (this was done in [77] for a large number of slicing conditions). Notably, for a fixed (non-evolved) shift vector β^i , BSSNOK is symmetric hyperbolic. Since its first publication, BSSNOK was quite successful for its robustness in numerical simulations and got an “industry standard” for numerical relativistic time evolutions of astrophysical spacetimes.

13 The Z4 family and CCZ4

The Z4 formulation of Einstein field equations (EFE) was formulated by Bona, Ledvinka, Palenzuela, Zacek [85, 86]. They recognize that in ADM formalism, the discrimination of the constraint equations (11.6,11.7) versus the evolution equations (11.8,11.9) in a “naive” unconstrained evolution breaks general covariance. In Z4, the derivative of a zero vector $Z_\mu = 0$ ²¹ is added to the field equations as a generalized Lagrangian multiplier (GLM) which then read in trace-reversed form [85]

$$R_{\mu\nu} + 2\nabla_{(\mu} Z_{\nu)} = 8\pi \left(T_{\mu\nu} - \frac{1}{2} T g_{\mu\nu} \right). \quad (13.1)$$

The field equations can also be derived from a minimal action principle [84]. They are first order in time, second order in space for the metric, first order in space for Z_μ .²² In the 3+1 split, with $Z_\mu = (\theta/\alpha, Z_i)$, the two new evolution quantities for θ and Z_i cannot be discriminated against the ones for γ_{ij} and K_{ij} and thus general covariance is maintained. Notably, these two

¹⁷ Here, only terms $\tilde{\nabla}_i A = \partial_i A$ and $\tilde{\nabla}_i B_j = \partial_i B_j - \tilde{\Gamma}_{ij}^k B_k$ appear.

¹⁸ Conventionally, the ADM system is typically displayed as $\mathcal{L}_n X = \mathcal{R}(X)$ while the BSSNOK and subsequent systems are typically displayed as $(\partial_t - \mathcal{L}_\beta) X = \alpha \mathcal{R}(X)$.

¹⁹ Elaborate splits of “helper” quantities (i.e., tensors derived from evolution quantities) will become even more present in the FO-CCZ4 system.

²⁰ In practice, this means a modification of the state vector before or after every timestep.

²¹ $Z_\mu = 0$ motivates the name: A “zero” vector of length 4, hence “Z4”. The vector vanishes analytically but gets non-zero in numerical simulations.

²² The actual evolution equations are given later compact for all proposed members of the Z4 family.

new evolution equations take the place of the ADM constraint equations, because $Z_\mu = 0$ are four constraints and non-zero values of Z_μ measure the “physicality” of an approximated (numerical) solution. This is a *different* measure for error than the regular ADM Hamiltonian and momentum constraint (violations) (11.6,11.7) which of course still can be determined similarly also in the Z4 system, independently of the Z_μ vector ²³. The resulting PDE system is then almost similar to the ADM equations (11.6-11.9), namely

$$(\partial_t - \mathcal{L}_\beta) \tilde{\gamma}_{ij} = -2\alpha K_{ij} \quad (13.2)$$

$$(\partial_t - \mathcal{L}_\beta) K_{ij} = -\nabla_i \nabla_j \alpha + \alpha [R_{ij} - 2K_{ij}K_j^k + (K - 2\Theta)K_{ij}] - 8\pi\alpha \left[S_{ij} - \frac{1}{2}\gamma_{ij}(S - E) \right] \quad (13.3)$$

$$(\partial_t - \mathcal{L}_\beta) \Theta = \frac{\alpha}{2} [R + 2\nabla_k Z^k + (K - 2\Theta)K - K_{ij}K^{ij}] - Z_k \nabla_k \alpha - 16\pi E \quad (13.4)$$

$$(\partial_t - \mathcal{L}_\beta) Z_i = \alpha [\nabla_j (K_i^j - \delta_i^j K) + \partial_i \Theta - 2K_i^j Z_j] - \Theta \nabla_i \alpha - 8\pi S_i \quad (13.5)$$

The first order version of Z4 was brought into a conservative form and is proven to be strongly hyperbolic [11]. The main drawbacks of the Z4 formulation is the lack of the Gamma driver (11.12), i.e., there are no good gauges which result in horizon growth in black hole simulations.

13.1 Conformal Z4 (Z4c)

The conformal Z4 (Z4c) version was developed as a conformal but non-covariant extension to Z4 [75, 118, 244, 396, 460]. The modified EFEs

$$R_{\mu\nu} + 2\nabla_{(\mu} Z_{\mu)} = 8\pi(T_{\mu\nu} - \frac{1}{2}Tg_{\mu\nu}) + \kappa_1 [2n_{(\mu} Z_{\nu)} - (1 + \kappa_2)g_{\mu\nu}n_\sigma Z^\sigma] \quad (13.6)$$

differ from the Z4 equations (13.1) only by the algebraic damping terms on the RHS, modulated by κ_1 and κ_2 which determine the damping amplitude used to drive the growth of constraint violations to zero. In the 3+1 split the Z4c formulation discard a number of terms which renders the evolution equations non-covariant but very close to BSSNOK. The resulting system is provably strongly hyperbolic for usual gauge choices.

The addition of the damping terms allows to advect and (if desired) damp nonzero constraints which appeared during evolution. The consequence is of course that the numerical solution stays much closer to a physical one, which is especially helpful for very long running simulations (compared to the average wave speed, i.e., the speed of light, or the mass of the space-time, respectively). The typical text-book motivation for this mechanism employs Gauss law in electromagnetism, i.e., preserving the solenoidal magnetic field $\vec{\nabla} \cdot \vec{B} = 0$, where the GLM is introduced as [153]

$$\partial_t B^i = \mathcal{R} \Rightarrow \partial_t B^i = \mathcal{R} - \partial^i \psi \quad (13.7)$$

$$\partial_i B^i = 0 \Rightarrow \partial_i B^i = \mathcal{D}(\psi) = c_{\text{cleaning}}^{-2} \partial_t \psi \quad (13.8)$$

In this minimal example, there is an evolution equation for the vector B^i with a spatial differential operator $\mathcal{R} = \mathcal{R}(B^i, \partial_i B^j, \dots)$. The new evolved scalar ψ couples the divergence freedom ($\partial_i B^i = 0$) to the evolution equation, following a differential operator \mathcal{D} . A hyperbolic choice for this oper-

²³ For a comparison of the quality of different formulations of EFEs, it is useful to fall back to (H, M_i) as the “lowest common denominator”, which always can be computed.

ator results in an advection quation for ψ . In a similar way, in Z4c, the four fields (Θ, Z_i) play the role of ψ in this example. ²⁴

²⁴ See section 21.4 for divergence cleaning techniques in magnetohydrodynamics.

13.2 Conformal and covariant Z4: (SO)-CCZ4

The CCZ4 (conformal and covariant Z4) system was developed to address the non-covariant property of Z4c [12]. The derivation starts with the same field equations (13.6) but do not discard terms at the 3+1 split. ²⁵

The conformal transformation applied in CCZ4 is similar to the BSSNOK one but usually given with a different conformal factor (here $f = W$ from Section 12.2),

$$\begin{aligned} W &:= \gamma^{-1/6}, & K &:= \gamma^{ij} K_{ij}, \\ \tilde{\gamma}_{ij} &:= W^2 \gamma_{ij}, & \tilde{A}_{ij} &:= W^2 [K]^{\text{TF}}, \\ \tilde{\Gamma}^i &:= \tilde{\gamma}^{jk} \tilde{\Gamma}_{jk}^i, & \hat{\Gamma}^i &:= \tilde{\Gamma}^i + 2\tilde{\gamma}^{ij} Z_j, \end{aligned} \quad (13.9)$$

In CCZ4, the new symbol $\hat{\Gamma}^i$ replaces Z_i as evolution quantity, while $\Theta = Z_0$ remains an evolution quantity.

The full CCZ4 system in 3+1 split is given by [12, 13]

$$\partial_t \tilde{\gamma}_{ij} = -2\alpha \tilde{A}_{ij} + 2\tilde{\gamma}_{k(i} \partial_{j)} \beta^k - \frac{2}{3} \tilde{\gamma}_{ij} \partial_k \beta^k + \beta^k \partial_k \tilde{\gamma}_{ij}, \quad (13.10)$$

$$\begin{aligned} \partial_t \tilde{A}_{ij} &= \phi^2 [-\nabla_i \nabla_j \alpha + \alpha (R_{ij} + \nabla_i Z_j + \nabla_j Z_i - 8\pi S_{ij})]^{\text{TF}} + \alpha \tilde{A}_{ij} (K - 2\Theta) \\ &\quad - 2\alpha \tilde{A}_{il} \tilde{A}_j^l + 2\tilde{A}_{k(i} \partial_{j)} \beta^k - \frac{2}{3} \tilde{A}_{ij} \partial_k \beta^k + \beta^k \partial_k \tilde{A}_{ij}, \end{aligned} \quad (13.11)$$

$$\partial_t \phi = \frac{1}{3} \alpha \phi K - \frac{1}{3} \phi \partial_k \beta^k + \beta^k \partial_k \phi, \quad (13.12)$$

$$\partial_t K = -\nabla^i \nabla_i \alpha + \alpha (R + 2\nabla_i Z^i + K^2 - 2\Theta K) + \beta^j \partial_j K - 3\alpha \kappa_1 (1 + \kappa_2) \Theta + 4\pi \alpha (S - 3\tau), \quad (13.13)$$

$$\partial_t \Theta = \frac{\alpha}{2} \left[R + 2\nabla_i Z^i - \tilde{A}_{ij} \tilde{A}^{ij} + \frac{2}{3} K^2 - 2\Theta K \right] - Z^i \partial_i \alpha + \beta^k \partial_k \Theta - \alpha \kappa_1 (2 + \kappa_2) \Theta - 8\pi \alpha \tau, \quad (13.14)$$

$$\begin{aligned} \partial_t \hat{\Gamma}^i &= 2\alpha \left[\tilde{\Gamma}_{jk}^i \tilde{A}^{jk} - 3\tilde{A}^i_j \frac{\partial_j \phi}{\phi} - \frac{2}{3} \tilde{\gamma}^{ij} \partial_j K \right] + 2\tilde{\gamma}^{ki} \left(\alpha \partial_k \Theta - \Theta \partial_k \alpha - \frac{2}{3} \alpha K Z_k \right) - 2\tilde{A}^{ij} \partial_j \alpha \\ &\quad + \tilde{\gamma}^{kl} \partial_k \partial_l \beta^i + \frac{1}{3} \tilde{\gamma}^{ik} \partial_k \partial_l \beta^l + \frac{2}{3} \tilde{\Gamma}^i \partial_k \beta^k - \tilde{\Gamma}^k \partial_k \beta^i + 2\kappa_3 \left(\frac{2}{3} \tilde{\gamma}^{ij} Z_j \partial_k \beta^k - \tilde{\gamma}^{jk} Z_j \partial_k \beta^i \right) \\ &\quad + \beta^k \partial_k \hat{\Gamma}^i - 16\pi \alpha \tilde{\gamma}^{ij} S_j - 2\alpha \kappa_1 \tilde{\gamma}^{ij} Z_j, \end{aligned} \quad (13.15)$$

$$\partial_t \alpha = -\alpha^2 g(\alpha) (K - K_0 - 2\Theta) + \beta^k \partial_k \alpha, \quad (13.16)$$

$$\partial_t \beta^i = f b^i + \beta^k \partial_k \beta^i, \quad (13.17)$$

$$\partial_t b^i = \partial_t \hat{\Gamma}^i - \beta^k \partial_k \hat{\Gamma}^i + \beta^k \partial_k b^i - \eta b^i, \quad (13.18)$$

Here, again, the Gamma driver and Bona-Masso slicing conditions were added, as in the case for the BSSNOK equations.

14 The first order CCZ4 equations (FO-CCZ4)

The first order (FO) rewrite of the second order (SO) CCZ4 system, as introduced in the previous section, is a necessary step for proving the hyperbolicity of the SO-CCZ4 system as well as its implementation with finite volume (Section 5 on page 26) or finite element (Section 6 on page 29) schemes. The derivation of this big PDE system is elaborate and it takes a full page to write down the PDE system with all the helper quantities itself. A short version of the derivation is part of our publication [168].

²⁵ Thus, the property “covariant” in CCZ4/Z4c is to be understood as “beeing more covariant then Z4”. However, as CCZ4 takes over the non-covariant “conformal connection functions” $\tilde{\Gamma}^i$ from BSSNOK (Section 12), CCZ4 is not covariant. Appendix A4 briefly presents a *fully* covariant CCZ4 system which implements the ideas of [394].

14.1 Introduction of the auxiliary variables and resulting ordering constraints

The following 33 auxilliary variables are introduced, in order to collect first spatial derivatives of metric terms, ²⁶

$$\begin{aligned} A_i &:= \partial_i \ln \alpha = \frac{\partial_i \alpha}{\alpha}, & B_k^i &:= \partial_k \beta^i, \\ D_{kij} &:= \frac{1}{2} \partial_k \tilde{\gamma}_{ij}, & P_i &:= \partial_i \ln \phi = \frac{\partial_i \phi}{\phi}. \end{aligned} \quad (14.1)$$

An immediate consequence of (14.1) and the Schwarz theorem on the symmetry of second-order derivatives are the following second order ordering constraints [229], which read:

$$\begin{aligned} \mathcal{A}_{ki} &:= \partial_k A_i - \partial_i A_k = 0, & \mathcal{B}_{kl}^i &:= \partial_k B_l^i - \partial_l B_k^i = 0, \\ \mathcal{D}_{klij} &:= \partial_k D_{lij} - \partial_l D_{kij} = 0, & \mathcal{P}_{ki} &:= \partial_k P_i - \partial_i P_k = 0. \end{aligned} \quad (14.2)$$

Since \tilde{A}_{ij} is by construction trace-free, the following additional constraint holds: $\tilde{\gamma}^{ij} \tilde{A}_{ij} = 0$, and thus

$$\mathcal{T}_k := \partial_k (\tilde{\gamma}^{ij} \tilde{A}_{ij}) = \partial_k \tilde{\gamma}^{ij} \tilde{A}_{ij} + \tilde{\gamma}^{ij} \partial_k \tilde{A}_{ij} = 0. \quad (14.3)$$

These relations will be important later on in order to derive a *strongly* hyperbolic system in first-order form. Furthermore, from the constraint $\det(\tilde{\gamma}_{ij}) = 1$ and via the Jacobi formula

$$\partial_k \det(\mathbf{A}) = \text{tr}(\det(\mathbf{A}) \mathbf{A}^{-1} \partial_k \mathbf{A}) \quad (14.4)$$

on the derivatives of the determinant of a matrix, the following additional algebraic constraints on the auxiliary variables D_{kij} is obtained (see also [101]):

$$\tilde{\gamma}^{ij} D_{kij} = 0. \quad (14.5)$$

From Eq. (14.5), another differential constraint follows, namely,

$$\partial_l \tilde{\gamma}^{ij} D_{kij} + \tilde{\gamma}^{ij} \partial_l D_{kij} = 0. \quad (14.6)$$

In practical implementations, however, we have not found particular benefits from making use of this additional constraint in the FO-CCZ4 formulation.

The evolution equations for the auxiliary quantities are obtained by applying the temporal derivative operator ∂_t to equations (14.1), by subsequently exchanging the spatial and temporal derivatives on the right-hand side of the resulting equations and by making use of the PDEs for $\tilde{\gamma}_{ij}$ (13.10), ϕ (13.12), α (13.16) and β^i (13.17).

Many different first-order formulations of the CCZ4 system are possible, since any non-purely algebraic term in the original second-order system can be written as a combination of conservative terms and non-conservative products (see [229, 245] for a parametric study of such families of systems).

Two extreme cases stand out: First, write as many terms as possible are written in a conservative flux-divergence form (Eq. 2.2, but with a source term that contains derivatives). For the first-order Z4 system, this was done in [11].

²⁶ The naming and definitions of these variables follows conventions seen in previous papers. For instance, the Z4 paper [85] defines already A_k and D_{kij} in a first order reduction of the Z4 equations to prove symmetric hyperbolicity in harmonic slicing. In that paper, the choices (like the logarithm in A_i and the factor $1/2$ in the definition of D_{kij}) were probably due to shortness of notation, while here we define A_i as the derivative of the logarithm for means of positivity preserving (more on this in the main text).

	Q_i	Nonconservative product $NCP_a(Q) = B_a^{ib}(Q)\partial_i Q_b$	Algebraic source $S_a(Q)$	Eqn.
ODE-ADM	$\ln \alpha$	0	$\beta^k A_k - \alpha g(\alpha)(K - K_0 - 2\Theta c)$	(14.10)
	β^i	0	$s\beta^k B_k^i + s f^i$	(14.11)
	$\tilde{\gamma}_{ij}$	0	$\beta^k 2D_{kij} + \tilde{\gamma}_{ki} B_j^k + \tilde{\gamma}_{kj} B_i^k - 2/3 \tilde{\gamma}_{ij} B_k^k - 2\alpha (\tilde{A}_{ij} - 1/3 \tilde{\gamma}_{ij} \text{tr} \tilde{A}) - 1/\tau (\tilde{\gamma} - 1) \tilde{\gamma}_{ij}$	(14.12)
	$\ln \phi$	0	$\beta^k P_k + 1/3 (\alpha K - B_k^k)$	(14.13)
SO-CCZ4	\tilde{A}_{ij}	$-\beta^k \partial_k \tilde{A}_{ij} + \phi^2 [-\nabla_i \nabla_j \alpha + \alpha (R_{ij} + \nabla_i Z_j + \nabla_j Z_i)]_{NCP}^{\text{TF}}$	$\tilde{A}_{ki} B_j^k + \tilde{A}_{kj} B_i^k - 2/3 \tilde{A}_{ij} B_k^k 1/3 \tilde{\gamma}_{ij} - \phi^2 [-\nabla_i \nabla_j \alpha + \alpha (R_{ij} + \nabla_i Z_j + \nabla_j Z_i)]_{\text{SRC}}^{\text{TF}}$ $+ \alpha \tilde{A}_{ij} (K - 2\Theta c) - 2\alpha \tilde{A}_{il} \tilde{\gamma}^{lm} \tilde{A}_{mj} - 1/\tau \tilde{\gamma}_{ij} \text{tr} \tilde{A} - \phi^4 8\pi (S_{ij} - 1/3 \tau \tilde{g}_{ij})$	(14.14)
	K	$-\beta^k \partial_k K + [\nabla^i \nabla_i \alpha - \alpha (R + 2\nabla_i Z^i)]_{NCP}$	$\alpha K (K - 2\Theta c) - 3\alpha \kappa_1 (1 + \kappa_2) \Theta - [\nabla^i \nabla_i \alpha - \alpha (R + 2\nabla_i Z^i)]_{\text{SRC}} + 4\pi (S - 3\tau)$	(14.15)
	Θ	$-\beta^k \partial_k \Theta - 1/2 \alpha e^2 [R + 2\nabla_i Z^i]_{NCP}$	$1/2 \alpha e^2 (2/3 K^2 - \tilde{A}_{ij} \tilde{A}^{ij}) - \alpha \Theta K c - Z^i \alpha A_i - \alpha \kappa_1 (2 + \kappa_2) \Theta - 8\pi \alpha \tau$ $+ 1/2 \alpha e^2 [R + 2\nabla_i Z^i]_{\text{SRC}}$	(14.16)
	$\hat{\Gamma}^i$	$-\beta^k \partial_k \hat{\Gamma}^i + 4/3 \alpha \tilde{\gamma}^{ij} \partial_j K - 2\alpha \tilde{\gamma}^{ki} \partial_k \Theta$ $- s \tilde{\gamma}^{kl} \partial_k (B_l^i) - s/3 \tilde{\gamma}^{ik} \partial_k (B_l^l) - s 2\alpha \tilde{\gamma}^{ik} \tilde{\gamma}^{nm} \partial_k \tilde{A}_{nm}$	$2/3 \tilde{\Gamma}^i B_k^k - \tilde{\Gamma}^k B_i^k + 2\alpha (\tilde{\Gamma}_{jk}^i \tilde{A}^{jk} - 3\tilde{A}^{ij} P_j) - 2\alpha \tilde{\gamma}^{ki} (\Theta A_k + 2/3 K Z_k) - 16\pi \alpha \tilde{\gamma}^{ij} S_j$ $- 2\alpha \tilde{A}^{ij} A_j - 4s \alpha \tilde{\gamma}^{ik} D_k^{nm} \tilde{A}_{nm} + 2\kappa_3 (2/3 \tilde{\gamma}^{ij} Z_j B_k^k - \tilde{\gamma}^{jk} Z_j B_k^i) - 2\alpha \kappa_1 \tilde{\gamma}^{ij} Z_j$	(14.17)
	b^i	$-s\beta^k \partial_k b^i$	$s(\partial_t \hat{\Gamma}^i - \beta^k \partial_k \hat{\Gamma}^i - \eta^i)$	(14.18)
FO-CCZ4	A_k	$-\beta^l \partial_l A_k + \alpha g(\alpha) (\partial_k K - \partial_k K_0 - 2c \partial_k \Theta)$ $+ s \alpha g(\alpha) \tilde{\gamma}^{nm} \partial_k \tilde{A}_{nm}$	$-s \alpha g(\alpha) \partial_k \tilde{\gamma}^{nm} \tilde{A}_{nm}$ $- \alpha A_k (K - K_0 - 2\Theta c) (g(\alpha) + \alpha g'(\alpha)) + B_k^l A_l$	(14.19)
	B_k^i	$-s\beta^l \partial_l B_k^i - s(f \partial_k b^i - \mu \tilde{\gamma}^{ij} (\partial_k P_j - \partial_j P_k))$ $+ \mu \tilde{\gamma}^{ij} \tilde{\gamma}^{nl} (\partial_k D_{ljn} - \partial_l D_{kjn})$	$B_k^l B_l^i$	(14.20)
	D_{kij}	$-\beta^l \partial_l D_{kij} - s/2 \tilde{\gamma}_{mi} \partial_k (B_m^i) - s/2 \tilde{\gamma}_{mj} \partial_k (B_i^m)$ $+ s/3 \tilde{\gamma}_{ij} \partial_k (B_m^m) + \alpha \partial_k \tilde{A}_{ij} - 1/3 \alpha \tilde{\gamma}_{ij} \tilde{\gamma}^{nm} \partial_k \tilde{A}_{nm}$	$B_k^l D_{lij} + B_j^l D_{kli} + B_i^l D_{klj} - 2/3 B_l^l D_{kij} + 1/3 \alpha \tilde{\gamma}_{ij} \partial_k \tilde{\gamma}^{nm} \tilde{A}_{nm}$ $- \alpha A_k (\tilde{A}_{ij} - 1/3 \tilde{\gamma}_{ij} \text{tr} \tilde{A})$	(14.21)
	P_k	$\beta^l \partial_l P_k - 1/3 \alpha \partial_k K + 1/3 \partial_k (B_i^i) - s/3 \alpha \tilde{\gamma}^{nm} \partial_k \tilde{A}_{nm}$	$1/3 \alpha A_k K + B_k^l P_l + s/3 \alpha \partial_k \tilde{\gamma}^{nm} \tilde{A}_{nm}$	(14.22)

Second, similar to the ideas outlined in [7], making maximum use of the first-order ordering constraints, so that the variables defining the 4-metric (α , β^i , ϕ and $\tilde{\gamma}_{ij}$) are only evolved by a nonlinear system of ordinary differential equations (ODEs) and where the rest of the dynamics is written in terms of non-conservative products (Section 2.1). The coefficients of these non-conservative products are only functions of α , β^i , ϕ and $\tilde{\gamma}_{ij}$ and no differential terms in these variables appear. The dynamical variables of the FO-CCZ4 system with Gamma-driver shift condition are then: \tilde{A}_{ij} , K , Θ , $\hat{\Gamma}^i$, b^i (the b^i vector is an auxiliary field used to write the Gamma-driver gauge condition [7, 12]) and the auxiliary variables A_k , B_k^i , P_k and D_{kij} .

We will follow the second approach, i.e., the final system of 58 evolution equations, evolving the state vector

$$\mathbf{Q}_{FOCCZ4} = (\gamma_{ij}, K_{ij}, \Theta, \hat{\Gamma}_i, \alpha, \beta^i, b_i, A_i, B_j^i, D_{ijk}, K, \phi, P_k), \quad (14.7)$$

which consist of

$$\mathbf{U} = (\gamma_{ij}, \alpha, \beta^i, \phi) \quad 11 \text{ ODEs and} \quad (14.8)$$

$$\mathbf{V} = (K_{ij}, \Theta, \hat{\Gamma}_i, b_i, A_i, B_j^i, D_{ijk}, K, P_k) \quad 47 \text{ PDEs} \quad (14.9)$$

and has a special structure discussed later in Section 14.3.

Table 14.1: FO-CCZ4 system (14.10-14.22) written in form (2.3), i.e., with a split of differential contributions (left column) and algebraic contributions (right column). The full PDE reads $\partial_t Q + B(Q) \nabla Q = S(Q)$. The semantics of the colors is the following: All ODE-ADM quantities have a helper counterpart at the bottom of the table (FO-CCZ4-exclusive quantities), which is shaded in the same colour. The colouring of the SO-CCZ4 quantities is however without meaning.

14.2 The FO-CCZ4 PDE system in the differential/algebraic split

The most natural first-order formulation of the CCZ4 system is non-conservative and appears in the form (2.3), but with a vanishing conservative

flux. Therefore the system matrices $A_i(Q) = B_i^{aj} \partial_a Q_j$ coincide with the nonconservative matrices and (2.3) coincides with the quasi-linear form (2.4). The final system is given in equations (14.10–14.22) in table 14.1. The tabular form clearly separates the differential component $\text{NCP}_a(Q)$ from the algebraic component $S_a(Q)$.

To obtain a *strongly* hyperbolic first-order system from the second-order CCZ4 formulation of Alic et al. [12] given by (13.10)–(13.18) we systematically use the constraints (14.2) and (14.3) and make *maximum possible use* of the auxiliary variables Eq. (14.1). In other words, our first-order CCZ4 system does *not* contain *any* spatial derivatives of α , β^i , $\tilde{\gamma}_{ij}$ and ϕ any more, but all these terms have been moved to the purely algebraic source term $\mathbf{S}(Q)$ by using (14.1). This has the immediate consequence that the evolution equations (14.12–14.13) reduce to *ordinary* differential equations instead of *partial* differential equations.

Indicated in red in the equations above are those terms that have been added to the PDE to obtain an approximate symmetrization of the sparsity pattern of the system matrices (see discussion in Sec. 14.3 and Fig. 14.2).

Second, in order to obtain the advective terms along the shift vector in the evolution equations of the auxiliary variables, we have used the identities (14.2). We stress that it is important to use the second-order ordering constraints (14.2) in an appropriate way to guarantee strong hyperbolicity, since a naive first-order formulation of the second-order CCZ4 system that just uses the auxiliary variables in order to remove the second-order spatial derivatives will only lead to a weakly hyperbolic system (see [229] for a detailed discussion on the use of second-order ordering constraints in second order in space first order in time hyperbolic systems). Third, we have found that the use of first and second-order ordering constraints alone is *not enough*, but that one must also literally derive the PDE (14.21) for D_{kij} from (13.10) by explicitly exploiting the fact that \tilde{A}_{ij} is trace-free via the use of the constraint \mathcal{T}_k by adding Eq. (14.3) to Eq. (14.21). Without the use of \mathcal{T}_k in Eq. (14.21), the system immediately loses its strong hyperbolicity (see also [118] for a similar observation in the Z4c system). Once again, these important additional terms in the FO-CCZ4 system related to the constraints (14.2) and (14.3) have been highlighted in red in Eqs. (14.12–14.22).

New constants

In addition to the parameters ²⁷ of the second order CCZ4 system, the following ones are added in this formulation:

- the constant τ is a relaxation time to enforce the algebraic constraints on the determinant of $\tilde{\gamma}_{ij}$ and on the trace of \tilde{A}_{ij} “weakly” (see the discussion in [12]).
- the constant e is a *cleaning speed* for the Hamiltonian constraint, following the ideas of the generalized Lagrangian multiplier (GLM) approach of Dedner et al. [153]. As the cleaning is a non-physical process, $e > 1$ is in principle allowed; this leads to faster constraint transport and thus can be used to obtain a better satisfaction of the constraints for *purely numerical* purposes, but $e \neq 1$ breaks the covariance of the FO-CCZ4 system.

²⁷ We use the terms *constant*, *parameter* and *coefficient* synonymously in this context. The defining property of these kind of variables is that they are not determined by the evolution law (PDE). Otherwise, they can be set freely and do not need to be constant in time.

	T	$T_{\text{NCP}}(Q, \nabla Q)$: Nonconservative part	$T_{\text{SRC}}(Q)$: Algebraic part	Eqn.
ODE-ADM	$\tilde{\Gamma}_{ij}^k$	0	$\tilde{\gamma}^{kl}(D_{ijl} + D_{jil} - D_{lij})$	(14.23)
	$\partial_k \tilde{\Gamma}_{ij}^m$	$\tilde{\gamma}^{ml}(\partial_{(k} D_{i)jl} + \partial_{(k} D_{j)il} - \partial_{(k} D_{l)ij})$	$-2D_k^{ml}(D_{ijl} + D_{jil} - D_{lij})$	(14.24)
	Γ_{ij}^k	0	$[\tilde{\Gamma}_{ij}^k]_{\text{SRC}} - \tilde{\gamma}^{kl}(\tilde{\gamma}_{jl} P_i + \tilde{\gamma}_{il} P_j - \tilde{\gamma}_{ij} P_l)$	(14.25)
	$\partial_k \Gamma_{ij}^m$	$+ \tilde{\gamma}^{ml}(\partial_{(k} D_{i)jl} + \partial_{(k} D_{j)il} - \partial_{(k} D_{l)ij})$ $- \tilde{\gamma}^{ml}(\tilde{\gamma}_{jl} \partial_{(k} P_{i)} + \tilde{\gamma}_{il} \partial_{(k} P_{j)} - \tilde{\gamma}_{ij} \partial_{(k} P_{l)})$	$[\partial_k \tilde{\Gamma}_{ij}^m]_{\text{SRC}} + 2D_k^{ml}(\tilde{\gamma}_{jl} P_i + \tilde{\gamma}_{il} P_j - \tilde{\gamma}_{ij} P_l)$ $- 2\tilde{\gamma}^{ml}(D_{kjl} P_i + D_{kil} P_j - D_{kij} P_l)$	(14.26)
SO-CCZ4	R_{ijk}^m	$[\partial_k \Gamma_{ij}^m]_{\text{NCP}} - [\partial_j \Gamma_{ik}^m]_{\text{NCP}}$ $+ [\Gamma]_{\text{NCP}ij}^l [\Gamma]_{\text{NCP}lk}^m - [\Gamma]_{\text{NCP}ik}^l [\Gamma]_{\text{NCP}lj}^m$	$[\partial_k \Gamma_{ij}^m]_{\text{SRC}} - [\partial_j \Gamma_{ik}^m]_{\text{SRC}}$ $+ [\Gamma]_{\text{SRC}ij}^l [\Gamma]_{\text{SRC}lk}^m - [\Gamma]_{\text{SRC}ik}^l [\Gamma]_{\text{SRC}lj}^m$	(14.27)
	R_{ij}	$[R]_{\text{NCP}imj}^m$	$[R]_{\text{SRC}imj}^m$	(14.28)
	R	$\phi^2 \tilde{\gamma}^{ij} [R]_{\text{NCP}i}^i$	$\phi^2 \tilde{\gamma}^{ij} [R]_{\text{SRC}i}^i$	(14.29)
SO-CCZ4	$\nabla_i \nabla_j \alpha$	$\alpha \partial_i A_j$	$\alpha A_i A_j - \alpha [\Gamma]_{\text{SRC}ij}^k A_k$	(14.30)
	$\nabla^i \nabla_i \alpha$	$\phi^2 \tilde{\gamma}^{ij} [\nabla_i \nabla_j \alpha]_{\text{NCP}}$	$\phi^2 \tilde{\gamma}^{ij} [\nabla_i \nabla_j \alpha]_{\text{SRC}}$	(14.31)
FO-CCZ4	$\tilde{\Gamma}^i$	0	$\tilde{\gamma}^{jl} [\tilde{\Gamma}_{jl}^i]_{\text{SRC}}$	(14.32)
	$\partial_k \tilde{\Gamma}^i$	$\tilde{\gamma}^{jl} [\partial_k \tilde{\Gamma}_{jl}^i]_{\text{NCP}}$	$-2D_k^{jl} [\tilde{\Gamma}_{jl}^i]_{\text{SRC}} + \tilde{\gamma}^{jl} [\partial_k \tilde{\Gamma}_{jl}^i]_{\text{SRC}}$	(14.33)
	Z^i	0	$\frac{1}{2} \phi^2 (\hat{\Gamma}^i - \tilde{\Gamma}^i)$	(14.34)
	$\nabla_i Z_j$	$\frac{1}{2} \tilde{\gamma}_{jl} (\partial_i \hat{\Gamma}^l - [\partial_i \hat{\Gamma}^l]_{\text{NCP}})$	$\frac{1}{2} \tilde{\gamma}_{jl} (0 - [\partial_i \hat{\Gamma}^l]_{\text{SRC}}) + D_{ijl} (\hat{\Gamma}^l - \tilde{\Gamma}^l) - \Gamma_{ij}^l Z_l$	(14.35)

- the constant $\mu > 0$ appears in Eq. (14.20) and allows one to adjust the contribution of second-order ordering constraints.
- the constant s contributes to the evolution equations for b^i , β^i and B_k^i and allows to turn on or off the evolution of the shift. For $s = 0$ we have the simple gauge condition $\partial_t \beta^i = 0$, while for $s = 1$ the usual Gamma-driver gauge condition is obtained.
- the constant c (not to be confused with the speed of light, which is set to unity) allows to remove some of the algebraic source terms of the Z4 system, but its default value is $c = 1$, see [12].
- instead of evolving the lapse α and the conformal factor ϕ , we evolve their *logarithms*, i.e., $\ln(\alpha)$ and $\ln(\phi)$. While not a standard choice, this is a very simple method to preserve the *positivity* of the lapse and the conformal factor also at the discrete level. Note also that when treating black holes as punctures, the lapse would vanish at the puncture location and its logarithm diverge. We therefore impose a positive lower limit in our numerical implementation. Since we employ a DG scheme where the solution in every element is represented by an interpolating polynomial, in an element surrounding the puncture the polynomial might actually reach values lower than the limit due to Runge's phenomenon;²⁸ even in this case, however, the logarithm would not diverge.

Table 14.2: Helper quantities which are used in Figure 14.1, in their explicit split $T(Q, \nabla Q) = T_{\text{NCP}}(Q, \nabla Q) + T_{\text{SRC}}(Q)$. The meaning of the colors is to guide related symbols, such as the Christoffel symbols vs. their derivatives.

²⁸ Runge's phenomenon is the problem of oscillatory polynomials of high degree on equispaced interpolation points. Runge's phenomenon is for polynomial approximation what Gibb's phenomenon is for Fourier series approximation. It can be shown that the Chebyshev nodal basis minimizes the effect of Runge's phenomenon.

Differential/algebraic split of further quantities

The PDE system (table 14.1) is completely split into the differential (NCP) and algebraic (SRC) part. While a similar split was already made in the BSS-NOK equations for the conformal decomposition of the Ricci tensor (12.15), here it is even more prominent since also by definition the covariant derivative ∇_i as well as the cleaning vectors Z^i must be split into their differential and algebraic contributions. Table 14.2 holds equations (14.23-14.35) which display all these quantities in their split, built up from the connection symbols $\tilde{\Gamma}_{ij}^k$ and Γ_{ij}^k as well as their derivatives.²⁹

Here, we have again made use of the second-order ordering constraints (14.2) by *symmetrizing* the spatial derivatives of the auxiliary variables as follows:

$$\begin{aligned}\partial_{(k} A_{i)} &:= \frac{\partial_k A_i + \partial_i A_k}{2}, & \partial_{(k} P_{i)} &:= \frac{\partial_k P_i + \partial_i P_k}{2}, \\ \partial_{(k} B_{j)}^i &:= \frac{\partial_k B_j^i + \partial_j B_k^i}{2}, & \partial_{(k} D_{l)ij} &:= \frac{\partial_k D_{lij} + \partial_l D_{kij}}{2}.\end{aligned}\quad (14.36)$$

We also stress that in our FO-CCZ4 formulation, the Ricci tensor R_{ij} is directly calculated from the Riemann tensor R_{ikj}^m and the Christoffel symbols and their derivatives *ab definitionem*, without making use of the typical splitting of the Ricci tensor as e.g., used in [12]. We also compute the contracted Christoffel symbols $\tilde{\Gamma}^i$ directly from their definition, without making use of the fact that the determinant of $\tilde{\gamma}_{ij}$ is unity, since in general this cannot be guaranteed to hold exactly at the discrete level, unless the algebraic constraints are rigorously enforced.

From a more formal and mathematical point of view, the additional use of the second-order ordering constraints (14.2) and the constraint \mathcal{T}_k (the terms colored in red) can be motivated by looking at the structure of the sparsity pattern of the system matrix $\mathbf{A} \cdot \mathbf{n}$ with and without the use of these constraints. In Fig. 14.2 we report the sparsity pattern of the system matrix in the normal direction $\mathbf{n} = 1/\sqrt{3}(1, 1, 1)$ for the Gamma-driver shift condition and the 1+log slicing condition for a randomly perturbed flat Minkowski spacetime, neglecting all matrix entries whose absolute value is below a threshold of 10^{-7} . The blue dots represent the original sparsity structure *without* the use of the second-order ordering constraints (14.2) and without using the constraint (14.3), while the combination of the blue and the red dots shows the sparsity pattern after the terms colored in red have been added to the PDE system. Our approach for finding a suitable form of the ordering constraints to be added is based on *approximate symmetrization* of the sparsity pattern of the system matrix, in order to avoid *Jordan blocks* (Fig. 14.1), which cannot be diagonalized. Such Jordan blocks are evident in the sparsity pattern given by the blue dots alone in Fig. 14.2.

We are not aware of works in which the constraint \mathcal{T}_k has been used in conformal first-order hyperbolic formulations of the 3+1 Einstein equations, but its effect becomes rather clear from Fig. 14.2. It is also directly evident from Fig. 14.2 that the first 11 quantities $\tilde{\gamma}_{ij}$, α , β^i and ϕ are only evolved by ODEs and that the entire system does not depend on spatial derivatives of these variables, since all entries in the first 11 rows and columns of the system matrix are zero.

²⁹ In a practical implementation (section 15 on page 61), this complicated split has to be carefully followed if one wants to adopt a Riemann solver. In contrast, a pure Finite-Differencing implementation does not need the split. See section 15 for details.

$$\left[\begin{array}{cc} \lambda_1 & 1 \\ \lambda_1 & 1 \\ \lambda_1 & \\ \lambda_2 & 1 \\ \lambda_2 & \\ \lambda_3 & \\ \ddots & \\ \lambda_n & 1 \\ & \lambda_n \end{array} \right]$$

Figure 14.1: Invertible Jordan blocks are the necessary condition for inverting the large FO-CCZ4 system matrix. The smallest possible uninvertable Jordan block is of order two, such as $A = \begin{pmatrix} 1 & 1 \\ 0 & 1 \end{pmatrix}$ or $B = \mathbb{1} - A$. It sustains the invertability of the whole system (in the shown figure for instance with $\lambda_2 = 1$).

Summary of key ideas to achieve strong hyperbolicity

Summarizing, the key ideas that have been used in order to obtain the *strongly hyperbolic* FO-CCZ4 system are:

1. maximum use of the first-order ordering constraints (14.1) in order to *split* the complete system into 11 pure ODEs (14.39) for the evolution of the quantities defining the 4-metric ($\alpha, \beta^i, \tilde{\gamma}_{ij}$ and ϕ), and with *no spatial derivatives* of these quantities appearing in the remaining PDE system (14.40). However, if we want to keep this very particular split structure of the PDE system, it is *not* possible to add damping terms proportional to the first-order ordering constraints (14.1) to the system, since this would make spatial derivatives of $\alpha, \beta^i, \tilde{\gamma}_{ij}, \phi$ appear again and may eventually lead to Jordan blocks which cannot be diagonalized. We therefore explicitly refrain from adding these terms, in contrast to what has been done in [101]. Following the philosophy above, also writing the system in a flux-conservative form like in [11, 89] is not possible, since the fluxes will in general depend on the 4-metric and thus, after application of the chain rule, spatial derivatives of $\alpha, \beta^i, \tilde{\gamma}_{ij}$ and ϕ would appear again in the quasi-linear form. We note that not adding any damping terms proportional to the first-order ordering constraints (14.1) may lead to a rapid growth of these constraints on the discrete level [305]. This effect, however, may be reduced by a periodic reinitialization of the auxiliary variables with appropriate discrete versions of Eq. (14.1), either after a certain number of timesteps, or if a large growth of the first-order constraint violations is detected.
2. *approximate symmetrization* of the sparsity pattern of the system matrix $\mathbf{A} \cdot \mathbf{n}$ by appropriate use of the second-order ordering constraints (14.2) and the constraint (14.3), i.e., by adding the terms highlighted in red in PDEs (14.12-14.22). Symmetrization of the first derivatives of the auxiliary variables by using (14.36), apart from the advective terms along the shift vector.
3. introduction of an *independent* constraint propagation speed e for the Hamiltonian constraint H in the PDE (14.16) for the variable Θ , following the GLM approach of Dedner et al. [153].
4. use of the *logarithms* of α and ϕ as evolution variables, in order to guarantee positivity for α and ϕ in a simple and natural way. These evolution quantities are consistent with the definitions of the auxiliary variables A_k and P_k .

14.3 Eigenstructure of the FO-CCZ4 system

As already shown briefly above, the FO-CCZ4 system (14.10-14.22) can be written in compact matrix-vector (quasi-linear form) form

$$\frac{\partial \mathbf{Q}}{\partial t} + \mathbf{A}_1(\mathbf{Q}) \frac{\partial \mathbf{Q}}{\partial x_1} + \mathbf{A}_2(\mathbf{Q}) \frac{\partial \mathbf{Q}}{\partial x_2} + \mathbf{A}_3(\mathbf{Q}) \frac{\partial \mathbf{Q}}{\partial x_3} = \mathbf{S}(\mathbf{Q}), \quad (14.37)$$

where the complete state vector is given by

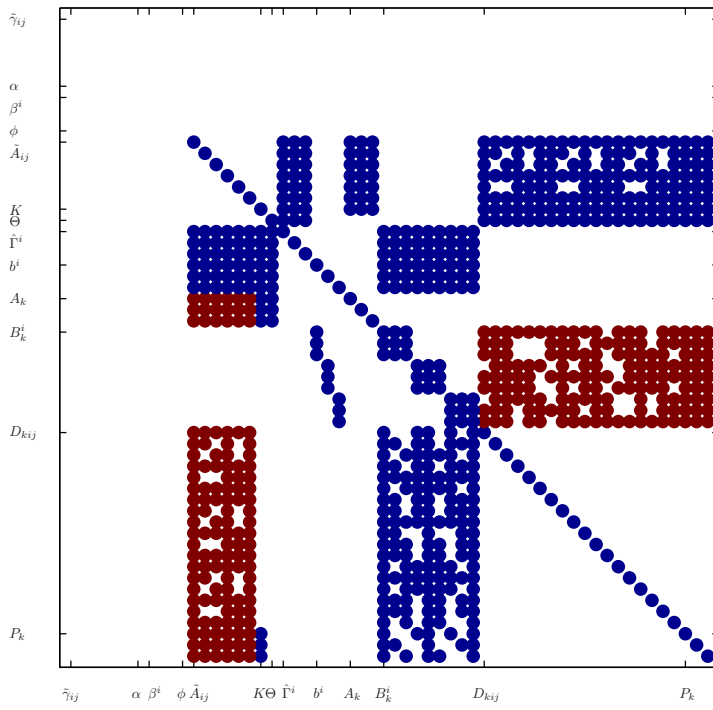


Figure 14.2: Sparsity pattern of the system matrix $\mathbf{A} \cdot \mathbf{n}$ with $\mathbf{n} = (1, 1, 1)/\sqrt{3}$ for randomly perturbed flat Minkowski space-time using the Gamma-driver shift condition ($s = 1$) and 1 + log slicing ($g(\alpha) = 2/\alpha$), without the use of the constraints (14.2) and (14.3) (blue dots) and with the use of these constraints (blue & red dots). The achieved *approximate symmetrization* of the sparsity pattern is evident. Note also the complete absence of non-zero entries in the first 11 lines and columns corresponding to the variables $\tilde{\gamma}_{ij}$, α , β^i and ϕ , which clearly highlights the special structure of our FO-CCZ4 system that can be split into a set of pure ODEs and a reduced PDE system, as discussed in Section 14.3. Figure published in [168].

$$\begin{aligned} \mathbf{Q} &= \left(\tilde{\gamma}_{ij}, \ln \alpha, \beta^i, \ln \phi, \tilde{A}_{ij}, K, \Theta, \hat{\Gamma}^i, b^i, A_k, B_k^i, D_{kij}, P_k \right) \\ &= \left(\tilde{\gamma}_{xx}, \tilde{\gamma}_{xy}, \tilde{\gamma}_{xz}, \tilde{\gamma}_{yy}, \tilde{\gamma}_{yz}, \tilde{\gamma}_{zz}, \ln \alpha, \beta^x, \beta^y, \beta^z, \ln \phi, \tilde{A}_{xx}, \tilde{A}_{xy}, \tilde{A}_{xz}, \tilde{A}_{yy}, \tilde{A}_{yz}, \tilde{A}_{zz}, K, \Theta, \hat{\Gamma}^x, \hat{\Gamma}^y, \hat{\Gamma}^z, \right. \\ &\quad b^x, b^y, b^z, A_x, A_y, A_x B_x^x, B_y^x, B_z^x, B_x^y, B_y^y, B_z^y, B_x^z, B_y^z, B_z^z, D_{xxx}, D_{xxy}, D_{xxz}, D_{xyy}, D_{xyz}, D_{xzz}, \\ &\quad \left. D_{yxx}, D_{yxy}, D_{yxz}, D_{yyy}, D_{yyz}, D_{yzz}, D_{zxx}, D_{zxy}, D_{zxz}, D_{zyy}, D_{zyz}, D_{zzz}, P_x, P_y, P_z \right), \end{aligned} \quad (14.38)$$

containing a total of 58 variables that have to be evolved in time. Following the split $\mathbf{Q} = (\mathbf{V}, \mathbf{U})$ from equations (14.8) and (14.9), from (14.10-14.22) and Fig. 14.2 it is obvious that the vector \mathbf{V} is evolved in time only via ODEs of the type

$$\frac{\partial \mathbf{V}}{\partial t} = \mathbf{S}'(\mathbf{Q}), \quad (14.39)$$

where $\mathbf{S}'(\mathbf{Q})$ contains the first 11 elements of the vector of purely algebraic source terms $\mathbf{S}(\mathbf{Q})$. Therefore, the eigenvalues associated with the ODE subsystem for \mathbf{V} are trivially zero. Since in our formulation of the FO-CCZ4 system we have made maximum use of the first-order ordering constraints, Eqs. (14.10-14.13) do not contain *any* spatial derivative of the quantities in \mathbf{V} , so that the columns in the matrices of the related eigenvectors are trivially the unit vectors. The remaining reduced system that needs to be analyzed contains the vector \mathbf{U} of the dynamic quantities and has the very particular structure

$$\frac{\partial \mathbf{U}}{\partial t} + \mathbf{B}_1(\mathbf{V}) \frac{\partial \mathbf{U}}{\partial x_1} + \mathbf{B}_2(\mathbf{V}) \frac{\partial \mathbf{U}}{\partial x_2} + \mathbf{B}_3(\mathbf{V}) \frac{\partial \mathbf{U}}{\partial x_3} = \mathbf{S}''(\mathbf{Q}), \quad (14.40)$$

where the source term $\mathbf{S}''(\mathbf{Q})$ contains the remaining elements of the source vector $\mathbf{S}(\mathbf{Q})$ and where the system matrices \mathbf{B}_i depend only on the vector

V defining the 4-metric and do *not* depend on the vector \mathbf{U} . The non-trivial eigenvectors of the complete system (14.37) can thus be obtained from those of the reduced system (14.40) by simply adding zeros corresponding to the quantities contained in V .

An immediate consequence of the very particular splitting of (14.37) into the ODEs (14.39) and the reduced PDEs (14.40) is that all waves appearing in the system (14.40) and thus in (14.37) are *linearly degenerate* (see [445] for a detailed discussion), since the eigenvalues λ_i depend only on V and not on \mathbf{U} and hence $\partial\lambda_i/\partial\mathbf{Q}\cdot\mathbf{r}_i = 0$, $\forall \lambda_i$. This also means that the FO-CCZ4 system cannot generate shock waves, since the formation of classical shock waves requires the compression of characteristics and thus the presence of genuinely nonlinear fields [387, 445].

In order to prove strong hyperbolicity of the FO-CCZ4 system proposed in this paper, we compute the *entire* eigenstructure of the system matrix \mathbf{B}_1 in the x_1 direction for two standard gauge choices: i) zero shift $\beta^i = 0$ (hence $s = 0$) with harmonic slicing, i.e., $g(\alpha) = 1$ and ii) the gamma driver shift condition ($s = 1$) with 1+log slicing, i.e. $g(\alpha) = 2/\alpha$ (see section 11.3 for details). Note that, in principle, the eigenstructure of the principal symbol of the system should be computed for every normal direction vector $\mathbf{n} \neq 0$ in space. However, this is not necessary in this case, since the Einstein equations are isotropic [399].

For the first shift condition, there is no need to evolve the quantities b^i and B_k^i , whose corresponding PDEs can therefore be neglected in the following analysis (the associated eigenvalues are simply zero and the eigenvectors are the unit vectors). For zero shift, the vector \mathbf{U} can thus be furthermore reduced to only 35 remaining dynamic quantities

$$\mathbf{U} = (\tilde{A}_{ij}, K, \Theta, \hat{\Gamma}^i, A_k, D_{kij}, P_k). \quad (14.41)$$

In this case the 35 eigenvalues of matrix \mathbf{B}_1 in the x_1 direction are

$$\begin{aligned} \lambda_{1,2,\dots,21} &= 0, & \lambda_{22,23} &= \pm\sqrt{\tilde{\gamma}^{11}}\phi\alpha e, \\ \lambda_{24,25,\dots,29} &= +\sqrt{\tilde{\gamma}^{11}}\phi\alpha, & \lambda_{30,31,\dots,35} &= -\sqrt{\tilde{\gamma}^{11}}\phi\alpha. \end{aligned} \quad (14.42)$$

The associated complete set of 35 right eigenvectors defining the right eigenvector matrix \mathbf{R} , as well as the inverse right eigenvector matrix ($\mathbf{L} = \mathbf{R}^{-1}$) that defines the left eigenvectors, are an appendix in our publication [168].

The fact that the FO-CCZ4 system has only real eigenvalues and a complete set of linearly independent eigenvectors (where the matrix of eigenvectors is uniformly bounded) is a necessary and sufficient condition for strong hyperbolicity. Note that for harmonic lapse the eigenvectors $\mathbf{r}_{22,23}$ are only linearly independent of $\mathbf{r}_{24,\dots,35}$ if $c = 1$, $\forall e > 0$ or for $e \neq 1$, $\forall c \geq 0$. The choice $c = 1$ and $e = 1$ corresponds to the standard setting typically used for second order Z4 and CCZ4 systems, and the importance of using $c = 1$ has already been shown in the hyperbolicity analysis for the first and second order Z4 system carried out in [86, 90]. In other words our results on the FO-CCZ4 system confirm previous findings made in the literature.

For the gamma driver shift condition, the hyperbolicity analysis is much more complex and requires the computation of all 47 eigenvectors of the reduced dynamical system (14.40), this time including also the quantities b^i and B_k^i . After tedious calculations it was possible to obtain analytical

expressions for the eigenvalues and all 47 eigenvectors also in this case (again, the results are reported in the appendix of [168]). To the best of our knowledge, this is the first time that a hyperbolicity analysis of a first-order reduction of the CCZ4 system including the gamma driver shift condition has been carried out. An analysis of the FO-CCZ4 system with other shift conditions, such as the generalized harmonic shift [87, 90], is left to future work.

At this point, we would like to add the following clarifying remark. The hyperbolicity analysis has been carried out for the FO-CCZ4 evolution system (14.10–14.22), which in principle admits violations of the algebraic constraints $\det(\tilde{\gamma}_{ij}) = 1$, $\tilde{\gamma}^{ij}\tilde{A}_{ij} = 0$ and $\tilde{\gamma}^{ij}D_{kij} = 0$. Hence, compared to the original Z4 system [11, 85, 86], it has an augmented solution space. Since our hyperbolicity analysis has been made without enforcing the algebraic constraints, it is valid for the FO-CCZ4 system with the augmented solution space, but should not be regarded as an analysis of the original Z4 system. However, if the initial data satisfies the algebraic constraints, a direct consequence of the system (14.10–14.22) is that the constraints will remain satisfied for all times, so that our hyperbolicity analysis also covers solutions that satisfy the algebraic constraints.

15 Implementation of the FO-CCZ4 equations

The implementation of the pure PDE terms (fluxes, non-conservative products and sources) of the FO-CCZ4 equations is *logicless* since they are given analytically³⁰. Therefore, implementing the huge PDE system is basically a question of care and diligence and can be done in principle in any computer readable language.

³⁰ in contrast for instance to the GRMHD equations where an iterative root-finding has to be applied to recover primitive variables from the conserved ones. Logic enters here in terms of an iterative loop with stop criterion.

15.1 About the cost of the FO-CCZ4 PDE system

The *costs* of a PDE system should measure its requirements in runtime, memory and storage when being evaluated in a computer. Certainly, in terms of memory requirements, due to the larger state vector, the costs of the FO-CCZ4 system (59 unknowns) are certainly higher than of the SO-CCZ4 system (34 unknowns), which again is much more demanding than the original ADM system (12 unknowns). When evaluated within the presented ADER-DG scheme, the cost of the FO system will again be higher than the cost of the SO system. This is due to the distinction between non-conservative product (NCP) and source terms is made and the evaluation of the NCP takes place several times within a timestep during the evaluation of the Riemann solver at the cell boundaries. However, the FO system can also be evaluated with traditional methods—Finite Differences and Runge Kutta (FDRK) where there is only the right hand side differential operator.

The determination of absolute costs is almost always inconclusive. For instance, the system matrix, being a $\mathbb{R}^{n \times n}$ matrix, obviously grows with $\mathcal{O}(n^2)$, where n is the state vector size. A naive attempt is to relate the cost ratio of FO/SO system to $58^2/34^2 \sim 2.9$. However, this obviously does not even take the evaluation of tensors into account. Figure 14.2 already shows that the FO-CCZ4 system matrix is sparse, and Figure 15.1 quantifies the differences in terms of necessary contractions to determine a certain element

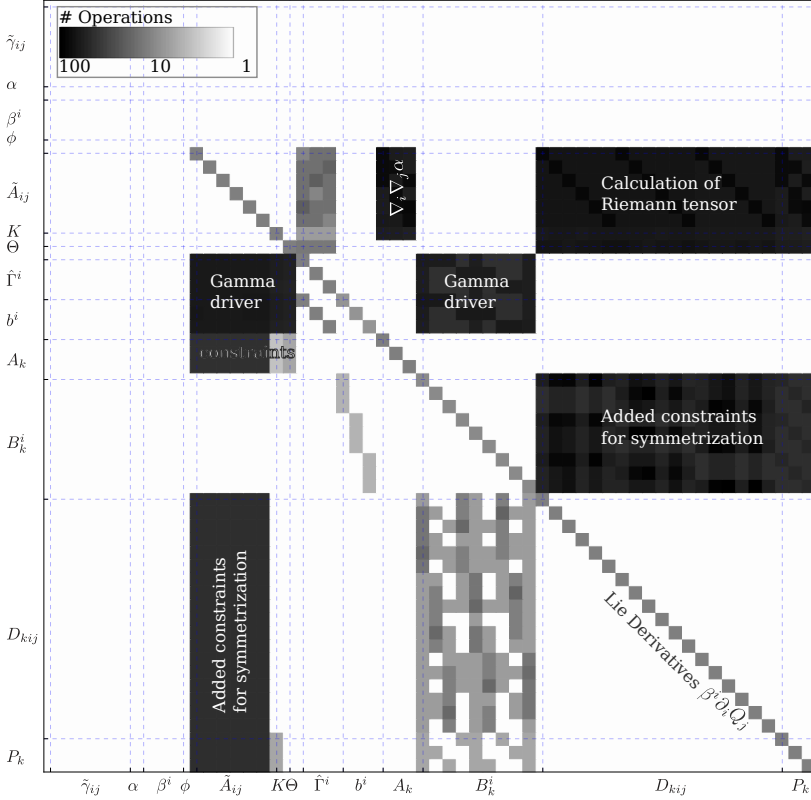


Figure 15.1: System matrix $\mathbf{A} \cdot \mathbf{n}$ with in radial direction $\mathbf{n} = (1, 1, 1)$ as in Figure 14.2. Here, the color (shading) encodes the number of basic operations (additions and multiplications due to tensor contractions) necessary to compute the non-conservative product of that matrix element on a logarithmic scale. The major blocks are labeled.

The figure shows the two major cost drivers: The complex computation of the Riemann (Ricci) tensor via the derivatives of the Christoffel symbols via D_{kij} (upper right) as well as the symmetrization contributions which almost double the computational cost of the NCP.

Conf.	C	#OP	t [sec]
Dense	G	8884	3.49
	I	17761	8.92
Sparse	G	5638	2.61
	I	2757	6.14
FullSimplify	G	4737	2.26
	I	2730	4.42
Optimized	G	5886	2.52
	I	2821	5.77
orderOpt	G	4141	2.76
	I	1480	3.47

Table 15.1: Measuring the impact of differently “optimized” generated code to compute the NCP of the Z4 system. The first column describes the experiment, the second column shows which compiler was used to compile the Fortran code to assembler (G=GNU compiler, I=Intel compiler), #OP indicates the number of assembler instructions which were generated while t shows the serial runtime for $6 \cdot 10^6$ evaluations of the NCP with arbitrary but same state vectors (pseudo-randomly generated with the same seed).

Experiments and interpretation are given in the main text.

A_{ij} . The amount of calculations varies over five orders of magnitude. In other words, a few elements contribute to the overall number of $\sim 40,200$ elementary arithmetic operations (counting special functions like n^x and x^n as one operation).

A completely different measure is the number of assembler instructions which have to be processed in order to compute a PDE function. Table 15.1 provides a small benchmark where different Fortran codes were generated by a CAS (Mathematica and Matlab were used). In the first setup, all matrix elements were specified, even the zero ones (*Dense*), while in a second step, the zero matrix elements were trivially removed (*Sparse*). In a subsequent step, a typical CAS “simplification” step (*FullSimplify*) was performed, where algebraic expressions are brought in a form which requires less evaluations (for instance by reducing polynomial expressions). The *Optimized* step further tried to store intermediate expressions to variables, avoiding the need of computing certain expressions over and over (trading memory for less arithmetic instructions). The *orderedOpt* step adopts a topological ordering of the required intermediate computations of the NCP (adopting a task based paradigm), which should also reduce cache misses.

The results of this benchmarks are given as follows: While the number of operations in principle can be decreased by one order of magnitude (17kOP for the dense matrix vs. 1.4kOP for the topological ordered and intermediate expressions computing version), the overall runtime stays in the same regime and sophisticated algebraic transformations of the computation order do not pay off.

The reasons for this are that optimizing for a small number of assembler

instructions is not the right measure at a CISC platform ³¹, while sophisticated vectorization units of the machine were not used at all ³². Therefore, a static analysis of code runtime is not meaningful.

15.2 Choosing the right language

There are several aspects that emerge when implementing large tensorial PDE systems. First, as in physics, where the suitable choice of a coordinate system can greatly reduce the complexity of a problem, or in mathematics, where the transformation of a problem to another theory can provide new insights and shortcuts, a suitable notation of the PDE system in a computer-readable language/form reduces the abstraction necessary from physics and the equations as they are written on the paper.

The smallest common denominator in modern scientific programming languages is that of *linear algebra*, providing a compact language to manipulate n -dimensional arrays in one expression (instead of looping over vector or matrix axes). However, linear algebra misses a number of features from differential geometry, for instance the distinction from covariant and contravariant tensors. There is in fact the need for a *domain specific language* (DSL) which implements a minimum on tensor algebra, i.e., general style contractions (applying Einstein sum convention).

As an example, an exemplaric contraction which shall compute D^i is given,

$$D^i := A^{ik} B^{nm} C_{knm} \quad (15.1)$$

with arbitrary tensors A, B, C , where not even symmetries such as $B^{nm} = B^{mn}$ shall be relevant at this point. While the mathematical expression (15.1) provides a clear instruction how D^i is defined by sums, thanks to associativity of addition and multiplication, several evaluation strategies may lead to D^i . For the FO-CCZ4 equations, using the `TensorTemplates` package allows to write down this expression precisely as

$$\vec{D} = \text{contract}_{\langle 1,0 \rangle} (A, \text{trace}_{\langle 0,2 \rangle} (\text{contract}_{\langle 0,2 \rangle} (B, C))) \quad (15.2)$$

This notation is declarative in a sense that it does not expose how a contraction or trace is computed internally ³³ and it reveals the intermediate evaluation sequence as

$$A^{ik} B^{nm} C_{knm} \rightarrow A^{ik} E_{mkn} \rightarrow A^{ik} E_k \rightarrow D^i. \quad (15.3)$$

Providing efficient tensor algebra as a library is a whole branch of HPC itself, and there is a plentitude of librarys available, however only a subset of them deals with covariance ³⁴.

16 Benchmarks for solving FO-CCZ4 with ADER-DG

In the following we present a battery of standard tests that explore the ability of our formulation to carry out long-term stable evolutions of a number of different spacetimes with increasing degree of curvature. If not stated otherwise, in all of the tests we set initially $\Theta = 0$, $\hat{\Gamma}^i = \tilde{\Gamma}^i$ and $b^i = 0$ and the HLLEM method is used (Section 6.2).

³¹ Complex instruction set computers (CISC) have machine instructions for various high level functions, which however can vary largely in execution time. In contrast, the presented measure is considerably more meaningful for reduced instruction set computers (RISC). In the current HPC landscape, CISC machines dominate, while there is however a trend for more RISC machines.

³² The lack of vectorization in CAS-generated code stems from the fact that the tensorial algebra was not expound to the CAS in the chosen approach. While tensorial packages for CAS are in principle available (cf. Section 3.1 on page 21), the freely available C/Fortran code generators from both Mathematica™ and Matlab™ do not generate optimized tensor contraction loops, such as discussed in Section 15.2.

³³ The technical advantage (which comes on top of readability) of this abstraction is the fact that the implementation of the operation can be done efficiently by the compiler, for instance by exploiting parallelization in terms of SIMD-vectorization.

³⁴ other covariance-aware tensor libraries are for instance the Deal.II Library [15, 54], the Tensor Contraction Engine [66, 67, 295], BARRACUDA [339], InTensLi [304]

In all tests the algebraic constraints on the unit determinant of $\tilde{\gamma}_{ij}$, the zero trace of \tilde{A}_{ij} as well as the constraint $\tilde{\gamma}^{ij}D_{kij} = 0$ (which is a consequence of $|\tilde{\gamma}_{ij}| = 1$) have all been *rigorously enforced* in the discrete solution $u_h(x, t^n)$ at the beginning of each timestep, but they have *not* been enforced during the computation of the spacetime predictor q_h . Note that the predictor q_h is only an auxiliary quantity that is overwritten after each timestep and which has a role similar to the evolution stage to the half timelevel in second-order MUSCL-Hancock type TVD finite-volume schemes. We therefore set $\tau \rightarrow \infty$ and thus neglect the corresponding source terms. In tests involving black holes, the lower limit on the lapse is set to be $\ln(\alpha) \geq -20$. We will use the notation P_N to indicate an ADER-DG scheme using piecewise polynomials of degree N to represent u_h .

16.1 Linearized gravitational-wave test

The first test problem is a simple one-dimensional wave-propagation test problem in the linearized regime. The computational setup follows the one suggested by in [8]. The computational domain is $\Omega = [-0.5, 0.5]$ with periodic boundary conditions in the x direction and two simulations are run until a final time of $t = 1000$: (i) a first one using 4 ADER-DG P_5 elements (i.e., a total number of 24 degrees of freedom) and (ii) a second one using only 2 ADER-DG P_9 elements (i.e., only 20 degrees of freedom). This test is run with the unlimited version of the ADER-DG scheme. The exact solution of the metric of the problem is given by

$$ds^2 = -dt^2 + dx^2 + (1+h)dy^2 + (1-h)dz^2, \quad (16.1)$$

$$\text{with } h := \epsilon \sin(2\pi(x-t)), \quad (16.2)$$

and the wave amplitude $\epsilon = 10^{-8}$ is chosen small enough in order to stay in the linear regime, so that terms $\mathcal{O}(\epsilon^2)$ can be neglected. Since the shift is zero in the metric (16.1) ($\beta^i = 0$), we set $s = 0$ in our FO-CCZ4 system and furthermore harmonic slicing is used, i.e., $g(\alpha) = 1$. We also set $K_0 = 0$, $c = 0$, $e = 2$ and use the *undamped* version of the system, setting $\kappa_1 = \kappa_2 = \kappa_3 = \eta = 0$. Using the metric (16.1), the definition of the extrinsic curvature reduces to $K_{ij} = -\frac{1}{2}\partial_t\gamma_{ij}/(\alpha)$, so that the various components are given by $K_{xx} = K_{xy} = K_{xz} = K_{yz} = 0$, $K_{yy} = -\frac{1}{2}\partial_t h$ and $K_{zz} = +\frac{1}{2}\partial_t h$. From this information, the conformal factor ϕ , the conformal spatial metric $\tilde{\gamma}_{ij}$, the traceless conformal extrinsic curvature \tilde{A}_{ij} and all auxiliary variables can be computed by a direct calculation according to their definitions.

In Fig. 16.1 we report the temporal evolution of all ADM constraints (Hamiltonian and momentum constraints) as well as the errors of the algebraic constraints on the determinant of the conformal metric and the error in the trace of \tilde{A}_{ij} in both cases, i.e., using the ADER-DG P_5 and P_9 scheme. A comparison of the extrinsic-curvature component \tilde{A}_{22} with the exact solution is also provided at the final time $t = 1000$, showing overall an excellent agreement between numerical and exact solution. The quality of the results obtained with the ADER-DG schemes used in this paper, which are uniformly high-order accurate in both space and time, is significantly superior to the results shown in [8] for the same test problem using a

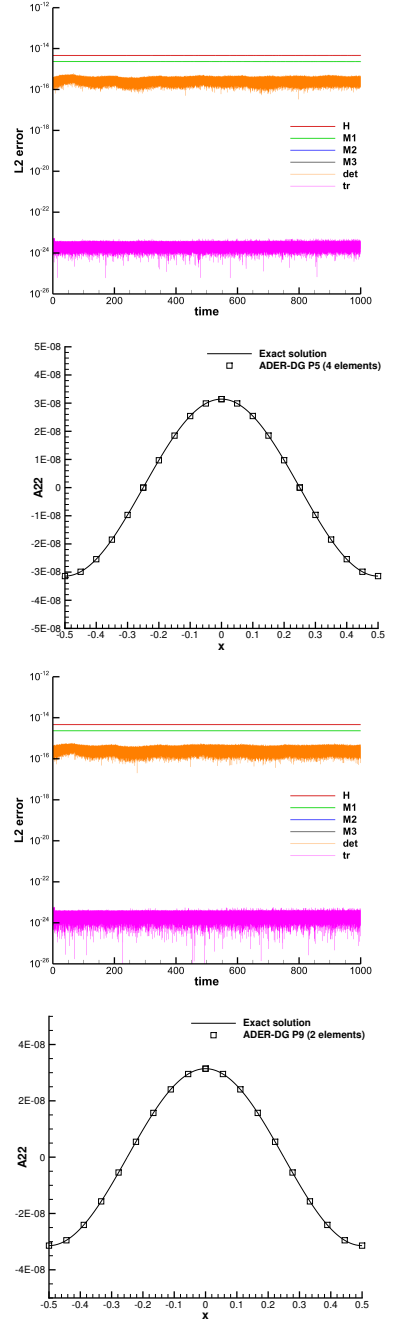


Figure 16.1: Linearized gravitational-wave test using an ADER-DG P_5 scheme with 4 elements (panels 1-2) and an ADER-DG P_9 scheme with only 2 elements (panels 3-4). The temporal evolution of the constraints (colour panels) is shown together with the waveform for the component \tilde{A}_{22} of the traceless conformal extrinsic curvature after 1000 crossing times at time $t = 1000$.

finite difference scheme with much more grid points (between 50 and 200) compared to the very coarse mesh containing only 20 to 24 degrees of freedom used in our simulations. Note that a fair comparison between high order finite-difference and DG schemes must be made in terms of points per wavelength for finite-difference methods and in degrees of freedom per wavelength for DG schemes.

16.2 Gauge-wave test

Also this classical test problem has been taken from the collection of standard tests of [8]. The metric in this case is given by

$$ds^2 = -H(x, t)dt^2 + H(x, t)dx^2 + dy^2 + dz^2, \quad (16.3)$$

with $H(x, t) := 1 - A \sin(2\pi(x - t))$.

The metric (16.3) implies zero shift ($\beta^i = 0$), hence we use once more $s = 0$ together with harmonic slicing $g(\alpha) = 1$. Also for this test we employ the *undamped* version of the FO-CCZ4 system, setting $\kappa_1 = \kappa_2 = \kappa_3 = \eta = 0$. The computational domain in this case is two-dimensional, with $\Omega = [-0.5, 0.5] \times [-0.05, 0.05]$ with periodic boundary conditions in all directions. Since $\beta^i = 0$, the extrinsic curvature is again given by $K_{ij} = -\partial_t \gamma_{ij}/(2\alpha)$, i.e., $K_{yy} = K_{zz} = K_{xy} = K_{xz} = K_{yz} = 0$ and the remaining primary variables are

$$\phi^2 = H^{-1/3}, \quad \alpha = \sqrt{H}, \quad K_{xx} = -\pi A \frac{\cos(2\pi(x - t))}{\sqrt{1 - A \sin(2\pi(x - t))}}.$$

We furthermore set $K_0 = 0$. The auxiliary variables can be obtained from their definition via a straightforward calculation.

We first simulate this test problem with a perturbation amplitude of $A = 0.1$ until $t = 1000$ with an unlimited ADER-DG P_3 scheme and using 100×10 elements to cover the domain Ω . We run this physical setup twice, once with the default parameters $e = c = 1$, according to the original second order CCZ4 system [12] and a *modified* setting with $e = 2$ and $c = 0$ to obtain an improved cleaning of the Hamiltonian constraint. In both cases the system is strongly hyperbolic. The time evolution of the ADM constraints is reported in Fig. 16.2, showing only a very moderate growth of the constraint M_2 that is sublinear in time and close to machine precision. The other constraints H and M_1 remain essentially constant during the entire simulation. We emphasize that we have used the *undamped* version of the FO-CCZ4 system, and nevertheless obtain stable results, while the original second-order CCZ4 formulation was reported to fail for this test problem in the undamped version, and only the damped CCZ4 system was stable (see [12] for details). It is also worth recalling that both the first- and the second-order formulation of the BSSNOK system fail for this test case after a rather short time [12, 101]. In Fig. 16.2 we also provide a direct comparison of the solution after 1000 crossing times for the conformal factor ϕ as well as for the trace of the extrinsic curvature K . Note the overall very good agreement between the numerical solution and the exact one. For the sake of clarity, in the plots of the waveforms we also report the numerical error computed as the difference between the numerical solution and the

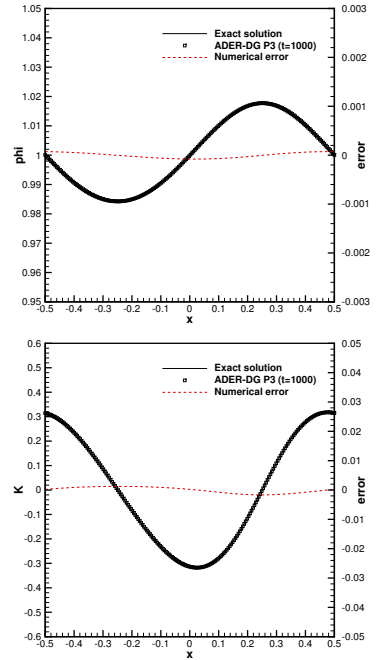


Figure 16.2: Gauge-wave test case with amplitude $A = 0.1$ using the undamped FO-CCZ4 system ($\kappa_1 = \kappa_2 = \kappa_3 = 0$) and improved cleaning speed $e = 2$ with no damping $c = 0$. Comparison with exact solution after $t = 1000$.

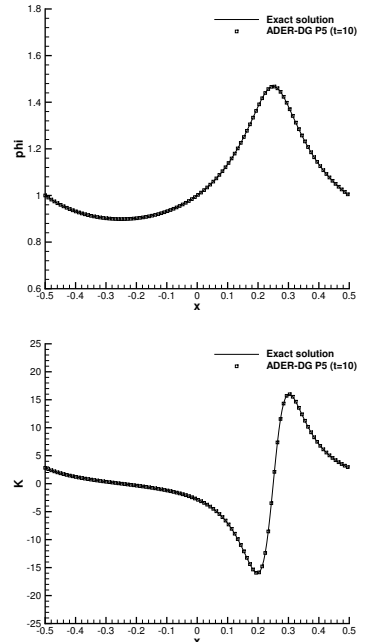


Figure 16.3: Highly nonlinear gauge-wave test case with very large amplitude $A = 0.9$. Comparison of the wave form with the exact solution at time $t = 10$ for an ADER-DG P_5 scheme and 100×10 elements.

$N_x \times N_y$	L_2 error ϕ	$\mathcal{O}(\phi)$	L_2 error α	$\mathcal{O}(\alpha)$	L_2 error K	$\mathcal{O}(K)$
$N = 3$						
60 × 6	2.8663E-05		5.4876E-05		3.8469E-03	
80 × 8	1.0574E-05	3.5	2.2314E-05	3.1	7.0357E-04	5.9
100 × 10	3.8760E-06	4.5	8.0170E-06	4.6	2.3112E-04	5.0
120 × 12	1.6311E-06	4.7	3.2521E-06	4.9	9.7392E-05	4.7
$N = 4$						
60 × 6	4.2966E-06		1.1408E-05		2.1910E-04	
80 × 8	8.9473E-07	5.5	2.3725E-06	5.5	5.0194E-05	5.1
100 × 10	2.5596E-07	5.6	6.8053E-07	5.6	1.5781E-05	5.2
120 × 12	9.0039E-08	5.7	2.4064E-07	5.7	6.1004E-06	5.2
$N = 5$						
40 × 4	8.9305E-07		2.1971E-06		1.3614E-04	
60 × 6	5.2103E-08	7.0	1.2756E-07	7.0	5.9568E-06	7.7
80 × 8	7.1947E-09	6.9	1.7348E-08	6.9	8.4259E-07	6.8
100 × 10	1.5357E-09	6.9	3.6421E-09	7.0	1.8093E-07	6.9
$N = 7$						
30 × 3	1.7693E-08		3.9004E-08		6.3103E-06	
40 × 4	1.8387E-09	7.9	4.1751E-09	7.8	5.5791E-07	8.4
60 × 6	6.2824E-11	8.3	1.4304E-10	8.3	2.1519E-08	8.0
80 × 8	5.6521E-12	8.4	1.3455E-11	8.2	1.7085E-09	8.8

exact solution at the final time $t = 1000$. It can be clearly noticed from the computational results shown in Fig. 16.2 that the constraints and the phase errors in the waveforms are significantly smaller for the modified setting $e = 2$, which may justify the use of a faster cleaning speed of the Hamiltonian constraint $e > 1$ for *purely numerical* purposes. In any case, our FO-CCZ4 system behaves well also with the default setting $e = c = 1$, which is typically used in the standard second order CCZ4 system [12].

Since the gauge-wave test has a smooth nontrivial exact analytical solution and is also valid in the nonlinear regime of the equations, we can use it in order to perform a numerical convergence study. For this purpose, we run the test again with different unlimited ADER-DG P_N schemes on a sequence of successively refined meshes. To make the test more difficult, we choose a very large perturbation amplitude of $A = 0.9$, which takes the system in the highly nonlinear regime, although in the end the test consists only in a nonlinear re-parametrization of the flat Minkowski spacetime. For this case we use $c = 0$ and $e = 2$. We set the final simulation time to $t = 10$ and continue using the *undamped* version of the FO-CCZ4 system.

The L_2 error norms of the conformal factor ϕ , the lapse α and the trace of the extrinsic curvature K , together with the observed order of accuracy of the different ADER-DG schemes are reported in Table 16.1. We observe essentially the expected order of accuracy of the scheme for $N = 3$ and $N = 4$, while a superconvergence is observed for $N = 5$ and $N = 7$. We think that this is due to the strong nonlinearities of the PDE system appearing in the regime in which we run this test case with $A = 0.9$ and that some leading errors may be dominated by quadratic terms in the metric and the conformal factor, which can lead to a faster error decay than $N+1$ for *coarse* meshes. However, we expect that this superconvergence will disappear on sufficiently refined meshes; but since the absolute errors are already getting close to machine accuracy on the meshes used here, it is not possible to refine the mesh much more with double-precision arithmetics, at least in the

Table 16.1: Numerical convergence results for the large amplitude gauge wave test problem with $A = 0.9$ at a final time of $t = 10$. The L_2 errors and corresponding observed convergence order are reported for the variables ϕ , α and K . Here, $\mathcal{O}(x)$ means the convergence order for x .

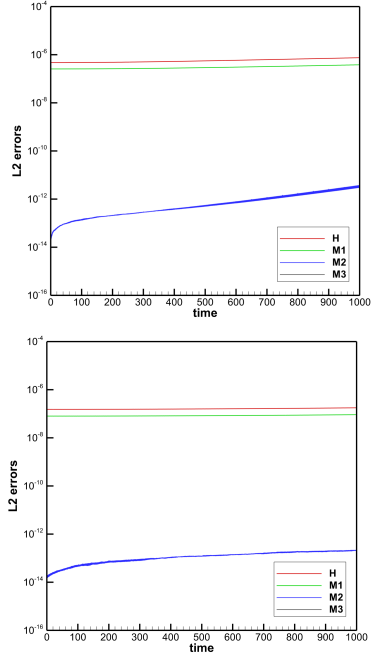


Figure 16.4: Growing of constraint violations during the Gauge Wave evolution. Note the logarithmic scale.

$N = 7$ case. For the ADER-DG P_5 scheme using 100×10 elements a comparison between numerical and exact solution of the nonlinear waveforms for ϕ , α , K and D_{xxx} is provided in Fig. 16.3 at $t = 10$, where we can note again an excellent agreement between exact and numerical solution.

16.3 Robust stability test

The robust stability test is the last standard test problem that we take from Ref. [8]. While in the previous test problems we have used a simple frozen shift condition $\partial_t \beta^i = 0$ by setting $s = 0$ in the FO-CCZ4 system, here we employ the classical Gamma-driver shift condition. Furthermore, we employ the $1 + \log$ slicing condition, setting the slicing function to $g(\alpha) = 2/\alpha$ and the parameter f of the Gamma driver to $f = 0.75$, which is also the typical value used for the BSSNOK system and for the classical second-order CCZ4 system [12]. We further set $e = 2$, $\kappa_1 = \kappa_2 = \kappa_3 = 0$, $K_0 = 0$, $c = 1$ and $\eta = 0$.

As customary in this test, we start from the flat Minkowski metric. We then add uniformly distributed *random perturbations* to *all* quantities of the FO-CCZ4 system, i.e., to all primary and auxiliary variables and also to Θ and $\hat{\Gamma}^i$. The two-dimensional computational domain is $\Omega = [-0.5, 0.5]^2$ and we run different simulations with an unlimited ADER-DG P_3 scheme on four successively refined meshes composed of $10\rho \times 10\rho$ elements, corresponding to $40\rho \times 40\rho$ degrees of freedom, where $\rho \in \{1, 2, 4, 8\}$ is the refinement factor. The perturbation amplitude is $\epsilon = 10^{-7}/\rho^2$, which corresponds to perturbation amplitudes that are three orders of magnitude larger than those suggested in [8].

The time evolution of the ADM constraints is reported in Fig. 16.5 for all four simulations. One can observe that after an initial decay the constraints remain essentially constant in time for all different grid resolutions, indicating that our FO-CCZ4 system indeed passes the robust stability test with the standard Gamma driver and $1 + \log$ gauge conditions (see [118] for similar tests with the Z4c system).

16.4 Convergence tests on three-dimensional black-hole spacetimes

In this test we consider the evolution of isolated Schwarzschild and Kerr black holes in 3D Cartesian Kerr-Schild coordinates, with $M = 1$ the mass of the black hole and a the dimensionless spin. The metric in these coordinates is known analytically and thus the primary variables of our evolution system are given by

$$\alpha = S^{-\frac{1}{2}}, \quad \beta^i = \frac{2H}{S} l_i, \quad \gamma_{ij} = \begin{pmatrix} 1 + 2Hl_x^2 & 2Hl_x l_y & 2Hl_x l_z \\ 2Hl_x l_y & 1 + 2Hl_y^2 & 2Hl_y l_z \\ 2Hl_x l_z & 2Hl_y l_z & 1 + 2Hl_z^2 \end{pmatrix}, \quad (16.4)$$

with

$$H := M \frac{r^3}{r^4 + a^2 z^2}, \quad S := 1 + 2H, \quad l_x := \frac{rx + ay}{r^2 + a^2}, \quad l_y := \frac{ry - ax}{r^2 + a^2}, \quad l_z := \frac{z}{r},$$

and

$$r := \sqrt{(x^2 + y^2 + z^2 - a^2)/2 + \sqrt{((x^2 + y^2 + z^2 - a^2)/2)^2 + z^2 a^2}}.$$

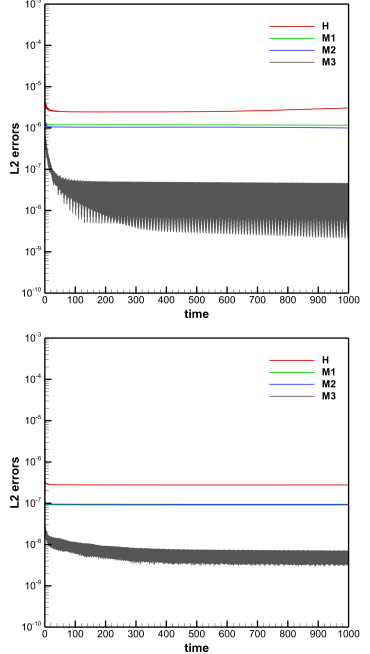


Figure 16.5: Robust stability test case with Gamma-driver shift condition and $1 + \log$ slicing with random initial perturbation of amplitude $10^{-7}/\rho^2$ in all quantities on a sequence of successively refined meshes on the unit square in 2D using an ADER-DG P_3 scheme. Upper: 10×10 elements, corresponding to 40×40 degrees of freedom ($\rho = 1$). Lower: 80×80 elements, corresponding to 320×320 degrees of freedom ($\rho = 8$).

We furthermore use the fact that the solution is stationary, i.e., $\partial_t \gamma_{ij} = 0$, hence the extrinsic curvature K_{ij} is computed as follows [387]

$$K_{ij} = \frac{1}{2\alpha} (\nabla_i \beta_j + \nabla_j \beta_i) . \quad (16.5)$$

The function K_0 is chosen as $K_0 = (K - \beta^k \partial_k \alpha) / (\alpha^2 g(\alpha))$, so that $\partial_t \alpha = 0$ and in this test the Gamma-driver shift condition is simplified to $\partial_t \beta^i = f b^i$, $\partial_t B_k^i = f \partial_k b^i$ and $\partial_t b^i = \partial_t \hat{\Gamma}^i$, with the consequence that the above exact solution corresponds to a stationary solution of the FO-CCZ4 system. In other words, we remove the advection terms from the evolution equations of the shift β^i and the variable b^i (see also [7]). The conformal factor ϕ and the auxiliary variables can be computed according to their definition. The computational domain is chosen as $\Omega = [1, 5]^3 M^3$, and the exact solution given by the initial condition is imposed on all boundaries in all variables at all times. Note that this choice of boundary conditions is appropriate to study convergence since the exact solution is also a stationary solution of our PDE system. Note also that the black hole is centered at $x = y = z = 0$, so that we evolve only a section of the domain offset from the singularity, but encompassing regions both inside and outside of the event horizon; this effectively amounts to employing an excision of the black-hole interior. We furthermore set $e = 2$, $c = 1$, $\eta = 0$, and consider the undamped CCZ4 system with the $1 + \log$ slicing, i.e., we set $\kappa_1 = \kappa_2 = \kappa_3 = 0$, $f = 0.75$ and $g(\alpha) = 2/\alpha$.

The simulations were performed with different ADER-DG schemes on a sequence of successively refined meshes until a final time of $t = 10 M$. The Rusanov method is used as approximate Riemann solver at the element interfaces. In the case of the Schwarzschild black hole we use $a = 0$, while for the Kerr black hole we set $a = 0.9$. The corresponding numerical convergence rates are reported for both cases in Table 16.2, where we observe that the designed order of accuracy $N + 1$ of our high-order fully-discrete one-step ADER-DG schemes has been properly reached.

16.5 Evolution of a single puncture black hole

We next have applied the FO-CCZ4 formulation to a single puncture black hole [97] with mass $M = 1$ and dimensionless spin $a = 0$ located at the origin of a three-dimensional computational domain $\Omega = [-150, 150]^3 M^3$ with periodic boundary conditions on all boundaries. The domain is discretized with an AMR mesh with grid spacing $\Delta x = \Delta y = \Delta z = 2.5 M$ within the inner box $\Omega_b = [-15, 15]^3 M^3$, while $\Delta x = \Delta y = \Delta z = 7.5 M$ is used in the outer part of the domain. In the innermost zone $\Omega_l =$

Table 16.2: Numerical convergence results of FO-CCZ4 with simplified Gamma driver for the Schwarzschild black hole (left) and the Kerr black hole (right) in 3D Cartesian Kerr-Schild coordinates at a final time of $t = 10$. The L_2 errors and corresponding observed convergence order are reported for the variables ϕ .

Schwarzschild black hole ($a = 0$)						Kerr black hole ($a = 0.9$)					
N_x	L_2 error ϕ	$\mathcal{O}(\phi)$	N_x	L_2 error ϕ	$\mathcal{O}(\phi)$	N_x	L_2 error ϕ	$\mathcal{O}(\phi)$	N_x	L_2 error ϕ	$\mathcal{O}(\phi)$
$N = 3$			$N = 5$			$N = 3$			$N = 5$		
10	9.9982E-06		5	2.1837E-06		10	1.4270E-05		5	2.6679E-06	
15	1.8439E-06	4.2	10	2.8327E-08	6.3	15	2.8279E-06	4.0	10	6.5136E-08	5.4
20	5.8521E-07	4.0	15	2.3649E-09	6.1	20	8.9487E-07	4.0	15	6.0944E-09	5.8
25	2.4322E-07	3.9	20	4.1176E-10	6.1	25	3.6468E-07	4.0	20	1.1087E-09	5.9

$[-3, 3]^3 M^3$ the third-order subcell ADER-WENO finite-volume limiter is activated throughout the entire simulation. For details on the AMR framework and the subcell finite-volume limiter we refer the interested reader again to [170, 471, 472]. We also stress that this simulation can be run only after activating the finite-volume subcell limiter, since a robust scheme is needed in order to deal with the puncture singularity. Without such a limiter, i.e., with a pure DG scheme, the code crashes after a few timesteps since the high-order unlimited DG scheme is *not* robust enough to deal with the puncture metric. In our simulation we use an ADER-DG P_3 scheme ($N = 3$), which leads to $2N + 1 = 7$ finite-volume subcells per DG element, i.e., the effective mesh spacing in terms of points (cell averages) inside the domain Ω_l is $\Delta x = \Delta y = \Delta z = 0.357 M$. Note that we set up the mesh so that the puncture is located at the boundary of the DG elements; given the location of the degrees of freedom in the subcell grid, no grid point coincides with the puncture. We set the CCZ4 parameters to $\kappa_1 = 0.1$, $\kappa_2 = 0$, $\kappa_3 = 0.5$ and $\eta = 0$. The constant μ accounting for the second-order ordering constraints in the evolution of B_k^i is set to $\mu = 1/5$, while for this test we use $c = 1$, $f = 0.75$ and $e = 1$ to be as close as possible to a standard second-order CCZ4 formulation, where the cleaning of the Hamiltonian constraint is done at the speed of light.

The initial metric and lapse are provided by the TwoPunctures initial data code [30] (part of the Einstein Toolkit [308]). Explicitly, the lapse is set initially to

$$\alpha = \frac{1}{2} \left(\frac{1 - \frac{1}{2} (M/r^*)}{1 + \frac{1}{2} (M/r^*)} + 1 \right), \quad (16.6)$$

where $r^* := (r^4 + 10^{-24})^{\frac{1}{4}}$ and r is the coordinate distance of a grid point from the puncture. The auxiliary quantities (which are spatial derivatives of the primary quantities) are obtained via a simple fourth order central finite difference applied to the primary variables α and γ_{ij} . Initially the shift and the extrinsic curvature are set to zero, i.e., $\beta^i = 0$ and $K_{ij} = 0$.

The evolution was carried out until a final time of $t = 1000 M$ and Fig. 16.6 reports the evolution of the average L_2 error of the ADM constraints, which we define as

$$\overline{L}_2 = \sqrt{\frac{\int_{\Omega} \epsilon^2 dx}{\int_{\Omega} dx}},$$

where ϵ denotes the local error of each of the ADM quantities, i.e., Hamiltonian H and momentum constraints M_i . In Fig. 16.6 also a view of the 3D grid setup is shown together with a zoom into the center region with the contour colors of the lapse function at a time of $t = 200 M$. It is probably worth recalling that, to the best of our knowledge, these are the first results obtained for a puncture black-hole spacetime using a fully three-dimensional DG finite-element method with AMR and LTS. Previous results obtained with high-order DG schemes for black-hole spacetimes were essentially limited to the one-dimensional case [101, 200, 329].

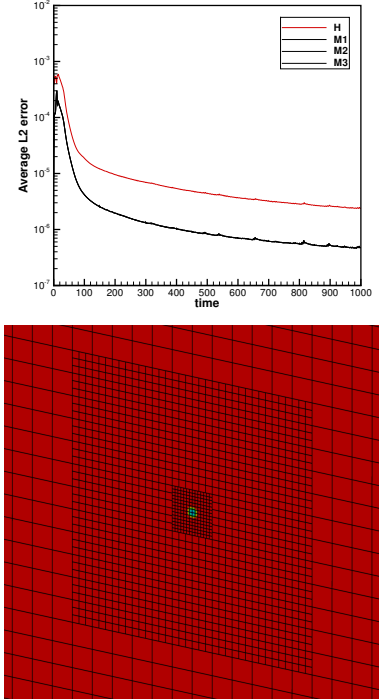


Figure 16.6: Time evolution of the ADM constraints for the single puncture black hole using an ADER-DG P_3 scheme with AMR and ADER-WENO subcell finite-volume limiter until $t = 1000$ (left). Color contours for the lapse at $t = 200$ and grid setup showing the domain Ω , the refined box Ω_b and the zone with active subcell finite-volume limiter Ω_l (center). Zoom into the center region at $t = 200$ with color contours for α (right).

16.6 Preliminary results for moving punctures

The last test considered is a preliminary application of the FO-CCZ4 system to a binary system of two moving punctures. In particular, we consider a head-on collision of two nonrotating black holes of equal mass $M = 1$ with zero linear momentum initially located at $x^- = (-1, 0, 0)$ and $x^+ = (+1, 0, 0)$. The three-dimensional computational domain is given by $\Omega = [-25, 25]^3 M^3$ and flat Minkowski spacetime is imposed as boundary condition everywhere. The CCZ4 parameters are set to $\kappa_1 = 0.1$, $\kappa_2 = 0$, $\kappa_3 = 0.5$, $\eta = 0$ and furthermore we choose $c = 1$, $e = 1$, $f = 1$ and $\mu = 1/5$. Again, the initial metric and the lapse are provided by the TwoPunctures initial data code [30], with the lapse set initially to

$$\alpha = \frac{1}{2} \left(\frac{1 - \frac{1}{2} (m_- / r_-^*) - \frac{1}{2} (m_+ / r_+^*)}{1 + \frac{1}{2} (m_- / r_-^*) + \frac{1}{2} (m_+ / r_+^*)} + 1 \right), \quad (16.7)$$

where r_-^* and r_+^* are the coordinate distances of a grid point from either puncture (defined analogously to the previous section) and m_- and m_+ are the bare masses of the two black holes (see [30]) and in this case they are equal. The auxiliary quantities are computed from the primary variables via a fourth-order central finite-difference method. We use the simple and robust Rusanov method as approximate Riemann solver on the element boundaries. The shift and extrinsic curvature are initially set to $\beta^i = 0$ and $K_{ij} = 0$.

The domain is discretized with an AMR mesh of mesh spacing $\Delta x = \Delta y = \Delta z = 5/12 M$ within the inner box $\Omega_b = [-2.5, 2.5]^3 M^3$, while $\Delta x = \Delta y = \Delta z = 1.25 M$ is used in the outer part of the domain. In the innermost zone $\Omega_l = [-5/3, 5/3]^3 M^3$ the third-order subcell ADER-WENO finite-volume limiter is activated throughout the entire simulation. As for a single puncture, we use an ADER-DG P_3 scheme ($N = 3$), whose $2N + 1 = 7$ finite-volume subcells lead to an effective mesh spacing inside the domain Ω_l of $\Delta x = \Delta y = \Delta z = 0.0595$. Once again we remark that the use of the finite-volume subcell limiter is essential in order to obtain a stable evolution.

The simulation is run until a final time of $t = 60 M$ and the evolution of the contour surfaces of the lapse and the shift vector are reported in Fig. 16.7. The contour surfaces of the conformal factor at the final time as well as the evolution of the ADM constraints are depicted in Fig. 17.1. Clearly, no sign of growth in the violation of the constraints appears after the two punctures have merged at $t \simeq 10 M$.

Although these results are meant mostly as a proof-of-concept rather than as a realistic modelling of the inspiral and merger on binary black-hole systems, they provide convincing evidence that binary systems of puncture black holes can be evolved stably with our path-conservative ADER-DG scheme with ADER-WENO subcell finite-volume limiter on AMR grids based on the FO-CCZ4 formulation proposed here. A more detailed and systematic investigation, which includes the emission of gravitational waves from binary systems of rotating black holes in quasi-circular orbits [12], will be the subject of future work.

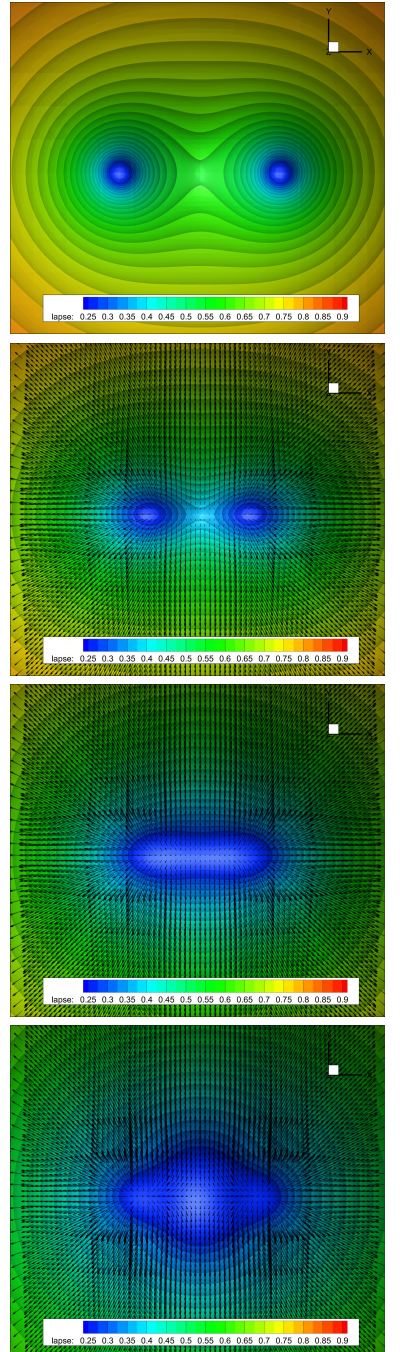


Figure 16.7: Time evolution of the contour surfaces of the lapse α and the shift vector β^i for the head-on collision of two puncture black holes of equal mass $M = 1$ at times $t = 0, 5, 7, 8, 10 M$ and $t = 15 M$, from top left to bottom right.

17 Summary

In Chapter II, the evolution from classical 3+1 formulation of Einsteins field equations over BSSNOK and the Z4 family to CCZ4 was passed. The rewriting of CCZ4 to a first order formulation was discussed in detail and remarks on mathematical and computer-science (implementation) related points were made. Afterwards, the ADER-DG scheme from Section 6 was applied in order to demonstrate the correctness of the PDE and applicability of the scheme in a couple of standard numerical relativity testbeds. Some of these tests are especially remarkable, since these are the first simulations of black-hole spacetimes ever performed in three spatial dimensions with high-order discontinuous galerkin methods. However, all examples shown in this sections were restricted to “vacuum solutions” of Einsteins equations, where the matter contribution $T_{\mu\nu}$ is exactly zero. Chapter III on the next page is dedicated to discuss the powerful and widespread theory of hydrodynamics for a non-zero assignment of $T_{\mu\nu}$ in the given equations, while providing its standalone evolution equations for individual quantities resembling the energy momentum tensor.

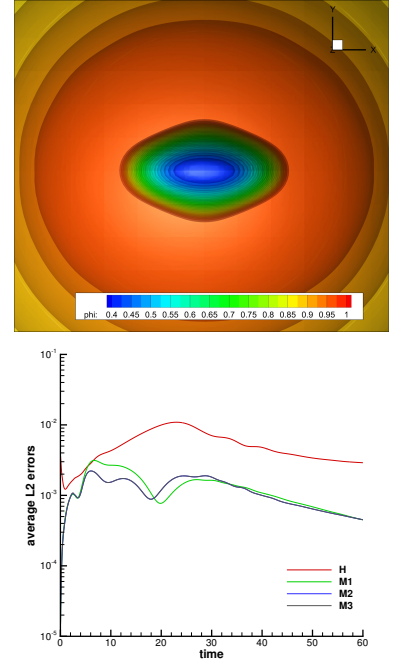


Figure 17.1: Head-on collision of two puncture black holes: contour surfaces of the conformal factor ϕ at time $t = 34 M$ after the merger (left) and time evolution of the ADM constraints (right). The curves for the second and third momentum constraint almost coincide.

Hydrodynamics

ADER-DG schemes for the general-relativistic magnetohydrodynamic equations

CHAPTER

III

This chapter summarizes efforts of solving the equations of general relativistic magnetohydrodynamics (GRMHD) with the finite-volume limited ADER-DG scheme introduced in Chapter I on page 17. An introduction into the problem and a review of previous work given in Section 0.3 on page 14. This chapter is prepended a motivation abou the physical modeling of neutron stars spacetimes. The subsequent Chapter IV on page 95 will demonstrate an actual application (beyond academic benchmark scenarios). This chapter relies partially on the publications [194, 274].

18 Motivation: An effective theory for dense and hot nuclear matter

The most compact astrophysical object after a black hole is a neutron star. Having roughly the mass of the sun, the star radius is only at the kilometer scale, thus only an order of magnitude larger then its Schwarzschild radius.

¹. Astrophysically, these objects are interesting as the endpoint of a supernovae. Pulsars, being neutron stars (or white dwarfs) emitting characteristic highly intensive beams of electromagnetic radiation, are amongst the most fascinating and best studied compact objects in astronomy.

For an high energy physicist, neutron stars are interesting because they allow to probe all fundamental forces: Of course gravity, electromagnetism, but also the weak and strong force. In neutron stars, energy and density regimes can be reached which are out of range for particle accelerators. An understanding of neutron star interiours thus allows to falsify or set limits in nuclear and fundamental theories. As an example, within the merger of a binary neutron star system, it is likely that the quark phase transition can be probed.

In order to describe the physics of a neutron star, the best fundamental theories available are the standard model of particle physics, written in the language of special-relativistic quantum field theory, and general relativity, the (non-quantum) theory of gravity ².

The typical approach to solve the *spacetime* of a single isolated neutron star requires taking in an averaged, thermalized energy-momentum tensor at a given spatial position. This motivates to find a suitable effective theory (or phenomenological model) for the matter dynamics which is thermodynamically motivated, leaving the (fundamental) particle physics picture behind ³. The physical branch of fluid mechanics provides a suitable theory, which is (relativistic) hydrodynamics.

¹ To provide some numbers, the solar mass $M_{\odot} \approx 2 \times 10^{30}$ kg complies with its Schwarzschild radius $R_{\odot} \approx 3$ km. n contrast, typical neutron stars with $M \approx 2M_{\odot}$ have a radius at the order of $R \approx 10$ km.

² In fact, a neutron star does not even come close to take backreactions of quantum matter onto the spacetime into account, and therefore quantum corrections are not required in Einstein field equations (in contrast as in section 35).

³ Section 25.3 on page 93 will go into detail of an ideal fluid model of a neutron star, the TOV solution.

19 Introduction of Hydrodynamics

Hydrodynamics adopts two features: Coarse graining, i.e., the averaged thermodynamic description of a system, and fast thermalization, i.e., the fact that the fluid is locally assumed to be in a well-defined thermodynamic equilibrium state ⁴. *Ideal* hydrodynamics is based on the *perfect fluid hypothesis*: Dynamical timescales are much larger than viscous or heat transfer timescales. Furthermore, the fluid is assumed to be isentropic, i.e., there are no preferred direction effects. This allows to assume stresses to be isotropic. Furthermore, there is no heat transport and viscosity and no dissipation. Beyond the ideal theory, there are (more) realistic theories of hydrodynamics which add particular features, such Navier-Stokes equations, the classical theory of viscous fluids ⁵.

The *dynamical timescale* of a gravitational systems is given by [387]

$$\tau_{\text{dyn}} \sim 1/\sqrt{G\bar{\rho}}, \quad (19.1)$$

with an average rest mass density $\bar{\rho}$ and here the explicit Newton's constant G . The dynamical time scale of nuclear matter (nuclear density $\rho_{\text{nuc}} \approx 2.3 \times 10^{17} \text{ kg/m}^3$) is $\tau_{\text{dyn}} \sim 2 \times 10^{-4} \text{ s}$. In comparison, the viscous and heat timescales are typically of the order of 10^{+8} s and therefore can be ignored.

The relativistic perfect ideal fluid is described by the stress energy tensor

$$T_{\mu\nu} = \rho h u_\mu u_\nu + p g_{\mu\nu}, \quad (19.2)$$

with rest mass density ρ , 4-velocity $u_\mu = dx^\mu/d\tau$ (which is timelike, $u^\mu u_\mu = -1$) and specific internal energy ϵ as part of the specific enthalpy $h = 1 + \epsilon + p/\rho$. The pressure p subsumes all physics on micro scales within an *equation of state* $p = p(\rho, \epsilon)$. The relativistic total energy density is $e = \rho(1 + \epsilon)$ and $g_{\mu\nu}$ is the usual 4-metric.

Widespread simple equations of state are the one-parametric ideal-fluid (or "Gamma-law") equation of state $p = \rho\epsilon(\Gamma - 1)$ with the adiabatic / polytropic index Γ , and the polytropic EOS $p = \kappa\rho^\Gamma$.

Hydrodynamics can be derived from a number of different fundamental principles, for instance the principle of minimal action [24] or from kinetic theory by applying a moment scheme to the Boltzmann equations [387]. While a derivation is out of the scope of this text, the equations of motion as well as the resulting PDEs are discussed in the subsequent sections. The fluid dynamics are dictated by two conservation equations for the 4-energy momentum tensor $T^{\mu\nu}$ and for the rest mass (density flux) ρu^μ , i.e.,

$$T^{\mu\nu} = 0, \quad \nabla_\mu(\rho u^\mu) = 0. \quad (19.3)$$

Instead of deriving the actual PDEs, the different parts of the flux-conservative formulation of general relativistic magnetohydrodynamics (GRMHD) shall be discussed in the next sections ⁶. The state vector of GRMHD,

$$Q_{\text{GRMHD}} = (Q_{\text{HD}}, Q_{\text{ADM}}, Q_{\text{MD}}), \quad (19.4)$$

is a composite of state vectors which origin from three different theories: The state vector of hydrodynamics Q_{HD} (discussed in this section), the curved background metric, collected in the parameter Q_{ADM} (discussed in Section 20)

⁴ For its power of describing effective phenomenae, hydrodynamics is sometimes called an "effective theory of everything".

⁵ In this thesis, only ideal fluids are covered, while references to extensions are given at some points.

⁶ Naturally, such a discussion can either be ordered *top-down*, i.e., starting from the advanced theory and advancing into the low-energy limit, or *bottom-up*, i.e., starting with the classical, easy theory and advancing by proposing additions necessary to fulfill relativity, curved background and to incorporate Maxwell's theory. Both approaches are well known in theoretical physics. In this text, I decided for the *bottom-up* strategy.

and the state vector of magnetodynamics Q_{MD} (Section 21). The separation of theories by fundamental building blocks is also sketched in Figure 19.1 and implemented in the SVEC GRMHD code.

19.1 Classical Hydrodynamics

Hydrodynamics can be introduced by defining the *primitive* and *conserved* state vector, where the later is evolved in time and the former is required for the system closure, given by the pressure/equation of state. The vectors are given as

$$\text{Primitive vector } u = \begin{pmatrix} \text{rest mass density} \\ \text{velocity} \\ \text{internal energy} \end{pmatrix} = \begin{pmatrix} \rho \\ v_i \\ \epsilon \end{pmatrix}, \quad (19.5)$$

$$\text{Conserved vector } Q_{HD} = \begin{pmatrix} \text{Conserved density} \\ \text{Momentum} \\ \text{Energy density} \end{pmatrix} = \begin{pmatrix} D \\ S_j \\ E \end{pmatrix}, \quad (19.6)$$

$$\text{related by } Q_{HD}(u) = \begin{pmatrix} \rho \\ \rho v_j \\ \rho/2v^2 + \epsilon \end{pmatrix} \quad ^7. \quad (19.7)$$

Classical hydrodynamics can be expressed in flux-conservative form (2.1),

$$\text{with fluxes } F_{HD}^i(u) = \begin{pmatrix} \text{fluxes for } D \\ \text{fluxes for } S_j \\ \text{fluxes for } E \end{pmatrix} = \begin{pmatrix} \rho v^i \\ W_j^i \\ v^i(E + p) \end{pmatrix}. \quad (19.8)$$

The other PDE terms in (2.1) are vanishing. Here, we used the hydrodynamic energy-momentum-tensor (EM tensor), given by ⁸

$$W^{ij} = S^i v^j + p \delta^{ij}. \quad (19.9)$$

Classical hydrodynamics is a nonlinear theory. Within the ExaHyPE code, it is widely used for performance measurements. Deriving the strong hyperbolicity of classical hydrodynamics is part of many books [387, 445]. The eigenvalues λ_i in k -direction in d dimensions are then found to be

$$\lambda_1 = v_k - c, \quad \lambda_{2,\dots,d+1} = v_k, \quad \lambda_{d+2} = v_k + c, \quad (19.10)$$

where $c = \sqrt{(\partial_\rho p)_s}$ is the *sound speed* of the fluid. The three different wave speeds stand out as different waves in the Riemann problem (Section 2.3).

19.2 Special relativistic hydrodynamics (SRHD)

Special relativistic hydrodynamics is the extension of classical hydrodynamics valid for high velocities ($v \rightarrow c$), but remaining on flat background spacetime.

The 3-velocity v^i of the fluid is extended in favour of the Lagrangian 4-velocity $u^\mu = (W, W v^\mu)$, with Lorentz factor $W = (1 - v^2)^{-1/2}$ ⁹. The 4-momentum/rest-mass current is then given by $S^\mu = \rho u^\mu$. The content of the primitive (19.5) and conserved vector (19.6) does not change. However, the relationship (19.7) is replaced by

$$Q_{SRHD}(u) = \begin{pmatrix} \rho W \\ \rho h W^2 v_j \\ \rho h W^2 - p - \rho W \end{pmatrix} \quad (19.11)$$

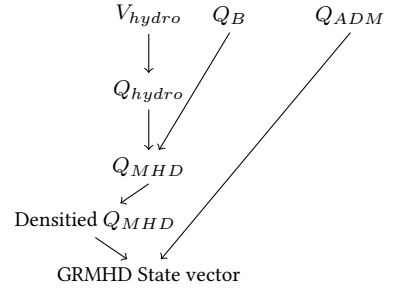


Figure 19.1: State vector composition in GRMHD, or in particular, in the SVEC code.

⁷ Note how easily the primitives $u(Q) = (\rho, S_j/\rho, E - \rho/(2v^2))$ can be analytically recovered from the conserved variables (in contrast to relativistic hydrodynamics, presented in the next section). Therefore, the fluxes in equation (20.2) are also an algebraic function of the conserved state vector only.

⁸ The EM tensor is also referred to as $W^{ij} = S^{ij}$ in the literature (and in Section 11.1).

⁹ In the literature, alternative popular namings are $W = \Gamma$, $E = U$. In any case, do not confuse W with the conformal factor used in some conformal formulations of Einstein Equations (see Section 12.2).

with specific enthalpy $h = 1 + \epsilon + p/\rho$ ¹⁰. The conservative formulation of SRHD is then given by is then given by the fluxes

$$F_{\text{HD}}^i(u) = \begin{pmatrix} \text{fluxes for } D \\ \text{fluxes for } S_j \\ \text{fluxes for } \tau \end{pmatrix} = \begin{pmatrix} Dv^i \\ W_j^i \\ S^i - v^i D \end{pmatrix}. \quad (19.12)$$

The SRHD equations are hyperbolic for causal EOS [25, 202]. The wave speeds decompose similarly as in (19.10), where however the relationship to the speed of sound c is nonlinear [202],

$$\lambda_{\pm} = \frac{v^k(1 - c^2) \pm c\sqrt{(1 - v^2)(1 - v^2c^2 - v_k^2(1 - c^2))}}{1 - v^2c^2} \quad (19.13)$$

and $\lambda_- := \lambda_1, \lambda_+ := \lambda_{d+2}$ in the notation of (19.10).

19.3 The primitive recovery in relativistic hydrodynamics

Due to the nonlinear Lorentz factor $W = W(v^2)$, the recovery of the primitive variables (19.5) from the conserved ones (19.6) is no more possible analytically in SRHD. Instead, the inverse of (19.11) can be approximated by numerical root finding. The standard approach is to solve a single or multiple nonlinear equations. For instance, the authors of [154, 350] propose to solve a simple nonlinear 2×2 system which reads for SRHD as

$$\left. \begin{array}{l} y^2x - S^2 = 0 \\ y - p - E = 0 \end{array} \right\}, \quad (19.14)$$

with $x = v^2, y = \rho h W^2$. Once x and y are determined numerically, all primitives can be recovered by computing $W = (1 - x)^{-1/2}, \rho = D/W, v_j = S_j/y, h = S_j/(v_j \rho W^2)$ and for instance with the ideal gas (from above), $\epsilon = h/(1 + W)$ ¹¹.

¹¹ Obviously any non-analytic EOS raises new issues at this point which are again subject to numerical treatment.

20 General relativistic hydrodynamics (GRHD)

General relativistic hydrodynamics is the theory which described fluids moving within an (external) gravitational potential. The (special) relativistic fluid follows the definitions from the previous section. The coupling of the background spacetime is mediated by a source term in the law of motion.

A fully general relativistic description implies also matter backreaction on the spacetime (the fluid bends spacetime itself), according to Einstein's field equations (EFE, Chapter II). In this case, the EFE determine the dynamics of the gravitational field under the presence of a source term (the energy momentum tensor of the fluid). Section 20.4 discusses the simplifications which can be made to the GRMHD equations when the backreaction is neglected.

20.1 3+1 split of special relativistic hydrodynamics

The “Valencia formulation” of GRHD presented in this thesis dates back to the pioneering work of Martí et al. [57, 253, 317] in 1991. They were the first to make a characteristic approach to relativistic hydrodynamics in a 3+1 split of spacetime¹².

¹² see Section 11.1 on page 44 for the definitions of normal vector n^μ , lapse α , shift β^i and 3-metric γ_{ij} .

In the 3+1 split, the Lagrangian velocity u^μ can be casted as $u^\mu = W(n^\mu + v^\mu)$ and the 3-velocity as $v^i = u^i/W + \beta^i/\alpha$. The 3+1 language also offers beatiful interpretations, for instance is the projection of the fluid 4-velocity on the purely spatial hypersurfaces just the Lorentz-decorated 3-velocity, $\gamma_\nu^\mu u^\nu = Wv^\mu$. Formally, the 3-energy-momentum-tensor can be interpreted as extension from the flat case,

$$W_{\text{HD}}^{ij} = W_{\text{SRHD}}^{ij} = S^i v^j + p \delta^{ij} \leftrightarrow W_{\text{GRHD}}^{ij} = S^i v^j + p \gamma^{ij}. \quad (20.1)$$

The SRHD fluxes are refined as

$$F_{\text{HD}}^i(u) = \begin{pmatrix} \text{fluxes for } D \\ \text{fluxes for } S_j \\ \text{fluxes for } \tau \end{pmatrix} = \begin{pmatrix} Dw^i \\ \alpha W_j^i - \beta^i S_j \\ \alpha(S^i - v^i D) - \beta^i \tau \end{pmatrix} \quad (\text{general } W^{ij}) \quad (20.2)$$

$$= \begin{pmatrix} Dw^i \\ S_j w^i + p \delta_j^i \\ \tau w^i + p v^i \end{pmatrix} \quad (\text{only } W^{ij} = S^i v^j + p \gamma^{ij}) \quad (20.3)$$

It is convenient to write the fluxes with the vector $w^i = \alpha v^i - \beta^i$ which is refered to as the advection velocity relative to the coordinates, or just *transport velocity*¹³. With the replacment of $v^i \rightarrow w^i$, the GRHD fluxes (20.3) have (almost) a similar shape as the SRHD fluxes (19.12).

In order to fully describe the state of a GRHD system, the local curvature must be encoded in the state vector¹⁴. Therefore, the ADM state vector is defined as

$$Q_{\text{ADM}} = (\alpha, \beta^i, \gamma_{ij}, K_{ij}). \quad (20.4)$$

The GRHD system is hyperbolic [201], and the eigenvalues in k direction are given by

$$\lambda_0 = \alpha v^k - \beta^k, \quad (20.5)$$

$$\lambda_{\pm} = \frac{\alpha}{1 - v^2 c_s^2} \left(v^k (1 - c_s^2) \pm c_s \sqrt{(1 - v^2) (\gamma^{kk} (1 - v^2 c_s^2) - v^k v^k (1 - c_s^2))} \right) - \beta^k, \quad (20.6)$$

with the local sound speed $c_s = \sqrt{\partial_\rho p + p / \rho^2 \partial_\epsilon p} / h$.

¹³ Note that w^i does not transform like a 3-vector. However, we introduce it only for abbreviation on the paper and for saving contractions in the computer.

¹⁴ The ADM state is constant for the GRHD PDE, as the modification of the background spacetime is prescribed by Einstein field equations, which are however a PDE on their own (Chapter II). In ExaHyPE language, an entry in the state vector which is not evolved by the PDE, i.e., which fulfills $\partial_t Q^k = 0$, is called a “material parameter”. This term comes from seismology where non-evolved parameters describe the immutable soil properties (in GR lingua, the “background” spacetime) which are unchanged by the waves described by the PDE.

¹⁵ Here the full system (2.3) is given, even if some terms are zero for certain systems (such as the algebraic and differential source for HD and SRHD).

20.2 Conformal factor

In the Valencia formulation, the PDE system is written in terms of tensor densities. The determinant of the metric $\gamma = \det(\gamma_{ij})$ relates the tensor densities with an ordinary tensor. The 3-determinant is related to the determinant of the four-metric by $\sqrt{-g} = \alpha \sqrt{\gamma}$. The system is then formulated as¹⁵

$$\partial_t(\sqrt{\gamma} Q) + \partial_i(\sqrt{\gamma} F^i) + \sqrt{\gamma} B^i \partial_i(\sqrt{\gamma} Q) = \sqrt{\gamma} S. \quad (20.7)$$

The PDE as given in (20.7) defines the state Q , the fluxes F^i , the non-conservative part B^i and the algebraic source S *without* the factor $\sqrt{\gamma}$. This convention will be retained for the following sections. Note that, however, the vector $\sqrt{\gamma} Q$ is evolved in time.

20.3 Sources for curved spacetimes

In presence of a curved background, the spacetime coupling introduces a source. The governing equations of GRHD are therefore a balance law (2.2) instead of a conservation law (2.1). The source term induced by the spacetimes, written with Christoffel symbols, read ¹⁶

$$S_{\text{HD}}(u) = \begin{pmatrix} \text{source for } D \\ \text{sources for } S_j \\ \text{source for } \tau \end{pmatrix} = \begin{pmatrix} 0 \\ T^{\mu\nu}\partial_\mu g_{\nu j} - \Gamma_{\nu\rho}^\delta g_{\rho j} T^{\mu\nu} \\ \alpha T^{\mu 0}\partial_\mu \ln \alpha - \alpha T^{\mu\nu} \Gamma_{\mu\nu}^0 \end{pmatrix}. \quad (20.8)$$

In order to determine the 4-energy-momentum-tensor

$$T^{\mu\nu} = \rho h W^2 (n^\mu + v^\mu)(n^\nu + v^\nu) + p(\gamma^{\mu\nu} - n^\mu n^\nu), \quad (20.9)$$

the 4-velocity u^μ or the normal vector n^μ have to be recovered. This can be circumvented by using spatial tensors only: The equivalent “Christoffel symbol free” source terms, as used in [378], read

$$S_{\text{HD}}(u) = \begin{pmatrix} 0 \\ \frac{\alpha}{2} S^{lm} \partial_j \gamma_{lm} + S_k \partial_j \beta^k - E \partial_j \alpha \\ \alpha S^{ij} K_{ij} - S^i \partial_i \alpha \end{pmatrix}. \quad (20.10)$$

The sources can also be written without computing the 3-energy-momentum-tensor S^{ij} , exploiting $(\partial_i \sqrt{\gamma}) / \sqrt{\gamma} = \frac{1}{2} \gamma^{lm} \partial_i \gamma_{lm}$, ¹⁷

$$S_{\text{HD}}(u) = \begin{pmatrix} 0 \\ \frac{\alpha}{2} S^l v^m \partial_j \gamma_{lm} + \alpha p \frac{1}{\sqrt{\gamma}} \partial_j \sqrt{\gamma} + S_k \partial_j \beta^k - E \partial_j \alpha \\ \alpha S^l v^m K_{lm} - \alpha p \gamma^{lm} K_{lm} - S^i \partial_i \alpha \end{pmatrix} \quad (20.11)$$

All terms in the source except the red one(s) contain derivatives of the ADM state vector (20.4). This motivates to extend the definition of the curvature state vector as

$$\tilde{Q}_{\text{ADM}} = (\alpha, \beta^i, \gamma_{ij}, K_{ij}, \partial_i \alpha, \partial_i \beta^j, \partial_i \gamma_{jk}). \quad (20.12)$$

If (20.12) is chosen in favour of (20.4), then the GRHD source term is a purely algebraic one. In preparation of a coupled evolution of GRHD with spacetime, either Q_{ADM} or \tilde{Q}_{ADM} must be evolved in time. In fact, all quantities (20.12) are part of the FO-CCZ4 state vector (14.7), proposed in Section 14. Therefore, the GRHD part in a coupled evolution of the presented GRHD system with the FO-CCZ4 formulation is of the form

$$\partial_t Q_{\text{HD}} + \partial_i F_{\text{HD}}^i(Q_{\text{HD}}, \tilde{Q}_{\text{ADM}}) = S_{\text{HD}}(Q_{\text{HD}}, \tilde{Q}_{\text{ADM}}). \quad (20.13)$$

In contrast, an ordinary second order formulation of EFE would instead evolve only Q_{ADM} in time, i.e., without the derivatives. In such a case, the differential and algebraic split of the source term (Section 2.1) is applicable. Part of the work carried out in [194] is to cast the PDE as (2.3), i.e., to cast all non-red summands as $B_k^{ij}(Q_{\text{ADM}}, Q_{\text{GRHD}}) \partial_i (Q_{\text{ADM}})_j$.

In order to cast these PDEs into the algebraic-differential source split (2.3), all black terms obtain an extra minus when they are moved from the RHS to the LHS. The final GRHD system reads then (colors now omitted):

$$(B_{\text{GRHD}})^{ij}_k \partial_i Q_j = \begin{pmatrix} 0 \\ -\frac{\alpha}{2} S^{lm} \partial_j \gamma_{lm} - S_k \partial_j \beta^k + E \partial_j \alpha \\ S^i \partial_i \alpha \end{pmatrix}, \quad S_{\text{GRHD}} = \begin{pmatrix} 0 \\ 0 \\ \alpha S^{ij} K_{ij} \end{pmatrix}. \quad (20.14)$$

¹⁶ Note the use of 4-dimensional tensors except the lapse α . See also Appendix A1.2 for the standard definitions of the Christoffel symbols of first kind Γ_{ij}^k and 4-metric $g_{\mu\nu}$.

¹⁷ However, (20.11) requires to compute $\partial_i \sqrt{\gamma}$, which must then be (formally) part of the state vector if the non-conservative product approach is chosen.

20.4 Cowling approximation

In case of a stationary spacetime (Cowling approximation [146], characterized by $\partial_t g_{ij} = 0$), one can simplify the source terms and get rid of the contraction [222, 330, 467]

$$S^{ij} K_{ij} = \frac{1}{2\alpha} S^{ik} \beta^j \partial_j \gamma_{ik} + \frac{1}{\alpha} S_i^j \partial_j \beta^i. \quad (20.15)$$

In this particular case, (20.10) simplifies to

$$S_{\text{HD,Cowling}}(u) = \begin{pmatrix} 0 \\ \frac{\alpha}{2} S^{lm} \partial_j \gamma_{lm} + S_k \partial_j \beta^k - E \partial_j \alpha \\ \frac{1}{2} S^{ik} \beta^j \partial_j \gamma_{ik} + S_i^j \partial_j \beta^i - S^i \partial_j \alpha \end{pmatrix}. \quad (20.16)$$

In this special case, it is possible to write the GRHD equations without any algebraic source term. All terms in (20.16) can then be casted in the form $B \partial_i Q$. This allows to split the PDE as ¹⁸

$$\partial_t Q^k + \underbrace{\partial_i F^i(Q)}_{\text{Hydro. contribution}} + \underbrace{B_{jk}^i \partial_i Q_j}_{\text{Background contribution}} = 0. \quad (20.17)$$

In the numerical schemes proposed in Section 6, the absence of an algebraic source is desirable, as it supports the well-balanced property of these schemes.

¹⁸ In the form (20.17), the flow on a background spacetime is described similarly as in the shallow-water equations, where the bottom-slope term (which accounts for gravitational forces) can also be cast as a non-conservative product [129, 130, 359].

21 General relativistic magnetohydrodynamics (GRMHD)

The general relativistic magnetohydrodynamics (GRMHD) equations are the consequence of the coupling of Euler equations (Hydrodynamics, GRHD) to Maxwell equations (Magnetodynamics, MD). In the popular ideal MHD approximation, the electric field $\vec{E} = \vec{B} \times \vec{v}$ is fully determined by the moving fluid. In this approximation, the Faraday tensor $F^{\mu\nu}$ (with 6 degrees of freedom, \vec{E} and \vec{B}) reduces to the magnetic field \vec{B} only, therefore the vector of conserved variables in Magnetodynamics is just $Q_{\text{MD}} = (B^i)$. ¹⁹ This approximation is appropriate to describe a wide variety of astrophysical phenomena where the electrical conductivity of the plasma (description of matter) is very high. In the ideal MHD approximation, the electrical conductivity $\sigma \rightarrow \infty$ is assumed to be divergent. The electrical field is completely determined by the fluid velocity and the magnetic field. The magnetic flux $\phi_B = B_i S^i$ over any surface S is conserved,

$$\oint_{\partial S} (\mathbf{E} + \mathbf{v} \times \mathbf{B}) \cdot d\ell = -\frac{d\phi_B}{dt} = 0, \quad (21.1)$$

and is advected with the fluid movement. The magnetic contribution to the hydrodynamics equations, i.e., the MHD equations, is then just a conservation equation for the magnetic field.

¹⁹ We add further evolution equations in case of the divergence cleaning technique. However, note that there is no distinction between primitive and conserved variables in Magnetodynamics.

21.1 Magnetodynamics

The photon field (Maxwell in vacuum, i.e., without charge carriers) has the momentum density $\mathbf{S} = \mathbf{E} \times \mathbf{B}$ (Poynting vector), total energy density $U = \frac{1}{2} (E^2 + B^2)$ and energy-momentum tensor $W^{jk} = U \gamma^{jk} - E^j E^k - B^j B^k$.

The electric field \mathbf{E} in the Eulerian frame is determined by the simplified Ohm's law i.e., $E_i = -\tilde{\epsilon}_{ijk}v^jB^k$ in the ideal MHD limit (i.e., for diverging electrical conductivities). The cross product is given by the spatial three-Levi-Civita tensor density $\tilde{\epsilon}$ (see Appendix A1.2 for the definition). Therefore, the momentum density and energy momentum tensor can be expressed, using only \mathbf{v} and \mathbf{B} , as

$$\begin{aligned} S_i^{\text{MD}} &= \tilde{\epsilon}_{ijk}E^jB^k = -\tilde{\epsilon}_{ijk}\tilde{\epsilon}^{jmn}v_mB_nB^k = v_i(B_kB^k) - B_i(v_kB^k), \\ W_{\text{MD}}^{jk} &= U\gamma^{jk} - B^jB^k/W^2 - (B^kv_k)v^jB^k. \end{aligned} \quad (21.2)$$

21.2 The GRMHD coupling

The Maxwell theory (Magnetodynamics) influence the hydrodynamic flow with the (energy) momentum contributions (21.2), while the Euler theory determines the electrical field in the presented ideal magnetodynamic approximation. Furthermore, the pressure p get's a magnetic contribution and is replaced in (20.1) and (20.9) as

$$p \rightarrow p_{\text{tot}} = p_{\text{HD}} + p_{\text{MD}} \quad \text{with} \quad p_{\text{MD}} = \frac{1}{2}(B_jB^j/W^2 + (B^jv_j)^2) \quad (21.3)$$

being the pressure contribution from ideal magnetodynamics. The total energy-momentum tensor is the sum of all involved theories, thus the GRMHD energy momentum tensor is given, for completeness, here as

$$\begin{aligned} W_{\text{GRMHD}}^{ij} &= W_{\text{HD}}^{ij} + W_{\text{MD}}^{ij} = W_{\text{HD}}^{ij}(p_{\text{HD}} + p_{\text{MD}}) + W_{\text{MD}}^{ij} \\ &= S^i v^j + p_{\text{tot}}\gamma^{ij} - \frac{B^i B^j}{W^2} - (B^kv_k)v^i B^j. \end{aligned} \quad (21.4)$$

Consequently, also the conserved quantities are given by

$$Q_{\text{GRMHD}}(u, Q_{\text{MD}}) = \begin{pmatrix} D \\ S_j \\ \tau \end{pmatrix} = \begin{pmatrix} \rho W \\ DhWv_j + B^2v_j - (B^iv_i)B_j \\ D(hW - 1) - p + \frac{1}{2}(B^2(1 + v^2) - (B^jv_j)^2) \end{pmatrix} \quad (21.5)$$

21.3 Fluxes and sources

The evolution variables in GRMHD are

$$Q_{\text{MHD}} = (Q_{\text{HD}}, Q_{\text{MD}}) = (D, S_j, \tau, B^j). \quad (21.6)$$

It should be emphasized that the vector of primitive variables (19.5) does not change (increase in size), the primitive recovery takes only place for the hydrodynamic part of the GRMHD equations. The MD conserved vector is just $Q_{\text{MD}} = (B^j)$ and its evolution is given by the induction equation

$$\partial_t B^j + \partial_i(w^i B^j - B^i w^j) = 0, \quad (21.7)$$

i.e., the new PDE has fluxes and sources

$$F^i(Q) = w^i B^j - B^i w^j, \quad S(Q) = 0. \quad (21.8)$$

The GRMHD equations are hyperbolic. For the characteristic wave speeds in GRMHD, a popular choice is the magnetosonic approximation [212]. The evolution equation (21.7) does not handle the magnetic field divergence, which is covered in the next section.

21.4 The divergence cleaning (constraint damping) formulation

The Maxwell magnetic monopole constraint $\partial_i B^i = 0$ can be casted as hyperbolic conservation law with a Generalized Lagrangian Multiplier approach (GLM) also referred to as *divergence cleaning*, initially proposed by [153]. In this approach, the MHD system is augmented with an additional auxiliary equation for an artificial scalar field ψ in order to propagate away numerical violations of the divergence-free constraint ²⁰. Hence, the PDE (21.7) is replaced by two different PDEs. The MD conserved vector is now $Q_{\text{MD}} = (B^j, \phi)$. The modified fluxes and sources read [157, 358, 364]

$$F^i(Q) = \begin{pmatrix} \text{fluxes for } B^j \\ \text{fluxes for } \phi \end{pmatrix} = \begin{pmatrix} w^i B^j - v^j B^i - B^i \beta^j \\ \alpha B^i - \phi \beta^i \end{pmatrix} \quad (21.9)$$

$$S(Q) = \begin{pmatrix} \text{sources for } B^j \\ \text{sources for } \phi \end{pmatrix} = \begin{pmatrix} -B^i \partial_i \beta^j - \alpha \gamma^{ij} \partial_i \phi \\ -\alpha \kappa \phi - \phi \partial_i \beta^i - \frac{1}{2} \phi \gamma^{ij} \beta^k \partial_k \gamma_{ij} + B^i \partial_i \alpha \end{pmatrix} \quad (21.10)$$

²⁰ There are in fact other techniques to ensure in the divergence freedom of the magnetic field on a numerical level, such as constrained transport.

Here, κ is the damping term which controls the amount of damping applied on the field ϕ . In the sake of a sane balance law with purely differential source terms, $\kappa = 0$ is a choice also carried out in [196]. This choice reflects pure transport and no damping.

Notably, the divergence cleaning formulation introduces additional sources which are mostly non-conservative (as in the case of GRHD) except of the damping term (displayed in red). Thus, from all presented equations, only a Cowling-GRMHD formulation with divergence cleaning and $\kappa = 0$ has zero algebraic sources.

22 Benchmarks and GRMHD codes

In the following sections, the solution of various academic benchmark scenarios is demonstrated. These solutions have been obtained with the path-conservative ADER-DG scheme presented in section 6.

In the ExaHyPE code, the full set of GRMHD equations on dynamical spacetime with divergence cleaning is implemented. The evolution quantities are given by $Q_{\text{GRMHD}} = (D, S_j, \tau, B^i, \phi)$ and the PDE (2.3) terms are given by ²¹

$$F^i(Q) = \begin{pmatrix} \text{fluxes for } D \\ \text{fluxes for } S_j \\ \text{fluxes for } \tau \\ \text{fluxes for } B^j \\ \text{fluxes for } \phi \end{pmatrix} = \begin{pmatrix} w^i D \\ \alpha W_j^i - \beta^i S_j \\ \alpha(S^i - v^i D) - \beta^i \tau \\ w^i B^j - v^j B^i - B^i \beta^j \\ \alpha B^i - \phi \beta^i \end{pmatrix}, \quad (22.1)$$

$$B^{ij} \partial_i Q_j = \begin{pmatrix} 0 \\ -\frac{\alpha}{2} S^{lm} \partial_j \gamma_{lm} - S_k \partial_j \beta^k + E \partial_j \alpha \\ S^i \partial_i \alpha \\ B^i \partial_i \beta^j + \alpha \gamma^{ij} \partial_i \phi \\ \phi \partial_i \beta^i + \frac{1}{2} \phi \gamma^{ij} \beta^k \partial_k \gamma_{ij} - B^i \partial_i \alpha \end{pmatrix}, \quad S = \begin{pmatrix} 0 \\ 0 \\ \alpha S^{ij} K_{ij} \\ 0 \\ -\alpha \kappa \phi \end{pmatrix}.$$

²¹ The PDE presented in [194] completely avoids the algebraic source $S = 0$, since all tests presented in the paper are carried out with stationary spacetime. Thus the hydrodynamic source term from Section 20.4 is shown in [194].

The numerical code consists of three parts: The fundamental AMR code, the numerical scheme which can solve a generic prototypic PDE (see in general Chapter I), and the particular PDE parts, provided in 22.1. Such an

Section	Name of Test (Initial Data)	BC	$\vec{B} \neq 0$	Smooth	Spacetime
23.1	Michel accretion onto a Schwarzschild black hole in 2D	exact	✗	✓	curved
23.2	Torus interior around a Schwarzschild black hole in 2D	exact	✗	✓	curved
23.3	3D Michel accretion with radial magnetic field	exact	✓	✓	curved
24.1	Riemann problems	exact	✓	✗	flat
24.2	Advection of a 2D magnetic field loop	periodic	✗	✗	flat
24.3	2D blast wave	outflow	✗	✗	flat
24.4	Orszag-Tang vortex	periodic	✗	✗	flat
25.1	2D torus around a Schwarzschild black hole	exact	✓	✗	curved
25.2	3D torus around a Schwarzschild black hole	exact	✓	✗	curved
25.3	Preliminary results on a TOV star	outflow	✓	✗	curved

implementation requires to perform a primitive recovery (Section 19.3) at every evaluation of F^i , B^{ij} and S .

Table 22.1: Overview of hydrodynamic benchmarks presented in the following sections. The columns are explained in the main text.

22.1 Benchmark description

Table 22.1 provides an overview about the benchmarks which are presented on the next pages. The tests require either one, two or three spatial dimensions ²². Some tests only cover the hydrodynamic part of the equations and set the magnetic field $\vec{B} = 0$. Furthermore, “smooth flows” are distinguished from “non-smooth flows”. *Smoothness* is defined as having continuous initial data which can be well-represented by DG polynomials and do not require limiting. For smooth flows, the actual convergence order of the scheme can be measured (and is provided). For non-smooth flows, the ability of the code to handle accurately shocks and large gradients will be illustrated. Unless stated otherwise, all tests share the following properties:

- (i) An ideal EOS is adopted with the adiabatic index has been chosen equal to $\Gamma = 4/3$.
- (ii) The refinement factor is always $\mathcal{R} = 3$.
- (iii) Any method requiring ADER-DG limiting employs the second-order MUSCL-Hancock TVD finite-volume method (described in section 5.4).
- (iv) As a Riemann solver, the the Rusanov (or local Lax-Friedrichs) approximate Riemann solver has been used.
- (v) problems in curved spacetimes have been solved employing Kerr-Schild coordinates, either spherical or Cartesian.

At the spatial boundary interface $\partial\Omega$ (column “BC” in Table 22.1), either exact boundary conditions are applied (i.e., the initial conditions are used as external domain boundary values) or “copy boundary conditions” with outflow properties for hydrodynamical flows are applied (i.e., the last internal state vector is used as an external value).

²² Since ExaHyPE supports only two and three dimensional setups, one dimensional tests are performed in two dimensions straightforward as setting the initial data $Q_0(x, y) = Q_0(x)$.

23 Smooth special-relativistic benchmarks

To ensure that the flow is actually smooth, in the following tests we will restrict our computational domain to regions that are fully filled with fluid. In

this way, after successively refining the mesh, we evaluate the L_2 and L_∞ error norms at different DG polynomial degrees and mesh resolutions so as to measure the convergence order of our numerical implementation and compare it with the expected mathematical one. Anticipating what will be shown in more detail in the following sections, the numerical results confirm the high order of accuracy of the presented numerical scheme. Indeed, using the results shown in Tables 23.3 and 23.1 we can conclude that the ADER-DG \mathbb{P}_N method reaches its design accuracy $N + 1$ in most cases.

23.1 Michel accretion onto a Schwarzschild black hole in 2D

As a first test of a smooth flow with an analytical solution we consider the spherical transonic accretion of an isentropic fluid onto a nonrotating black hole known as Michel solution [327]. For the sake of completeness we give the explicit expressions of the lapse, the shift and the spatial metric of a Kerr black hole with mass M and spin a in Cartesian Kerr-Schild coordinates $\vec{r} = (x, y, z)$:

$$\alpha = S^{-\frac{1}{2}}, \quad \beta^i = \frac{2H}{S} l_i, \quad H = M \frac{r^3}{r^4 + a^2 z^2}, \quad S = 1 + 2H, \quad (23.1)$$

$$\gamma_{ij} = \begin{pmatrix} 1 + 2Hl_x^2 & 2Hl_x l_y & 2Hl_x l_z \\ 2Hl_x l_y & 1 + 2Hl_y^2 & 2Hl_y l_z \\ 2Hl_x l_z & 2Hl_y l_z & 1 + 2Hl_z^2 \end{pmatrix}, \quad (23.2)$$

$$\text{with } l_x := \frac{rx + ay}{r^2 + a^2}, \quad l_y := \frac{ry - ax}{r^2 + a^2}, \quad l_z := \frac{z}{r} \quad (23.3)$$

$$\text{and } r = \sqrt{\frac{|\vec{r}|^2 - a^2}{2}} + \sqrt{\left(\frac{|\vec{r}|^2 - a^2}{2}\right)^2 + z^2 a^2}. \quad (23.4)$$

Conversely, the Kerr metric in spherical Kerr-Schild coordinates (r, θ, ϕ) is given by [273]

$$\alpha = (1 + z)^{-\frac{1}{2}}, \quad \beta^i = \left(\frac{z}{1 + z}, 0, 0 \right), \quad (23.5)$$

$$\gamma_{ij} = \begin{pmatrix} 1 + z & 0 & -a \sin^2 \theta (1 + z) \\ 0 & \rho^2 & 0 \\ -a \sin^2 \theta (1 + z) & 0 & \Sigma \sin^2 \theta / \rho^2 \end{pmatrix}, \quad (23.6)$$

$$\text{with } \rho^2 := r^2 + a^2 \cos^2 \theta, \quad z := \frac{2r}{\rho^2}, \quad (23.7)$$

$$\Delta := r^2 + a^2 - 2Mr, \quad \Sigma = (r^2 + a^2)^2 - a^2 \Delta \sin^2 \theta. \quad (23.8)$$

The metric (23.6) without spin ($a = 0$), with black hole mass $M = 1$ and (arbitrarily chosen) critical radius $r_c = 8M$ and critical density $\rho_c M^2 = 1/16$ allows to determine the Michel solution analytically [387].

This test was performed in spherical Kerr-Schild coordinates with a spatial domain $(r, \theta) \in \Omega = [1.5, 100] \times [0.15, 3.0]$, i.e., the simulation domain penetrates the event horizon but does not include the singularity. The spatial domain is discretized with a uniform mesh of 200×32 elements and

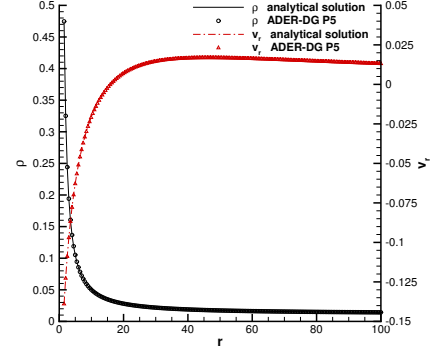


Figure 23.1: Numerical solution for the two-dimensional Michel accretion test in KSS coordinates obtained with our ADER-DG \mathbb{P}_5 at $t = 100$. The numerical solution of density (black) and radial velocity (red) interpolated along 200 points at $\theta = 1.5$ are shown.

	N_x	\mathcal{E}_{L_2}	\mathcal{E}_{L_∞}	L_2	L_∞
DG- \mathbb{P}_1	10	5E-05	9E-05	—	—
	20	1E-05	2E-05	2.13	2.08
	40	3E-06	5E-06	2.06	2.05
	80	7E-07	1E-06	2.03	2.02
DG- \mathbb{P}_2	6	2E-05	3E-05	—	—
	12	3E-06	4E-06	2.93	2.87
	18	1E-06	1E-06	2.93	2.91
	30	2E-07	3E-07	2.94	2.93
DG- \mathbb{P}_3	4	3E-07	1E-06	—	—
	6	5E-08	1E-07	4.65	4.59
	8	1E-08	4E-08	4.21	4.51
	12	3E-09	8E-09	3.96	4.35
DG- \mathbb{P}_4	2	3E-06	5E-06	—	—
	3	4E-07	5E-07	5.51	5.77
	4	9E-08	1E-07	5.22	4.97
	5	2E-08	4E-08	5.18	4.93
DG- \mathbb{P}_5	2	6E-08	3E-08	—	—
	3	4E-09	2E-09	6.68	6.50
	4	6E-10	3E-10	6.31	6.30
	5	1E-10	1E-10	6.27	5.83
DG- \mathbb{P}_6	2	1E-08	4E-09	—	—
	3	4E-10	2E-10	7.81	7.21
	4	5E-11	3E-11	7.43	6.72
	5	1E-11	8E-12	7.37	6.71

Table 23.1: L_2 and L_∞ errors and convergence rates for the 2D Michel accretion in spherical Kerr-Schild coordinates for the ADER-DG- \mathbb{P}_N scheme. We report the convergence results for the rest-mass density ρ at $t = 10$ up to $N = 6$, and contrast the results with the expected rate. The domain has been chosen different (enlarged) for the cases $N = 5$ and $N = 6$ in order to keep away the numerical error from the machine limit. Similar results have also been obtained for all other flow variables.

solved with the ADER-DG \mathbb{P}_5 scheme. A graphical representation of the numerical results and their comparison with the analytic solution is shown in Fig. 23.1, while the results of the convergence study are provided in Table 23.1. Clearly, we can note an excellent agreement between analytical and numerical solution and that the latter converges at the expected and high order.

23.2 Torus interior around a Schwarzschild black hole in 2D

In this test, a numerical convergence study of a stationary solution of a thick disk (also referred to as Polish donut or axisymmetric test-fluid torus) orbiting around a Schwarzschild black hole ($a = 0$) of mass $M = 1$ in 2D spherical Kerr-Schild coordinates. The theory of the equilibrium of these non-selfgravitating fluids in GRHD has been first proposed by [2, 283] and has been the subject of a vast literature. For completeness, we give in the following a brief description of the setup of the primitive variables of this test problem, referring to [31, 154, 203, 387] for details about a more general configuration of the fluid, depending on the selected values of physical parameters.

Torus description

The acceleration experienced by a test fluid rotating around a Schwarzschild black hole (cylindrical symmetry) can be cast into the following differential equation

$$d \log |u_t| - \left(\frac{\Omega}{1 - \Omega\ell} \right) d\ell + \frac{dp}{\rho h} = 0, \quad (23.9)$$

$$\text{with specific angular momentum } \ell(r, \theta) := -\frac{u_\phi}{u_t}, \quad (23.10)$$

$$\text{and (coordinate) angular velocity } \Omega(r, \theta) := \frac{u^\phi}{u_t}, \quad (23.11)$$

For barotropic fluids the last differential on the right in Eq. (23.9) is exact, i.e., one can define the effective potential \mathcal{W} via

$$\mathcal{W} - \mathcal{W}_{\text{in}} := - \int_0^p \frac{d\tilde{p}}{\rho h} = \log |u_t| - \log |(u_t)|_{\text{in}} - \int_{\ell_{\text{in}}}^{\ell} \frac{\Omega d\tilde{\ell}}{1 - \Omega\tilde{\ell}}. \quad (23.12)$$

In the case considered here, the specific angular momentum is assumed to be constant $\ell = \ell_0 = \text{const.}$, so that it is possible to obtain an explicit and simplified expression for the potential

$$\mathcal{W}(r, \theta) = \log |u_t|, \quad (23.13)$$

where, for a Schwarzschild black hole, one has

$$u_t = -r \sin \theta \left(\frac{r - 2}{r^3 \sin^2 \theta - \ell^2(r - 2)} \right)^{\frac{1}{2}}. \quad (23.14)$$

In the axisymmetric equilibrium torus, there are some special radial positions in the equatorial plane ($\theta = \pi/2$) that are worthwhile recalling: the

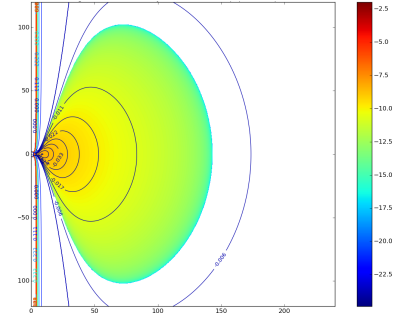


Figure 23.2: Example of a thick torus configuration, two dimensional cut in the azimuthal plane ($\theta = 0$). Colour encodes the rest mass density ρ (Logarithm of solar mass units) within the Roche lobe. Solid lines indicate equipotentials.

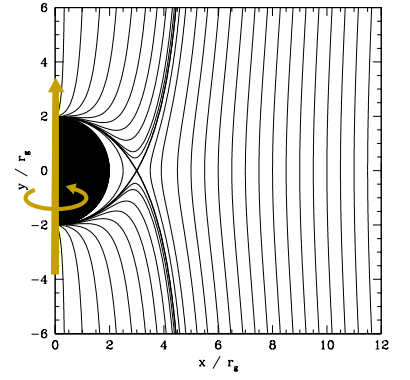


Figure 23.3: Surfaces with constant $\Omega = \Omega(\ell)$ are also referred to as von Zeipel's cylinders. Figure modified from [203].

inner and outer edge of the torus r_{in} and r_{out} ; the radial position of the cusp, r_{cusp} ; the radial position of the maximum pressure peak, r_c , which is the center of the torus; the radial position of the “marginally stable” and “marginally bound” orbit, r_{ms} and r_{mb} . The cusp position r_{cusp} and the centre r_c can be identified as the local extrema of the effective potential, but also by the condition $\ell_K = \ell_0$, where ℓ_K is the Keplerian specific angular momentum which is given by $\ell_K^2(r) := Mr^3/(r-2M)^2$. Similarly, also r_{ms} and r_{mb} are identified by the condition $\ell_K = \ell_{\text{ms}}$ and $\ell_K = \ell_{\text{mb}}$. For a Schwarzschild (nonrotating) black-hole: $\ell_{\text{ms}} = (3\sqrt{6}/2)M$ and $\ell_{\text{mb}} = 4M$, so that the corresponding to the radial positions are $r_{\text{ms}} = 6M$ and $r_{\text{mb}} = 4M$.

Finally, the inner and outer radial position, r_{in} and r_{out} , can be estimated by the condition $\Delta\mathcal{W} := \mathcal{W}_{\text{in}} - \mathcal{W}_{\text{cusp}} = 0$. Indeed, whenever $\Delta\mathcal{W} > 0$ the orbit of the corresponding fluid particle is open, whenever $(\mathcal{W}_c - \mathcal{W}_{\text{in}}) < \Delta\mathcal{W} < 0$ the orbits are closed. The spatial volume delimited by the widest closed equipotential surface of the torus, i.e., $\mathcal{W} = \mathcal{W}_{\text{cusp}}$ is named as the “Roche lobe” of the torus. Using these definitions, several constraints need to be satisfied: first, the cusp r_{cusp} must necessarily be located within r_{mb} and r_{ms} , and the inner edge r_{in} can be located anywhere within r_{cusp} and r_c . For isentropic fluids obeying the polytropic EOS ($p = K\rho^\Gamma$), an analytical expression for the rest-mass density exists and takes the form

$$\rho(r, \theta) = \left[\frac{\Gamma - 1}{K\Gamma} (\exp(\mathcal{W}_{\text{in}} - \mathcal{W}(r, \theta)) - 1) \right]^{1/(\Gamma-1)} \quad (23.15)$$

After choosing the value of the polytropic constant K , polytropic exponent Γ , the specific angular momentum ℓ_0 , and the potential gap $\Delta\mathcal{W}$, then the Keplerian points are estimated after ensuring the following scalar equalities: for the radial cusp position r_{cusp} ,

$$\ell_K(r) = \ell_0, \quad \text{with } r_{\text{hor}} < r < r_{\text{ms}}, \quad (23.16)$$

for the center r_c , r_{hor} being the radial position of the horizon,

$$\ell_K(r) = \ell_0, \quad \text{with } r_{\text{ms}} < r. \quad (23.17)$$

Then, the corresponding potentials $\mathcal{W}_{\text{cusp}}$ and \mathcal{W}_c are evaluated according to Eq. (23.13). On the other hand, the effective potential at the inner edge \mathcal{W}_{in} is computed according to the prescribed potential gap $\Delta\mathcal{W}$ after estimating

$$(u_t)_{\text{in}} = (u_t)_{\text{cusp}} e^{\Delta\mathcal{W}}. \quad (23.18)$$

Then, since the fluid distribution is inside the Roche lobe, the inner and outer edge positions r_{in} and r_{out} are computed through the conditions

$$u_t(r) = (u_t)_{\text{in}} \quad \text{with } r_{\text{cusp}} < r < r_c, \quad (23.19)$$

$$\text{and } u_t(r) = (u_t)_{\text{in}} \quad \text{with } r_c < r, \quad (23.20)$$

respectively. The rest-mass density at the center ρ_c is provided directly by the analytical solution (23.15), the corresponding pressure p_c through the EOS. Finally, for every spatial position (r, θ) within the torus, i.e., which fulfills the condition

$$r > r_{\text{in}} \quad \text{and} \quad \mathcal{W} < \mathcal{W}_{\text{in}}, \quad (23.21)$$

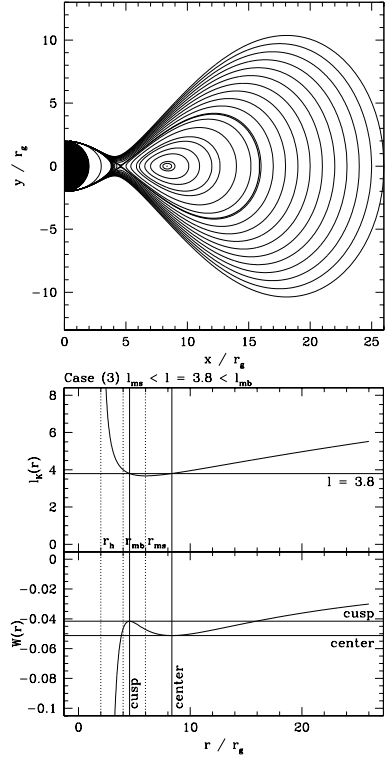


Figure 23.4: Torus potentials, Figure modified after [203]

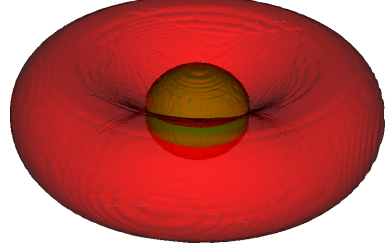


Figure 23.5: The theory of thick tori can also be applied to other spacetimes with cylindrical symmetry, for instance to the spacetime of a neutron star (shown here in a surface countour plot of the rest mass density ρ). This artificially created object (linear superposition of two spacetimes) remains surprisingly stable during evolution.

the angular velocity $\Omega(r, \theta)$ is computed through the definition (23.10), the rest-mass density ρ directly from (23.15), and the velocity is given by

$$(v^r, v^\theta, v^\phi) = \left(\frac{\beta^r}{\alpha}, 0, \frac{1}{\alpha}(\Omega + \beta^\phi) \right). \quad (23.22)$$

Torus evolution

The free parameters of the problem have been chosen to be a specific angular momentum of $\ell_0 = 3.8$, a potential gap $\Delta W = -10^{-3}$ (inside and nearly filling its Roche lobe). The polytropic constant and exponent have been chosen equal to $K = 0.0496$ and $\Gamma = 4/3$, respectively.

Also in this case, for a rigorous testing of the convergence order we have simulated only an inner portion of the torus which is fully filled by fluid, namely, the one covered by the coordinate patch $(r, \theta) \in \Omega = [7, 10.5] \times [1.47, 1.67]$. The corresponding measured convergence order after evolving the set of the GRHD equations in spherical Kerr-Schild coordinates are reported in Table 23.2, once again showing the expected high order of convergence of our ADER-DG scheme. We conclude this test by remarking that torus simulations where the torus is fully contained in the computational domain, which therefore includes also a region set to atmosphere, will be presented in Sec. 25.1.

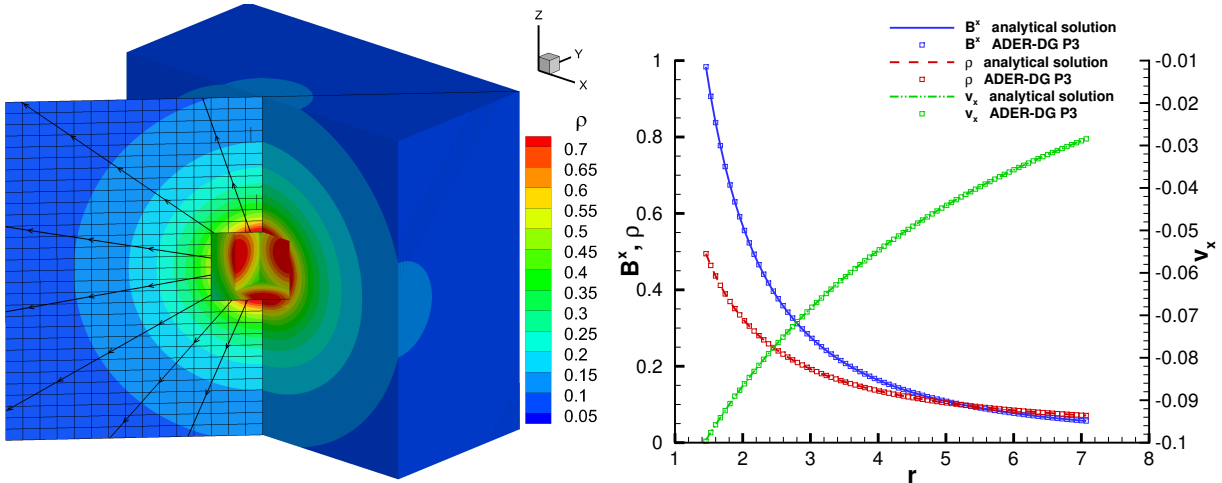


Figure 23.6: Numerical solution for the 3D Michel accretion test with radial magnetic field in KSC coordinates obtained with our ADER-DG \mathbb{P}_3 at $t = 20$. *Left panel:* 3D visualization of the numerical solution and mesh: the space elements at $y < 0$ are artificially blanked (not-visible), at $y > 0$ are coloured by the rest-mass density. Moreover, the computed density is shown also along the 2D cut-plane $y = x \leq 0$ together with the stream-traces of the magnetic field. *Right panel:* numerical solution interpolated along 200 points at $z = 0$ and $y = x$ for the rest-mass density (red), the x component of the velocity (green) and magnetic field (blue) vectors are plotted next to the analytical solution. The numerical domain is $\mathbf{x} \in \Omega = [-5, 5]^3$. Published in [194].

23.3 3D Michel accretion with radial magnetic field

This is the 3D version of the similar test presented in Sec. 23.2, with the addition of one spatial dimension (corresponding to the azimuthal Killing vector) and of a radial magnetic field. Although such a magnetic field is unphysical, since it leads to a nonzero divergence and hence to the presence of a magnetic monopole, it is nevertheless widely used for testing GRMHD codes [192]. Here, we use it to test the convergence order of our high-order method by considering also the magnetic component of the set of partial differential equations. In addition, to stress-test our numerical infrastructure, we have employed for this test 3D Cartesian KS coordinates, so that the magnetic field lines are not aligned with any of the coordinate axis. The

	N_x	\mathcal{E}_{L_2}	\mathcal{E}_{L_∞}	L_2	L_∞
DG- \mathbb{P}_1	10	5E-07	2E-06	—	—
	20	1E-07	9E-07	1.68	1.55
	30	7E-08	4E-07	1.83	1.84
	40	4E-08	2E-07	1.86	1.92
DG- \mathbb{P}_2	10	5E-08	1E-07	—	—
	15	1E-08	5E-08	2.65	2.47
	20	8E-09	2E-08	2.64	2.78
	30	2E-09	7E-09	2.70	2.70
DG- \mathbb{P}_3	8	3E-09	1E-08	—	—
	10	1E-09	9E-09	3.69	3.13
	15	3E-10	2E-09	4.04	3.79
	20	1E-10	7E-10	3.69	3.64
DG- \mathbb{P}_4	2	1E-07	3E-07	—	—
	3	1E-08	3E-08	5.57	5.44
	4	3E-09	1E-08	4.10	4.29
	5	1E-09	5E-09	4.08	3.04

chosen contravariant components of the radial magnetic field take the form

$$B^i(\mathbf{x}, t) = \gamma^{-\frac{1}{2}} M^2 B_0 \frac{x^i}{r^2}, \quad \text{with} \quad B_0 = \frac{2.688}{M} \left(\frac{b^2}{\rho} \right)_{\text{hor}}^{\frac{1}{2}}, \quad (23.23)$$

where the black-hole mass is again set to $M = 1$ and b^μ is the magnetic field measured by the Lagrangian observer comoving with the fluid, i.e.,

$$b^\mu := \frac{(\delta_\nu^\mu + u^\mu u_\nu) B^\nu}{-n_\nu u^\nu}. \quad (23.24)$$

The spatial domain is in this case given by $(x, y, z) \in \Omega = [-5, +5]^3$ and is partitioned with a uniform mesh of 30^3 elements, where we have employed a very simple cubic excision to avoid the singularities at the coordinates' origin location of the black hole as shown in the left panel of Fig. 23.6. At the excision boundary, we impose the exact solution of the problem as boundary condition in all variables.

After adopting a ratio $(b^2/\rho)_{\text{hor}} = 4$ at the horizon, the results of the convergence study are presented in Table 23.3, while graphical representation of the numerical results is offered in the right panel of Fig. 23.6, which reports the numerical solution interpolated along 200 points at $z = 0$ and $y = x$ for the rest-mass density and the x -component of the velocity and of the magnetic field vectors as plotted against the analytical solutions. Clearly, also in this case the numerical solution is shown to converge at the expected order of accuracy, confirming the validity of our implementation in the presence of a magnetic field and of a nontrivial coordinate mapping.

24 Non-smooth special-relativistic benchmarks

The tests considered in this section are considerably different from those discussed so far in that they do not involve smooth flows and allow therefore for the presence of nonlinear waves, either in the form of shocks or of steep gradients as those present at the fluid interface with an atmosphere.

24.1 Riemann problems

We start by considering two standard Riemann (or shock-tube) problems, here referred to respectively as RP1 and RP2, and originally proposed in the context of special relativistic MHD by [50]. Although these tests are solved on flat spatial hypersurfaces, i.e., $\gamma_{ij} = \delta_{ij}$, they employ different setups for the gauge variables, the lapse function and the shift vector. In particular, Table 24.1 provides all the considered initial conditions for the MHD variables of RP1 and RP2, while the lapse, the x -component of the shift and the final time are chosen as in Table 24.2. The adiabatic index for RP1 and RP2 has been set to be $\Gamma = 2$ and $\Gamma = 5/3$, respectively.

For these tests, the HLL approximate Riemann solver has been used. Figure 24.2 offers a 3D view of the rest-mass density variable for the proposed shock-tube problems and the corresponding AMR grid and limiting status, for the case $\alpha = 2$, obtained with our ADER-DG- \mathbb{P}_3 scheme using a level-zero mesh of 40×5 space-elements onto with $\ell_{\text{max}} = 2$ maximum refinement levels are added, and an ADER-DG- \mathbb{P}_5 scheme on a level-zero grid

	N_x	\mathcal{E}_{L_2}	\mathcal{E}_{L_∞}	L_2	L_∞
DG- \mathbb{P}_1	10	6E-04	2E-04	—	—
	20	1E-04	8E-05	1.9	1.3
	30	7E-05	4E-05	2.0	1.6
	40	4E-05	2E-05	2.0	1.8
DG- \mathbb{P}_2	10	3E-05	2E-05	—	—
	15	1E-05	7E-06	2.5	2.9
	20	6E-06	3E-06	2.4	2.4
	30	2E-06	1E-06	2.4	2.4
DG- \mathbb{P}_3	8	1E-06	1E-06	—	—
	10	6E-07	3E-07	4.4	5.0
	15	1E-07	6E-08	4.3	4.2
	20	3E-08	1E-08	4.2	4.5
DG- \mathbb{P}_4	6	4E-07	4E-07	—	—
	8	1E-07	9E-08	5.0	5.0
	12	1E-08	1E-08	5.0	5.1
	16	3E-09	2E-09	5.0	5.3
DG- \mathbb{P}_5	4	1E-07	3E-07	—	—
	6	1E-08	3E-08	6.5	5.8
	8	2E-09	6E-09	5.9	6.1
	10	6E-10	1E-09	5.8	6.1
DG- \mathbb{P}_6	6	1E-06	1E-06	—	—
	8	1E-07	3E-07	6.9	5.2
	10	4E-08	1E-07	6.3	5.7
	12	1E-08	3E-08	6.1	5.9

Table 23.3: L_2 and L_∞ errors and convergence rates for the 3D Michel accretion with radial magnetic field in Cartesian Kerr-Schild coordinates for the ADER-DG- \mathbb{P}_N scheme. We report the convergence results for the magnetic field component B^x at $t = 10$ up to $N = 6$, and contrast the results with the expected rate. Similar results have also been obtained for all other flow variables.

	RP1		RP2	
	$x > 0$	$x \leq 0$	$x > 0$	$x \leq 0$
ρ	0.125	1.0	1.0	1.08
v_x	0	0	-0.45	0.40
v_y	0	0	-0.2	0.3
v_z	0	0	0.2	0.2
p	0.1	1.0	1.0	0.95
B^x	0.5	0.5	2.0	2.0
B^y	-1.0	1.0	-0.7	0.3
B^z	0	0	0.5	0.3

Table 24.1: Initial conditions of the MHD variables for the Riemann problems.

α	β^x	t_{final}
0.5	0	0.8
1	0	0.4
1	0.4	0.16
2	0	0.2

Table 24.2: Background spacetime and final time for different Riemann problem runs.

of 120×5 elements with one single refinement level $\ell_{\max} = 1$. The corresponding one-dimensional (1D) cuts relative to the \mathbb{P}_5 solutions are presented instead in Fig. 24.3 relatively to the test configurations listed in Table 24.1; shown with solid lines are the corresponding solutions from the exact Riemann solver of [215]. In the presence of moving discontinuities, the expected order of convergence of any shock capturing method is at most one. In Fig. 24.1 we show the results of a numerical convergence study for RP2, indicating that the numerical method converges indeed with the expected order of one for flows with shocks and discontinuities.

Overall, the results of these tests confirm the high-resolution shock-capturing capability, but also the robustness, of the new class of ADER-DG \mathbb{P}_N schemes. In addition, they show that the a-posteriori finite-volume subgrid limiter is activated only in very small portions of the domain and, in the case of genuine shocks, it is very narrowly concentrated near the discontinuity.

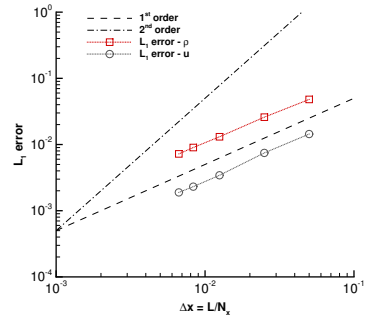
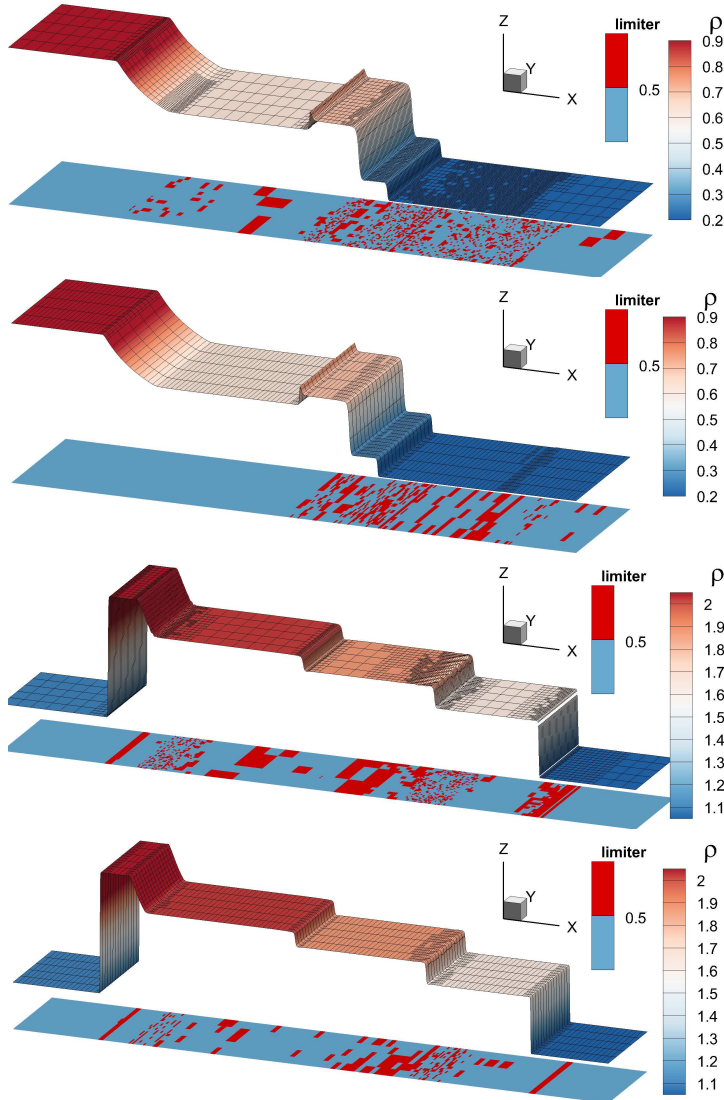


Figure 24.1: Convergence study against Riemann problem RP2 of Table 24.1. L_1 errors are plotted against the discretization step $\Delta x = L/N_x$, with $L = 1$ being the length of the one-dimensional domain, N_x the discretization number, i.e., the number of high-order space-elements in the x -direction. Published in [194].

Figure 24.2: 3D view of the rest-mass density, the corresponding AMR grid and, on the horizontal plane, the corresponding limiting status, obtained with our ADER-DG \mathbb{P}_N with finite-volume subcell limiting. From the top panel to the bottom, from left to right: i) RP1 at $t_{\text{final}} = 0.2$ with $\alpha = 2$, \mathbb{P}_3 , with a coarsest grid of 40×5 elements, $\ell_{\max} = 2$; ii) RP1 at $t_{\text{final}} = 0.2$ with $\alpha = 2$, \mathbb{P}_5 , with a coarsest grid of 120×5 elements, $\ell_{\max} = 1$; iii) RP2 at $t_{\text{final}} = 0.275$ with $\alpha = 2$, \mathbb{P}_3 , with a coarsest grid of 40×5 elements, $\ell_{\max} = 2$; iv) RP2 at $t_{\text{final}} = 0.275$ with $\alpha = 2$, \mathbb{P}_5 , with a coarsest grid of 120×5 elements, $\ell_{\max} = 1$. The limited cells, using the subcell ADER-TVD finite-volume scheme, are highlighted in red along the horizontal plane below the 3D plot of the rest-mass density ρ , while unlimited DG- \mathbb{P}_N cells are highlighted in blue. Published in [194].

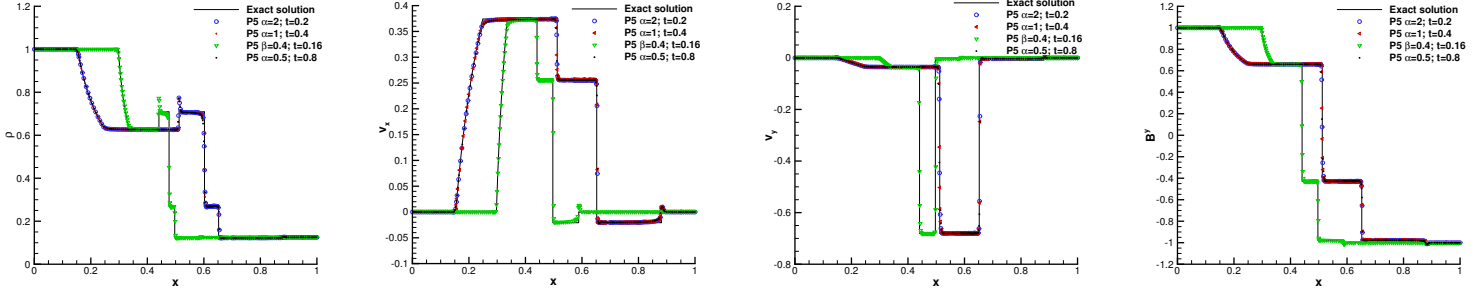


Figure 24.3: Riemann Problem 1 (RP1): the different panels show the various physical variables interpolated along a 1D cut, starting from a coarsest grid of 120×5 elements by using the ADER-DG-P₅ scheme supplemented with the *a posteriori* ADER-TVD subcell and one single refinement level $\ell_{\max} = 1$. Shown with solid lines are the corresponding solutions from an exact Riemann solver. Published in [194].

24.2 Advection of a 2D magnetic field loop

In this special-relativistic 2D problem we advect a loop of magnetic field which is at a magnetic pressure much smaller than the corresponding fluid pressure. The computational domain in Cartesian coordinates is given by is $(x, y) \in \Omega = [-1, +1] \times [-0.5, 0.5]$ with periodic boundary conditions everywhere. Using unitary (dimensionless) rest-mass density and gas pressure, i.e., $\rho = p = 1$, the velocity field is set to be constant with and initialised as $(v_x, v_y) = (2, 1)V_0$, where $V_0 = 1/5$. The magnetic-field vector is derived from the magnetic vector potential, which is specified as

$$A_z = \begin{cases} A_0(R - r) & \text{for } r \leq R, \\ 0 & \text{otherwise,} \end{cases} \quad (24.1)$$

where r is the radial coordinate, $R = 0.3$ is the radius of the advected loop and the parameter $A_0 = 10^{-3}$ modules the magnetic field. The discontinuity at the loop boundaries has been initially slightly smoothed, e.g., by means of a standard linear smoothing in the form

$$B_x = \begin{cases} A_0 \frac{y}{r} & \text{for } r \leq R, \\ s(r) A_0 \frac{y}{r} & \text{for } R < r \leq R_1, \\ 0 & \text{otherwise.} \end{cases} \quad (24.2)$$

$$B_y = \begin{cases} -A_0 \frac{x}{r} & \text{for } r \leq R, \\ -s(r) A_0 \frac{x}{r} & \text{for } R < r \leq R_1, \\ 0 & \text{otherwise.} \end{cases} \quad (24.3)$$

where $s(r) = 1 - (r - R)/(r - R_1)$ is the adopted linear taper-function, with R_1 chosen to be close to R , e.g., $R_1 = 0.315$.

Given the initial conditions and the periodic boundary conditions, the magnetic loop is advected across the computational domain and we have performed simulations using the lapse function set either to $\alpha = 1$ or to $\alpha = 2$, so that the corresponding simulation times to recover the initial configuration are $t = 5$ and $t = 2.5$, respectively; conversely, the shift vector β^i is set to zero.

This test has been solved using a level-zero mesh of 20^2 space elements with the maximum refinement levels $\ell_{\max} = 2$ via an ADER-DG-P₄ scheme, supplemented with the *a posteriori* TVD subcell limiter and by adopting an HLL Riemann solver. At this point we would like to emphasize that instead

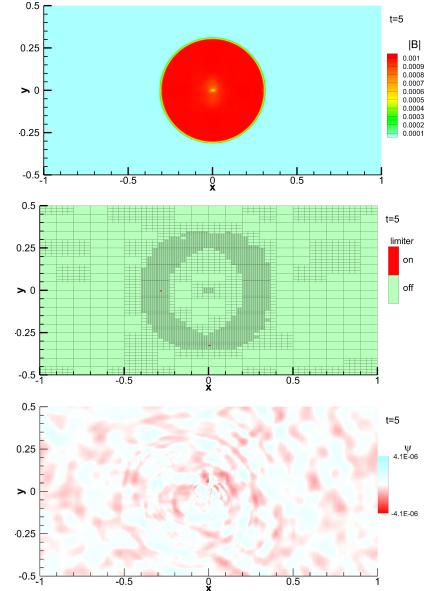


Figure 24.4: Advected magnetic field loop problem (SRMHD) obtained with the ADER-DG-P₄ scheme supplemented with the *a posteriori* TVD subcell limiter. Color encoded are, from top to bottom: The magnetic field magnitude $|\vec{B}|$, the limiter status and the divergence cleaning scalar ψ . Published in [194].

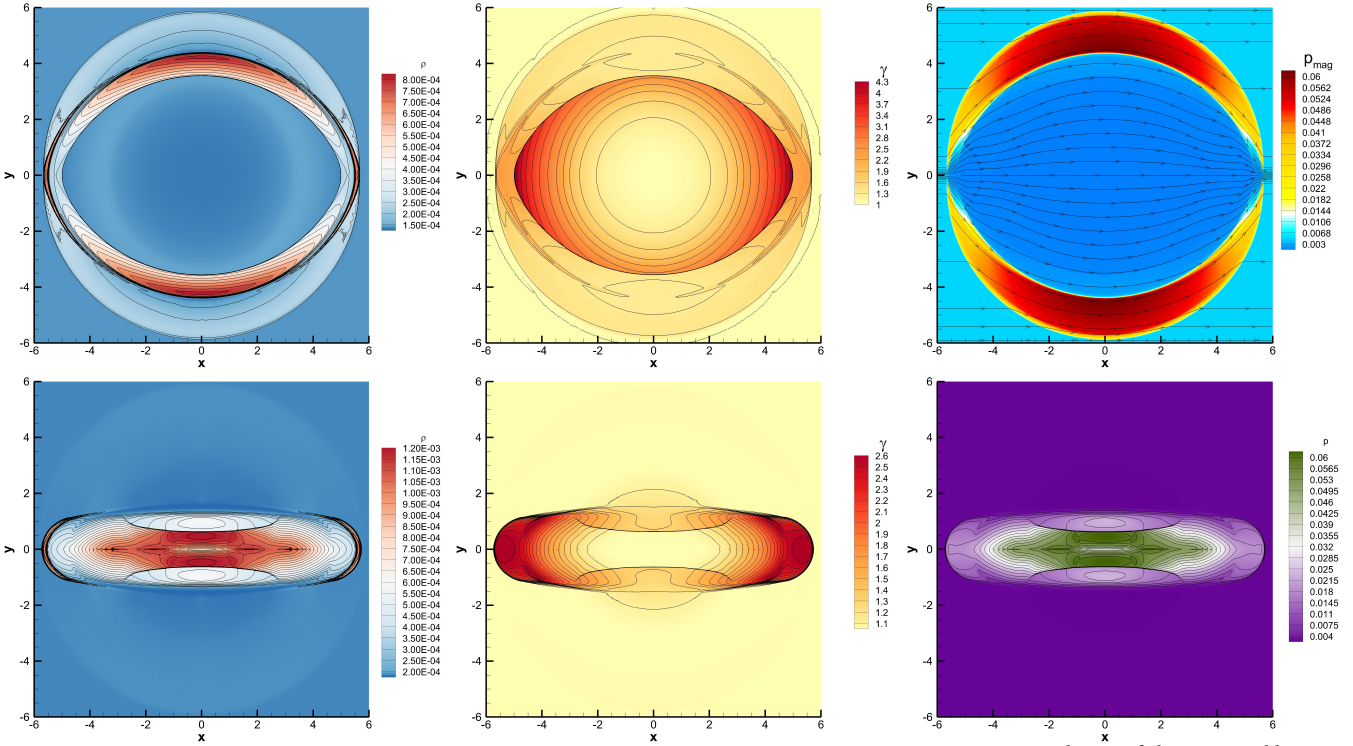


Figure 24.5: Solution of the SRMHD blast wave with $B_x = 0.1$ at time $t = 4.0$, obtained with the ADER-DG \mathbb{P}_3 scheme supplemented with the *a posteriori* second-order TVD subcell limiter. The three columns show rest-mass density ρ , Lorentz factor γ and magnetic pressure p_{mag} . Published in [194].

of HLL or Rusanov-type Riemann solvers any other stable and monotone numerical flux could have been used equally well. The Riemann solver has to be understood as a building block of the DG scheme, exactly in the same way as it is in the finite-volume context. Figure 24.4 reports the numerical results, which basically show the preservation of the initial condition. Furthermore, the limiter is only rarely activated, as expected for this test case, and the divergence cleaning scalar ψ never reaches a larger absolute value than $|\psi| \sim 5 \times 10^{-6}$.

24.3 2D blast wave

Another standard test of the RMHD equations is represented by the cylindrical blast wave problem. In this benchmark, the plasma is initially at rest and subject to a constant magnetic field along the x -direction; we have therefore considered two different configurations strengths of the magnetic field, i.e., $B_x = 0.1$ and $B_x = 0.5$, representing the case of a moderately and of a highly magnetized plasma, respectively.

The initial conditions for the rest-mass density and pressure are given respectively by

$$(\rho, p) = \begin{cases} (0.01, 1) & \text{if } r < R, \\ 10^{-4} \times (1, 5) & \text{otherwise,} \end{cases} \quad (24.4)$$

and together with the magnetic-field strength are sufficient to fully specify the initial setup. Also in this case, and following see [52], a linear smoothing is used in order to avoid sharp discontinuities in the initial conditions.

The computations have been carried out in 2D with a Cartesian coordinate system over a computational domain given by $\Omega = [-6, 6]^2$, with 40^2 elements on the coarsest mesh level, and a maximum refinement level

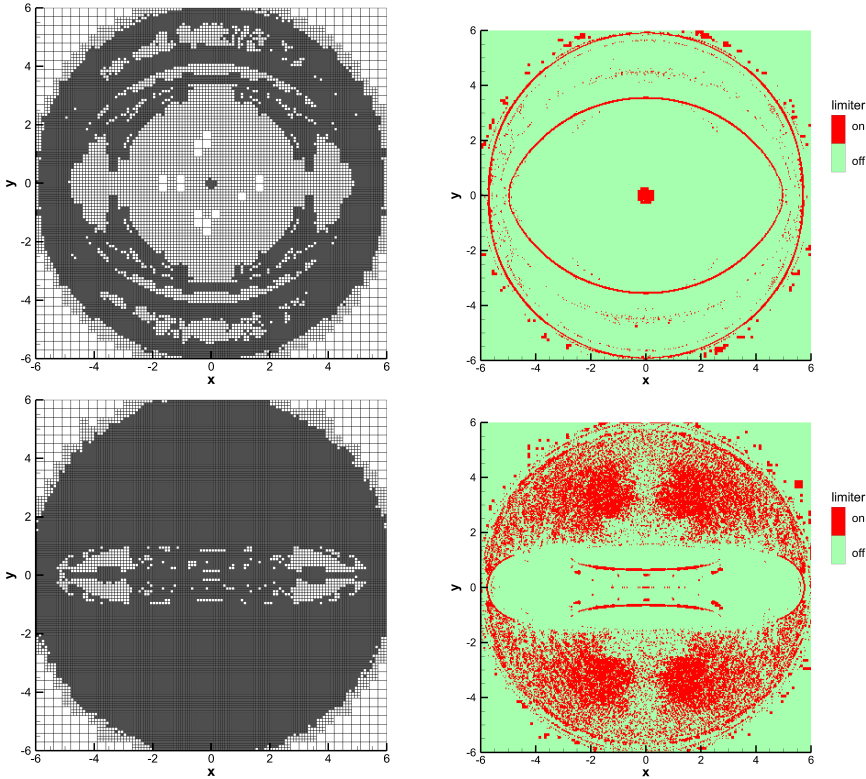


Figure 24.6: Solution of the SRMHD blast wave with $B_x = 0.5$ at time $t = 4.0$, obtained with the ADER-DG \mathbb{P}_3 scheme supplemented with the *a posteriori* second-order TVD subcell limiter. Top panels: AMR grid, bottom panels: limiter map with troubled cells marked in red and regular unlimited cells marked in green. Published in [194].

$\ell_{\max} = 2$. We have used the Rusanov Riemann solver with our ADER-DG- \mathbb{P}_3 scheme. The computed results for different physical quantities, the AMR grid and the limiter status are shown in Fig. 24.6 for the highly magnetized case. Note in the bottom-right panels of figures the map of the “troubled cells” and how these are limited in extent and nicely map the dynamics of the discontinuities in the magnetic field. Clearly, the fraction of troubled cells in the case of the low-magnetisation setup represent only a very small fraction of the evolved cells (see Fig. 24.6); this is to be contrasted with what happens in the case of the much more challenging case of high magnetisation, where however the troubled cells still represent less than 50% of the evolved cells (see Fig. 24.6).

Lacking an analytic solution to compare with, the assessment of the results in this case is harder, but it is reassuring that the results match well those presented in other tests in the literature, e.g., by [154, 157, 470].

24.4 Orszag-Tang vortex

Our final special-relativistic test of non-smooth flows is another classic benchmark represented by the relativistic version of the Orszag-Tang vortex system [355]. This is a useful application of our numerical infrastructure as it involves the development of a complex and non-smooth magnetic-field structure and hence it explores geometries without trivial symmetries.

The initial conditions in this case are given by the vector of conserved variables

$$(\rho, u, v, w, p, B_x, B_y, B_z) = \left(1, -\frac{3}{4\sqrt{2}} \sin y, \frac{3}{4\sqrt{2}} \sin x, 0, 1, -\sin y, \sin 2x, 0\right),$$

with $\Gamma = 4/3$. The computational domain is $\Omega = [0, 2\pi]^2$, with 30^2 elements on the level-zero grid, a maximum refinement level of $\ell_{\max} = 2$, periodic boundary conditions and a Rusanov Riemann solver for the sub-cell finite-volume limiter.

Figure 24.7 shows the numerical results for the AMR grid with limiter status, the rest-mass density and the divergence-cleaning scalar ψ at different times, together with the corresponding numerical solution obtained with the same scheme on a fine uniform 270^2 mesh, corresponding to the finest mesh resolution at $\ell = \ell_{\max}$ and which serves here as a reference. The figure, in particular, refers to simulations in which the \mathbb{P}_5 -version of our ADER-DG has been adopted. Also for this test, a rigorous accuracy analysis is not trivial but we note the very good agreement between the AMR simulations and the fine uniform-grid reference solution, as well as with the corresponding solutions that are published in [364, 470]. Note also how the AMR grid structure and the troubled-cells patterns closely follow the development of steeper gradients and discontinuities.

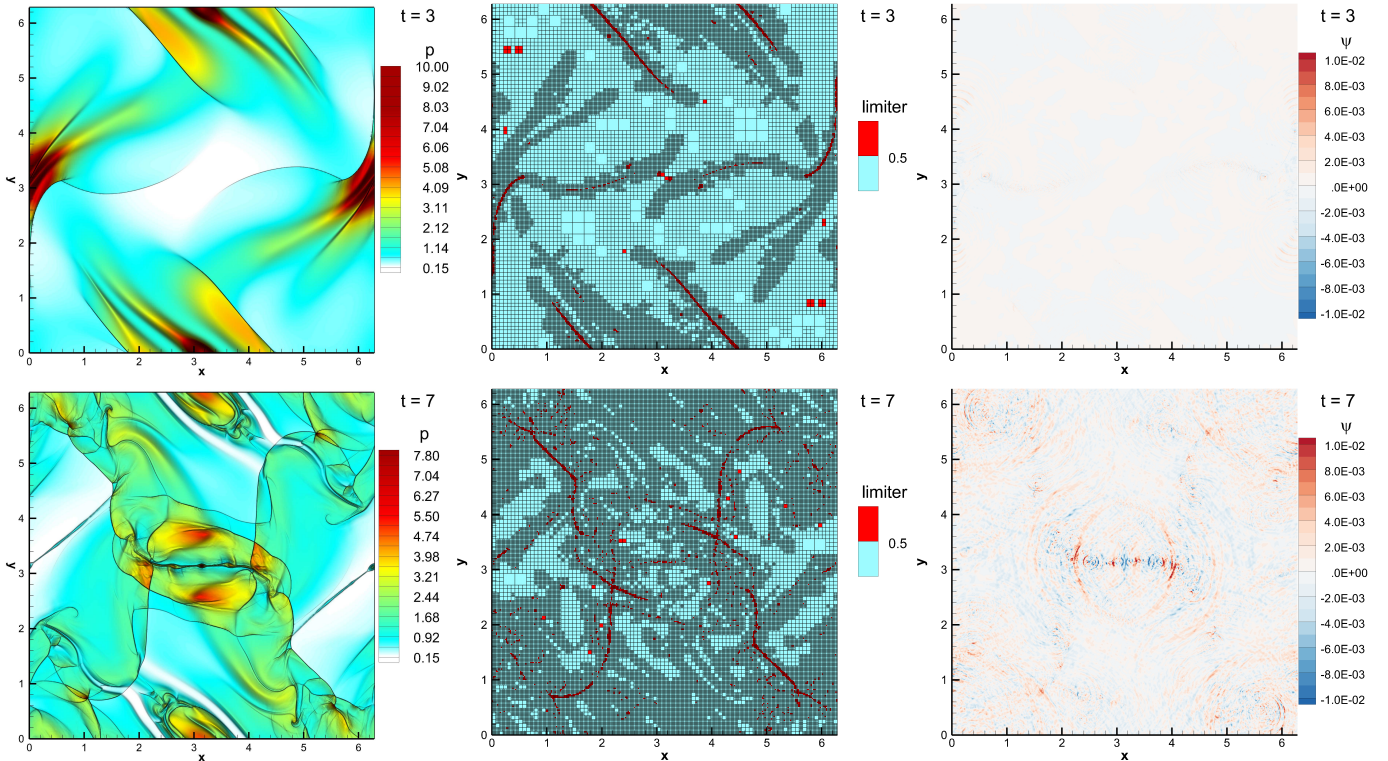


Figure 24.7: SRMHD Orszag-Tang vortex problem at times $t = 3$ (upper row) and $t = 7$ (lower row), obtained through the ADER-DG- \mathbb{P}_5 scheme supplemented with the *a posteriori* TVD subcell limiter on a 30^2 elements on the coarsest grid ($\ell = 0$), two maximum refinement levels and a refinement factor $\mathcal{R} = 3$. Color encoded, from left to right, are: Rest mass density ρ , AMR grid and limiter status, divergence cleaning scalar ψ . Published in [194]

25 Non-smooth general-relativistic benchmarks

In the following two sections we discuss the use of our ADER-DG method in non-smooth general-relativistic flows, either in 2D and spherical coordinates or in 3D and Cartesian coordinates. The tests involve the evolution of non-selfgravitating tori as those presented in Sec. 24 with the important difference that the computational domain here fully contains the torus, whose exterior is therefore filled with a uniform atmosphere at a rest-mass

density of $\rho_0 = 10^{-9}$ that is five orders of magnitude smaller than the one at the torus centre.

25.1 2D torus around a Schwarzschild black hole

First, we consider a thick torus in equilibrium orbiting around a black-hole with the parameters previously described in Sec. 23.2 and using horizon-penetrating spherical KS coordinates in 2D. The computational domain $(r, \theta) \in \Omega = [2, 18] \times [0.5, 2.5]$ is discretized with a uniform mesh of 50^2 elements using an ADER-DG- \mathbb{P}_3 scheme with TVD subcell finite-volume limiter (as a comparison, the torus has an inner radius $r_{\text{in}} = 5.5M$ and an outer radius $r_{\text{out}} = 13.8M$, so that the entire torus is resolved with only 26 elements in radial direction and 14 elements in angular direction). On the outer edge we impose the initial data as boundary condition in all variables.

A 1D cut of the rest-mass density in the radial direction is shown in the left panel of Fig. 25.1 and is plotted over the analytic solution at $t = 100 M$. Note the excellent agreement between the numerical results and the exact solution, with differences in the central rest-mass density that are less than 0.7%.

It is useful to remark that the low-density atmosphere has been successfully simulated and robustly evolved in time with a high-order ADER-DG scheme and that inside the computational domain the limiter is activated only on the border of the torus, where spurious oscillations may generate possibly negative-valued densities and pressures in the high-order DG polynomials. However, the a-posteriori subcell finite-volume limiter appears to be robust enough to accurately treat the atmosphere of the torus. Furthermore, we note that the fluid in this low-density region is treated so as to be evolved as a standard fluid, i.e., the velocity is not set to zero in a computational cell that is marked to host the atmosphere. As a result, during the simulations, the atmosphere the fluid in the atmosphere starts accreting onto the black hole; in practice the amount of matter accreted in this manner is minute and does not influence with the dynamics of the much denser matter lost from the torus.

25.2 3D torus around a Schwarzschild black hole

In this section, a fully 3D evolution of the torus (from the previous section) is considered, i.e., the azimuthal spatial dimension is added.

For this, we use a horizon-penetrating Cartesian KS coordinates which cover a computational domain chosen to be $(x, y, z) \in \Omega = [-18, +18] \times [2, 18] \times [-8, +8]$. The portion of the domain around the origin is excised following the same logic discussed in sec. 23.3. The solution has been computed using an ADER-DG- \mathbb{P}_3 scheme on a uniform mesh composed of $40 \times 20 \times 20$ elements.

The 1D cut of the rest-mass density profile on the equatorial plane $\theta = \pi/2$ and along different angular directions $\phi = \pi/4, \pi/2$ and $3\pi/4$ at $t \sim 30 M$. The various numerical solutions are overlayed with the corresponding analytic solutions in the right panel of Fig. 25.1. Once again, we can observe an excellent agreement between numerical and exact solution, with differences in the central rest-mass density that are less than 1.5%.

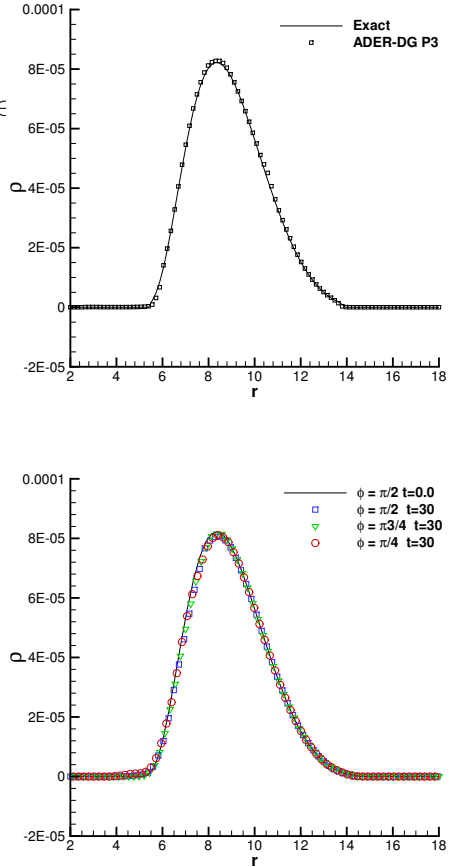
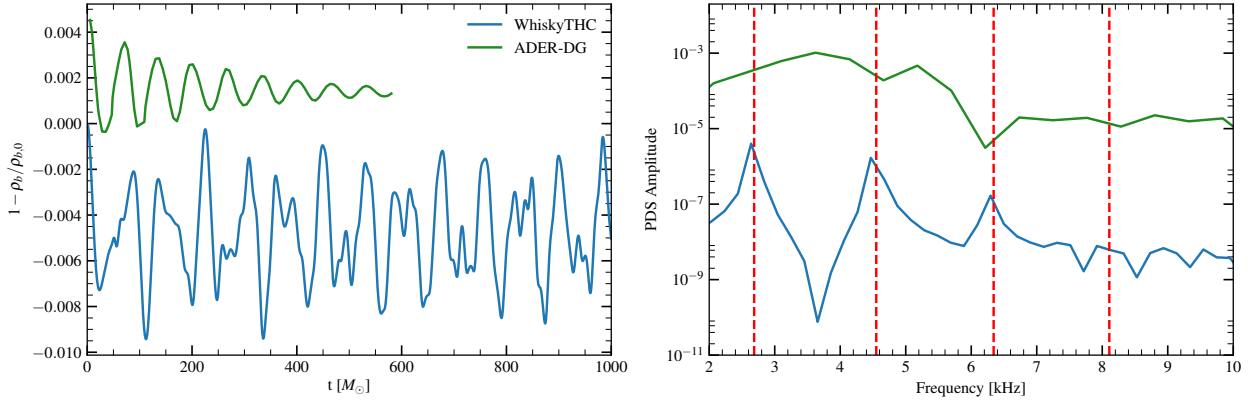


Figure 25.1: Radial 1D cut of the thick torus, comparison of the ADER-DG \mathbb{P}_3 solution with second-order TVD subcell limiter after $t = 100M$ compared with exact solution. The right panel shows different azimuthal angles.



25.3 Preliminary results on a TOV star

The Tolman-Oppenheimer-Volkoff (TOV) solution of general relativity is a popular choice for modelling neutron stars. It is a spherically symmetric static spacetime of an isotropic fluid in equilibrium. For such an energy momentum tensor, Einstein equations reduce to the TOV equations [354, 442]

$$\frac{dp}{dr} = -\frac{\rho m(r)}{r^2} \left(1 + \frac{p}{\rho}\right) \left(1 + \frac{4\pi r^3 p}{m(r)}\right) \left(1 - \frac{2}{r}\right)^{-1} \quad (25.1)$$

where $m(r) = \int_0^r 4\pi \tilde{r}^2 \rho d\tilde{r}$ is the total mass within a shell of radius r . TOV equations can be solved numerically, i.e., solve the system in favour of a requested total mass $M = \lim_{r \rightarrow \infty} m(r)$ or a requested central hydrodynamic quantity such as the central density ρ_0 . However, the full arsenal of GR approximations (Section 10) can be applied to TOV equations, such as Post-Newtonian approximations.

In this test, we created initial data for a $1.45 M_\odot$ neutron star with radius $R = 5.84 M_\odot = 8.6\text{km}$ in isotropic coordinates and central rest mass density $\rho_c = 1.28 \times 10^{-3} M_\odot^4 = 4.9 \times 10^{18} \text{kg/m}^3$, described by a polytropic EOS with $\Gamma = 2, K = 100$ (in geometric units). The initial can be solved with an arbitrary numeric TOVSolver ²³. The star is evolved in full 3D on a domain with an extend of at least $\Omega = [-10M_\odot, 10M_\odot]^3$ with outflow (copy) boundary conditions on all boundaries.

While the interpolation of the initial data on the evolution grid always adds a little perturbation, an additional well-defined “physical” perturbation should be added which produces deterministic results in a code comparison.

Our findings are presented in Figure 25.2. Here, we compare a 1% pressure perturbation evolved with WhiskyTHC [371, 379], i.e., a finite differencing code, vs. the ADER-DG code, but with artificial viscosity turned on. One can clearly see that the artificial viscosity, which shall avoid the activation of the limiter at the surface, damps all errors, artificially stabilizes the simulation but removes the physical modes (vibrations) which characterize the star.

Figure 25.2: Evolution of central density error (left panel), vs. power density spectrum (norm of fourier transform, right panel) of the two curves, with the frequency of peaks predicted by perturbation theory marked in red. The figure shows two codes compared to each other. The better the peaks are reproduced, the better the code performs in this test.

²³ See Appendix B3 for a list of ODE solver codes which where used within this text.

26 Summary

In the present Chapter III, the equations of general relativistic magnetohydrodynamics (GRMHD) have been reviewed and casted in a form with conserved and nonconserved fluxes. In a couple of static spacetime benchmark scenarios, their correct implementation with a sophisticated ADER-DG scheme, presented in section 6, is demonstrated. Preliminary results on astrophysically interesting scenarios, such as the TOV star, were given.

CHAPTER

IV

Binary Neutron Star lifetimes

General-relativistic measurement of the threshold mass to prompt collapse

In this chapter, the lifetimes of the remnant produced by the merger of two neutron stars is studied. By determining a maximum mass at which a binary neutron star system collapses immediately to a black hole, constraints on neutron star masses as well as a lower limit on their radii can be given. This chapter relies partially on the coauthored publication [275]. An introduction into the problem and a review of previous work given in Section 0.4 on page 15. As a motivation, the physical content of the tested nuclear equations of state are revisited.

27 Motivation: Nuclear equation of state

In order to describe neutron stars with the coupled Einstein-Euler equations (Chapters II and III), a suitable (realistic) equation of state must be chosen which encodes all microscopic phenomenology (Section 18). The equation of state depends on thermodynamic/hydrodynamic quantities such as (rest mass) matter (baryon) density ρ , internal energy ϵ and temperature T . One of the common approximations made (in high energy physics in general) is to ignore thermal effects, assuming a “cold” EOS in the limit of $T = 0$. In fact, these EOSs can be used in the inspiral phase of binary neutron stars (where the two stars are approximatively still “cold”), but after merger, when the temperatures of the merged objects reaches values of several tens of MeV, the approximation breaks down. To counter this, it is not uncommon [69, 429] to model the post-merger dynamics by modifying zero-temperature EOS and modelling thermal effects in terms of a “thermal contribution” via an ideal-fluid EOS [387] that accounts for the shock heating [256]. This approach is not self-consistent but robust and the use of thereby defined “hybrid EOSs” has been employed extensively in the literature [43].

In contrast, “hot” equations of state try to model nuclear matter with taking temperature into account. A couple of examples shall be given which are relevant in this chapter.

The Lattimer-Swesty (LS) EOS [294] is a popular EOS in both core-collapse supernovae and binary merger simulations which models the nucleous as a finite-temperature compressible liquid droplet with Skyrme nuclear pseudo-potential [297, 299]. For heavy nuclei, the single nucleus approximation (SNA) is adopted. The number 220 in LS220 refers to the chosen nuclear incompressibility $K_0 = 220\text{MeV}$.

TM1 is the name of a popular EOS which name refers to a particular parametrization used in the employed relativistic mean field (RMF) theory, formulated in [425] who added a nonlinear σ model to describe nuclear matter with relativistic Hartree approximation. TM1 was first used in [299, 450] with a Thomas-Fermi distribution for temperature effects. Hempel and Schaffner-Bielich adopted a nuclear statistical equilibrium (NSE) model and a different RMF parametrization for the TM1 EOS, leading to the modified HS-TM1 EOS [239, 240] which is used in place of the original one in this text.

DD [449] presents another RMF model with adopts density dependent (DD) meson-nucleon coupling. DD2 has an improved experimental nucleon mass, introduced by [450]. As with TM1, there is the HS-DD2 variant [239] which is adopted in this text.

The Steiner-Fischer-Hempel (SFH) EOS [422] employs a non-linear Waldecker model (nucleon mean-field interaction via σ , ω and ρ mesons) with some covariant interactions added to the Lagrangian. The SFHo model is fitted to observations from [423].

The Banik-Hempel-Bandyopadhyay (BHB) EOS [55] uses the DD2 RMF parameter set for nucleons, the HS NSE model for light and heavy nuclei and includes strangeness (only the $\Lambda^0 = u\bar{d}s$ hyperon and the $\phi \approx s\bar{s}$ meson for hyperon-hyperon interaction, hence the name BHB- $\Lambda\Phi$) and a first-order phase transition between the baryonic phase and the quark phase, i.e., the quark-gluon plasma.

The Togashi EOS [440, 441] includes Λ and Σ hyperons and is obtained with cluster variational methods.

In fact, SFHo, TM1, DD2 and BHB- $\Lambda\Phi$ are ruled out by observations [373], while LS220 was ruled out already earlier by unitary-gas considerations/constraints of chiral perturbation theory [436], leaving Togashi alone as not-yet-ruled-out in the battery of presented EOS.

28 Methods

We have numerically solved Einsteins equations in the BSSNOK formulation (Section 12), fully coupled to the relativistic Euler equations (Section 20). We used the Einstein Toolkit [190, 308, 475] to solve these coupled partial differential equations at the same time with Method of Lines and a strong stability preserving RK3 method (Section 4.1). The same techniques were employed in a number of other works [95, 231].

We evolved spacetime with the McLachlan code [63, 64, 100, 383, 413], which employs 4th order finite differencing with artificial dissipation added. The lapse was evolved with $1 + \log$ slicing and the shift with the Gamma driver.

In contrast, we evolved matter with the WhiskyTHC code [375, 377, 378]. Here, we employed a 4th order finite volume scheme with LLF flux splitting, HLL Riemann solver [235], MP5 reconstruction operator [426] and positivity-preserving limiter [250].

The three dimensional Cartesian grid was managed by the Carpet code [220, 403, 405] which provided mesh refinement to evolve both the merger as well as the wave zone. We adopted six fixed mesh refinement levels and

EoS	ρ_0/ρ_{nuc}
BHB-LP	8.0
DD2	7.2
LS220	9.4
SFHo	9.8
TM1	6.7
Togashi	7.4

Table 27.1: Central energy density ρ_0 of the maximum nonrotating mass star, in units of the nuclear saturation density $\rho_{\text{nuc}} = 2.7 \times 10^{11} \text{ kg/m}^3$ for the EOS discussed in section 27. See table 30.1 for further properties.

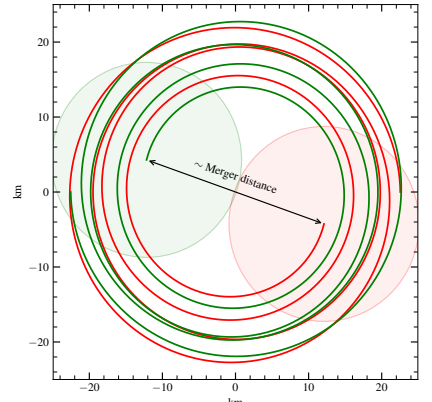


Figure 28.1: Cartoon of the distance measure for merger time determination: Orbita of a BHBAΦ $M = 1.55M_\odot$ binary in the equitorial plane. The shaded circles in the background indicate the TOV radii $R = 8.78 \text{ km}$. The distance $d = 2R$ is displayed in black. Interestingly, the orbits also exhibit large eccentricity since they overlap.

cubic cells $h = \Delta x = \Delta y = \Delta z$. The finest resolution within a given simulation is $h = 0.15M_{\odot} \sim 0.215\text{km}$ if not denoted otherwise. The outer boundary of the domain extends to at least $500M_{\odot} \sim 700\text{km}$. For the outer boundary conditions, radiative boundary conditions (Appendix A5) were used.

29 Definition of merger and collapse time

In order to do a quantitative study, a number of time measures and their determination shall be introduced. We define the survival time $T = t_c - t_m$ of a merger product as the timespan between the merger event t_m and the collapse to a black hole t_c . The individual times t_c, t_m are measured in coordinate (simulation) time, i.e., their clocks start when the initial data are evolved. Clearly, there is no unique definition of the collapse and merger, which determine t_c and t_m . In the following, a couple of different definitions are reviewed.

29.1 Definition of merger time

For the definition of the binary merger (time t_m), we examined either the gravitational wave (GW) signal, the proper separation of the binary neutron stars or a decreasing threshold value of the global minimum of the lapse function (indicating a characteristic maximum strength of the gravitational potential). We do not find the peak of the global maximum (L_{inf} integral) of the rest mass density a good measure for the merger time.

In our simulation, we derive the complex Weyl scalar Ψ_4 from the Riemann tensor (see Appendix A6 for gravitational wave extraction) on a spherical surface at a large separation (typically $300M_{\odot}$ or $500M_{\odot}$). The magnitude $|\Psi_4|^2$ can serve as a prototypic gravitational wave signal. However, one can also proceed to integrate the strain h_+ and h_- and define the merger time t_c by the maximum of the actual gravitational wave strain $h = (h_+^2 + h_-^2)^{1/2}$ [429]. While we found subtle differences between the peak of the gravitational wave strain and the magnitude of the Weyl scalar Ψ_4 , for many EOSs it is $\Delta t_c \ll M_{\odot}$.

The neutron star positions can be determined by tracking the two (Newtonian) center of masses \vec{r}_i during the evolution (Figure 28.1). The separation $d = |\vec{r}_1 - \vec{r}_2|$ can be measured in the local coordinate frame. The merger time can be defined as the first time when $d < 2R$ with R the radius of the individual TOV stars. ¹

29.2 The lapse as indicator

For the definition of the black hole formation (time t_c), we decided to use the global minimum of the dimensionless lapse α . Thanks to the singularity avoiding Bona-Masso slicing conditions [46, 117], the minimum of the lapse can serve as an indicator for the curvature of the spacetime. Furthermore, this quantity has been shown to be a very good proxy for the tracking and appearance of an apparent horizon [7]. ²

The simplest criterion which can be derived from $\min(\alpha)$ is a threshold value α_{merged} in order to define t_m as soon as $\min(\alpha) < \alpha_{\text{merged}}$ for the

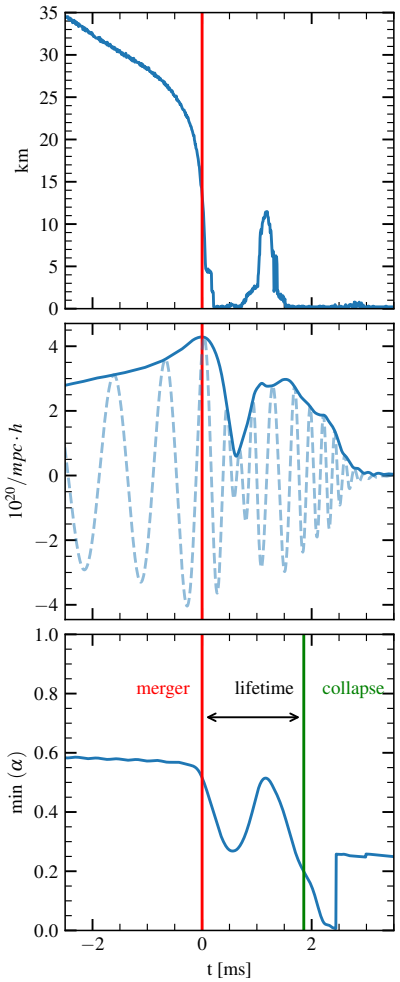


Figure 29.1: Cartoon for demonstrating the definition and extraction of the *survival time* of a merger remnant. The red line compares the merger time determination in three different ways, from top to bottom: Separation d , Gravitational wave strain (polarization h_+ dashed, envelope h solid), global lapse α minimum. The green line shows the merger time, indicated by the lapse.

This example shows an equal mass binary $M = 1.55M_{\text{TOV}}$ for the BHB- $\Lambda\Phi$ equation of state.

¹ It can be useful to introduce a dimensionless scale factor a to adopt for the tidal deformation in the late inspiral, thus defining merger time when $d = 2aR$. The value of a could be derived empirically, a typical value is $a = 0.8$.

² We also evaluated numerical apparent horizon finders [28, 404]. However, they seriously slow down the time efficiency of the code. In Cactus, it is affordable to determine field reductions every $\Delta T_r \sim 20M \lesssim 0.1\text{ms}$, whereas the horizon finder is only computed every $\Delta T_h \sim 150M \sim 0.75\text{ms}$. Therefore there is a need for the high time resolution *proxy* of the appearance of an apparent horizon.

first time. In addition, one can adopt the lapse function α for not only defining the collapse time t_c but also the merger time t_m . Following the same argument as above, the merger time t_m can be defined as soon as $\min(\alpha) < \alpha_{\text{collapsed}}$ for the first time.

The evolution of the minimum of the lapse has particular *features* which are recognisable in Figure 29.1: There is a sudden dropoff at merger time and a change in the slope around collapse time. Figure 29.2 illustrates this by showing also the first and second time derivative of $\min(\alpha)$ for a reference run. In all our simulations we observe that slightly before merger, the second derivative drops and has a minimum at GW peak. Similarly, at collapse the first derivative has a minimum. These features are not robust, but serve as a motivation for the threshold values

$$\alpha_{\text{collapsed}} = 0.35 \quad \text{and} \quad \alpha_{\text{merged}} = 0.2. \quad (29.1)$$

Considering the definition of the merger time t_m , we conclude that all presented methods (GW strain, coordinate distance, falling below a minimal lapse) are equally suited for defining the start of the merger and provide similar times within a small error in time. Within this chapter, we concentrate on using exclusively the lapse because it turned out to be most robust.

29.3 The free fall timescale

Quite generically, one expects that the lifetime T of an hypermassive neutron star (HMNS) will decrease as the mass of the system is increased. In order to allow comparable times T for different EOSs, the collapse time T is considered as a dimensionless quantity by expressing it in terms of the matter free-fall time τ_{ff} , i.e., [387]

$$\tau_{\text{ff}} = \frac{\pi}{2} \sqrt{\frac{R^3}{2M}}, \quad (29.2)$$

for an object of mass M and radius R . As only equal mass binaries are considered, M is the mass of a single star and R its radius. The smallest free-fall time will be achieved for the maximum-mass model (since $R \sim 1/M$). Therefore, the shortest free-fall timescale is set to be with $\tau_{\text{TOV}} := \tau_{\text{ff}}(M_{\text{TOV}}, R_{\text{TOV}})$. Hence, we define the threshold mass M_{th} as the one for which the merger remnant will collapse over such a timescale, i.e., $M/M_{\text{TOV}} \rightarrow M_{\text{th}}/M_{\text{TOV}}$ for $T/\tau_{\text{TOV}} \rightarrow 1$. Any survival time $T < \tau_{\text{TOV}}$ is classified as a *prompt* collapse to a black hole.

29.4 Angular momentum

Our approach is to evolve a series of BNS initial data for different system masses for a given equation of state (Figure 30.1 shows an open circle for each simulation run). We found that nearby masses might not be comparable because the individual BNS systems do a different number of orbits, resulting in a substantially different amount of angular momentum present at the merger time. In order to investigate the effect of the angular momentum, we also performed head-on collisions with no angular momentum (only linear momentum, i.e. a boost of $v = 0.1c$). In such a case, we observed all systems to collapse promptly at any given mass. We conclude that angular

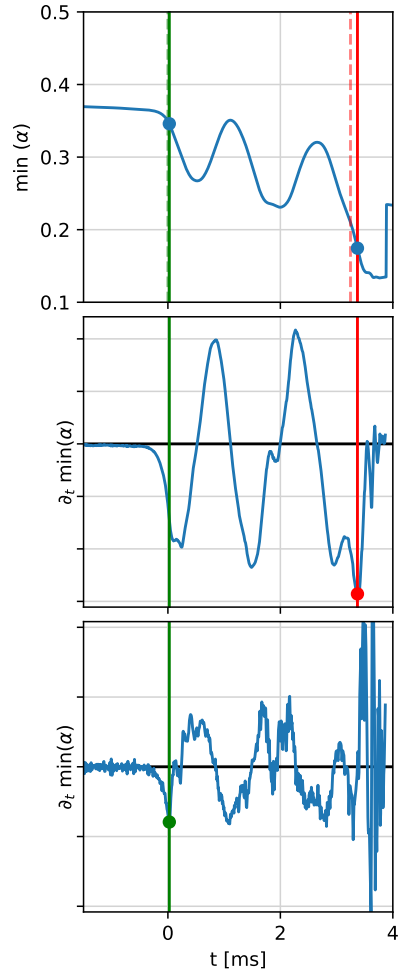


Figure 29.2: Time evolution in a reference binary system around merger time. The three panels show the lapse minimum $\min(\alpha)$, its first and second time derivative. The time is measured since merger (defined by GW peak), i.e., $t_m = 0$ in these units. The green line indicates merger by $\partial_t^3 \min \alpha = 0$. The red line indicates collapse by $\partial_t^2 \min \alpha = 0$ at $t \sim 3.5\text{ms}$.

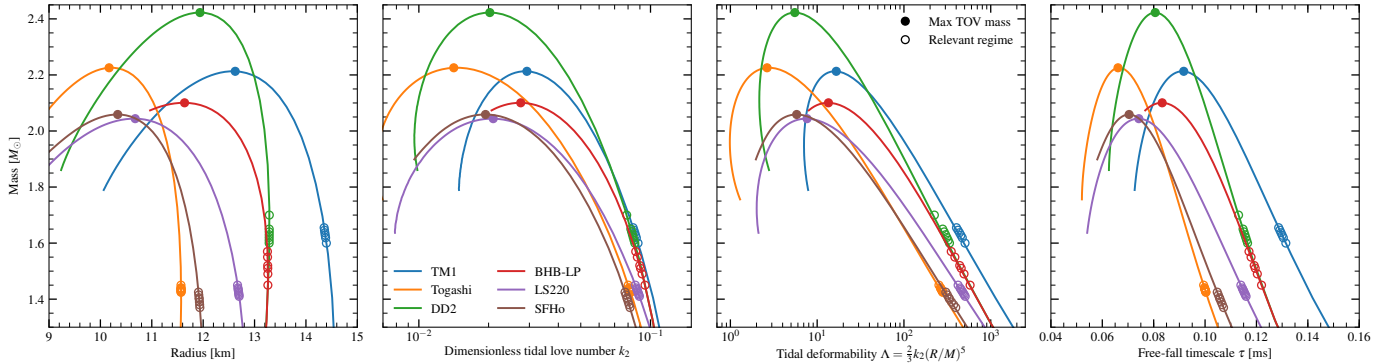


Figure 30.1: Properties of TOV sequences: Radius R , dimensionless tidal love number k_2 , tidal deformability Λ and free fall timescale τ as functions of the star mass M . The maximum masses M_{TOV} and their relevant quantities R_{TOV} , κ_{TOV} , Λ_{TOV} and τ_{TOV} are displayed with filled circles. Open circles refer to models used as initial data. First panel published in [275].

momentum is (1.) crucial to yield a finite survival time $T > 0$ and thus initial data in quasi-circular orbits are required and (2.) the final angular momentum has to be comparable between different binary masses in order to have a well-defined collapse time.

30 Initial data and EOS

We model the neutron stars with realistic tabulated hot equations of states which are freely available at [stellarCollapse.org](#). We compute equilibrium solutions of the Tolman-Oppenheimer-Volkoff equations (TOV) with the `PizzaTOV` code [263] and its successor `MargheritaTOV` [335]. If not mentioned otherwise, initial data for the time evolution (ie. binary neutron star initial data) are computed under the assumption of irrotational quasi-circular equilibrium with Lorene [92, 151, 221]. The initial separation is 45km, so that the binaries perform around five orbits before the merger. We note that since the threshold mass for equal-mass binaries is always larger than for unequal-mass binaries, i.e., $M_{\text{th}}(q=1) > M_{\text{th}}(q < 1)$, the use of equal-mass binaries is not a restriction but optimises the search for M_{th} [70].

30.1 Nuclear equations of state taken into account

Since the overall goal is that of determining as accurately as possible the threshold mass to prompt gravitational collapse, it is essential that the description of the thermal effects in the matter is as realistic and self-consistent as possible. In turn, this forces us to consider EOSs that have a physically consistent dependence on temperature (Section 27). Unfortunately, the number of EOSs that can be employed for this scope and that do not violate some basic nuclear-physics requirement (as it is the case for the widely employed LS220 EOS [299, 436]), is much more restricted.

Table 30.1: Various TOV properties of the equations of states taken into account. These are the maximum mass of a nonrotating star M_{TOV} , its radius R_{TOV} , its compactness $C_{\text{TOV}} = M_{\text{TOV}}/R_{\text{TOV}}$, its tidal Love number $\kappa_{2,\text{TOV}}$, its derived tidal deformability Λ_{TOV} , and its free-fall timescale τ_{TOV} . Furthermore, the literature which introduces the particular EOS is given for completeness in the last column. See also Table 27.1 for the central density ρ_c of the maximum nonrotating mass configuration.

EoS	$M_{\text{TOV}}[M_{\odot}]$	$R_{\text{TOV}}[\text{km}]$	C_{TOV}	$M_{b,\text{TOV}}[M_{\odot}]$	$\kappa_{2,\text{TOV}}$	Λ_{TOV}	$\tau_{\text{TOV}}[\mu\text{s}]$	Literature
BHB- $\Lambda\Phi$	2.10	11.64	0.26	2.74	0.020	13.50	83.31	[55]
DD2	2.42	11.94	0.30	3.28	0.020	5.52	80.60	[79, 240]
LS220	2.04	10.68	0.29	2.79	0.014	7.65	74.22	[294]
SFHo	2.06	10.34	0.29	2.79	0.019	5.81	70.44	[408]
TM1	2.22	12.60	0.26	2.86	0.029	16.60	91.70	[299, 450]
Togashi	2.23	10.17	0.32	3.13	0.014	2.65	66.12	[440, 441]

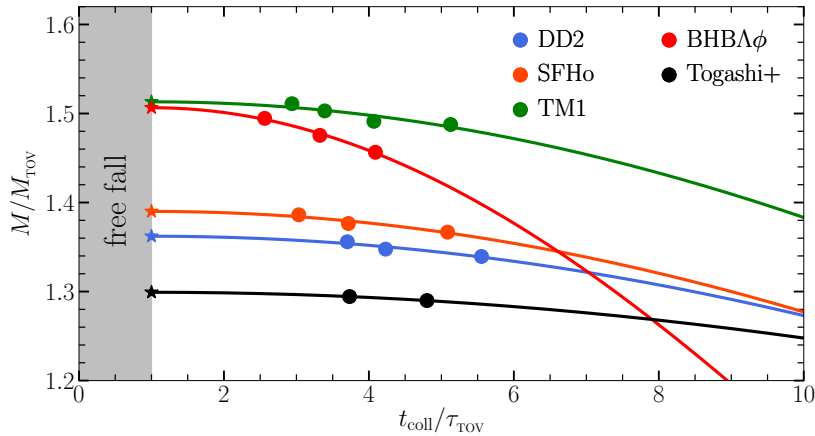


Figure 31.1: The scatter plot of measured survival (collapse) times T , here denoted as $t_{\text{coll}} \equiv T$ for the different EOS (circles). The solid line represents a Gaussian fit. Stars represent the extrapolated threshold mass M_{th} , predicted by the fit. All survival times $t_{\text{coll}} < \tau_{\text{TOV}}$ are considered as prompt collapse. Figure published in [275].

Notwithstanding this limitation, we have employed here all of the (five) “hot” EOSs that have been proposed recently and whose properties are reported in Table 30.1 when expressed in terms of the masses and radii of the maximum-mass of the nonrotating configuration (hereafter indicated as TOV). Similarly, Fig. 30.1, provides a graphical representation of the masses and radii of the corresponding TOV equilibrium solutions, both stable (solid lines) and unstable (dashed lines). The solid circles mark the maximum-mass solutions, while the open circles refer to models used as initial data (see below).

We recognize the maxima of each TOV properties to serve as characteristic values for the particular equation of state. These values can be used to normalize all properties of any matter distribution described with the equation of state ³. Especially for the free-fall timescale τ , which serves for normalization in the next sections, there is a large discrepancy between τ_{TOV} and the numbers in the relevant regime, which is up to a factor two. However, we performed the whole analysis with both a dynamical $\tau(M)$ as well as a fixed $\tau(M_{\text{TOV}})$ and find only a minimal difference $\Delta T \ll M_{\odot}$.

31 Results on the threshold mass

In order to calculate the threshold mass of a given EOS, over 200 simulations were run for system masses with a short, but finite, collapse time. From these runs, only 15 suitable runs were selected for the analysis which had survival times $T < 1.0\text{ms}$.

Figure 31.1 reports the survival times T normalised to the free-fall timescale of the maximum mass models τ_{TOV} for the individual EOS. These times then are shown as a function of the initial mass M of the binary system normalized to the EOS maximum mass. The adoption of such set of dimensionless quantities has the goal of revealing a universal behaviour in the threshold mass, if one is present [98, 457, 464].

The coordinates of filled circles of different colors in Fig. 31.1 are given by the system masses (initial data) and their read-off lifetime (after evolution). For the Tagoshi+ EOS we only report two values and that these differ by only 3.7% in mass (i.e., $M = 1.440 M_{\odot}$ and $M = 1.435 M_{\odot}$);

³ The TOV approximation can be further motivated by the fact that the irrotational stars within the binary share universal properties with their TOV counterparts. That is, the authors of [98] have shown that the maximum mass of a rotating neutron star can brought into a simple relationship to the non-rotating solution, $M_{\text{max,rot}} \approx 1.203M_{\text{TOV}}$, and therefore it is sufficient to discuss non-rotating stars only in this section.

any other binary with a slightly smaller mass (e.g., $M = 1.430 M_{\odot}$) leads to a hypermassive neutron star that is effectively stable over the timescales investigated here (i.e., up to $1-10\tau_{\text{TOV}}$). Finally, since t_{coll} should diverge for vanishingly small values of M , we fit the numerical data with a simple exponentially decaying function of the type

$$M/M_{\text{TOV}} = \tilde{a} \exp[-\tilde{b}(t_{\text{coll}}/\tau_{\text{TOV}})^2]. \quad (31.1)$$

The behaviour reported in Fig. 31.1 reveals that a universal behaviour is present only very approximately and that the threshold mass, averaged over all EOSs, is roughly given by

$$\frac{M_{\text{th}}}{M_{\text{TOV}}} \approx 1.415, \quad (31.2)$$

with a statistical error of $\Delta M_{\text{th}} = 0.05 M_{\odot}$, i.e., with a variance of about 4% (see Table 31.1 for the individual values). When comparing with a linear approximation, as it was done in [68],

$$M/M_{\text{TOV}} = \tilde{a} + \tilde{b}(t_{\text{coll}}/\tau_{\text{TOV}}), \quad (31.3)$$

we find it yields a systematic overestimate of the threshold mass (Figure 31.2). When considering which of the functional behaviours, (31.1) vs. (31.3), fits the data best, the statistics do not provide a distinction criterion due to the small number of points.⁴ More importantly, we believe it is not reasonable to expect that near the free-fall limit the behaviour should be a linear one. Such a limit, in fact, should be thought as a regime where only infinitesimal changes in the mass should lead to a prompt collapse, exactly because the merged object is very close to a stability limit. Such a behaviour, which is seen frequently in critical-collapse calculations (see e.g., [228] for a review), necessarily requires that the function M/M_{TOV} should have vanishing derivative in the limit $t_{\text{coll}}/\tau_{\text{TOV}} \rightarrow 1$. Clearly, the nonlinear fitting (31.1) reflects this behaviour while a linear one (31.3) does not.

Predicting the threshold mass from the TOV compactness

The existence of a relation between the threshold mass and the corresponding maximum mass has been suggested initially by [68], who, by employing

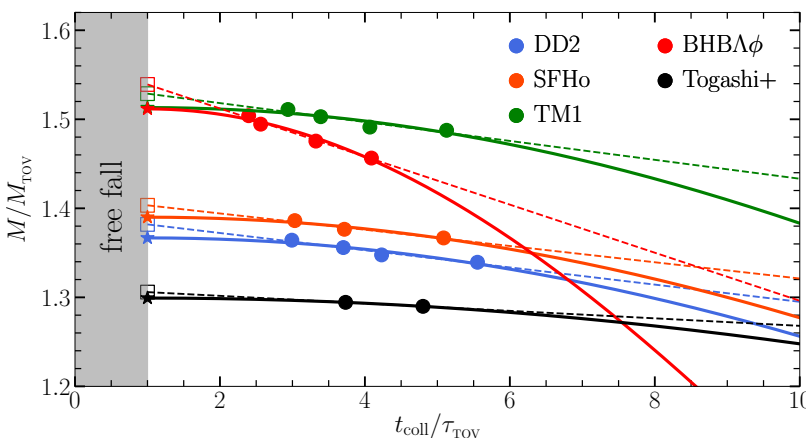


Table 31.1: Results for the threshold mass, including uncertainties. The masses are given in units of M_{TOV} . Errors are discussed in Section 33.

⁴ The reduced χ^2 are 0.0055 for the linear fit and slightly better, 0.0089, for the nonlinear fit.

Figure 31.2: Same as Fig. 31.1, but also showing the linear extrapolation to the critical mass as a dashed line, as done in [68]. In all cases, the extrapolation values for the critical mass (shown as open squares) are systematically larger than in the exponential model (see main text).

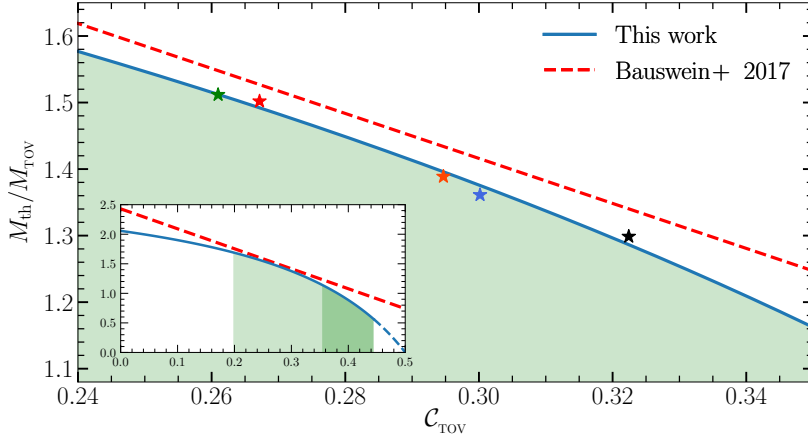


Figure 31.3: Universal relations for the threshold mass with the stars matching the ones in figure 31.1. The solid blue line is the non-linear fit 31.8 while the red dashed line is the linear fit 31.4 from [68]. The green shaded area displays the compactness expected for neutron stars (see main text). The inset shows a bird's eye view on the possible whole range of compactness, i.e., $C_{\text{TOV}} \in [0, 1/2]$. Figure published in [275].

a smooth-particle approximation for the hydrodynamics and a conformally flat approximation to general relativity, conclude the linear relationship

$$M_{\text{th}}/M_{\text{TOV}} = \hat{a} C_{\text{TOV}} + \hat{b} \quad (31.4)$$

with $C_{\text{TOV}} := M_{\text{TOV}}/R_{\text{TOV}}$ the maximum compactness. The universal ansatz proposed by [68] is that $M_{\text{th}}/M_{\text{TOV}}$ is independent of the EOS, with

$$\hat{a} = 3.38, \hat{b} = 2.43. \quad (31.5)$$

Such a linear ansatz does represent a reasonable first approximation to the data. However, it clearly overestimates the threshold mass in the limit $C_{\text{TOV}} \rightarrow 0$, as we would assume

$$M_{\text{th}}/M_{\text{TOV}} \rightarrow 2 \quad \text{for} \quad C_{\text{TOV}} \rightarrow 0. \quad (31.6)$$

This limit physically represents an infinitely extended self-gravitating object.⁵ We do *not* impose this limit on the fitting function. However, it is interesting (and revealing) that the data and the fitting function naturally provides this limit (31.6): For $C_{\text{TOV}} \rightarrow 0$ the merged system would need to be nonrotating and hence with a threshold mass that is exactly twice the TOV mass.

Furthermore, and more importantly, the linear relationship (31.4) does not provide the expected black hole limit, which predicts that

$$M_{\text{th}}/M_{\text{TOV}} \rightarrow 0 \quad \text{for} \quad C_{\text{TOV}} \rightarrow 1/2. \quad (31.7)$$

This constraint requires some clarification. For neutron stars, the threshold mass M_{th} must be larger than the TOV mass M_{TOV} , as the latter is the limit for stability to collapse. However, neutron stars make only a part of Figure 31.3, shaded in light green, i.e., the most likely range of possible values of C_{TOV} for stable neutron stars, with the lower limit $C_{\text{TOV}} \gtrsim 0.2$ being deduced from a large statistical sample of possible EOSs [336], while the upper limit $C_{\text{TOV}} \lesssim 0.35$ is set by the limit on causality [281, 298]. It is useful to consider the Buchdahl theorem [387], which states that any self-gravitating object whose compactness is larger than $C_B = 4/9$ cannot be in equilibrium and must collapse to a black hole. The theorem, which

⁵ Loosely speaking, the limit $C_{\text{TOV}} \rightarrow 0$ is also a classical one, as one moves from relativistic self-gravitating configurations over to Newtonian ones.

is valid for any EOS, does not specify what is the mass of the object nor what is the corresponding TOV mass. All that is required to produce a collapse for such ultra-compact configurations is to reach such a compactness. Hence, it is possible to construct a self-gravitating object with finite mass whose compactness is only infinitesimally smaller than \mathcal{C}_B and then add the (infinitesimal) amount of mass that would lead the compactness to exceed \mathcal{C}_B . This object would collapse promptly even if its mass is not large at all. Taking this line of argument to the limit, the threshold mass will have to go to zero when a black hole is already formed, i.e., for $\mathcal{C} \rightarrow 1/2$. The (extended) regime of extremely compact objects (ECOs) is shaded in dark green in Figure 31.3.

Hence, we correct the linear approximation via a *nonlinear* fit of the type

$$\frac{M_{\text{th}}}{M_{\text{TOV}}} = a - \frac{b}{1 - c \mathcal{C}_{\text{TOV}}}, \quad (31.8)$$

where a, b, c are to be determined from the data. However, imposing the fulfilment of the black hole constraint limit (31.7) removes one free parameter and sets $a = 2b/(2 - c)$.

Figure 31.3 reports in blue the fit of Eq. (31.8) with

$$b = 1.01, \quad c = 1.34, \quad (31.9)$$

against the numerical-relativity data shown with stars of the same colors as in Fig. 31.1. ⁶ Also shown with a red-dashed line is the linear approximation of [70], which clearly suggests larger threshold masses. We believe this result is a consequence of our fully general-relativistic approach, which properly accounts for the strong-curvature highly dynamical behaviour that characterizes the threshold to black hole collapse and that are probably underestimated in the conformally flat approximation of [68]. At the same time, the difference with the linear approximation of [70] is small (8% at most for the EOS considered here).

32 Constraining Neutron Star radii

The nonlinear expression (31.8) can be used to provide more stringent (larger) lower limits on the radii of possible stellar models in the light of the recent detection of the event GW170817 [437]. In particular, following [70], our threshold mass model (31.8) can be used to constrain neutron star radii. To do so, we write (31.8) formally as

$$M_{\text{th}}(M, R) = \left(a - b \left[1 - c \left(\frac{M}{R} \right) \right]^{-1} \right) M \quad (32.1)$$

and then plot $M_{\text{th}}(M)$ for different R in Figure 32.1 (black lines). Also reported in Fig. 32.1 with a gray-shaded area is the limit set by causality and that requires $M_{\text{TOV}}/R_{\text{TOV}} \lesssim 0.354$ [281, 298].

As noted by [70], given a measurement of a binary neutron-star merger with a given total mass M_{tot} , and assuming that the merger product has collapsed to a black hole, it is possible to set a lower limit on M_{th} and, in turn, a lower limit (although not very stringent) on R_{TOV} . This is shown graphically in the left panel Fig. 32.1, where we report with a horizontal blue-dashed line and the total gravitational mass estimated for GW170817 [437],

⁶ See Table 31.1 for errors in the fit. We also made a linear fit (31.4) to our data (not shown). Considering the quality of the fit with the χ^2 test, e.g., for DD2 we find for the linear fit a $\chi^2 = 1.4 \times 10^{-5}$ while the nonlinear fit has $\chi^2 = 1.1 \times 10^{-5}$. Given the small number of data points (as in Section 31), the χ^2 for the nonlinear fit is slightly better, but the statistics do not provide a sufficient distinction criterion (in contrast to the proposed physical arguments). Naturally, the linear model of Bauswein can be understood as the first term in a series expansion the nonlinear model (31.8). It is also qualitatively obvious from Figure 31.3 that the linear result of [70] is a tangent to our curve.

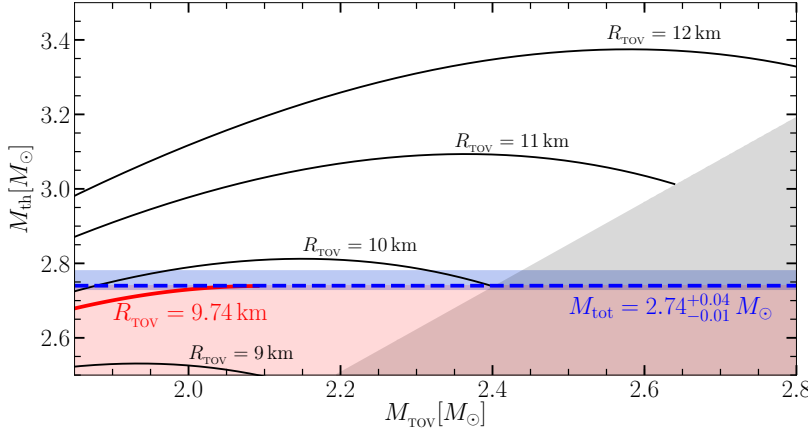


Figure 32.1: The lower bound on R_{TOV} (red) using the universal relation Eq. (31.8). The horizontal dashed blue line represents the observed mass of GW170817. The red shaded area shows the values excluded by the detection. The grey shaded area represents values excluded by the causality constraint. Figure published in [275].

$$M_{\text{tot}} = 2.74^{+0.04}_{-0.01} M_{\odot}. \quad (32.2)$$

The corresponding uncertainty band (blue-shaded area) gives a lower constraint on M_{th} , since GW170817 did not lead to a prompt collapse.

The blue band thus cuts (“constrains”) the red shaded area from below. Especially it gives us an estimate of a neutron star *minimal* radius, $R_{\text{TOV}} \geq 9.74^{+0.14}_{-0.04}$ km (red solid line); this is to be contrasted with the value deduced by [70], i.e., $R_{\text{TOV}} \geq 9.26^{+0.17}_{-0.03}$ km, on the basis of their linear approximation. Interestingly, in order to obtain a similar stringent constraint derived here, the authors of [70] require a hypothetical detection of a binary with a comparatively larger mass $M_{\text{tot}} \simeq 2.9 M_{\odot}$.

All of the procedure followed so far to derive the nonlinear fit (31.8) for \mathcal{C}_{TOV} can be repeated for the compactness of a fixed mass M_x , i.e., $\mathcal{C}_x := M_x/R_x$, thus allowing us to set constraints not only on R_{TOV} , but on any radius R_x within a reasonable range. The result of this series of fits is shown in Fig. 32.2, where the values of M_x and R_x are indicated with a blue crosses. Also reported in black is the quadratic fit

$$R_x = -0.88 M^2 + 2.66 M + 8.91. \quad (32.3)$$

The importance of (32.3) is that it now offers a very simple and handy

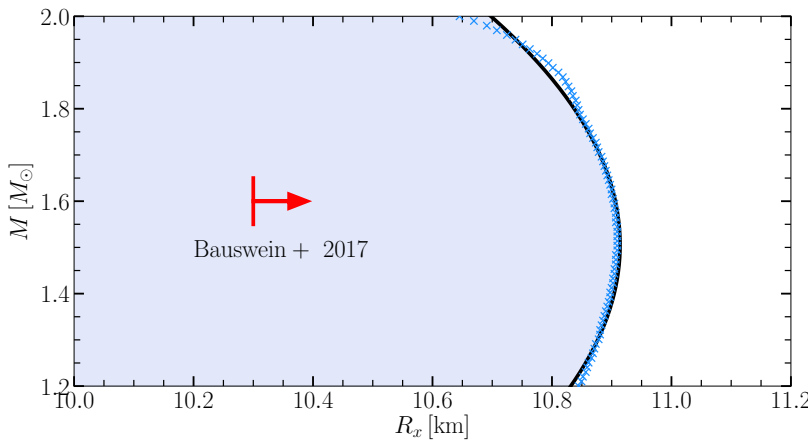
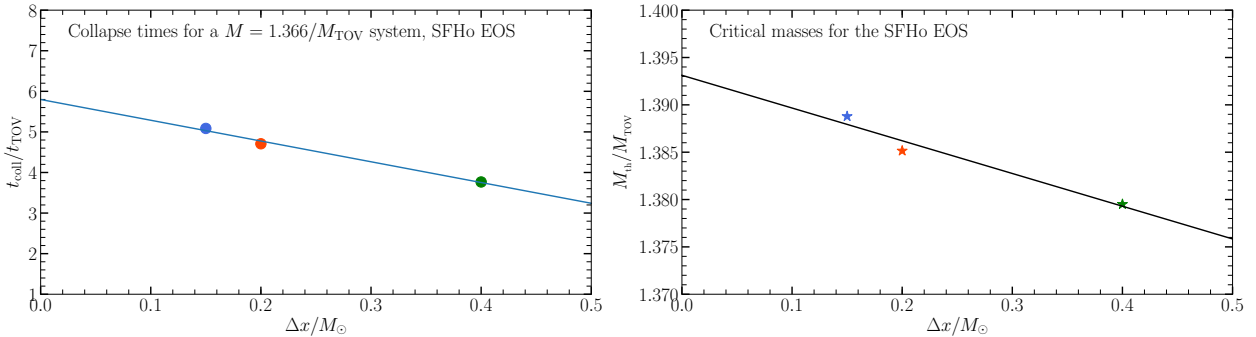


Figure 32.2: Universal relation (black) for the lower limit on R_x for a given mass M (blue crosses); the red arrow is the constraint from [70] for a $1.6 M_{\odot}$ star. Figure published in [275].



expression for the lower limit of stellar models as deduced from GW170817. A similar procedure has been followed also by [70], but only for a fixed mass of $1.6 M_{\odot}$, and it was deduced that $R_{1.6} \geq 10.30$ km; this result should be contrasted with the the value derived from (32.3), which is instead $R_{1.6} \geq 10.90$ km. Similarly, for a reference star of $1.4 M_{\odot}$ we obtain $R_{1.4} \geq 10.92$ km, which is close to the estimate by [70] for $1.6 M_{\odot}$ ⁷. Our $R_{1.4}$ estimate is in good agreement with those made by [336], who have expoited a statistical exploration of possible EOSs and building a set of one billion stellar models, i.e., $12.00 < R_{1.4}/\text{km} < 13.45$.

33 Convergence and error budget

For a typical equation of state (SFHo), we made a convergence study with different resolutions of $\Delta x=215, 287$ and 573m ($\Delta x/M_{\odot} = 0.15, 0.20, 0.40$). Figure 33.1 shows the variation of the collapse time and threshold mass as a function of resolution. The linear continuum extrapolation clearly shows the first order convergence of the results.

Concerning the error budget, systematic errors are introduced by the time resolution of the repeated output of field integrals and derived quantities. For instance, for efficiency we determine field reductions only every 128 timesteps ($\Delta T \sim 20M \lesssim 0.1\text{ms}$). This read-off error goes into the threshold mass determination. However, since a two-parametric function is fitted to two to three data points (Fig. 31.1), there is virtually no statistical read-off error of the threshold mass (as demonstrated by Table 31.1). These negligible errors are at the order of $\Delta M_{\text{th}} \sim 0.05M_{\odot}$, i.e., at the order of 1%. These errors go into the universal relations plot (Fig. 31.3) where again a two-parametric function is fitted to five data points, resulting again in an inconclusive error budget of $\sim 1\%$. The 5% deviation from [70] is obviously a systematic consequence of the overall technique and not part of statistical errors. Therefore, the radius constraining plot (Fig. 32.1) has no significant errors coming from the model (31.8) and the error given on the radius constraint is dominated by the observational error from GW170817.

34 Summary

In Chapter IV, a large number of general relativistic simulations of binary neutron star mergers has been carried out in order to investigate the open

Figure 33.1: Convergence plots on the collapse times and the determined critical masses for an exemplaric system and equation of state. The colors of the dots represent the different resolutions.

⁷ In [70], an estimate is only provided for $R_{1.6}$.

question about the mass leading to a prompt collapse; which again is informative on the material neutron stars could be made of (i.e., the nuclear equation of state). Using a fully general-relativistic approach and a novel method for the determination of the threshold mass, we have carried out simulations making use of all of the realistic EOSs available to describe this process. In this way, we have found a nonlinear universal relation for the threshold mass as a function of the maximum compactness and which is potentially valid for all compactnesses. At least for the temperature-dependent EOSs considered here, this universal relation improves the linear relation found recently with methods that are less accurate, but that also yield quantitatively similar results. Furthermore, exploiting the detection of GW170817, we have used the universal relation to set lower limits on the stellar radii for any any mass.

CHAPTER

V

Models for Quantum Black Holes

Generalized Uncertainty Principle and Black Holes in Higher Dimensional Self Complete Gravity

This chapter summarizes efforts in modeling black hole solutions in a first order quantum gravity theory. This phenomenological model is obtained by adding momentum-dependent terms to Heisenbergs uncertainty principle, resulting in a certain $f(R)$ gravity modification which is subsequently studied in its geometric and thermodynamics properties. For an introduction into the problem and a review of previous work, see Section 0.2 on page 13. As a motivation, this chapter starts with higher dimensional spacetime. This chapter is based on parts of [290] as well as the upcoming publication [276].

35 Motivation: Higher dimensional Black Hole spacetimes

Higher dimensional black hole solutions play an important role in theoretical research for an array of reasons. On the more formal side, they are a key element of proposals aiming to a unified description of fundamental interactions, e.g., Superstring theory and related paradigms, like the gauge/gravity duality. On the more phenomenological side, microscopic higher dimensional black holes would be the “smoking gun” for the terascale quantum gravity [56, 156, 216] and a viable resolution of the hierarchy problem [32, 33, 35, 36, 380, 381].

The common ideas of higher dimensional gravity can be motivated by a number of concepts. For instance, gravitational radiation can penetrate the n -dimensional bulk space, while standard model forces are restricted to the 3-dimensional bulk (Figure 35.1). On the other hand, micro black holes are supposed to be so small that the geometry of the extra dimensions plays no role. This concept is depicted with a toroidal extra dimension in Figure 35.2, where the black hole event horizon r_H is much smaller than the compact torus radius R_C . For reviews about microscopic black holes in particle physics, see [82, 83, 116, 127, 131, 247, 260, 261, 296, 344, 360, 463].

In this work, we consider hyper-spherical black hole spacetimes, that is, Schwarzschild-Tangherlini spacetimes [191, 431]

$$ds^2 = -(1 - f(r)) dt^2 + (1 - f(r))^{-1} dr^2 + r^2 d\Omega_{n-1}^2, \quad (35.1)$$

with the $(n - 1)$ -dimensional hyper-spherical surface element $d\Omega_{n-1}^2$ and a gravitational function, which is $f(r) = 2G_N M/r$ in the classical case. These theories can fit in both the large extradimension scenario, i.e., the 1998 pioneered ADD model (Arkani-Hamed, Dimopoulos, Dvali [32, 35, 36]), and in the universal extradimension scenario [33], i.e., an extension

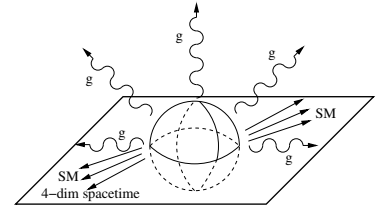


Figure 35.1: Cartoon of the 4-dimensional spacetime (brane), where standard model (SM) particles are allowed to propagate on, while gravitational degrees of freedom (i.e., gravitons, g) can propagate in the extra dimensions. The ball shall indicate the extension of the hyper-spherical black hole. Modified from [132].

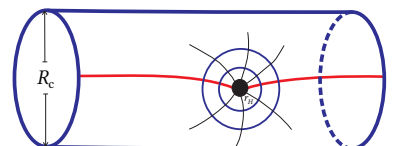


Figure 35.2: Embedding of a black hole with $r_H \ll R_c$, where R_c is the compactification radius of an extra dimension. In such a case, the black hole does not notice the extra dimensional periodic boundary geometry. Colorized from [247].

to the 1921 developed Kaluza Klein theory [219, 356] which proposes only one space-like extradimension.

For sake of simplicity, however, we assume as a new fundamental scale $M_* = M_{\text{Pl}}^{2/(n+2)} C_n V_n$ according to the large extradimension model only, where M_{Pl} is the 4-dimensional Planck mass scale and V_n is the volume of the n extra dimensions. For a toroidal compactification (Figure 35.2) with an extent R_c , the volume is $V_n = (2\pi R_c)^n$ and $C_n = \mathcal{O}(1)$ a dimensionless prefactor. Unless differently specified, all quantities are expressed in units of the fundamental Planck mass M_* , or of the fundamental length $L_* = 1/M_*$. According to this notation, the effective gravitational coupling constant reads $G_* = 1/M_*^2$.

36 A brief introduction into the Generalized Uncertainty principle

Mathematically, the Generalized Uncertainty Principle (motivated in Section 0.2) can be casted as commutator relation

$$[x^i, p_j] = i \hbar \delta_j^i (1 + f(\vec{p}^2)) \quad (36.1)$$

where the function f is customarily assumed as $f(\vec{p}^2) \simeq \beta \vec{p}^2 + \dots$ at first order. From (36.1), one obtains that spatial resolution better than $\sqrt{\beta}$ is no longer possible, since the uncertainty relations reads

$$\Delta x \Delta p \geq \frac{\hbar}{2} (1 + \beta(\Delta p)^2). \quad (36.2)$$

In order to study nonlocal gravity, one can formally shift the nonlocalities from the energy momentum tensor to the Einstein tensor, i.e., consider a nonlocal version of Einsteins equations [60, 284, 331, 443]

$$G_N^{-1} (L^2 \square) G_{\mu\nu} = 8\pi T_{\mu\nu} \quad (36.3)$$

where the Newton's constant becomes a differential operator, \square is the covariant d'Alembertian and L is a length scale. Eq. (36.3) can be either used to described large scale degravitating effects [34, 61, 62, 184] or short scale modified gravity theories [115, 204, 210, 332, 342]. One can select a specific profile of $G_N^{-1} (L^2 \square)$ to reproduce the GUP momentum space deformation

$$d^3 \vec{p} \rightarrow \frac{d^3 \vec{p}}{1 + \beta p^2} \quad (36.4)$$

for the static potential due to virtual particle exchange by setting $L = \sqrt{\beta}$. The resulting non-rotating black hole metric (reviewed in the next Section) allows for horizon extremisation with consequent formation of a zero temperature black hole remnant at the end of the evaporation [254]. Such a black hole solution not only supersedes the aforementioned limitations of the scenario proposed in [4, 5], but offers additional interesting properties: it removes the scale ambiguity of the Schwarzschild metric and fulfills the *gravity ultraviolet self completeness* by preventing black hole radii smaller than the Planck length (Figure 36.1); it allows for a semiclassical description of the whole evaporation process for the presence of the SCRAM phase ¹ before the remnant formation. If the theory of study has a free parameter, it can be tuned in a way that the minimal length black hole mass M_0

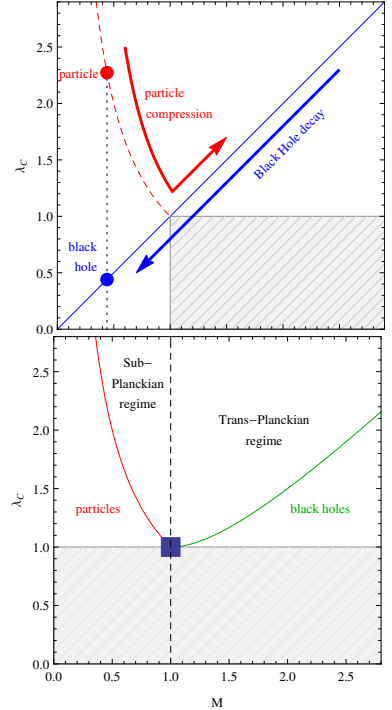
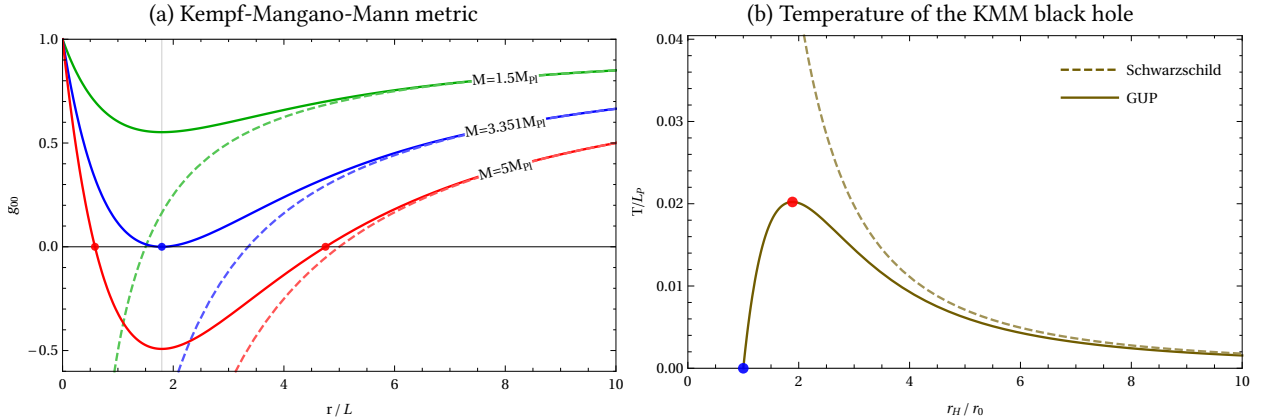


Figure 36.1: Size vs. Energy relation in Planck units. Upper panel: Particle size (Compton wavelength $\lambda_C \sim M^{-1}$) in red, vs. black hole size (Schwarzschild radius $r \sim M$). The shaded area is inaccessible in the particle acceleration/compression process. At the sub-Planckian ($M < 1 M_P$) regime, a length scale ambiguity arises. The lower panel shows the solution proposed by the self-complete gravity paradigm. (Figure published in [204]).

¹ The black hole SCRAM is a cooling down phase during the final stages of the evaporation. The term SCRAM has been introduced in [343] by borrowing it from nuclear reactor technology. SCRAM is a backronym for "Safety control rod axe man", introduced by Enrico Fermi in 1942 during the Manhattan Project at Chicago Pile-1. It still indicates an emergency shutdown of a nuclear reactor.



coincides with the fundamental mass of general relativity M_* (self completeness). For certain theories, also the size of the minimal length black hole r_0 can be identified as the fundamental length scale L_* [204].

37 Review of GUP Black Holes in the Kempf-Mangano-Mann momentum measure

To begin with, we review the calculation of the GUP modified Schwarzschild solution [254] in $(3+1)$ dimensions. We chose a specific profile of the operator $\mathbb{G}^{-1}(L^2\Box)$ such that effectively the momentum measure is modified as in the model by Kempf Mangano Mann (KMM) [266].

37.1 3+1 Dimensional GUP inspired Black Holes

Equation (36.3) can be cast in the form

$$R_{\mu\nu} - \frac{1}{2}g_{\mu\nu}R = 8\pi\mathbb{G}(L^2\Box)T_{\mu\nu}, \quad (37.1)$$

that is equivalent to coupling Einstein gravity to a non-standard energy momentum tensor. In case of a static, spherically symmetric spacetime, one has

$$T_0^0 = -M\delta^{(3)}(\vec{x}), \quad (37.2)$$

corresponding to a vanishing mass distribution, apart from the origin where a curvature singularity is present [47, 48, 152]. The action of the operator $\mathbb{G}(L^2\Box)$ determines a smearing of the source term that reads

$$\mathbb{T}_0^0(\vec{x}) \equiv \frac{1}{G_N}\mathbb{G}(L^2\Box)T_0^0 = -\rho(\vec{x}). \quad (37.3)$$

Since the Dirac delta distribution $\delta^{(3)}(\vec{x})$ can be represented as the Fourier transform of the plane wave,

$$\delta^{(3)}(\vec{x}) = \frac{1}{(2\pi)^3} \int d^3\vec{p} e^{i\vec{x}\cdot\vec{p}}. \quad (37.4)$$

one can apply the Kempf momentum space measure (36.4) in order to “smear out” the matter distribution,

$$\rho_\beta(\vec{x}) = \frac{M}{(2\pi)^3} \int \frac{d^3\vec{p}}{1+\beta p^2} e^{i\vec{x}\cdot\vec{p}} = M \frac{e^{-\frac{x}{\sqrt{\beta}}}}{4\pi x \beta}, \quad (37.5)$$

Figure 37.1: (a) The Kempf GUP metric (37.7) component $g_{00}(r)$ shown for different black hole masses. For comparison, the dashed line show the corresponding curves for the unmodified Schwarzschild metric, i.e., $\mathcal{M}(r) = 1$ in Eq. (37.7). For heavy masses, there are two horizons (blue line, locations marked at $g_{00} = 0$), for a critical mass these horizons merge to a single one (red line). For a subcritical mass, there is no horizon (red line). Since there is still a divergent Ricci scalar, this is a naked singularity. (b) Temperature of the GUP black hole in $n = 3$ spatial dimensions as a function of the outer horizon radius r_+ . For comparison, the Hawking temperature of a traditional Schwarzschild black hole displayed. The blue and red dots mark the cold and hot remnants, respectively.

with an energy scale $\beta^{-1/2}$ (or length scale $\sqrt{\beta}$, respectively). The nonlocal operator

$$\mathbb{G}(L^2 \square) = \frac{G_N}{1 - L^2 \square} \quad (37.6)$$

is chosen to mimic GUP effects (the modified momentum measure) and is equivalent to the usual Einstein's equations with ρ_β as source.

From (37.6) it can be seen that in the low energy regime $-\square \ll L^{-2}$, (37.1) match Einstein equations and $\mathbb{G}(L^2 \square) \rightarrow G_N$. Conversely for $-\square \sim L^{-2}$, strong non-local corrections enter the game, gravity becomes increasingly weaker ($\mathbb{G}(L^2 \square) \ll G_N$), and the source can no longer be compressed as in (37.2). We note that the profile in (37.6) modifies the momentum measure in the same way as in (36.4), namely the KMM model [266].

Solving Einstein's Field Equations with this source *à la* Schwarzschild gives the four dimensional line element

$$ds^2 = - \left(1 - \frac{2G_N \mathcal{M}(r)}{r} \right) dt^2 + \left(1 - \frac{2G_N \mathcal{M}(r)}{r} \right)^{-1} dr^2 + r^2 d\Omega^2, \quad (37.7)$$

i.e., the generic static, spherically symmetric metric with

$$\mathcal{M}(r) = \int_{B_r} d^3 \vec{x} \rho(\vec{x}) \quad (37.8)$$

representing the cumulative mass distribution, i.e., the matter contained within a 3-ball B_r of radius r . Given (37.7), the conservation of the energy momentum tensor implies its form, namely $\mathbb{T}_\mu^\nu = \text{diag}(-\rho, p_r, p_\perp, p_\perp)$ with radial pressure $p_r = -\rho$ and perpendicular pressure $p_\perp = -\rho - \frac{1}{2}r(d\rho/dr)$. By assuming $\rho(\vec{x})$ given in (37.5), one finds ²

$$\mathcal{M}(r) = M \gamma \left(2; \frac{r}{\sqrt{\beta}} \right) = M \left[1 - e^{-\frac{r}{\sqrt{\beta}}} - \frac{r}{\sqrt{\beta}} e^{-\frac{r}{\sqrt{\beta}}} \right]. \quad (37.9)$$

The behaviour of the metric (in comparison to the same mass Schwarzschild metric) can best be seen when plotting the metric coefficient $g_{00}(r)$ as in Figure 37.1. The horizon structure resembles that of the (mass dominated) Reissner-Norström solution: there exist an outer event horizon r_+ and an inner Cauchy horizon r_- . The two eventually merge at the critical mass parameter $M = M_0 = 1.68\sqrt{\beta}/G_N$, corresponding to an extremal configuration. The curvature still diverges at the origin (Ricci scalar $R \rightarrow 1/4\pi\beta r$), but less “brutally” than in the Schwarzschild case. This can be seen from the fact that, in contrast to the Schwarzschild case, the metric is no longer divergent at the origin. That is, only the first and higher derivatives of the metric are singular at this point, which implies a “softer” singularity. ³

Such a property of the GUP inspired black holes is similar to that of the recently proposed holographic metric [204, 348]. For other quantum corrected black hole solutions, however, the metric and all its derivatives are regular at the origin implying a removal of the curvature singularities [342, 343, 345, 346, 349]. Despite the singular behavior of the spacetime (37.7) the gravitational field, $\vec{g} = \vec{\nabla} g_{00}$, can be computed in a neighborhood of the origin: it turns out to be constant and repulsive. Much in the same way as the aforementioned regular geometries, the quantum fluctuations of

² Here, $\gamma(s; x)$ is the lower incomplete gamma function, see Appendix A1.2 for general definitions.

³ Another quantitative argument is the Kretschmann scalar, which diverges for Schwarzschild as $K \sim 1/r^6$ and for the GUP only as $K \sim 1/r^2$.

the manifold provide an outer pressure that prevents the energy density to collapse in a Dirac delta profile.

The existence of an extremal configuration has an impact on the thermodynamics. The Hawking temperature does not diverge as the black hole evaporates, but rather reaches a maximum before the SCRAM phase, *i.e.* an asymptotic cooling towards a zero temperature black hole remnant. Figure 37.1 shows the temperature [254]

$$T(r_+) = \frac{\kappa}{2\pi} = \frac{1}{4\pi} \left. \frac{dg_{00}}{dr} \right|_{r=r_+} = \frac{1}{4\pi r_+} \left(1 - \frac{r_+^2}{\beta} \frac{e^{-r_+/\sqrt{\beta}}}{\gamma(2; r_+/\sqrt{\beta})} \right), \quad (37.10)$$

of the metric (37.7). It can be determined from the surface gravity κ at the outer horizon r_+ .

The Hawking temperature of the GUP inspired black holes resembles the behaviour of the Reissner-Nordström, Kerr and Kerr-Newman metrics. One has to note, however, that despite the similar profile, the evaporation of Reissner-Nordström, Kerr and Kerr-Newman metrics is drastically different. Indeed the SCRAM phase never takes place in such cases. Rather than cooling down, such charged, rotating, charged-rotating metrics reach a Schwarzschild configuration at the end of the balding and spin-down phases, that fatally occur in the presence of emissions like Hawking evaporation and superradiance. On the other hand, the metric in (37.7) extends the thermodynamics of the Schwarzschild phase by properly taking into account the quantum backreaction. To see this one can consider the ratio $T/M < T_{\max}/M_0 \approx 5.21 \times 10^{-3}$, where M is the mass of the black hole. The mass of the extremal configuration is determined as $M_0 = M(r_0) \approx 1.66\sqrt{\beta} m_{\text{Pl}}$ at radius $r_0 \approx 1.793\sqrt{\beta}$, while the maximum temperature is $T_{\max} = T(r_0) \approx 9.34 \times 10^{-3}/\sqrt{\beta}$.

The SCRAM phase goes along with a positive heat capacity and ends in a zero temperature remnant which is however reached only in the limit of an infinite evaporation time.

38 Higher Dimensional KMM Black Holes

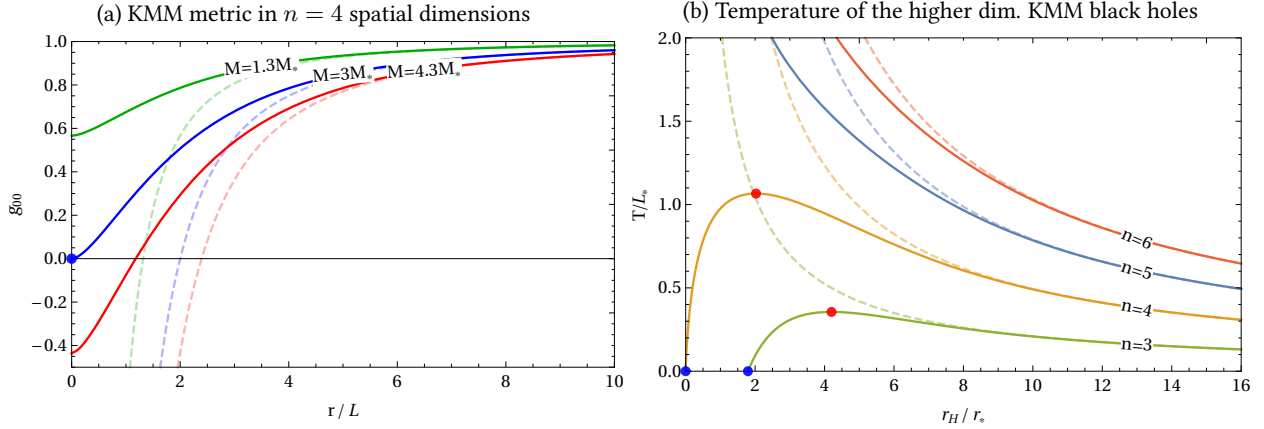
A problem arises when naively generalizing this model from 3 to n spatial dimensions by keeping the same momentum space regularization (39.2). in higher dimensions, as it is proposed by [266],

$$d^n \vec{p} \rightarrow \frac{d^n \vec{p}}{1 + \beta p^2}. \quad (38.1)$$

Following the previous exposition, one has to start by determining the energy momentum tensor $\mathbb{T}_{\mu\nu}$. Apart from the higher dimensional gravitational constant G_* in place of G_N , the profile of the operator \mathbb{G} ($L^2 \square$) remains the same as in the $(3+1)$ -dimensional case, (37.6). As a result, this leads to the modified energy density [271, 290],

$$\mathcal{T}_0^0(\vec{x}) = -\rho(\vec{x}) = \frac{M}{(2\pi)^N} \int d^n \vec{p} \frac{e^{-i\vec{x}\cdot\vec{p}}}{1 + \beta \vec{p}^2}. \quad (38.2)$$

The integration includes $d - 4$ additional spatial dimensions and leads to



the following result:

$$\rho(\vec{x}) = -\frac{M}{(2\pi)^{n/2}} \left(\frac{x}{\sqrt{\beta}}\right)^{1-n/2} K_{\frac{n}{2}-1} \left(\frac{x}{\sqrt{\beta}}\right), \quad (38.3)$$

where $n = d - 1$ is the number of spatial dimensions and $K_\alpha(x)$ is the modified Bessel function of second kind. Integrating equation (38.3) over an n -ball B_r of radius r yields the cumulative mass distribution

$$\mathcal{M}(r) = \int_{B_r} d^n \vec{x} \rho_\beta(\vec{x}) = \frac{(2\pi)^{n/2}}{\Gamma(n/2)} \int_0^r dx \rho_\beta(x) \quad (38.4)$$

$$= M \left[1 - \frac{2^{1-n/2}}{\Gamma(n/2)} \left(\frac{r}{\sqrt{\beta}}\right)^{n/2} K_{n/2} \left(\frac{r}{\sqrt{\beta}}\right) \right]. \quad (38.5)$$

The metric can be written as a Schwarzschild-Tangherlini metric (35.1) where the metric function $f_n(r)$ is given by

$$f_n(r) = \frac{8\pi G \Gamma(n/2)}{(n-1)\pi^{n/2-1}} \frac{\mathcal{M}(r)}{r^{n-2}}. \quad (38.6)$$

The Ansatz for the metric (38.6) requires a conserved energy momentum tensor of the form $\mathbb{T}_\mu^\nu = \text{diag}(-\rho, p_r, p_\perp, p_\perp, \dots)$ with $p_r = -\rho$ and $p_\perp = -\rho - \frac{r}{n-1}(\frac{d\rho}{dr})$.

38.1 Extremal configuration

The metric coefficient can be cast in a more compact form as

$$f_n(r) = 1 - \frac{G_* m \mu(r)}{r^{n-2}}. \quad (38.7)$$

$$\text{where } \mu(r) \equiv 1 - \frac{2^{1-n/2}}{\Gamma(n/2)} \left(\frac{r}{\sqrt{\beta}}\right)^{n/2} K_{n/2} \left(\frac{r}{\sqrt{\beta}}\right), \quad (38.8)$$

$$\text{and } m \equiv M \frac{8\Gamma(n/2)}{(n-1)\pi^{n/2-1}}. \quad (38.9)$$

By solving the system of equations

$$\begin{cases} f_n(r) = 0 \\ \frac{df_n(r)}{dr} = 0, \end{cases} \quad (38.10)$$

Figure 38.1: KMM model in higher dimensions: (a) shows the gravitational potential for one extra dimension, (b) shows the temperatures for a couple of extra dimensions. This figure extends Figure 37.1 where only the $n = 3$ -dimensional case is shown.

one can look for a solution $r = r_0$ representing the vanishing minimum of $f_n(r)$. If the solution exists for a specific value $m = m_0$, one has determined what is physically known as an extremal black hole configuration. For $n = 3$ one finds $m_0 = 2M_0 = 3.36\sqrt{\beta}/G_N$ and $r_0 = 1.79\sqrt{\beta}$, as we have already seen in the previous section. For $n > 4$, the system has no positive defined solution. This can be easily seen by considering the expansion of the function $\mu(r)$ for small arguments:

$$\mu(r) \xrightarrow[r \ll \sqrt{\beta}]{} (2n - 4)^{-1} \left(\frac{r}{\sqrt{\beta}} \right)^2 \quad (38.11)$$

Being $\mu \sim r^2$ from small radii, the function f_n diverges negatively at the origin for $n > 4$, while it reproduces the Minkowski space at large distances, $\mu \approx 1$. This behaviour suggests that that f_n is a monotonic increasing function having a single zero, *i.e.*, the event horizon (Figure 38.1).

For $n = 4$, one finds a surprising case. The solution of the system is $m_0 = 3\sqrt{\beta}/G_*$ and $r_0 = 0$. Evidently this does not represent an extremal configuration, but instead reveals the presence of a gravitational object of a different nature. By using (38.11), one can write the metric in a region near the origin for $n = 4$ as

$$ds^2 \approx - \left(1 - \frac{2G_*M}{3\pi\beta} \right) dt^2 + \left(1 - \frac{2G_*M}{3\pi\beta} \right)^{-1} dr^2 + r^2 d\Omega_3^2. \quad (38.12)$$

We note the Newtonian potential is constant at short scales. This implies that the mass does not produce any gravitational field near the origin. One can see this by rescaling the r and t variables and by expressing the above metric in the form

$$ds^2 = -dt^2 + dr^2 + \left(1 - \frac{2G_*M}{3\pi\beta} \right) r^2 (d\theta_2^2 + \sin^2 \theta_2 (d\theta_1^2 + \sin^2 \theta_1 d\phi^2)), \quad (38.13)$$

introducing a deficit angle and a conical singularity. This can be seen by considering the surface $t = \text{const.}$, $\theta_1 = \theta_2 = \pi/2$, which has the geometry of a cone. This conical singularity is a curvature singularity. The behaviour of the energy density for $n = 4$ at short scales, $\rho(\vec{x}) \sim |x|^{-2}$, confirms this pathology of the manifold. The above scenario reveals that for $n = 4$, the gravitational object at the origin is a Barriola-Vileking global monopole [59], *i.e.*, a particular example of cosmic string [206]. Interestingly, the metric is an exact solution that smoothly interpolates the space-time region of the monopole a short scales with that of a black hole at large scales.

38.2 Thermodynamics

A study of the related thermodynamics can be done by considering the Hawking temperature

$$T_H = \frac{n-2}{4\pi r_+} \left[1 - \frac{r_+}{n-2} \frac{\mu'(r_+)}{\mu(r_+)} \right]. \quad (38.14)$$

Before displaying the exact result for the temperature, we consider its asymptotic nature. Since the function $\mu \rightarrow 1$ for $r \gg \sqrt{\beta}$, T_H approaches the

standard semiclassical result at large distances. Conversely at short scales, (38.11) leads to

$$T_H \approx \frac{n-2}{4\pi r_+} \left[1 - \frac{2}{n-2} \right], \quad \text{for } r \ll \sqrt{\beta}. \quad (38.15)$$

For $n > 4$ the temperature has a divergent behavior as in the semiclassical case. On the other hand, for $n = 4$ the temperature vanishes in the limit $r_+ \rightarrow 0$. This means the the temperature admits a maximum and undergoes a SCRAM phase. Interestingly, following what is discussed above, the horizon structure prevents the formation of an extremal configuration. As a result, the final state of the evaporation is nothing but a global monopole with mass $M_0 = 3\pi\beta/2G_* \simeq 4.71M_*$ for $\beta = M_*^{-2}$. Finally we explicitly write the temperature for any n , it reads [271]

$$T_H = \frac{\pi^{n/2} r^{n/2} (r(K_{\frac{n}{2}-1}(r) + K_{\frac{n}{2}+1}(r)) + (n-4)K_{\frac{n}{2}}(r)) - (n-2)(2\pi)^{n/2}\Gamma(\frac{n}{2})}{2r\Gamma(\frac{n+2}{2})(2r^{n/2}K_{\frac{n}{2}}(r) - 2^{n/2}\Gamma(\frac{n}{2}))} \quad (38.16)$$

Figure 38.1 shows the temperature profiles, where $n = 3$ and $n = 4$ (discussed in the previous section) clearly stand out, while for all $n \geq 5$ there is no qualitative difference to Schwarzschild even on shortest scales.

Clearly, the GUP momentum suppression in $n \geq 5$ spatial dimensions is not enough to cure the diverging temperature or curvature, in general. This raises the need for a dimension-dependent modification of the GUP.

39 Ambiguity of GUP in higher dimensional spacetimes

According to the KMM model [266], the GUP manifests itself via a deformation of the integration measure in momentum space. Following (36.1), the Hilbert space representation of the identity becomes

$$\mathbb{I} = \int \frac{d^{d-1}\vec{p}}{1 + \beta\vec{p}^2} |p\rangle \langle p|, \quad (39.1)$$

where \vec{p} is a $(d-1)$ -dimensional spatial vector. While momentum operators preserve their feature as in quantum mechanics, position operators no longer admit physical eigenstates, as one should expect in the presence of a minimal resolution length $\sqrt{\beta}$. A closer inspection of (39.1) shows that the measure is suppressed in the ultraviolet regime

$$dV_p \equiv \frac{d^{d-1}p}{1 + \beta p^2} \underset{\beta p^2 \gg 1}{\approx} |\vec{p}|^{d-4} d|\vec{p}|. \quad (39.2)$$

We note that for $d = 4$ one recovers (36.4), and the momentum term on the right-hand side disappears. Conversely for $d > 4$, the measure diverges in the ultraviolet regime. As d increases, the effect of the GUP becomes increasingly weaker, when being used to improve the higher dimensional Newtonian potential.

There are, however, other proposals. Gravitational effects in quantum mechanics, such as the GUP, can be motivated with the Gedankenexperiment of Heisenberg's microscope [3, 123]. Specifically, next to the spatial uncertainty $\Delta x \sim \Delta x_C$ arising from the Compton wavelength of a particle $\Delta x_C \sim \lambda \sim 1/\Delta p$, one can introduce an additional displacement Δx_g for

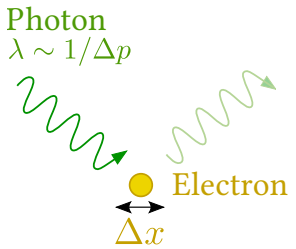


Figure 39.1: A simplified cartoon for the Heisenberg's microscope. The classical argument is, that the uncertainty δx of determining the position of the electron is related to the wavelength $\lambda \sim h/\Delta p \sin(\varphi)$ of a scattering photon within a focussed beam on the electron of an angle φ . Due to a classical optics argument, $\Delta x \sim \lambda/\sin(\varphi)$. This motivates the original Heisenberg's uncertainty principle $\Delta x \Delta p \sim h$. In the main text, an electron displacement due to gravitational interaction is added.

the electron due to the gravitational interaction with the incoming photon. By assuming a Newtonian description, ones finds that

$$\Delta x_g \sim G_N \frac{M_{\text{eff}}}{r^2} \left(\frac{r^2}{c^2} \right) \sim G_N \Delta p \sim (\sqrt{\beta})^2 \Delta p \quad (39.3)$$

for $d = 4$, where $M_{\text{eff}} = h/(\lambda c)$ is the effective photon mass and $\sqrt{\beta} \sim \ell_{\text{Pl}}$. The total uncertainty is obtained by adding Δx_g to the standard quantum uncertainty, namely $\Delta x = \Delta x_C + \Delta x_g$ with $\Delta x_C \sim 1/\Delta p$. Following the reasoning of Scardigli and Casadio [400], as well as Carr and Lake [122, 123, 126, 291, 292, 293], the extension of the above calculation to the case $d > 4$ leads to

$$\Delta x_g \sim G_* \frac{M_{\text{eff}}}{r^{d-2}} \left(\frac{r^2}{c^2} \right) \sim G_* \frac{\Delta p}{r^{d-4}} \rightsquigarrow \Delta x_g^{d-3} \sim L_*^{d-2} \Delta p, \quad (39.4)$$

having assumed $r \sim \Delta x_g < R_c$. The uncertainty relation then reads

$$\Delta x \Delta p \geq \frac{\hbar}{2} \left(1 + \left(\sqrt{\beta} \Delta p \right)^{\frac{d-2}{d-3}} \right), \quad (39.5)$$

where $\sqrt{\beta} \sim L_*$. On the other hand, for $r \sim \Delta x_g > R_c$, the uncertainty relation is assumed to be that for $d = 4$ displayed in (36.2). From (39.5) one can show that the momentum space measure can be expressed as

$$d\mathcal{V}_p \equiv \frac{d^{d-1}p}{1 + (\beta \vec{p}^2)^{\frac{1}{2} \frac{d-2}{d-3}}} \underset{\beta \vec{p}^2 \gg 1}{\approx} |\vec{p}|^{d-3} d|\vec{p}|, \quad (39.6)$$

for $d > 4$. This means that in such a scenario the GUP corrections are even milder than those of the KMM model. However, it assumes a modified higher dimensional GUP as

$$\Delta x \Delta p \geq \frac{\hbar}{2} \left(1 + \left(\sqrt{\beta} \Delta p \right)^{\frac{d-2}{d-3}} \right). \quad (39.7)$$

Eq. (39.7) is consistent with what proposed in [122, 123, 291, 292, 321, 400] and clearly reproduces the higher dimensional Schwarzschild radii for energies above the terascale.

Given the ambiguity in results described above, we proposed another revision to the Heisenberg microscope in [290]. From (39.4) one obtains that $\Delta x_g \geq L_*$ only for $\Delta p \geq M_*$. As a result, for any $\Delta p \leq M_*$ the gravitational uncertainty is negligible, $\Delta x_g < \Delta x_C < R_c$. In such a regime the typical interaction distance is controlled by the Compton wavelength, $r \sim \Delta x_C \sim 1/\Delta p$. In Figure 39.2, this complies with “approaching” the quantum gravity scale from the left (Sub-Planckian Regime). This implies that

$$\Delta x_g \sim G_* \frac{M_{\text{eff}}}{r^{d-2}} \left(\frac{r^2}{c^2} \right) \sim G_* \frac{\Delta p}{r^{d-4}} \sim L_*^{d-2} \Delta p^{d-3}. \quad (39.8)$$

The above relation relaxes the proportionality condition between Δx_C , Δx_g and the radius of the Tangerlini-Schwarzschild black hole [290]. As a byproduct, however, one obtains a stronger correction in momentum space since gravity will begin to probe extra dimensions at scales $r < R$. This can be inferred from the condition

$$d\mathcal{V}_p \equiv \frac{d^{d-1}p}{1 + (\beta \vec{p}^2)^{\frac{d-2}{2}}} \underset{\beta \vec{p}^2 \gg 1}{\approx} d|\vec{p}|, \quad (39.9)$$

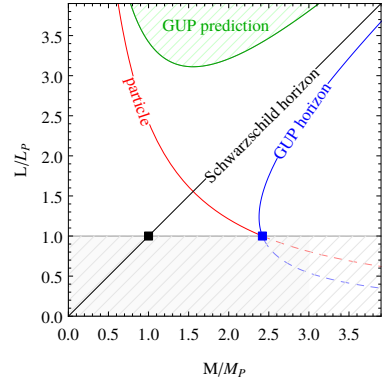


Figure 39.2: Completeness plot with the $(3+1)$ -dimensional GUP solution. Compare with Figure 36.1. Published in [290].

namely it is uniformly suppressed irrespective of the number of dimension d .

There are three arguments in support of the above reasoning. First, the requirement that a quantum gravity correction Δx_g is proportional to a classical quantity like the Tangerlini-Schwarzschild black hole is not fully consistent. It makes sense only for $r > R$, namely at length scales at which gravity becomes classical and only four dimensions are visible. Second, investigations of string scattering showed that the position-momentum uncertainty relation is of the form (36.2) [19, 21]. Such a result has, however, been obtained in the eikonal limit and higher order corrections for the ultra-violet regime of momentum space are expected. Third, the above corrections are consistent with the algebra proposed in [159, 320, 322].

In the remainder of this paper, we present higher dimensional black hole solutions that emerge from the non-local field equations (36.3) that account for GUP effects following from (39.2), (39.6) and (39.9) according to the method first proposed in [254].

40 Revised GUP in higher dimensions

In this section, the imprint of the improved higher dimensional GUP (39.9) is studied. As a start, one has to determine the corresponding operator $\mathbb{G}(L^2\Box)$, namely

$$\mathbb{G}(L^2\Box) = \frac{G_*}{1 - (L^2\Box)^{\frac{n-1}{2}}} \equiv G_* \sum_{N=0}^{\infty} \left[(L^2\Box)^{\frac{n-1}{2}} \right]^N, \quad (40.1)$$

where, in case of half integer exponents, $\frac{n-1}{2} = \frac{3}{2}, \frac{5}{2}, \frac{7}{2}, \dots$, the following Schwinger representation can be used to express powers of an arbitrary operator, \hat{O} :

$$\hat{O}^\alpha = \frac{1}{\Gamma(-\alpha)} \int_0^\infty ds s^{-\alpha-1} e^{-s\hat{O}}, \quad \alpha \in \mathbb{R} \setminus \mathbb{N}. \quad (40.2)$$

The resulting energy momentum tensor has the same form of that presented in Section 38, namely $\mathbb{T}_\mu^\nu = \text{diag}(-\rho, p_r, p_\perp, p_\perp, \dots)$ with $p_r = -\rho$ and $p_\perp = -\rho - \frac{r}{n-1} \left(\frac{dp}{dr} \right)$. The energy density and the other components have, however, a different profile. To determine \mathbb{T}_0^0 , one has to consider the integral

$$\mathbb{T}_0^0(\vec{x}) = -\rho(\vec{x}) = -\frac{M}{(2\pi)^n} \int \frac{d^n \vec{p}}{1 + (\sqrt{\beta} p)^{n-1}} e^{i\vec{x} \cdot \vec{p}} \quad (40.3)$$

Eq.	Short name	Volume element	Large p limit
	No GUP	$d^{d-1}p$	$p^{d-2}dp$
(39.6)	Carr	$d^{d-1}p/(1 + (\sqrt{\beta} p)^{(d-2)/(d-3)})$	$p^{d-3}dp$
(36.4)	KMM	$d^{d-1}p/(1 + (\sqrt{\beta} p)^2)$	$p^{d-4}dp$
(39.9)	Adjusted	$d^{d-1}p/(1 + (\sqrt{\beta} p)^{d-2})$	dp

Table 39.1: An overview of different GUP formulations in higher dimensions (also “no GUP” is considered, for reference), with their mathematical definition (including a text reference) and their classical limit.

40.1 Calculation of the energy density

The modified source term can be written as a Fourier Transform of a spherically symmetric function $\mathcal{F}\{f(p)\}(x) \equiv \frac{1}{(2\pi)^{n/2}} \int d^n \vec{p} f(p) e^{i\vec{x} \cdot \vec{p}}$

$$\rho(x) = \frac{M}{(2\pi)^n} \int \frac{d^n \vec{p}}{1 + (\sqrt{\beta} p)^{n-1}} e^{i\vec{x} \cdot \vec{p}} \quad (40.4)$$

$$= \frac{M}{(2\pi)^{n/2}} \mathcal{F} \left\{ \frac{1}{1 + (\sqrt{\beta} p)^{n-1}} \right\} (x) \quad (40.5)$$

$$= \frac{M}{(2\pi)^{n/2}} \frac{1}{x^{\frac{n-2}{2}}} \int_0^\infty dp p^{\frac{n}{2}} \frac{1}{1 + (\sqrt{\beta} p)^{n-1}} J_{\frac{n-2}{2}}(xp), \quad (40.6)$$

$$= \frac{M\beta^{-n/2}}{(2\pi)^{n/2}} \frac{1}{z^{\frac{n-2}{2}}} \int_0^\infty dq q^{\frac{n}{2}} \frac{1}{1 + q^{n-1}} J_{\frac{n-2}{2}}(zq), \quad (40.7)$$

where the Bessel function of first kind $J_\alpha(x)$ comes from integrating out the angles. Due to the complexity of the adjusted GUP, no general closed algebraic expressions could be derived and instead a numerical approach was taken.

By introducing the dimensionless variables $z = r/\sqrt{\beta}$ and $q = \sqrt{\beta}p$, the above integral reads:

$$\rho(z) = \frac{M\beta^{-n/2}}{(2\pi)^{n/2}} \frac{1}{z^{\frac{n-2}{2}}} \int_0^\infty dq q^{\frac{n}{2}} \frac{1}{1 + q^{n-1}} J_{\frac{n-2}{2}}(zq). \quad (40.8)$$

For small arguments the Bessel function behaves as

$$J_\alpha(z) \approx \frac{1}{\Gamma(\alpha+1)} \left(\frac{z}{2}\right)^\alpha. \quad (40.9)$$

This means the integral is well defined at the lower bound. For large arguments the Bessel function can be written

$$J_\alpha(z) \approx \frac{1}{|z|}. \quad (40.10)$$

This guarantees the expected convergence of the integral for $q \rightarrow \infty$. On these grounds, the numerical evaluation is possible by integrating from zero-crossing (i.e. the z where $J_\alpha(z) = 0$) to zero-crossing in order to stabilize the integration and to ensure convergence (Figure 40.1). For numerical purposes, the density can be approximated as

$$\rho(z) \approx \frac{M\beta^{-n/2}}{(2\pi)^{n/2}} \frac{1}{z^{\frac{n-2}{2}}} \sum_{k=0}^K \sum_{i=0}^{I\Delta q} \Delta q q_{i,k}^{\frac{n}{2}} \frac{1}{1 + q_{i,k}^{n-1}} J_{\frac{n-2}{2}}(zq_{i,k}). \quad (40.11)$$

Here, $K \in \mathbb{N}$ are the number of zero crossings taken into account (typical values are $K = 3000$), and $I \in \mathbb{N}$ are the total number of integration support points, each given by $q_{i,k} = j_k + i\Delta q$, with j_k the coordinate of the k th root of $J_{(n-2)/2}(zq)$. Clearly, with $I, K \rightarrow \infty$ and $\Delta q \rightarrow 0$, the continuous integral (40.8) is recovered. We checked convergence with different grid sizes $I, K \in \{10^2, 10^3, 10^4\}$. For the actual numerical integration, a standard Gaussian quadrature rule is applied. The function values $\rho_{\beta,n}(z)$ are then available on a discrete sample set $\{z_i\} \subset \mathbb{R}$ with arbitrary resolution and coverage. With this numerical approach, one can also integrate the mass distribution,

$$\mathcal{M}(r) = M \int_{B_r} d^n \vec{x} \rho_\beta(x) = M A_{n-1} \int_0^r dx x^{n-1} \rho(x), \quad (40.12)$$

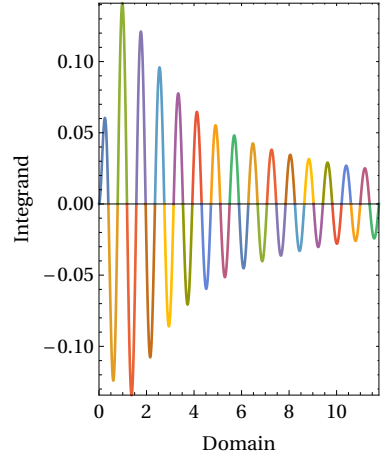


Figure 40.1: The key part for a successful numerical integration of the highly oscillatory Hankel transformation $\int_0^\infty f(x) J_\alpha(xy) dx$ with kernel $f(x)$ and $\lim_{x \rightarrow \infty} f(x) = 0$ is to correctly track the zero crossings of the oscillating Bessel function. Here, every color indicates a separate integration domain.

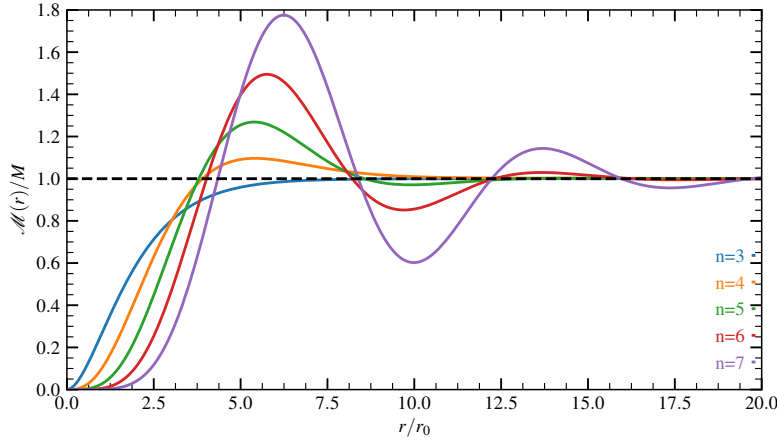


Figure 40.2: Mass distributions (40.12) for the revised GUP model (39.9), for different number of spatial dimensions n . While $n = 3$ complies with a smeared Heaviside function, there are oscillations around the spacetime mask, which however quickly decline for larger radii (the scale is $r_0 \sim L_* \sim L_{\text{Pl}}$). Note that for larger radii, even regions with $\mathcal{M}(r) < 0$ are possible.

where $A_{n-1} = 2\pi^{n/2}/\Gamma(n/2)$. Again, this integral is carried out numerically as a cumulative sum in a straightforward manner. From the matter distribution, one obtains the metric coefficients (38.6). Figure 40.3 shows the mass distribution $\mathcal{M}(r)$ for a number of extra dimensions. Interestingly the case $n = 3$ is the only having $\mathcal{M}(r)$ described by a monotonic increasing function. For $n > 3$ there is a surprising new behavior: the function oscillates with an amplitude that increases with n and decreases with r . A naive interpretation of the oscillations is the presence of negative contributions in the energy density for some regions close to the spatial origin. We recall that such negative density regions are not a remote possibility, at least during the early stages of the Universe, for the presence of strong quantum fluctuations of the spacetime manifold [315, 334].

One can also advance another interpretation based on the presence of $n - 1$ tachyon states of mass, $i/\sqrt{\beta} \sim iM_*$, emerging from the poles of the integrand function in (40.3). As a consequence the energy density $\rho(\vec{x})$, despite being positive defined at the origin, oscillates around zero for larger values of r . A possible explanation can be found in the fact that the GUP captures only part of the non-perturbative corrections of quantum gravity.

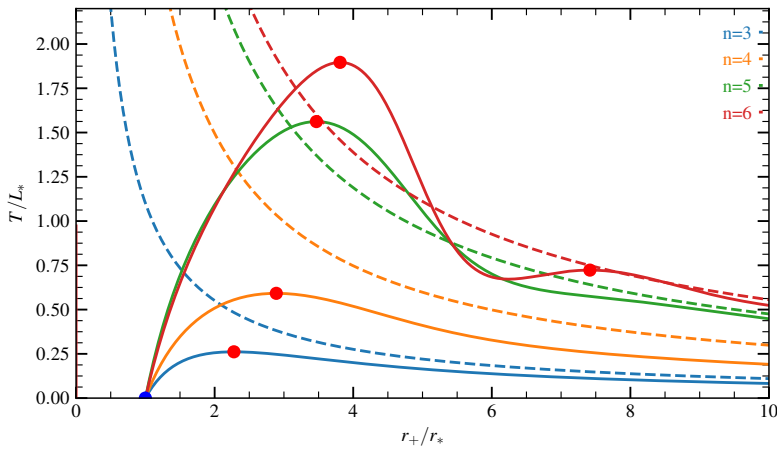


Figure 40.3: Temperature profiles (defined as in (38.14), with the revised GUP of Section 40) in different number of dimensions, compared with the respective Schwarzschild-Tangherlini temperature (dashed lines). The red disks mark local maxima, while the blue disk marks the evaporation endpoint. Since the abscissa is given in multiples of the respective endpoint radius, all temperatures end at the same point.

Interestingly, such oscillations of the Newtonian potential have been found in a variety of formulations aiming to amend Einstein gravity. These include $f(R)$ -gravity [76, 119, 120, 145, 197, 351, 352, 353, 401], string induced, ghost free, non-local gravity [185, 207] and other non-local formulations [265]. On the other hand, in the low energy limit for which only the 3 spatial dimensions are visible, the oscillations disappear as expected in similar quantum gravity contexts [237, 362]. This scenario is consistent with the fact that GUP corrections descend from the eikonal limit of string collisions at the Planck scale [17, 18, 19, 20, 21, 225, 226].

Even if the above effects are just a short-scale, quantum mechanical property of the solution, they have important repercussions on the thermodynamics of the system. The profile of the temperature is presented in Fig. 40.3. One can see that the oscillations of $\mathcal{M}(r)$ produce temperature oscillations corresponding to phase transitions from negative to positive heat capacity phases. The resulting variable luminosity of the black hole can be termed as a *light-house effect*. Interestingly such an effect increases with n . For lower n one obtains small amplitude oscillations of the temperature.

Different endpoints for small and big black holes

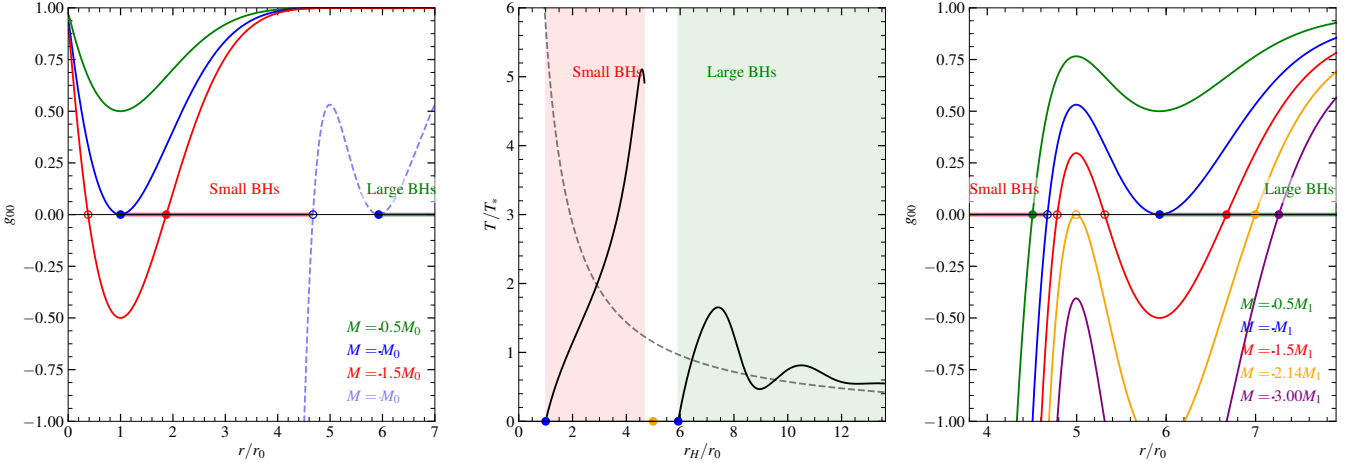
More importantly, further scenarios are possible. In Figure 40.4, the case of $d = 9$ space time dimensions is depicted. For this number of dimensions, two scenarios are possible, depending on the black hole mass. For big mass black holes, $M > M_1$, the temperature oscillation determined an anticipated shut-down of the Hawking emission with the formation of zero temperature remnants; we refer to the masses of these zero temperature configurations as $M_1 = 3.73 \times 10^6 M_*$. Such a large mass regime is characterized by a rich horizon structure. For $M > 2.14M_1$, there are just two horizons, an event horizon, r_+ and an inner Cauchy horizon, r_- . For $M = 2.14M_1$, the function g_{00} admits a double zero between the aforementioned two horizons. For smaller masses $M_0 < M < 2.14M_1$, the function g_{00} admits 4 simple zeros, i.e., $r_- < r_2 < r_3 < r_+$. Finally for $M = M_1 = 3.73 \times 10^6 M_*$, there is the merge between r_3 and r_+ that form a double zero, corresponding to the extremal configuration, i.e., the end stage of the evaporation. In terms of horizon radii, there is a regime that do not occur, i.e. $r_i < r < r_1$, where $r_1 = 5.93r_0$ is the size of the large black hole evaporation endpoint, and an intermediate radius $r_i = 5.0r_0$. For even smaller masses, $M < M_1$ however, there are horizons again, r_\pm , that eventually merge in a new extremal configuration $r_0 = r_- = r_+$ for $M = M_0 = 5.15 \times 10^3 M_*$.

Here, the self-completeness paradigm was implemented by choosing the free parameter β in a way, that the Compton wavelength $\lambda_C = h/M_0c$ of the zero temperature configuration is equal to its horizon radius r_0 . The determination of β cannot even be done analytically in 3+1 dimensions. Therefore, numerical results are given in Table 40.1.

In conclusion, there is a small mass and a large mass regime for black holes. The former can be thought to form due the high density fluctuation of the early Universe [124] or by de Sitter space decay, as predicted in terms of the instanton formalism [94, 313, 314].

n	$\sqrt{\beta_0}$	r_0	m_0
3	1.45	2.60	2.42
4	0.71	1.18	5.31
5	0.48	0.85	7.43
6	0.38	0.71	8.88
7	0.32	0.64	9.89
8	0.27	0.59	10.6
9	0.25	0.56	11.1
10	0.23	0.55	11.5

Table 40.1: Numerical values for $\sqrt{\beta_0}$ in the self complete paradigm. These values are of no further meaning, they just demonstrate that it is possible to apply the self-complete paradigm in any number of extra dimensions.



We have also to note that the presence of two remnant masses posits an ambiguity of the scale at which gravity may be self complete [178, 182, 337, 347, 420]. In other words gravity is able to mask singularities by covering them with an extremal configuration but the latter has no unique mass scale.

41 Summary

The fact that the black hole temperature diverges for small black holes is one of the indicators that a theory of quantum gravity is needed. The Generalized Uncertainty Principle is a quantum gravity effect and modifies this behavior (SCRAM phase). Since the GUP can for example be motivated by string theory which needs extra dimensions this strongly suggests that the cure of the temperature divergence should also work in higher dimensions.

In 3+1 dimensions the GUP gives rise to a SCRAM phase for Planckian black holes. We showed that the GUP as it has been used in the 3+1 dimensional case does not give rise to SCRAM phase in higher dimensions. However, we note that in the 4+1 dimensional case, the GUP gives rise to a conical singularity. We generalized the GUP to higher dimensions in the form $1/(1 + (\sqrt{\beta}p)^{n-1})$, with n spatial dimensions, motivated by the reasoning in an earlier work [290]. In this revised GUP we recovered the SCRAM phase.

We also found that there are new oscillations in the density $\rho(r)$ around zero. These oscillations lead to oscillations in the mass function $M(r)$, but are damped in the metric $g_{00}(r)$. Nevertheless they again show up in the temperature which now shows a Lighthouse Effect of oscillating temperature around the Planck size. Starting at 8+1 dimensions, there are additional zeroes of the temperature, giving rise to a complex phase structure, where the small black holes can be formed in the primordial universe.

Figure 40.4: Comprehensive presentation of the possible configurations of the revised GUP model (Section 40) in $n = 8$ spatial dimensions. The central panel shows the temperature (solid line) compared to the Schwarzschild-Tangherlini solution (dashed). There are two regimes, shaded in red (small black holes) and green (big black holes). Typical gravitational potentials for different masses for the small black holes are depicted in the left panel, while the right panel holds the same for the large black holes. Dots always denote horizons. The different scenarios are discussed in the main text.

Appendix A7 shows this diagram in another representation and also covers the $n = 9$ case, for comparison.

CHAPTER

VI

Conclusions

In this thesis, the applicability of sophisticated family of high order and communication avoiding discontinuous Galerkin (DG) schemes were examined for solving partial differential equations in relativistic astrophysics. These schemes were supplemented with an ADER time integration and a finite volume limiter in order to deal with space-time singularities and hydrodynamical discontinuities (i.e., shocks). Different to what has been done in literature before, an explicit split of differential contributions in source terms combined with a path-conservative treatment, first proposed by Castro and Parés in the finite-volume context [129, 359] and later extended also to ADER-DG schemes in [166, 169], was carried out. The schemes were implemented in different state of the art adaptive mesh refinement (AMR) codes.

In order to employ the Einstein equations for the proposed schemes, a novel first order formulation with conformal and constraint correcting features had to be found: The conformal and covariant Z4 formulation. This formulation was proven to be strongly hyperbolic for popular gauge choices. The evolution laws for the ADM quantities $\alpha, \beta^i, \tilde{\gamma}_{ij}$ as well as the conformal factor ϕ could be reduced to a pure system of ODEs, thanks to the auxiliary variables which render derivatives as purely algebraic source terms. These ODEs have zero eigenvalues and unit eigenvectors, leaving a PDE system with 47 variables open for hyperbolization. For the remaining system of 47 variables, first approximate symmetrization by use of ordering constraints is a key ingredient, and second the dependency of the ADM (composing) variables $\alpha, \beta^i, \tilde{\gamma}_{ij}$ and ϕ only results in a fully linearly degenerate PDE system. Furthermore, the adoption of the genuinely non-conservative form (in contrast to a flux-conservative form such as in [11, 89]) was also essential for applying the previously mentioned simplifications, as the Jacobian $\partial F_k^i / \partial Q^j$ of the flux $F_k^i(Q)$ in direction k also depends on the dynamical variables. The quasi-linear form of the flux-conservative system therefore contains differential terms in the ADM variables. The proof of strong hyperbolicity was given for two standard gauge choices, i.e., harmonic lapse and zero shift as well as 1+log slicing with Gamma driver. In both cases, the full eigenstructure was computed. This is the first time that hyperbolicity of a first-order reduction of the CCZ4 system is analyzed, in particular including the Gamma-driver shift condition. However, the system is *not* symmetric hyperbolic in the sense of Friedrichs [205]. Further work in this direction will be necessary to try and achieve a symmetric hyperbolic form of FO-CCZ4 with a convex extension.

Subsequently, the equations of relativistic hydrodynamics were brought into a similar form, with a clear separation between conserved hydrodynamic flux and non-conserved differential gravitational source, induced by the curved spacetime. This much simpler rewrite did not change the hyperbolic nature of the PDE system. At this stage, the development of exactly well-balanced numerical methods for the GRMHD equations is still out of scope, but further developments in this direction would definitely deserve attention.

In a variety of tests, the applicability of the ADER-DG scheme was demonstrated on the Einstein-Euler system. Here, the spacetime evolution was tested still separately from the hydrodynamic matter evolution, which itself was evolved on a fixed background spacetime. Nevertheless, these were the first simulations of black hole spacetimes and (fixed) general relativistic magnetohydrodynamic flows performed in three spatial dimensions with a high-order DG code. All previous simulations of black-hole spacetimes with high-order DG schemes, in fact, were limited to the one-dimensional case only.

Future research will consider the implementation of the algorithms within a code which scales well on thousands of codes/computers. Furthermore, the coupled FO-CCZ4 and GRMHD system, solved with a single numerical scheme,

will be evolved using such a code. This will allow to simulate binary neutron star merger binaries with the Limiting ADER-DG scheme.

We have also considered a general-relativistic estimate on the threshold mass which separates prompt collapse from a delayed collapse scenario in the case of binary neutron star mergers. As part of a systematic parameter study, a large number of binary neutron star merger simulations was carried out, adopting a series of realistic nuclear equations of state. A number of universal laws were found, which either relate the threshold mass of a particular equation of state to its maximum stable static equilibrium (TOV) solution or its compactness. We also could constraint the maximum radius and mass of neutron stars in general which go hand in hand with observational constraints from gravitational wave observations.

These results can be improved in at least two ways. First, as new hot equations of state becomes available for numerical simulations, it will be possible to extend the analysis carried here, reducing its uncertainty. Second, as new detections from binary neutron-star mergers will be revealed, the masses of these systems and their electromagnetic counterparts will be used to set ever more precise lower bounds on the radii of neutron stars.

As a final project, we have studied higher-dimensional black hole solutions and their thermodynamics from GUP-inspired approaches. These include the Kempf-Mann-Mangano (KMM) momentum measure, a new modified momentum measure, and also the Scardigli-Casadio-Carr-Lake (SCCL) approach. The fact that the standard Hawking temperature diverges for small mass black holes is one of the indicators that a theory of quantum gravity is needed. The GUP is such a candidate and has been shown to modify this behaviour in the standard $(3+1)$ -dimensional case (SCRAM phase). Since the GUP can for example be motivated by string theory which needs extra dimensions this strongly suggests that the cure of the temperature divergence should also work in higher dimensions.

In the former case, we have shown that for $n = 4$ spatial dimensions, the metric function admits an extremal solution whose temperature exhibits the SCRAM phase of the regular $(3+1)$ -D KMM black hole. Additionally, the solution reveals a conical singularity at the origin, which can be interpreted as a Barriola-Vileking like monopole. For $n > 4$, however, the GUP has no effect and the temperatures diverge as with the standard Schwarzschild solution.

We have also investigated a revised GUP approach that produces an alternate momentum measure that uniformly suppresses the GUP in the limit of large \vec{p} . In this case, the solution reveals a much richer thermodynamic behaviour that is characterized by a “lighthouse effect”. That is, for increasing $n > 4$, both the mass distribution and temperature oscillate as the black hole evaporates. This is possibly due to negative energy density contributions close to the origin, or alternatively due to the presence of tachyon states.

The metric function also admits multiple horizon structures depending on the black hole mass, relative to a critical value M_0 . This particular characteristic has the effect of dividing the solutions into two classes, *i.e.* small and large black holes.

A variety of future investigations are possible, in particular those which involve different interpretations of the GUP (e.g., a higher dimensional version of the metric derived in [125]). Alternatively, GUP-inspired Reissner-Nordström and Kerr metrics might introduce additional new physics similar to the lighthouse effect discussed herein.

CHAPTER

A

Appendix

A1 Notation and conventions

The notation chosen in this work mostly follows the standard notations in general relativity: Indices of four-dimensional tensors ¹ are denoted with lower-case greek letters, as in $X_{\alpha\beta\gamma\dots}^{\mu\nu\eta\dots}$. These indices run over $[0, 1, 2, 3]$ (or $[1, 2, 3, 4]$, if preferred). Three-dimensional tensors are denoted with lower-case latin letters, as in $X_{abc\dots}^{ijk\dots}$. These indices run over $[1, 2, 3]$. Explicitely higher dimensional spatial tensors are denoted with upper case latin letters, as in $X_{ABC\dots}^{IJK\dots}$. The indices run over $[1, 2, 3, \dots, n]$ in n spatial dimensions.

Einstein sum convention is applied all over the text. For symbols which do not follow the concept of covariance (i.e., not described with differential geometry), the index ordering (upper or lower) is arbitrarily chosen in order to meet Einstein sum convention. With such symbols, lower latin indices are also used for various kind of indices. For instance, state vector indices are typically given with lower case indices, but they do not count over $[0 \dots 3]$ but over $[1, \dots, N]$, where N is the number of state vector variables. Another example are Gaussian basis functions which run over a specific set $[1, \dots, N]$ where N is the typically the order of the method/number of basis points.

An higher-dimensional object *may* be written without indices. In general relativity, this concept is known as *abstract index notation* and allows to write simple contractions as scalar products, revealing a descriptive meaning of some terms. For covariant symbols, this notation is avoided within this text. However, it is widely adopted for other types, such as three-vectors or state vectors. Generally, the arrow in \vec{x} indicates that $\vec{x} = (x_1, x_2, x_3)$

² is a three-vector. In contrast, a symbol in bold typeface such as \mathbf{x} or \boldsymbol{x} only indicates that the symbol is an abstract object with one or more indices. For instance, fluxes \mathbf{F}^{ij} are written in bold, meaning that the fundamental object is F_k^{ij} (which however does not transform like a tensor). The shortened notation where only a few indices are written out emphasizes the implementation where only the $n \times n$ matrix is of interest. Therefore, the index-free notation is adopted *only* in situations when the clarity shall be preserved, for instance because objects are decorated with discreteness indicators. Another example is Q_k , this may indicate the k th component of the state vector Q , but Q_n^s is the whole state vector at spatial position x_n and time index t^s .

Furthermore, since this thesis deals with field theory, almost all objects are fields, i.e., $X = X(t, \vec{x})$. Again, this information can only be provided by context.

¹ or symbols, in general like the Christoffel symbols

² Intentionally, I do not formally distinguish between a definition $\vec{x} = (x_1, x_2, x_3)$ or $\vec{x} = (x_1, x_2, x_3)^T$, i.e., column and row vector, because the nature of the object typically depends on the surrounding: A numerical or CAS implementation or as part of a linear algebra calculation where its shape matters.

A1.1 Units

This work uses geometric units with gravitational coupling $G = 1$, speed of light $c = 1$. In astrophysical simulations, we set the solar mass (mass of the sun) $M_\odot = 1$ and measure subsequently all quantities in these units. In context of quantum mechanics, natural units are adopted, where furthermore the reduced Planck constant $\hbar = 1$ and the Boltzmann constant $k_B = 1$.

A1.2 Symbols

- States (state vectors) in PDEs are usually denoted as Q or u . V is typically the symbol for a primitive vector.
- Landau symbol \mathcal{O} for the physical “at the order of” or the computer science complexity.
- Levi-Civita-Symbol (total antisymmetric tensor); in two dimensions:

$$\epsilon^{ik} = \begin{pmatrix} 0 & 1 \\ -1 & 0 \end{pmatrix} \quad (\text{A1.1})$$

- Levi-Civita-Symbol in three dimensions: Spatial 3-Levi-Civita tensor density $\tilde{\epsilon}$ given by

$$\tilde{\epsilon}^{ijk} = \gamma^{-\frac{1}{2}} [ijk], \quad \tilde{\epsilon}_{ijk} = \gamma^{\frac{1}{2}} [ijk]. \quad (\text{A1.2})$$

where $[ijk]$ is the regular total antisymmetric symbol, commonly known as epsilon tensor/Levi-Civita tensor in flat space,

$$[ijk] = \begin{cases} 1 & \text{for even permutations of } (1, 2, 3), \\ -1 & \text{for odd permutations,} \\ 0 & \text{otherwise.} \end{cases}. \quad (\text{A1.3})$$

- $\Theta = \Theta(x)$ is in general the symbol for the Heaviside step function

$$\Theta(x) = \begin{cases} 1 & x > 0 \\ 0 & x < 0 \end{cases}, \quad (\text{A1.4})$$

but sometimes also used for other cases ³

³ An example is $Z_\mu = (\Theta, Z_i)$ in the FO-CCZ4 PDE (Chapter II).

- δ is either the Dirac delta function $\delta = \delta(x)$, also referred to as unit impulse or Dirac distribution, defined via its property

$$f(a) = \int f(x)\delta(a)dx. \quad (\text{A1.5})$$

In n spatial dimensions, the symbol is referred to as $\delta^{(n)}(\vec{x})$. δ can also be the discrete version, i.e., the Kronecker Delta

$$\delta_{ij} = \begin{cases} 1 & \text{if } i = j \\ 0 & \text{else (if } i \neq j) \end{cases} \quad (\text{A1.6})$$

- Lower incomplete Gamma function

$$\gamma(s; x) = \int_0^x dt t^{s-1} e^{-t} \quad (\text{A1.7})$$

- the p norm, or L^p norm, is defined as

$$|\vec{x}|_p = \left(\sum_{i=1}^k |x_i|^p \right)^{1/p} \quad (\text{A1.8})$$

with a vector $\vec{x} \in \mathbb{R}^k$ and $|r|$ with the absolute of a real number $r \in \mathbb{R}$.

The norms define L^p function spaces.

- Symmetric and antisymmetric part of tensors, exemplary for a $(0, 2)$ tensor: Symmetric part $T_{(ab)} = 1/2(T_{ab} + T_{ba})$, antisymmetric part $T_{[ab]} = 1/2(T_{ab} - T_{ba})$.
- Covariant derivative ∇_μ , exemplary for a scalar field ϕ , a covector field t^μ , a $(2, 0)$ tensor $A^{\mu\nu}$:

$$\nabla_\mu \phi = \partial_\mu \phi \quad (\text{A1.9})$$

$$\nabla_\alpha t^\nu = \partial_\alpha t^\nu + \Gamma_{\alpha\gamma}^\nu t^\gamma \quad (\text{A1.10})$$

$$\nabla_\lambda A^{\mu\nu} = \sum_\delta \partial_\lambda A^{\mu\nu} + \Gamma_{\delta\lambda}^\mu A^{\delta\nu} + \Gamma_{\delta\lambda}^\nu A^{\mu\delta} \quad (\text{A1.11})$$

- Lie derivative \mathcal{L}_ξ , for a vector field ξ_μ and the same fields from above:

$$\mathcal{L}_\xi \phi = \xi^\alpha \partial_\alpha \phi \quad (\text{A1.12})$$

$$\mathcal{L}_\xi t^\nu = \xi^\alpha \partial_\alpha t^\nu - t^\alpha \partial_\alpha \xi^\nu \quad (\text{A1.13})$$

$$\mathcal{L}_\xi A^{\mu\nu} = \xi^\alpha \partial_\alpha A^{\mu\nu} - \xi^\mu \partial_\alpha A^{\alpha\nu} - \xi^\nu \partial_\alpha A^{\mu\alpha} \quad (\text{A1.14})$$

Sometimes, \mathcal{L}_ξ is written as \mathcal{L}_ξ for brevity.

A1.3 Symbols with canonical physical meaning

- Christoffel symbols of first kind

$$\Gamma_{ij}^k = \frac{1}{2} g^{kl} (\partial_i g_{jl} + \partial_j g_{il} - \partial_l g_{ij}) \quad (\text{A1.15})$$

- 4-metric, expressed by ADM quantities:

$$g_{\mu\nu} = \begin{pmatrix} -\alpha^2 + \beta_i \beta^i & \beta_i \\ \beta_i & \gamma_{ij} \end{pmatrix} \quad (\text{A1.16})$$

- See Table A1.1 for an overview of symbols used within the context of quantum black holes.

A2 Convergence, consistency and stability of PDEs

This section shall briefly collect a couple of standard definitions which complement the introductory section 2 on page 18 about PDEs.

Definitions

The initial boundary value problem on the spatial domain Ω is defined as

$$\partial_t Q(t, x) = \mathcal{D} Q(t, x) \quad (\text{A2.1})$$

symbol	semantics
M	Generic total mass of a black hole
L	Any length scale
T	Hawking temperature
d	Number of total space-time dimensions
n	Number of total spatial dimensions
G_N	Newton's constant in 3+1 dimensions.
M_{Pl}	Planck mass in 3+1 dimensions.
L_{Pl}	Planck length in 3+1 dimensions.
$\mathbb{G}(\dots)$	Newton's constant as differential operator
M_*	Fundamental mass scale in any dimension
L_*	Fundamental length scale in any dimension
$\sqrt{\beta}$	Length scale in the GUP
$\mathcal{M}(r)$	Cumulative mass distribution
M_0	Mass of critical black hole configuration
r_0	Radius of critical black hole configuration
T_{\max}	Temperatur of critical black hole (maximum temperature)
\mathbb{T}_{ν}^{μ}	Nonlocal energy-momentum tensor
$\rho(\vec{x})$	Density distribution
$f_n(r)$	Metric function in n spatial dimensions
r_{\pm}	The inner and outer horizons radii.
r_0	The size of the extremal black hole configuration.
r_C	The critical radius, at this radius the temperatures are maximal.

Table A1.1: This is an overview of symbols as they are introduced and used in Chapter V, exclusively.

with solution vector Q and (spatial) differential operator \mathcal{D} , equipped with initial conditions $Q_0(t_0, x)$ and boundary conditions $Q_0(t, x), x \in \partial\Omega$.

For discretization, we define a set of discrete points x_i (not necessarily a grid) which cover the discretized domain $\tilde{\Omega}$, as well as time steps t^n (again not necessarily uniformly distributed). The real solution u_n^i is further approximated by a discretization in the solution vector space \tilde{u}_i^n , and the differential operator $\tilde{\mathcal{D}}$ which is acting on $\tilde{\Omega}$. Furthermore, we introduce a discrete time evolution operator \mathcal{T}_s which fulfills

$$f(t_2) = \mathcal{T}_{t_2-t_1} f(t_1), \quad \text{and} \quad \mathcal{T}_t \circ \mathcal{T}_s = \mathcal{T}_{t+s}, \quad (\text{A2.2})$$

where the later makes \mathcal{T}_s a member of a semi-group [227, 287]. This operator allows to write the IVP (A2.1) with discrete time evolution as

$$\tilde{u}(t + \Delta t) = \tilde{\mathcal{T}}_{\Delta t}^{\Delta} \tilde{u}(t). \quad (\text{A2.3})$$

We then define the

- Pointwise error $E_i^n = \tilde{u}_i^n - u_i^n$ and subsequent global error $|E(t)| = \left(\sum_{i,n} |E_i^n|^p \right)^{1/p}$ as L_p norm (A1.8) with typically $p = 1, 2$.
- Convergence $\leftrightarrow \lim_{\Delta \rightarrow 0} |E(t)| = 0 \quad \forall t$ ⁴
- Local truncation error $H_i^n = \tilde{\mathcal{D}}u - \mathcal{D}u$
- Truncation error $H(t) = (\tilde{\mathcal{T}}_{\Delta t}^{\Delta} - \mathcal{T}_{\Delta t}) u(t)$

⁴ This short notation used in this section is actually predicate logic, \rightarrow is the implication (material conditional), \equiv is the logic biconditional.

- Total variation diminishing (TVD) $\leftrightarrow |\tilde{\mathcal{T}}_{\Delta t}^{\Delta} u|_{TV} \leq |u|_{TV}$.
- Consistency $\leftrightarrow \lim_{\Delta \rightarrow 0} |H(t)| = 0 \forall t \in \mathbb{R}$
- Convergence order is $p \leftrightarrow |H(t)| = \mathcal{O}(\Delta^p)$.
- Stability $\leftrightarrow \sup_{u \neq 0} \frac{|H(t)|}{|u|} \leq C \quad \forall t$ with a constant $C \in \mathbb{R}$.
- Well-posedness iff $|u(t, x)| \leq k e^{\alpha t} |u_0(x)|$, with a norm $|\cdot|$ and k, α constants. The non-continuous dependency of the solution on the initial data is especially obvious for a small perturbation with $k \ll 1$ and $\alpha \gg 1$, which however will change the solution to a very different one in finite time.

Theorems for stability

For linear equations, there is the *Lax-Richtmeyer equivalence theorem* which reads in short [300, 389]

$$(\text{stable} \wedge \text{consistent}) \rightarrow \text{convergence}, . \quad (\text{A2.4})$$

A direct consequence is that (again only for linear systems) any scheme of order p has a global error $E(t) = \mathcal{O}(\Delta^p)$.

For nonlinear PDEs, there is the *Lax-Wendroff theorem* which states

$$(\text{convergent solution found}) \rightarrow \text{solution is weak}. \quad (\text{A2.5})$$

The total variation of a function $f(x)$ shall be defined as

$$|f|_{TV} = \sup_{h \rightarrow 0} \frac{1}{h} \int_{\Omega} |f(x) - f(x-h)| dx = \int_{\Omega} |f'(x)| dx, \quad (\text{A2.6})$$

where the second equivalence sign holds only if f is differentiable (i.e., the derivative exists). Most TV-stable schemes are TVD. Monotonicity \rightarrow TVD. Monotone schemes are at most first order accurate, monotonicity preserving schemes, but can archive high accuracy.

A3 ADER-DG vs RK-DG: Strong MPI scaling and performance comparison

In this section ⁵ we provide a detailed and quantitative performance analysis of the new ADER-DG schemes for the GRMHD equations proposed in this work. We compare CPU times and MPI scaling results for ADER-DG in comparison with classical Runge-Kutta DG (RKDG) schemes. We furthermore provide CPU time comparisons between ADER-DG and ADER-WENO finite-volume (FV) methods.

As first test we run the Michel accretion problem again on the domain $\Omega = [3, 5.5] \times [1, \pi-1]$ in two space dimensions using a sequence of successively refined meshes of $N_x \times N_x$ DG elements and $N_x(N+1) \times N_x(N+1)$ finite-volume zones until a final time of $t = 10$. We use a third-order ADER-DG scheme ($N = 2$) and compare with a third-order ADER-WENO finite-volume scheme, see [167, 177]. In order to make the comparison fair, the mesh of the FV scheme is $N + 1$ times finer than the one of the DG scheme, since the DG method has $N + 1$ degrees of freedom per cell and per space

⁵ Parts of the texts and results in this section are published in [194]. The benchmarks of this section belong to the hydrodynamics chapter III. In contrast, the numerical methods covered here belong to chapter I.

	N_x	L_2 error	L_∞ error	WCT [s]	TDU [s]
DG \mathcal{O}_3	6	2.53E-05	3.26E-05	15.9	1.0470E-04
	12	3.32E-06	4.46E-06	74.4	6.3726E-05
	18	1.01E-06	1.37E-06	193.5	4.9770E-05
	30	2.26E-07	3.07E-07	733.4	4.1173E-05
FV \mathcal{O}_3	18	2.77E-05	5.99E-05	37.7	5.1765E-04
	36	6.40E-06	1.72E-05	231.9	4.0117E-04
	54	2.73E-06	8.81E-06	694.0	3.5679E-04
	90	9.44E-07	3.78E-06	2754.8	3.0694E-04

dimension. The total number of degrees of freedom is therefore the same for both methods. We present the L_2 and L_∞ errors for the density ρ obtained with both methods. We also report the wall clock time (WCT) measured in seconds and the time needed by the scheme to update one single degree of freedom on one single CPU core (TDU), measured also in seconds. The inverse of this number represents the number of degrees of freedom that the scheme is able to update in one second on one CPU core and can be compared with other finite-volume and finite-difference methods. As computer hardware for this test we use one single CPU core of a workstation with an Intel i7-4770 CPU with 3.4 GHz clock speed and 16 GB of RAM. The results are shown in Table A3.1, from which it becomes clear that the ADER-DG scheme is faster and more accurate than the ADER finite-volume scheme using the same number of degrees of freedom. Similar results have already been reported in [167] and [163] for the Euler equations of hydrodynamics, the MHD equations and the compressible Navier-Stokes equations, using the unified framework of $P_N P_M$ schemes.

As second test case we take the large amplitude Alfvén wave problem in flat Minkowski spacetime described in [154] and also used later in [167] and [468]. We use the 3D computational domain $\Omega = [0, 2\pi]^3$, which is discretized with ADER-DG schemes of increasing order of accuracy in space and time and using a sequence of successively refined meshes of size $N_x \times N_x \times N_x$. To provide a direct comparison, we solve the same test problem also with high order Runge-Kutta DG schemes [143, 144]. Since ADER-DG schemes are uniformly high order accurate in space and time, for the RKDG method we use appropriate Runge-Kutta schemes in time whose temporal order of accuracy exactly matches the spatial one. In particular, we use the classical third and fourth-order RK schemes of [288], the fifth order Runge-Kutta scheme of [199] and the first one of the sixth order Runge-Kutta schemes proposed in [114]. Note that due to the well-known Butcher barriers that apply to high order RK schemes for nonlinear ODE systems, the fifth order RK scheme has six stages, and the sixth order RK scheme has seven stages. We run the test problem with both schemes without any limiter up to a final time of $t = 1$ and report the errors of the variable B_y measured in L_2 norm.

The computational results for ADER-DG and Runge-Kutta DG schemes are reported in Table A3.2, together with the measured wall clock times (WCT) in seconds and the time needed by each scheme to update one single degree of freedom (TDU) in microseconds. Again, the inverse of TDU in seconds represents the number of degrees of freedom that the scheme is

Table A3.1: Comparison of L_2 and L_∞ errors for the Michel accretion problem in 2D. Wall clock times (WCT) and CPU time per degree of freedom update (TDU) in seconds for a third-order ADER-DG scheme ($N = 2$) compared with a third-order ADER-WENO finite-volume (FV) scheme.

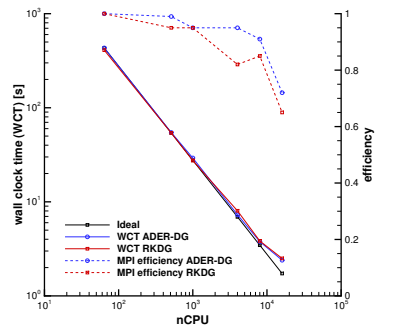


Figure A3.1: Strong scaling test for the 3D GRMHD equations and performance comparison between fourth-order ADER-DG and RKDG schemes ($N = 3$). The test case is the large amplitude Alfvén wave problem solved in 3D up to $t = 1$ on a uniform Cartesian mesh composed of $40 \times 40 \times 40$ elements. The results were obtained with a pure MPI implementation on the SuperMUC phase I system at the LRZ in Garching, Germany, using 64 to 16,000 CPU cores. On 16k cores, each MPI rank has only 4 elements to update.

N_x	L_2 error	L_2 order	WCT [s]	TDU [μ s]	N_x	L_2 error	L_2 order	WCT [s]	TDU [μ s]
ADER-DG ($N = 3$)					RKDG ($N = 3$)				
8	7.6396E-04		0.093	33.8	8	8.0909E-04		0.107	39.2
16	1.7575E-05	5.44	1.371	31.5	16	2.2921E-05	5.14	1.394	32.0
24	6.7968E-06	2.34	6.854	31.0	24	7.3453E-06	2.81	6.894	31.2
32	1.0537E-06	6.48	21.642	31.1	32	1.3793E-06	5.81	21.116	30.3
ADER-DG ($N = 4$)					RKDG ($N = 4$)				
8	6.6955E-05		0.363	46.8	8	6.8104E-05		0.456	51.4
16	2.2712E-06	4.88	5.696	45.9	16	2.3475E-06	4.86	6.666	51.0
24	3.3023E-07	4.76	28.036	44.9	24	3.3731E-07	4.78	29.186	45.3
32	7.4728E-08	5.17	89.271	45.2	32	7.7084E-08	5.13	87.115	43.4
ADER-DG ($N = 5$)					RKDG ($N = 5$)				
8	5.2967E-07		1.090	53.1	8	5.7398E-07		1.219	55.9
16	7.4886E-09	6.14	16.710	51.2	16	8.1461E-09	6.14	17.310	52.5
24	7.1879E-10	5.78	84.425	51.2	24	7.7634E-10	5.80	83.777	49.4
32	1.2738E-10	6.01	263.021	50.3	32	1.3924E-10	5.97	260.859	49.5

able to update in one second on one single CPU core and can be directly compared with existing finite-volume and finite-difference codes. We observe that the CPU times and error norms are comparable for both schemes. For all mesh sizes N_x and polynomial approximation degrees N we have used 512 CPU cores of the Phase I system of the SuperMUC of the LRZ in Garching, Germany. This means that for the coarsest mesh with $N_x = 8$, each MPI rank has only one single element to update. The results of Table A3.2 clearly show that for a small number of elements per MPI rank our *communication avoiding* ADER-DG schemes are computationally less expensive than RKDG schemes of the same order, since RKDG requires MPI communication in each Runge-Kutta stage. We finally run this test problem on a fixed grid of 64,000 elements ($N_x = 40$) using fourth-order ADER-DG and RKDG schemes on an increasing number of CPUs, from 64 to 16,000. The parallel implementation is based on pure MPI and thus each CPU core corresponds to one MPI rank. The speedup graph and the parallel efficiency as measured on the Phase I system of the SuperMUC supercomputer of the LRZ in Garching, Germany, are presented in Fig. A3.1. It shows the better MPI scaling of the communication avoiding ADER-DG schemes compared to conventional RKDG methods.

A4 FO-FCCZ4: a first-order fully covariant Z4 formulation

This section provides a *fully* covariant formulation of the (first order formulation of the) CCZ4 equations (Section 14 on page 52) as a proof of concept, i.e., it demonstrates the calculations necessary to derive such a set of equations. The concept follows [394]. A discussion about the practicability will be given in the end.

The general idea of this approach is to introduce a (non-evolved) background three-metric $\tilde{\gamma}_{ij}$ which, together with the new evolved metric ϵ_{ij} , composes the metric $\tilde{\gamma}_{ij}$ in the Cartesian coordinate system,

$$\tilde{\gamma}_{ij} := \mathring{\gamma}_{ij} + \varepsilon_{ij}. \quad (\text{A4.1})$$

In the following, a number of calculation rules are derived which define how the coordinate transformation is defined. These rules can then be applied to transform the right hand side/differential operator in the FO-CCZ4

Table A3.2: Accuracy and cost comparison between ADER-DG and RKDG schemes of different orders for the GRMHD equations in three space dimensions. The test problem is the large amplitude Alfvén wave solved in the domain $\Omega = [0, 2\pi]^3$ up to $t = 1$ on a sequence of successively refined Cartesian meshes with N_x^3 elements. The errors refer to the variable B_y . The table also contains total wall clock times (WCT) measured in seconds and the time needed by the scheme to update one single degree of freedom on one single CPU core (TDU) measured in microseconds. All simulations have been performed in parallel on 512 MPI ranks of the SuperMUC phase I system at the LRZ in Garching, Germany. Note that for the coarsest grid with $N_x = 8$, each MPI rank has only one single element to update.

The notation uses different decorators to express the belonging of a particular symbol to a particular reference frame. As a guide, for a given symbol φ , it is

$\tilde{\varphi}$ With tilde: Ordinary 3-symbol in Cartesian space

$\mathring{\varphi}$ Ring underlines that these quantities are relative to the background metric $\mathring{\gamma}_{ij}$ (i.e., measured in curved space)

φ four dimensional symbol

Furthermore, when applicable, this notation is used:

\mathcal{X}_{ij} Tensors, derived from covariant derivatives

X_{ij} Not transforming as tensors, as derived from partial derivatives

equations to the new coordinate system. Schematically,

$$\partial_t Q = \mathcal{R}(Q, \partial_i Q) \rightarrow \partial_t \dot{Q} = \mathcal{R}(\dot{Q}, \dot{\nabla}_i \dot{Q}) \quad (\text{A4.2})$$

To do so, the auxilliary quantities $X \in \{B_j^i, A_i, P_k, D_{ijk}\}$, as defined in (14.1), need to be replaced by variants \mathcal{X} which use the covariant derivative, furthermore the metric itself as well as the contracted Christoffel symbol $\hat{\Gamma}^i$. The time evolution $\partial_t \mathcal{X} = \partial_t X + \dots$ must be determined, furthermore the replacement law $\partial_i X = \partial_i \mathcal{X} + \dots$.

The vector of evolved quantities will then be

$$Q_{\text{FO-FCCZ4}} = (\epsilon_{ij}, K_{ij}, \Theta, \Lambda_i, \alpha, \beta^i, b_i, A_i, \mathcal{B}_j^i, \mathcal{D}_{ijk}, K, \phi, \mathcal{P}_k) \quad (\text{A4.3})$$

whereas the material parameters

$$Q_{\text{background}} = (\dot{\gamma}_{ij}, \dot{\Gamma}_{jk}^i) \quad (\text{A4.4})$$

need to be stored. Note that the transformations only add algebraic source terms, and thus the differential structure (hyperbolicity) of the FO-FCCZ4 system does not change.

Vector transformation

For a vector, the spatial covariant derivative respective to the $\dot{\tilde{\gamma}}$ metric is defined as

$$\dot{\nabla}_i X^k = \partial_i X^k + \dot{\Gamma}_{il}^k X^l, \quad \dot{\nabla}_i X_k = \partial_i X_k - \dot{\Gamma}_{ik}^l X_l, \quad (\text{A4.5})$$

Since $\dot{\Gamma}$ is related to the cartesian metric, $\dot{\Gamma}_{jk}^i = 0$, and therefore $\dot{\nabla}_i B_k = \partial_i X_k$, i.e., there is no need to change any occurrence of a spatial derivative on A_i and P_k .

(1,1)-tensor transformation

We recognize $B_k^i = \partial_k \beta^i$ being the evolved tensor in the FO-CCZ4 scheme, while $\dot{\mathcal{B}}_k^i := \dot{\nabla}_k \beta^i$ will be evolved in FO-FCCZ4. Its time evolution equation (14.20) gets another contribution

$$\partial_t \dot{\mathcal{B}}_k^i = \partial_t B_k^i + \dot{\Gamma}_{lk}^i \partial_t \beta^l, \quad (\text{A4.6})$$

where $\partial_t \beta^l$ is just the algebraic source term in (14.11). Occurrences of spatial derivatives on B_j^i have to be replaced according to

$$\partial_l B_k^i = \partial_l \dot{\mathcal{B}}_k^i - \partial_l (\dot{\Gamma}_{km}^i) \beta^m - \dot{\Gamma}_{km}^i \dot{\mathcal{B}}_l^m - \dot{\Gamma}_{km}^i \dot{\Gamma}_{nl}^m \beta^n \quad (\text{A4.7})$$

(0,3)-tensor transformation

In order to determine the replacement necessary for the time evolution $\partial_t D_{ijk}$ and spatial derivatives of $\partial_l D_{ijk}$, we define $2\dot{D}_{ijk} := \dot{D}_i \dot{\gamma}_{jk} = \dot{D}_i \varepsilon_{jk}$, so that $\dot{D}_i \varepsilon_{jk} = \partial_i \varepsilon_{jk} - \dot{\Gamma}_{ij}^l \varepsilon_{lk} - \dot{\Gamma}_{ik}^l \varepsilon_{lj} = \dot{D}_{ijk}$. The time evolution (14.21) is then replaced by

$$2 \partial_t \dot{D}_{ijk} = 2 \partial_t D_{ijk} - \dot{\Gamma}_{ij}^l \partial_t \varepsilon_{lk} - \dot{\Gamma}_{ik}^l \partial_t \varepsilon_{lj} \quad (\text{A4.8})$$

Spatial derivatives are however replaced by

$$\begin{aligned} 2 \partial_l D_{ijk} &= 2 \partial_l \dot{D}_{ijk} + \partial_l \partial_i \dot{\gamma}_{jk} + (\partial_l \dot{\Gamma}_{ij}^m) \varepsilon_{mk} \\ &\quad + (\partial_l \dot{\Gamma}_{ik}^m) \varepsilon_{mj} + \dot{\Gamma}_{ij}^m \partial_l \varepsilon_{mk} + \dot{\Gamma}_{ik}^m \partial_l \varepsilon_{mj}, \end{aligned} \quad (\text{A4.9})$$

with $\partial_i \varepsilon_{jk} = \dot{\nabla}_i \varepsilon_{jk} + \dot{\Gamma}_{ij}^l \varepsilon_{lk} + \dot{\Gamma}_{ik}^l \varepsilon_{lj}$.

Contracted Christoffel symbol

Instead of $\hat{\Gamma}^i$, the evolution variable in FO-FCCZ4 will be referred to as Λ^i , which is defined via the difference of the Christoffel symbols $\Delta^i_{kl} := \tilde{\Gamma}^i_{kl} - \hat{\Gamma}^i_{kl}$, which transforms like a vector. Its relationship to $\hat{\Gamma}^i$ can be derived as

$$\begin{aligned}\Lambda^i &:= \Delta^i + 2\tilde{Z}^i = \tilde{\gamma}^{kl}\Delta^i_{kl} + 2\tilde{Z}^i \\ &= \tilde{\gamma}^{kl}(\tilde{\Gamma}^i_{kl} - \hat{\Gamma}^i_{kl}) + 2\tilde{Z}^i \\ &= \tilde{\Gamma}^i - \tilde{\gamma}^{kl}\hat{\Gamma}^i_{kl} + 2\tilde{Z}^i = \hat{\Gamma}^i - \tilde{\gamma}^{kl}\hat{\Gamma}^i_{kl}.\end{aligned}\quad (\text{A4.10})$$

Therefore, the spatial and temporal derivatives are given by

$$\partial_t \hat{\Gamma}^i = \partial_t \Lambda^i + (\partial_t \tilde{\gamma}^{kl})\hat{\Gamma}^i_{kl} \quad (\text{A4.11})$$

$$\partial_i \hat{\Gamma}^j = \partial_i \Lambda^j + 2D_{ijk}\hat{\Gamma}^i_{kl} + \tilde{\gamma}_{kl}\partial_i \hat{\Gamma}^j_{kl} \quad (\text{A4.12})$$

A5 Boundary conditions for Einstein Equations

This appendix briefly reviews a number of boundary condition choices adopted within the implementation of the Einstein solver within the codes discussed in Chapter II.

When evolving full spacetimes of compact objects (i.e., extended or collapsed matter located within a small region around the origin of the coordinate system), boundary conditions must take care of the finite simulation domain (sometimes referred to as “finite volume effect”), i.e., the fact that the physical domain is by concept infinite while the numerical one is finite. Any kind of unphysical effects at this boundary, such as reflection of outgoing waves, shall be prevented.

In a cartesian grid, the box-like geometry of the boundary renders this requirement to a complex task. The grid-level solution is to overcome the cartesian geometry and to adopt a spherical one in the outer wave zone/near the boundary. Then, wave-absorbing Riemann solvers can be applied which have good properties for orthogonally arriving waves.

However, within the Einstein Toolkit, the application of radiative boundary conditions have turned out to be sufficiently successful for long-term evolutions (such as binary mergers) without significant reflections at the boundary. Therefore, the focus within this section is on that candidate, next to exact Riemann solvers. Other boundary conditions which were successfully adopted are periodic boundary conditions (i.e., evolving a *lattice* of black holes) and exact boundary conditions (not successful in black hole spacetimes, but sufficient for simpler benchmarks).

A5.1 Sommerfeld boundary conditions

This section shortly reviews a simple version of the Sommerfeld boundary conditions, also known as radiative boundary conditions. The key idea of the “radiative” boundary conditions is to solve a different PDE at the boundary which models radial outgoing scalar waves, independently for every component of the state vector for a given system. This PDE can be cast in a similar fully non-conservative way as the CCZ4 PDE system itself, i.e.,

$$\partial_t Q + B(Q)\nabla Q = S(Q). \quad (\text{A5.1})$$

A motivational ‘toy’ deviation introduces the scalar field $f = f(\vec{r}, t)$ as a place holder for a gravitational wave field, a component of the metric tensor or any other field from the FO-CCZ4 state vector. For f , the *outgoing radial wave assumption*

$$rf(r, t) = \text{const} \quad (\text{A5.2})$$

is claimed, with $r = |\vec{r}|$. The time derivative of this assumption gives a partial differential equation:

$$0 = \frac{d}{dt}(rf) = vf + r \left(\frac{\partial f}{\partial t} + \sum_i \frac{\partial f}{\partial r_i} \frac{dr_i}{dt} \right) \quad (\text{A5.3})$$

with a radial velocity $v = dr/dt$. The *radial wave assumption*

$$\frac{dr_i}{dt} = v^i \approx v e^i := v \frac{r^i}{r} \quad (\text{A5.4})$$

approximates the velocity \vec{v} as a radial velocity $v = |\vec{v}|$. v is now related to the propagation speed of the f which is the speed of light, i.e. $v = c \equiv 1$ (however, for the sake of clarity the symbol v is kept for the time being). One thus ends up with the nonconservative PDE

$$\partial_t f + v \frac{r^i}{r} \partial_i f = -v \frac{f}{r} \quad (\text{A5.5})$$

The outgoing radial wave assumption implies $\lim_{r \rightarrow \infty} f(r) = 0$. For some ADM variables (like α or γ_{ii}), the limits are $f_0 \neq 0$. In such a case, we define $g = f - f_0$, insert g at the place of f into the PDE and obtain for the actual f a different source term:

$$\partial_t f + v \frac{r^i}{r} \partial_i f = -\frac{f - f_0}{r} \quad (\text{A5.6})$$

This PDE can be seen as the generic case for an outgoing wave with value f_0 at the boundary.

In the CCZ4 system, we solve such a PDE for every single field of the 59 fields. This gives us 59 non-coupled differential equations.

To be explicit, (A5.6) shall be applied as follows: As initial data, the system’s solution at or near the boundary is taken. Depending on the numerical interpretation, one might also extrapolate the solution “to” or “beyond” the boundary to serve as initial data. The boundary conditions itself adopted while integrating (A5.6) are negligible, copy/outflow BC are appropriate.

Diffusive Boundaries

Solving a different PDE “at the boundary” is a blurry formulation. In a FD/FV code, where ghostzones are maintained for holding the information just outside the simulation domain, (A5.6) can be solved directly in the ghostzone, if the scheme is at least second order (so the ghostzones are three-dimensional). In a DG code, where no ghostzones exist, (A5.6) could be solved evolving the whole last DG patch with the boundary PDE. This either shifts the boundary into the simulation domain or is implemented in a way that the cell is evolved with the actual PDE (say FO-CCZ4) but the results of the boundary PDE are read off the lower-dimensional boundary.

This gives rise to decouple the two meanings of the term “boundary”: The mathematical simulation boundary does not necessarily need to correspond to the physical boundary. The generic formalization of the DG approach reads as follows: The prototypic PDE (A5.1) functions could be composed as a “meta” PDE where any PDE term $X \in \{B, S\}$ is substituted by

$$X = \alpha X_{\text{FO-CCZ4}} + (1 - \alpha) X_{\text{Boundary}} \quad (\text{A5.7})$$

Here, the scalar field α encodes the simulation domain, where $\alpha = 1$ means “within” the domain, $\alpha = 0$ means “outside” the domain and any $\alpha \in (0, 1)$ corresponds to the diffusive interface between inside and outside. An example for $\alpha(\vec{x})$ would be the radially symmetric Logistic function

$$\alpha(\vec{r}) = \frac{1}{1 + \exp \{-k(r - r_0)\}} \quad (\text{A5.8})$$

with r_0 encoding the de-facto extend of the physical domain (i.e., a typical value in a BNS merger would be $r_0 \sim 2000M$) and k encodes the width of the diffusive interface (a typical value would be $k = 1$). This idea was rigorously implemented for linear elasticity equations in [433], but without solving a PDE outside the physical domain.

A5.2 Exact Riemann Solver for wave-absorbing Boundary Conditions

For the FO-CCZ4 system the full eigenstructure is known, all eigenvalues and eigenvectors for typical gauge choices are provided at [168]. The pure computational costs of evaluating the full eigenvector system of FO-CCZ4 makes it way too expensive to adopt an exact Riemann solver in a numerical scheme. However, this cost might be worth being spent in the boundary: Ideally, thanks to AMR, there are only a small number of boundary cells. This was implemented in the robustness tests for FO-CCZ4, however *greasing waves* accumulate in the corners of the rectangular domains.

A6 Extracting gravitational waves

This appendix section is a tiny review of standard definitions in gravitational wave definitions (continuum) and their extraction in numerical simulations. For reviews, see e.g., [65, 80, 133].

Definitions

Gravitational waves are defined within linearized gravity, i.e., where the metric $\gamma_{\mu\nu} = \eta_{\mu\nu} + h_{\mu\nu}$ is the sum of the (Minkowski) vacuum $\eta_{\mu\nu}$ and a perturbation $h_{\mu\nu}$ which is small ($|h| \ll 1$). The wave equations for the perturbation are found after defining the trace reversed perturbation $\bar{h} = h - \frac{1}{2}\eta h^\alpha_\alpha$ and imposing the Coulomb gauge $\nabla_\mu \bar{h}^{\mu\nu} = 0$; they are given by the EFE $\nabla_\alpha \nabla^\alpha \bar{h}_{\mu\nu} = \square \bar{h}_{\mu\nu} = 0$, with the covariant d’Alambert operator \square . The remaining gauge freedom allows to fix transverse metric perturbations (yielding in a transverse traceless formulation), so that $\bar{h} = h$. In Cartesian coordinates, a gravitational wave (GW) propagating in z direction can then

be written as

$$h_{\mu\nu} = \begin{bmatrix} 0 & 0 & 0 & 0 \\ 0 & h_+ & h_\times & 0 \\ 0 & h_\times & -h_+ & 0 \\ 0 & 0 & 0 & 0 \end{bmatrix}.$$

Here, the scalars h_+ and h_\times are identified as the two polarization states of the wave. Typically, they are collected in a complex field $y := h_+ + ih_-$. The GW strain is then defined as $\xi_i = \frac{1}{2}\partial_t^2 h_{ij}\xi^j$. The experimentally accessible relative displacement $\delta\xi/\xi \sim h$ is proportional to h .

Implementation

The gravitational wave strains h_+ and h_- can be computed online in a time evolution code. At large distance from a central massive object (formally at infinity in Schwarzschild coordinates), typically at radius $R = \mathcal{O}(500)M$, where M is the mass of the spacetime, a curvature invariant (Weyl scalar Ψ_4 , in EinsteinToolkit following [44, 341]) is derived from the spacetime (i.e., from the Riemann or Weyl tensor which is derived from the 4-metric or the ADM quantities, see also [113, 340] for definitions). A spherical harmonic mode decomposition is then performed, where the GW DOF are encoded in the $l = 2, m = 2$ mode of Ψ_4^{lm} .

In a postprocessing step, the PyCactusET software is used for time integrating the strain $h_{+,\times}$ from Ψ_4 , following [384]. Figure 29.1 on page 97 shows an example of a GW signal from a binary neutron star merger obtained with this method, with a cutoff angular frequency $w_0 = 0.02$ for fixed frequency iteration.

A7 Adjusted GUP profiles

Figures A7.1 and A7.2 are provided as an alternative to display Figure 40.4 on page 120. The different metric functions $g_{00}(M)$ are plotted here in a single panel (for different M). The units are given in such a way that the large BH remnant is (arbitrarily) set to $r_1 = r_*$.

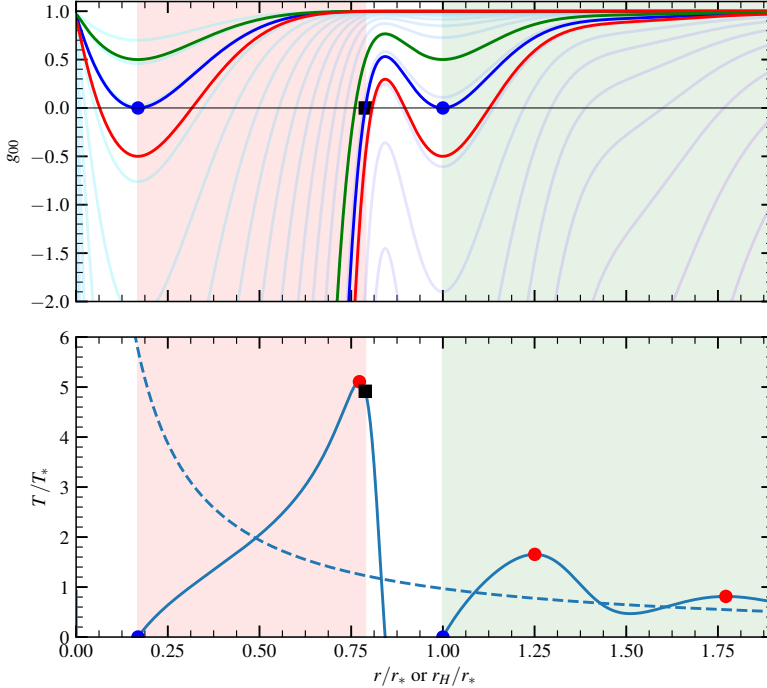


Figure A7.1: Upper panel: Metric component g_{00} for the adjusted GUP in $n = 8$ spatial dimensions over radius, for different masses (each line corresponds to a particular mass). Lower panel: Hawking temperature for a given horizon r_H for the adjusted GUP in $n = 8$ spatial dimensions, compared to the corresponding ordinary temperature of the Schwarzschild-Tangherlini metric. Radii are given in fundamental Planck units r_* , β is tuned for self-completeness (see main text).

Here, the two panels are put ontop of each other with a single radius axis, which however has a different meaning in the different panels. The diagram can be read as that for a metric profile (upper panel), at the outer horizon by going to the bottom panel, the temperature can be read off.

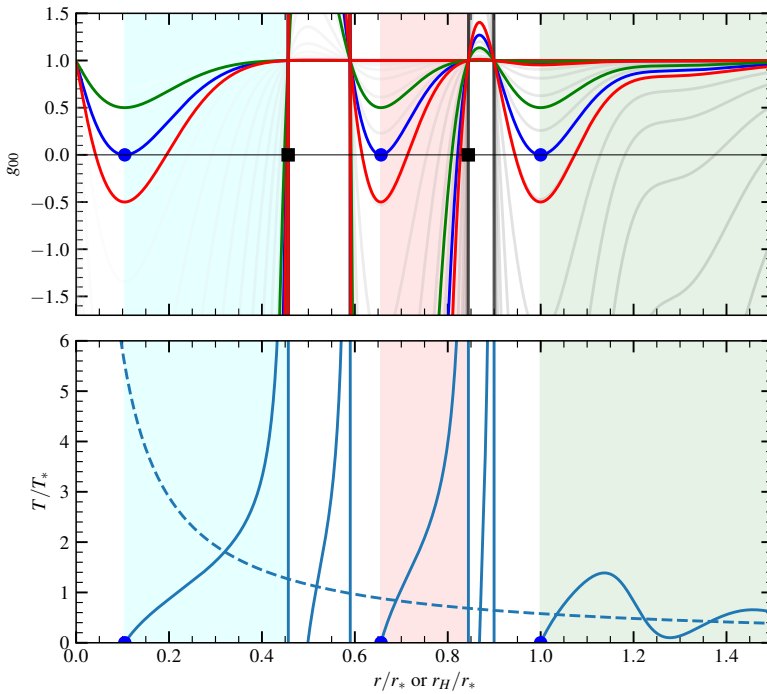


Figure A7.2: A diagram similar to Figure A7.1 but in $n = 9$ spatial dimensions. Adding only one dimension made the situation much more dramatic, as there is a third self-complete region and the regions are separated by very high temperature peaks $\sim 10^4 T_*$. It is likely that the semiclassical description fails to describe the inner part of the black hole already below $r < r_*$.

CHAPTER

B

References

This list helps to find and identify figures; they are labeled by their size and type (illustration or plots) and marked if they were not self-made.

B1 List of figures

2.1	PDE standard classification, TikZ figure, Exclusive material.	20
2.2	Riemann problem cartoon, TikZ figure, Exclusive material.	20
3.1	Expression tree cartoon, output by Mathematica, Exclusive material.	21
3.2	Sketch of a simple analog computing problem. Modified after [230]	22
4.1	MOL figure, Colorized from [402]	23
4.2	FD stencil motivational cartoon, Colorized from [217]	25
4.3	Sketch of the ghost cell ratio to payload ratio, Exclusive material.	25
5.1	Cartoon of a Finite Volume description, drawn with Inkscape, Exclusive material.	26
5.2	FV Higher order reconstruction, Cartoon drawn with Inkscape, Exclusive material.	27
5.3	2nd order FV ExaHyPE ghost cell problem, drawn with Inkscape, Exclusive material.	28
6.1	1D DG Motivational example, Matplotlib sketch, Published in [406]	29
6.2	Gaussian quadrature nodal basis examples, TikZ figure, Part of own publication [168].	31
6.3	Sketch of the DG-FV limiting projection/restriction, Modified after [170, 406]	35
7.1	Sketch of Carpet grid covering, Modified after [121]	37
7.2	Carpet FMR region sketch, Colorized from [403]	37
7.3	AMR vs unigrid in 2D, cartoon, Modified after [419]	37
7.4	Space-Tree illustration, TikZ figure Author: Fambri, Published in [196]	38
7.5	Idealized ExaHyPE/Peano task graph. Modiefied from [135].	38
7.6	Finite state machines of Peano, Modified after [459]	38
7.7	AMR and DG cartoon, drawn Author: Fambri, Published in [196]	39
7.8	Restriction and projection with AMR, drawin Author: Fambri, Published in [196]	40
8.1	FV vs DG derivatives for ID, drawn with Inkscape, Exclusive material.	41
10.1	EFE 2body parameter space, drawn with Inkscape. Exclusive material.	43
11.1	ADM definitions, drawn with Inkscape, Exclusive material.	45
11.2	Gauge orbits, Colorized from [326]	46
14.1	Jordan blocks cartoon (TikZ matrix), Exclusive material.	57
14.2	FO-CCZ4 system sparsity pattern, Part of own publication [168]	59
15.1	FO-CCZ4 System matrix, evaluation costs (Mathematica sketch) Exclusive material.	62
16.1	Linearized GW test, 1D cuts and time series Part of own publication [168]	64
16.2	Gauge-wave test, linear regime Part of own publication [168]	65
16.3	Gauge-wave test, nonlinear regime Part of own publication [168]	65
16.4	GaugeWave: Constraint evolution Part of own publication [168]	66
16.5	Robust scability test Part of own publication [168]	67
16.6	Single puncture black hole, constraint evolution Part of own publication [168]	69

16.7	BH-BH head-on collision, time evolution snapshots, Part of own publication [168]	70
17.1	BH Head-on collision, final snapshot and error time evolution, Part of own publication [168]	71
19.1	GRMHD State vector composition, Cartoon (tikZ), Exclusive material.	74
23.1	Michel accretion, Part of own publication [194]	82
23.2	Rest mass density in thick torus spacetime, Matplotlib, Exclusive material.	83
23.3	Zeipel's cylinders, Modified after [203]	83
23.4	Torus potentials, Modified after [203]	84
23.5	3D plot of a NS-Torus spacetime, rendered with Visit, Exclusive material.	84
23.6	Michel accretion, 3D Part of own publication [194]	85
24.1	Riemann problem convergence plot Part of own publication [194]	87
24.2	MHD Riemann problems Part of own publication [194]	87
24.3	RP1 Riemann problem (4 panels), Published in [196]	88
24.4	SRMHD Magnetic field loop, \vec{B} and ψ Part of own publication [194]	88
24.5	SRMHD blast wave, fields view Part of own publication [194]	89
24.6	SRMHD blast wave, grid Part of own publication [194]	90
24.7	SRMHD Orszag-Tang vortex Part of own publication [194]	91
25.1	Radial tori plots Part of own publication [194]	92
25.2	TOV preliminary data Exclusive material.	93
28.1	2D Cartoon, showing the inspiral of two NS with trajectories, Exclusive material.	96
29.1	Cartoon for the different time definitions for BNS, Exclusive material.	97
29.2	Three panels of the evolution of the lapse, with first and second derivative, Exclusive material.	98
30.1	TOV curves, showing different properties (Mass, tidal love number, tidal deformability, free-fall timescale), Exclusive material., only first panel was used in our publication [275].	99
31.1	BNS lifetime extrapolation to free fall timescale, Published in [275]	100
31.2	Lifetimes, exponential vs. linear extrapolation, taken from private referee communication about [275].	101
31.3	Universal relations plot, Published in [275]	102
32.1	BNS Lifetimes: Radius constraints, Published in [275]	104
32.2	Universal relations for different neutron star sizes, Published in [275]	104
33.1	BNS Lifetimes, convergence study plot for collision time and critical mass determination, Exclusive material.; part of private conversation with our referee within [275].	105
35.1	Brane world physics, figure modified from [132] [279])	107
35.2	Embedding of mini black holes in compactified extra dimensions, figure modified from [247].	107
36.1	Size vs Energy relations at the Planck scale, Published in [204]	108
37.1	Two panels: KMM metric and temperature (done myself), Published in [276]	109
38.1	Two panels: KMM in higher dimensions, metric and temperature, made with Mathematica, Published in [276]	112
39.1	Heisenberg microscope figure motivating sketch, Exclusive material.	114
39.2	Completness plot solved with GUP, Published in [290]	115
40.1	Besselintegrator, with Mathematica, Exclusive material.	117
40.2	Revised GUP, Mass distributions Published in [276]	118
40.3	Revised GUP, Temperature profiles Published in [276]	118
40.4	GUP potential for $n = 8$, selfmade (Python), Exclusive material.	120
A3.1	ADERDG vs RKDG strong scaling test (GRMHD), Published in [196]	128
A7.1	Adjusted GUP potential for $n = 8$, selfmade (Python), Exclusive material.	135
A7.2	Adjusted GUP potential for $n = 9$, selfmade (Python), Exclusive material.	135

B2 List of tables

14.1	FO-CCZ4 equation system, published in a similiar style in [274].	54
14.2	Helper quantities to define the Fo-CCZ4 system, inspired by Figure 14.1, but Exclusive material.. .	56
15.1	Performance results of generating an optimized Z4 implementation	62
16.1	Gauge Wave convergence table Part of own publication [168]	66
16.2	Convergence results for different BH coordinates, Part of own publication [168]	68
22.1	Overview of hydrodynamic benchmarks presented in chapter III	81
23.1	Convergence table for 2D Michel accretion	82
23.2	Convergence table for 2D spherical Kerr-Schild torus	85
23.3	Convergence table for 3D Michel accretion	86
24.1	Initial condition parameters for the MHD Riemann problem	86
24.2	Different Riemann problem curved background parameters	86
27.1	Nuclear EOS, small table: Central energy density and pressure	96
30.1	TOV maximum mass properties (mass, radius, compactness, baryon mass, tidal Love number, deformability, lifetime, literature reference)	99
31.1	Numerical results of BNS prompt collapse threshold mass	101
39.1	Overview of different GUP formulations in higher dimensions	116
40.1	Self-completeness values for the adjusted GUP	119
A1.1	List of symbols used in the GUP chapter	126
A3.1	Convergence norms for 2D Michel accretion	128
A3.2	ADERDG vs RKDG: Convergence table and runtime	129

B3 List of computer codes and libraries

This section lists codes which where used within this work, and adresses of internet websites where it is possible to download them.

B3.1 Initial data codes

The following codes are a selection of codes which I modified in order to be read in by the ExaHyPE code.

Lorene An extensive code and library for creating general-relativistic initial data for various compact objects, such as single rotating (magnetized) stars and binary neutron stars. Whenever binary neutron star systems were evolved in this work, the initial data stems from Lorene.

The code is available at lorene.obspm.fr or bitbucket.org/relastro/lorene as well as bitbucket.org/relastro/lorene-pointwiseexport.

RNSID A fast code for creating rotating neutron star initial data. This code is also part of the Einstein Toolkit, available at bitbucket.org/einsteintoolkit/einsteininitialdata but also at bitbucket.org/relastro/rnsid_standalone

ToriID A code for creating torus initial data (hydrodynamic quantities) on a given spacetime from a compact object. This code is available at bitbucket.org/relastro/toriid-standalone.

TOV Solvers Various codes for solving the TOV equations were used in this work, for instance the TOVSolver from EinsteinToolkit which is available as a standalone version at bitbucket.org/relastro/tovsolver_hybrid. Other codes used are the closed soure codes PizzaTOV and MargheritaTOV.

TwoPunctures The TwoPunctures code allows to create a spacetime with an arbitrary number of puncture black holes. A version is available at bitbucket.org/relastro/twopunctures-standalone.

B3.2 Time evolution codes

EinsteinToolkit The Einstein toolkit is a mature and extensive code collection which is available as open source at einsteintoolkit.org. It is a modular code based on Cactus. The Carpet code [220, 403, 405] provides by de-

fault the computational grid/meshing. The GRHydro and IllinoisGRMHD are two open source relativistic hydrodynamic codes which are part of the Einstein toolkit. However, there are also a large number of proprietary extensions/modules, such as any recent instance of the Whisky code.

WhiskyTHC The Whisky templated hydrodynamics code [371, 374]. It is the merger of various codes for evolving hydrodynamics, such as the Pizza code. It gets its name from templated C++ and is a high order FD/FV code for general relativistic hydrodynamics. It is supposed to be used within the Einstein toolkit. It is closed source.

ExaHyPE ExaHyPE is a next generation ADER-DG code with dynamic AMR. Its computational grid/meshing is provided by the Peano framework [109, 458]. It is available at exahype.eu and/or peano-framework.org.

SVEC The State vector enhancement code is a general relativistic magnetohydrodynamics code which can provide the PDE parts within the ExaHyPE framework. The code is available at bitbucket.org/svek/svec/ but also part of ExaHyPE.

Antelope Antelope is a code for solving Einsteins equations in a MoL framework, as provided by the Einstein toolkit. It has different formulations of Einsteins equations implemented (Z4, Z4c, CCZ4, FO-CCZ4) and is based on the TensorTemplates framework. At the time being, Antelope is closed source.

B4 List of co-authored papers

In the following, all co-authored papers written within the relativistic astrophysics group in Frankfurt are listed, with my individual contributions. See also page 169 for my curriculum vitae which lists all peer reviewed papers, i.e., also single authored publications and publications written not within the relativistic astrophysics group.

- [168] FO-CCZ4 (Chapter II): Parallel/comparative system matrix analysis with Mathematica and Maple, both for a preliminary FO-Z4 candidate as the FO-CCZ4 system, implementation and code generation for C++/Fortran/-TensorTemplates, running benchmarks and tests on different supercomputers, producing figures and texts for the paper, revised and improved article during review.
- [196] ADER-GRMHD (Chapter III): Implementation and tests with Fortran/C++ version of PDE system, producing texts for the paper, revised and improved article during review.
- [275] BNS Lifetimes (Chapter IV): Operating over 200 (completed) binary neutron star merger simulations on different supercomputers, Interpreting the data, Writing an analysis code and contributing to a comparative second one maintained by the coworker, Producing figures and text for the paper, Running a convergence study, testing different parameter spaces (like head-on mergers), revised and improved article during review.

Bibliography

- [1] B. P. Abbott, R. Abbott, T. D. Abbott, M. R. Abernathy, F. Acernese, K. Ackley, C. Adams, T. Adams, P. Addesso, R. X. Adhikari, and et al. Observation of Gravitational Waves from a Binary Black Hole Merger. *Phys. Rev. Lett.*, 116(6):061102, February 2016. (Cited on page 12.)
- [2] M. Abramowicz, M. Jaroszynski, and M. Sikora. Relativistic, accreting disks. *Astron. Astrophys.*, 63:221–224, February 1978. (Cited on page 83.)
- [3] R. J. Adler. Six easy roads to the Planck scale. *Am. J. Phys.*, 78:925–932, 2010. (Cited on pages 16 and 114.)
- [4] R. J. Adler, P. Chen, and D. I. Santiago. The generalized uncertainty principle and black hole remnants. *Gen.Rel.Grav.*, 33:2101–2108, 2001. (Cited on pages 16 and 108.)
- [5] Ronald J. Adler and David I. Santiago. On gravity and the uncertainty principle. *Mod. Phys. Lett.*, A14:1371, 1999. (Cited on pages 16 and 108.)
- [6] M. Alcubierre, B. Brügmann, P. Diener, M. Koppitz, D. Pollney, E. Seidel, and R. Takahashi. Gauge conditions for long-term numerical black hole evolutions without excision. *Phys. Rev. D*, 67(8):084023, April 2003. (Cited on page 47.)
- [7] Miguel Alcubierre. *Introduction to 3 + 1 Numerical Relativity*. Oxford University Press, Oxford, UK, 2008. (Cited on pages 44, 45, 46, 54, 68, and 97.)
- [8] Miguel Alcubierre, Gabrielle Allen, Carles Bona, David Fiske, Tom Goodale, F. Siddharta Guzmán, Ian Hawke, Scott H. Hawley, Sascha Husa, Michael Koppitz, Christiane Lechner, Denis Pollney, David Rideout, Marcelo Salgado, Erik Schnetter, Edward Seidel, Hisa aki Shinkai, Belá Szilágyi, Deirdre Shoemaker, Ryoji Takahashi, and Jeffrey Winicour. Toward standard testbeds for numerical relativity. *Class. Quantum Grav.*, 21:589, 2004. (Cited on pages 13, 64, 65, and 67.)
- [9] Miguel Alcubierre and Bernd Brügmann. Simple excision of a black hole in 3+1 numerical relativity. *Phys. Rev. D*, 63:104006, 2001. (Cited on page 47.)
- [10] M. G. Alford, L. Bovard, M. Hanuske, L. Rezzolla, and K. Schwenzer. Viscous Dissipation and Heat Conduction in Binary Neutron-Star Mergers. *Phys. Rev. Lett.*, 120(4):041101, January 2018. (Cited on page 15.)
- [11] D. Alic, C. Bona, and C. Bona-Casas. Towards a gauge-polyvalent numerical relativity code. *Phys. Rev. D*, 79(4):044026, February 2009. (Cited on pages 13, 51, 53, 58, 61, and 121.)
- [12] D. Alic, C. Bona-Casas, C. Bona, L. Rezzolla, and C. Palenzuela. Conformal and covariant formulation of the Z4 system with constraint-violation damping. *Phys. Rev. D*, 85(6):064040, March 2012. (Cited on pages 13, 52, 54, 55, 56, 57, 65, 66, 67, and 70.)
- [13] D. Alic, W. Kastaun, and L. Rezzolla. Constraint damping of the conformal and covariant formulation of the Z4 system in simulations of binary neutron stars. *Phys. Rev. D*, 88(6):064049, September 2013. (Cited on pages 13 and 52.)

- [14] M.A. Aloy and I. Cordero-Carrión. Minimally implicit Runge-Kutta methods for Resistive Relativistic MHD. *Journal of Physics: Conference Series*, 719:12015, 2016. DOI: 10.1088/1742-6596/719/1/012015. (Cited on page 14.)
- [15] G. Alzetta, D. Arndt, W. Bangerth, V. Boddu, B. Brands, D. Davydov, R. Gassmoeller, T. Heister, L. Heltai, K. Kormann, M. Kronbichler, M. Maier, J.-P. Pelteret, B. Turcksin, and D. Wells. The deal.II Library, Version 9.0. *Journal of Numerical Mathematics*, 2018, accepted. (Cited on page 63.)
- [16] Herbert Amann. *Ordinary Differential Equations: An Introduction to Nonlinear Analysis*. De Gruyter Studies in Mathematics, 1990. (Cited on page 33.)
- [17] D. Amati, M. Ciafaloni, and G. Veneziano. Superstring Collisions at Planckian Energies. *Phys. Lett.*, B197:81, 1987. (Cited on page 119.)
- [18] D. Amati, M. Ciafaloni, and G. Veneziano. Classical and Quantum Gravity Effects from Planckian Energy Superstring Collisions. *Int. J. Mod. Phys.*, A3:1615–1661, 1988. (Cited on page 119.)
- [19] D. Amati, M. Ciafaloni, and G. Veneziano. Can Space-Time Be Probed Below the String Size? *Phys.Lett.*, B216:41, 1989. (Cited on pages 16, 116, and 119.)
- [20] D. Amati, M. Ciafaloni, and G. Veneziano. Higher Order Gravitational Deflection and Soft Bremsstrahlung in Planckian Energy Superstring Collisions. *Nucl. Phys.*, B347:550–580, 1990. (Cited on page 119.)
- [21] D. Amati, M. Ciafaloni, and G. Veneziano. Effective action and all order gravitational eikonal at Planckian energies. *Nucl. Phys.*, B403:707–724, 1993. (Cited on pages 16, 116, and 119.)
- [22] M. Bugli and L. Del Zanna and N. Bucciantini. Dynamo action in thick discs around Kerr black holes: High-order resistive GRMHD simulations. *Mon. Not. R. Astron. Soc.*, 440:L41–L45, 2014. (Cited on page 14.)
- [23] M. Anderson, E. W. Hirschmann, L. Lehner, S. L. Liebling, P. M. Motl, D. Neilsen, C. Palenzuela, and J. E. Tohline. Magnetized Neutron-Star Mergers and Gravitational-Wave Signals. *Phys. Rev. Lett.*, 100(19):191101, May 2008. (Cited on page 14.)
- [24] Nils Andersson and Gregory L. Comer. Relativistic fluid dynamics: Physics for many different scales. *Living Rev. Relativ.*, 10(1):1–83, 2007. (Cited on page 73.)
- [25] A. M. Anile. *Relativistic Fluids and Magneto-fluids*. Cambridge University Press, February 1990. (Cited on pages 14 and 75.)
- [26] E. Annala, T. Gorda, A. Kurkela, and A. Vuorinen. Gravitational-Wave Constraints on the Neutron-Star-Matter Equation of State. *Phys. Rev. Lett.*, 120(17):172703, April 2018. (Cited on page 15.)
- [27] P. Anninos, C. Bryant, P.C. Fragile, A.M. Holgado, C. Lau, and D. Nemergut. Cosmosdg: An hp-adaptive discontinuous Galerkin code for hyper-resolved relativistic MHD. *The Astrophysical Journal Supplement Series*, 231(2):17, 2017. (Cited on page 14.)
- [28] Peter Anninos, K. Camarda, J. Libson, Joan Massó, E. Seidel, and W.-M. Suen. Finding apparent horizons in dynamic 3D numerical spacetimes. *Phys. Rev. D*, 58:024003, 1998. (Cited on page 97.)
- [29] Peter Anninos, P. Chris Fragile, and Jay D Salmonson. Cosmos++: Relativistic magnetohydrodynamics on unstructured grids with local adaptive refinement. *Astrophys. J.*, 635:723, 2005. (Cited on page 14.)
- [30] Marcus Ansorg, Bernd Brügmann, and Wolfgang Tichy. A single-domain spectral method for black hole puncture data. *Phys. Rev. D*, 70:064011, 2004. (Cited on pages 69 and 70.)

- [31] L. Antón, O. Zanotti, J. A. Miralles, J. M. Martí, J. M. Ibáñez, J. A. Font, and J. A. Pons. Numerical 3+1 General Relativistic Magnetohydrodynamics: A Local Characteristic Approach. *Astrophys. J.*, 637:296–312, January 2006. (Cited on pages 14 and 83.)
- [32] I. Antoniadis, N. Arkani-Hamed, S. Dimopoulos, and G.R. Dvali. New dimensions at a millimeter to a Fermi and superstrings at a TeV. *Phys.Lett.*, B436:257–263, 1998. (Cited on page 107.)
- [33] Thomas Appelquist, Hsin-Chia Cheng, and Bogdan A. Dobrescu. Bounds on universal extra dimensions. *Phys. Rev.*, D64:035002, 2001. (Cited on page 107.)
- [34] N. Arkani-Hamed, S. Dimopoulos, G. Dvali, and G. Gabadadze. Non-local modification of gravity and the cosmological constant problem. 2002. (Cited on pages 16 and 108.)
- [35] N. Arkani-Hamed, S. Dimopoulos, and G.R. Dvali. The Hierarchy problem and new dimensions at a millimeter. *Phys.Lett.*, B429:263–272, 1998. (Cited on page 107.)
- [36] N. Arkani-Hamed, S. Dimopoulos, and G.R. Dvali. Phenomenology, astrophysics and cosmology of theories with submillimeter dimensions and TeV scale quantum gravity. *Phys.Rev.*, D59:086004, 1999. (Cited on page 107.)
- [37] R. Arnowitt, S. Deser, and C. W. Misner. Republication of: The dynamics of general relativity. *General Relativity and Gravitation*, 40:1997–2027, September 2008. (Cited on page 44.)
- [38] A. Ashtekar. New Variables for Classical and Quantum Gravity. *Phys. Rev. Lett.*, 57:2244–2247, 1986. (Cited on page 44.)
- [39] A. Aurilia and E. Spallucci. Planck’s uncertainty principle and the saturation of Lorentz boosts by Planckian black holes. 2013. (Cited on page 16.)
- [40] M. C. Babuic et al. Implementation of standard testbeds for numerical relativity. *Class. Quantum Grav.*, 25:125012, 2008. (Cited on page 13.)
- [41] L. Baiotti, B. Giacomazzo, and L. Rezzolla. Accurate evolutions of inspiralling neutron-star binaries: Prompt and delayed collapse to a black hole. *Phys. Rev. D*, 78(8):084033, October 2008. (Cited on page 15.)
- [42] L. Baiotti, I. Hawke, P. J. Montero, F. Löffler, L. Rezzolla, N. Stergioulas, J. A. Font, and E. Seidel. Three-dimensional relativistic simulations of rotating neutron-star collapse to a Kerr black hole. *Phys. Rev. D*, 71(2):024035, January 2005. (Cited on page 14.)
- [43] Luca Baiotti and Luciano Rezzolla. Binary neutron-star mergers: a review of Einstein’s richest laboratory. *Rept. Prog. Phys.*, 80(9):096901, 2017. (Cited on pages 15 and 95.)
- [44] John Baker, Manuela Campanelli, Carlos O. Lousto, and Ryoji Takahashi. Modeling gravitational radiation from coalescing binary black holes. *Phys. Rev. D*, 65:124012, 2002. (Cited on page 134.)
- [45] John G. Baker, Manuela Campanelli, Frans Pretorius, and Yosef Zlochower. Comparisons of binary black hole merger waveforms. *Class. Quantum Grav.*, 24:S25–S31, 2007. (Cited on page 12.)
- [46] John G. Baker, Joan Centrella, Dae-Il Choi, Michael Koppitz, and James van Meter. Gravitational wave extraction from an inspiraling configuration of merging black holes. *Phys. Rev. Lett.*, 96:111102, 2006. (Cited on pages 12 and 97.)
- [47] H. Balasin and H. Nachbagauer. The energy-momentum tensor of a black hole, or what curves the Schwarzschild geometry? . *Class. Quant. Grav.*, 10:2271, 1993. (Cited on page 109.)
- [48] Herbert Balasin and Herbert Nachbagauer. Distributional energy momentum tensor of the Kerr-Newman space-time family. *Class.Quant.Grav.*, 11:1453–1462, 1994. (Cited on page 109.)

- [49] R. Balbinot, A. Fabbri, S. Fagnocchi, and R. Parentani. Hawking radiation from acoustic black holes, short distance and back-reaction effects. *Riv. Nuovo Cim.*, 28(3):1–55, 2005. (Cited on page 22.)
- [50] D. Balsara. Total Variation Diminishing Scheme for Relativistic Magnetohydrodynamics. *Astrophysical Journal Suppl. Series*, 132:83–101, January 2001. (Cited on page 86.)
- [51] D. S. Balsara, C. Altmann, C.-D. Munz, and M. Dumbser. A sub-cell based indicator for troubled zones in RKDG schemes and a novel class of hybrid RKDG+HWENO schemes. *Journal of Computational Physics*, 226:586–620, September 2007. (Cited on page 34.)
- [52] D. S. Balsara and D. Spicer. Maintaining Pressure Positivity in Magnetohydrodynamic Simulations. *Journal of Computational Physics*, 148:133–148, January 1999. (Cited on page 89.)
- [53] D.S. Balsara, C. Meyer, M. Dumbser, H. Du, and Z. Xu. Efficient implementation of ADER schemes for Euler and magnetohydrodynamical flows on structured meshes – Speed comparisons with Runge–Kutta methods. *Journal of Computational Physics*, 235:934–969, 2013. (Cited on page 36.)
- [54] W. Bangerth, R. Hartmann, and G. Kanschat. deal.II – a General Purpose Object Oriented Finite Element Library. *ACM Trans. Math. Softw.*, 33(4):24/1–24/27, 2007. (Cited on page 63.)
- [55] S. Banik, M. Hempel, and D. Bandyopadhyay. New Hyperon Equations of State for Supernovae and Neutron Stars in Density-dependent Hadron Field Theory. *Astrohys. J. Suppl.*, 214:22, October 2014. (Cited on pages 96 and 99.)
- [56] Tom Banks and Willy Fischler. A Model for high-energy scattering in quantum gravity. 1999. (Cited on page 107.)
- [57] F. Banyuls, J. A. Font, J. M. Ibáñez, J. M. Martí, and J. A. Miralles. Numerical 3+1 general-relativistic hydrodynamics: A local characteristic approach. *Astrophys. J.*, 476:221, 1997. (Cited on page 75.)
- [58] Carlos Barceló, Stefano Liberati, and Matt Visser. Analogue gravity. *Living Reviews in Relativity*, 14(1):3, May 2011. (Cited on page 22.)
- [59] Manuel Barriola and Alexander Vilenkin. Gravitational Field of a Global Monopole. *Phys. Rev. Lett.*, 63:341, 1989. (Cited on page 113.)
- [60] A. O. Barvinsky. Nonlocal action for long distance modifications of gravity theory. *Phys. Lett.*, B572:109–116, 2003. (Cited on pages 16 and 108.)
- [61] A. O. Barvinsky. On covariant long-distance modifications of Einstein theory and strong coupling problem. *Phys. Rev.*, D71:084007, 2005. (Cited on pages 16 and 108.)
- [62] A. O. Barvinsky. Dark energy and dark matter from nonlocal ghost-free gravity theory. *Phys. Lett.*, B710:12–16, 2012. (Cited on pages 16 and 108.)
- [63] T. W. Baumgarte and S. L. Shapiro. Numerical integration of Einstein’s field equations. *Phys. Rev. D*, 59(2):024007, January 1999. (Cited on pages 13, 48, and 96.)
- [64] T. W. Baumgarte and S. L. Shapiro. *Numerical Relativity: Solving Einstein’s Equations on the Computer*. Cambridge University Press, Cambridge, UK, 2010. (Cited on pages 44 and 96.)
- [65] T. W. Baumgarte and S. L. Shapiro. *Numerical Relativity: Solving Einstein’s Equations on the Computer*. Cambridge University Press, Cambridge UK, 2010. (Cited on page 133.)
- [66] G. Baumgartner, A. Auer, D. E. Bernholdt, A. Bibireata, V. Choppella, D. Cociorva, Xiaoyang Gao, R. J. Harrison, S. Hirata, S. Krishnamoorthy, S. Krishnan, Chi-chung Lam, Qingda Lu, M. Nooijen, R. M. Pitzer, J. Ramamujam, P. Sadayappan, and A. Sibiryakov. Synthesis of High-Performance Parallel Programs for a Class of ab Initio Quantum Chemistry Models. *Proceedings of the IEEE*, 93(2):276–292, Feb 2005. (Cited on page 63.)

- [67] Gerald Baumgartner, Daniel Cociorva, Chi-Chung Lam, and P. Sadayappan. Compile-Time Optimizations for Tensor Contraction Expressions. 2003. (Cited on page 63.)
- [68] A. Bauswein, T. W. Baumgarte, and H.-T. Janka. Prompt Merger Collapse and the Maximum Mass of Neutron Stars. *Phys. Rev. Lett.*, 111(13):131101, September 2013. (Cited on pages 15, 101, 102, and 103.)
- [69] A. Bauswein and H.-T. Janka. Measuring Neutron-Star Properties via Gravitational Waves from Neutron-Star Mergers. *Phys. Rev. Lett.*, 108(1):011101, January 2012. (Cited on page 95.)
- [70] A. Bauswein, O. Just, H.-T. Janka, and N. Stergioulas. Neutron-star Radius Constraints from GW170817 and Future Detections. *Astrophys. J. Lett.*, 850:L34, December 2017. (Cited on pages 15, 99, 103, 104, and 105.)
- [71] M. J. Berger and P. Colella. Local adaptive mesh refinement for shock hydrodynamics. *Journal of Computational Physics*, 82:64–84, 1989. (Cited on page 39.)
- [72] M. J. Berger and A. Jameson. Automatic adaptive grid refinement for the Euler equations. *AIAA Journal*, 23:561–568, 1985. (Cited on page 39.)
- [73] M. J. Berger and J. Oliger. Adaptive Mesh Refinement for Hyperbolic Partial Differential Equations. *Journal of Computational Physics*, 53:484, 1984. (Cited on page 39.)
- [74] A. Bermúdez and M.E. Vázquez. Upwind methods for hyperbolic conservation laws with source terms. *Computers and Fluids*, 23:1049–1071, 1994. (Cited on page 27.)
- [75] Sebastiano Bernuzzi and David Hilditch. Constraint violation in free evolution schemes: comparing BSSNOK with a conformal decomposition of Z4. *Phys. Rev. D*, 81:084003, 2010. (Cited on pages 13 and 51.)
- [76] Christopher P. L. Berry and Jonathan R. Gair. Linearized f(R) Gravity: Gravitational Radiation and Solar System Tests. *Phys. Rev.*, D83:104022, 2011. [Erratum: Phys. Rev.D85,089906(2012)]. (Cited on page 119.)
- [77] Horst Beyer and Olivier Sarbach. On the well posedness of the Baumgarte-Shapiro- Shibata-Nakamura formulation of Einstein’s field equations. *Phys. Rev. D*, 70:104004, 2004. (Cited on page 50.)
- [78] M. Bezares, C. Palenzuela, and C. Bona. Final fate of compact boson star mergers. *Phys. Rev. D*, 95(12):124005, June 2017. (Cited on page 13.)
- [79] L. Bildsten and C. Cutler. Tidal interactions of inspiraling compact binaries. *Astrophys. J.*, 400:175–180, November 1992. (Cited on page 99.)
- [80] N. T. Bishop and L. Rezzolla. Extraction of gravitational waves in numerical relativity. *Living Reviews in Relativity*, 19:2, October 2016. (Cited on page 133.)
- [81] Jiří Bičák and Jacek Tafel. Exact solutions and their interpretation - session A1. *Gen. Rel. Grav.*, 46(5):1685, 2014. (Cited on page 22.)
- [82] M. Bleicher and P. Nicolini. Large extra dimensions and small black holes at the LHC. *J. Phys. Conf. Ser.*, 237:012008, 2010. (Cited on page 107.)
- [83] Marcus Bleicher and Piero Nicolini. Mini-review on mini-black holes from the mini-Big Bang. *Astron. Nachr.*, 335:605, 2014. (Cited on page 107.)
- [84] C. Bona, C. Bona-Casas, and C. Palenzuela. Action principle for Numerical Relativity evolution systems. *Phys. Rev. D*, 82:124010, 2010. (Cited on page 50.)
- [85] C. Bona, T. Ledvinka, C. Palenzuela, and M. Zácek. General-covariant evolution formalism for numerical relativity. *Phys. Rev. D*, 67(10):104005, May 2003. (Cited on pages 13, 50, 53, and 61.)

- [86] C. Bona, T. Ledvinka, C. Palenzuela, and M. Zácek. Symmetry-breaking mechanism for the Z4 general-covariant evolution system. *Phys. Rev. D*, 69(6):064036, March 2004. (Cited on pages 13, 50, 60, and 61.)
- [87] C. Bona, L. Lehner, and C. Palenzuela-Luque. Geometrically motivated hyperbolic coordinate conditions for numerical relativity: Analysis, issues and implementations. *Phys. Rev. D*, 72:104009, 2005. (Cited on pages 47 and 61.)
- [88] C. Bona, J. Massó, E. Seidel, and J. Stela. New Formalism for Numerical Relativity. *Phys. Rev. Lett.*, 75:600–603, July 1995. (Cited on page 47.)
- [89] C. Bona, Joan Massó, E. Seidel, and J. Stela. First order hyperbolic formalism for numerical relativity. *Phys. Rev. D*, 56:3405–3415, 1997. (Cited on pages 58 and 121.)
- [90] C. Bona and C. Palenzuela. Dynamical shift conditions for the Z4 and BSSN formalisms. *Phys. Rev. D*, 69(10):104003, May 2004. (Cited on pages 60 and 61.)
- [91] C. Bona, C. Palenzuela-Luque, and C. Bona-Casas. *Elements of Numerical Relativity and Relativistic Hydrodynamics: From Einstein's Equations to Astrophysical Simulations*. Lecture Notes in Physics. Springer, Berlin Heidelberg, 2009. (Cited on page 44.)
- [92] S. Bonazzola, E. Gourgoulhon, and J. A. Marck. Numerical models of irrotational binary neutron stars in general relativity. *Phys. Rev. Lett.*, 82:892, 1999. (Cited on page 99.)
- [93] Nick Bostrom. *Superintelligence: Paths, Dangers, Strategies*. Oxford University Press, 2014. (Cited on page 21.)
- [94] R. Bousso and S. W. Hawking. Pair creation of black holes during inflation. *Phys. Rev.*, D54:6312–6322, 1996. (Cited on page 119.)
- [95] L. Bovard, D. Martin, F. Guercilena, A. Arcones, L. Rezzolla, and O. Korobkin. On r-process nucleosynthesis from matter ejected in binary neutron star mergers. *Phys. Rev. D*, 96:124005, December 2017. (Cited on pages 15 and 96.)
- [96] G. Bozzola, N. Stergioulas, and A. Bauswein. Universal relations for differentially rotating relativistic stars at the threshold to collapse. *ArXiv e-prints*, September 2017. (Cited on page 15.)
- [97] S. Brandt and B. Brügmann. A simple construction of initial data for multiple black holes. *Phys. Rev. Lett.*, 78(19):3606–3609, 1997. (Cited on page 68.)
- [98] C. Breu and L. Rezzolla. Maximum mass, moment of inertia and compactness of relativistic stars. *Mon. Not. R. Astron. Soc.*, 459:646–656, June 2016. (Cited on page 100.)
- [99] David Brown, Peter Diener, Olivier Sarbach, Erik Schnetter, and Manuel Tiglio. Turduckening black holes: an analytical and computational study. *Phys. Rev. D*, 79:044023, 2009. (Cited on page 13.)
- [100] David J. Brown. Covariant formulations of Baumgarte, Shapiro, Shibata, and Nakamura and the standard gauge. *Phys. Rev. D*, 79(10):104029, May 2009. (Cited on pages 13, 48, 49, and 96.)
- [101] J. D. Brown, P. Diener, S. E. Field, J. S. Hesthaven, F. Herrmann, A. H. Mroué, O. Sarbach, E. Schnetter, M. Tiglio, and M. Wagman. Numerical simulations with a first-order BSSN formulation of Einstein's field equations. *Phys. Rev. D*, 85(8):084004, April 2012. (Cited on pages 13, 53, 58, 65, and 69.)
- [102] Lars Brucher. Automatic Feynman diagram calculation with xloops: A Short overview. In *6th Rhine Workshop on Computer Algebra Sankt Augustin, Germany, March 31-April 3, 1998*, 1998. (Cited on page 22.)
- [103] B. Brügmann, J. A. González, M. Hannam, S. Husa, U. Sperhake, and W. Tichy. Calibration of moving puncture simulations. *Phys. Rev. D*, 77(2):024027, January 2008. (Cited on page 48.)

- [104] Bernd Brügmann, José A. González, Mark Hannam, Sascha Husa, Ulrich Sperhake, and Wolfgang Tichy. Calibration of moving puncture simulations. *Phys. Rev. D*, 77:024027, 2008. gr-qc/0610128. (Cited on page 12.)
- [105] N. Bucciantini and L. Del Zanna. General relativistic magnetohydrodynamics in axisymmetric dynamical spacetimes: the X-ECHO code. *Astron. Astrophys.*, 528:A101, April 2011. (Cited on page 14.)
- [106] N. Bucciantini and L. Del Zanna. A fully covariant mean-field dynamo closure for numerical 3 + 1 resistive GRMHD. *Mon. Not. R. Astron. Soc.*, 428:71–85, January 2013. (Cited on page 14.)
- [107] M. Bugner, T. Dietrich, S. Bernuzzi, A. Weyhausen, and B. Brügmann. Solving 3D relativistic hydrodynamical problems with weighted essentially nonoscillatory discontinuous Galerkin methods. *Phys. Rev. D*, 94(8):084004, October 2016. (Cited on pages 13 and 14.)
- [108] Marcus Bugner. *Discontinuous galerkin methods for general relativistic hydrodynamics*. PhD thesis, Friedrich-Schiller-Universität Jena, Jan 2018. (Cited on page 13.)
- [109] H.J. Bungartz, M. Mehl, T. Neckel, and T. Weinzierl. The PDE framework Peano applied to fluid dynamics: An efficient implementation of a parallel multiscale fluid dynamics solver on octree-like adaptive Cartesian grids. *Computational Mechanics*, 46:103–114, 2010. (Cited on pages 39 and 139.)
- [110] A. Buonanno and T. Damour. Effective one-body approach to general relativistic two-body dynamics. *Phys. Rev. D*, 59(8):084006, April 1999. (Cited on page 44.)
- [111] Alessandra Buonanno and B. S. Sathyaprakash. Sources of Gravitational Waves: Theory and Observations. pages 287–346. 2014. (Cited on page 43.)
- [112] G. F. Burgio, A. Drago, G. Pagliara, H.-J. Schulze, and J.-B. Wei. Are Small Radii of Compact Stars Ruled out by GW170817/AT2017gfo? *Astrophys. J.*, 860:139, June 2018. (Cited on page 15.)
- [113] Lior M. Burko, Thomas W. Baumgarte, and Christopher Beetle. Towards a novel wave-extraction method for numerical relativity: III. analytical examples for the Beetle–Burko radiation scalar. *Phys. Rev. D*, 73:024002, 2006. (Cited on page 134.)
- [114] J.C. Butcher. On Runge–Kutta processes of high order. *Journal of the Australian Mathematical Society*, 4(2):179–194, 1964. (Cited on page 128.)
- [115] Gianluca Calcagni, Leonardo Modesto, and Piero Nicolini. Super-accelerating bouncing cosmology in asymptotically-free non-local gravity. *Eur. Phys. J.*, C74(8):2999, 2014. (Cited on pages 16 and 108.)
- [116] Xavier Calmet. A Review of Quantum Gravity at the Large Hadron Collider. *Mod. Phys. Lett.*, A25:1553–1579, 2010. (Cited on page 107.)
- [117] M. Campanelli, C. O. Lousto, P. Marronetti, and Y. Zlochower. Accurate Evolutions of Orbiting Black-Hole Binaries without Excision. *Phys. Rev. Lett.*, 96(11):111101, March 2006. (Cited on pages 12 and 97.)
- [118] Z. Cao and D. Hilditch. Numerical stability of the Z4c formulation of general relativity. *Phys. Rev. D*, 85(12):124032, June 2012. (Cited on pages 51, 55, and 67.)
- [119] S. Capozziello, A. Stabile, and A. Troisi. The Newtonian Limit of f(R) gravity. *Phys. Rev. D*, 76:104019, 2007. (Cited on page 119.)
- [120] Salvatore Capozziello, Mariafelicia De Laurentis, and Valerio Faraoni. A Bird’s eye view of f(R)-gravity. *Open Astron. J.*, 3:49, 2010. (Cited on page 119.)
- [121] Adaptive mesh refinement with Carpet. <http://www.carpetcode.org/>. (Cited on pages 37 and 136.)

- [122] B. Carr. Black holes, the generalized uncertainty principle and higher dimensions. *Mod. Phys. Lett. A*, 28:1340011, 2013. (Cited on pages 16 and 115.)
- [123] B. J. Carr. The Black Hole Uncertainty Principle Correspondence. *Springer Proc. Phys.*, 170:159–167, 2016. (Cited on pages 16, 114, and 115.)
- [124] B. J. Carr and S.W. Hawking. Black holes in the early Universe. *Mon. Not. Roy. Astron. Soc.*, 168:399–415, 1974. (Cited on page 119.)
- [125] Bernard J. Carr, Jonas Mureika, and Piero Nicolini. Sub-Planckian black holes and the Generalized Uncertainty Principle. *JHEP*, 07:052, 2015. (Cited on pages 16 and 122.)
- [126] B. J. Carr. Quantum Black Holes as the Link Between Microphysics and Macrophysics. *Springer Proc. Phys.*, 208:85–94, 2018. (Cited on pages 16 and 115.)
- [127] A. Casanova and E. Spallucci. TeV mini black hole decay at future colliders. *Class.Quant.Grav.*, 23:R45–R62, 2006. (Cited on page 107.)
- [128] E. Casoni, J. Peraire, and A. Huerta. One-dimensional shock-capturing for high-order discontinuous Galerkin methods. *International Journal for Numerical Methods in Fluids*, 71(6):737–755, 2013. (Cited on page 35.)
- [129] M.J. Castro, J.M. Gallardo, and C. Parés. High-order finite volume schemes based on reconstruction of states for solving hyperbolic systems with nonconservative products. applications to shallow-water systems. *Mathematics of Computation*, 75:1103–1134, 2006. (Cited on pages 28, 31, 32, 78, and 121.)
- [130] M.J. Castro, A. Pardo, C. Parés, and E.F. Toro. On some fast well-balanced first order solvers for nonconservative systems. *Mathematics of Computation*, 79:1427–1472, 2010. (Cited on pages 28 and 78.)
- [131] M. Cavaglia. Black hole and brane production in TeV gravity: A Review. *Int.J.Mod.Phys.*, A18:1843–1882, 2003. (Cited on page 107.)
- [132] Marco Cavaglia. Black hole and brane production in TeV gravity: A Review. *Int.J.Mod.Phys.*, A18:1843–1882, 2003. (Cited on pages 107 and 137.)
- [133] J. Centrella, J. G. Baker, B. J. Kelly, and J. R. van Meter. Black-hole binaries, gravitational waves, and numerical relativity. *Reviews of Modern Physics*, 82:3069–3119, October 2010. (Cited on page 133.)
- [134] J. Cesenek, M. Feistauer, J. Horacek, V. Kucera, and J. Prokopova. Simulation of compressible viscous flow in time-dependent domains. *Applied Mathematics and Computation*, 219:7139–7150, 2013. (Cited on page 34.)
- [135] Dominic E. Charrier and Tobias Weinzierl. Stop talking to me - a communication-avoiding ADER-DG realisation. 2018. (Cited on pages 12, 14, 17, 38, 40, and 136.)
- [136] P. Chen and R. J. Adler. Black hole remnants and dark matter. *Nucl.Phys.Proc.Suppl.*, 124:103–106, 2003. (Cited on page 16.)
- [137] S. Clain, S. Diot, and R. Loubère. A high-order finite volume method for systems of conservation laws–multi-dimensional optimal order detection (MOOD). *Journal of Computational Physics*, 230(10):4028 – 4050, 2011. (Cited on page 34.)
- [138] B. Cockburn. The Runge Kutta Discontinuous Galerkin Method for Conservation Laws V Multidimensional Systems. *Journal of Computational Physics*, 141:199–224, April 1998. (Cited on page 34.)
- [139] B. Cockburn. Discontinuous Galerkin methods. *Zamm*, 83(11):731–754, November 2003. (Cited on page 30.)
- [140] B. Cockburn, S. Hou, and C.-W. Shu. TVB Runge Kutta Local Projection Discontinuous Galerkin Finite Element Method for Conservation Laws IV: The Multidimensional Case. *Math. Comp.*, 54:545, 1990. (Cited on page 30.)

- [141] B. Cockburn, G. E. Karniadakis, and C.-W. Shu. *Discontinuous Galerkin Methods: Theory, Computation and Applications*. Lecture Notes on Computational Science and Engineering. Springer, 2000. (Cited on page 30.)
- [142] B. Cockburn, S.-Y. Lin, and C.-W. Shu. TVB Runge Kutta Local Projection Discontinuous Galerkin Finite Element Method for Conservation Laws III: One-Dimensional Systems. *Journal of Computational Physics*, 84:90, September 1989. (Cited on page 30.)
- [143] B. Cockburn and C.W. Shu. The Runge–Kutta discontinuous Galerkin method for conservation laws V: multidimensional systems. *Journal of Computational Physics*, 141(2):199–224, 1998. (Cited on pages 30 and 128.)
- [144] Bernardo Cockburn and Chi-Wang Shu. Runge-Kutta discontinuous Galerkin methods for convection-dominated problems. *Journal of Scientific Computing*, 16(3):173, 2001. (Cited on pages 30 and 128.)
- [145] G. Cognola, E. Elizalde, S. Nojiri, S. D. Odintsov, L. Sebastiani, and S. Zerbini. A Class of viable modified f(R) gravities describing inflation and the onset of accelerated expansion. *Phys. Rev.*, D77:046009, 2008. (Cited on page 119.)
- [146] T. G. Cowling. The non-radial oscillations of polytropic stars. *Mon. Not. R. Astron. Soc.*, 101:367, 1941. (Cited on page 78.)
- [147] I. Cravero and M. Semplice. On the accuracy of weno and cweno reconstructions of third order on nonuniform meshes. *Journal of Scientific Computing*, 67(3):1219–1246, 2016. (Cited on page 39.)
- [148] M. MacCallum D. Kramer, H. Stephani and E. Herlt. *Exact Solutions of Einstein’s Field Equations*. Cambridge University Press, Cambridge, 1980. (Cited on page 43.)
- [149] G. Dal Maso, P. G. LeFloch, and F. Murat. Definition and weak stability of nonconservative products. *Journal de mathématiques pures et appliquées*, 74:483–548, 1995. (Cited on page 32.)
- [150] Thibault Damour. Introductory lectures on the Effective One Body formalism. *Int. J. Mod. Phys.*, A23:1130–1148, 2008. (Cited on page 44.)
- [151] Thibault Damour, Eric Gourgoulhon, and Philippe Grandclément. Circular orbits of corotating binary black holes: Comparison between analytical and numerical results. *Phys. Rev. D*, 66:024007, 2002. (Cited on page 99.)
- [152] A. DeBenedictis. *Developments in black hole research: classical, semi-classical, and quantum*, pages 371–426. Classical and Quantum Gravity Research. Nova Science Publishers, May 2008. (Cited on page 109.)
- [153] A. Dedner, F. Kemm, D. Kröner, C. D. Munz, T. Schnitzer, and M. Wesenberg. Hyperbolic Divergence Cleaning for the MHD Equations. *Journal of Computational Physics*, 175:645–673, January 2002. (Cited on pages 51, 55, 58, and 80.)
- [154] L. Del Zanna, O. Zanotti, N. Bucciantini, and P. Londrillo. ECHO: a Eulerian conservative high-order scheme for general relativistic magnetohydrodynamics and magnetodynamics. *Astron. Astrophys.*, 473:11–30, October 2007. (Cited on pages 75, 83, 90, and 128.)
- [155] T. Dietrich and M. Ujevic. Modeling dynamical ejecta from binary neutron star mergers and implications for electromagnetic counterparts. *Classical and Quantum Gravity*, 34(10):105014, May 2017. (Cited on page 15.)
- [156] Savas Dimopoulos and Greg L. Landsberg. Black holes at the LHC. *Phys.Rev.Lett.*, 87:161602, 2001. (Cited on page 107.)
- [157] K. Dionysopoulou, D. Alic, C. Palenzuela, L. Rezzolla, and B. Giacomazzo. General-relativistic resistive magnetohydrodynamics in three dimensions: Formulation and tests. *Phys. Rev. D*, 88(4):044020, August 2013. (Cited on pages 14, 80, and 90.)

- [158] S. Diot, R. Loubère, and S. Clain. The MOOD method in the three-dimensional case: Very-high-order finite volume method for hyperbolic systems. *International Journal of Numerical Methods in Fluids*, 73:362–392, 2013. (Cited on page 34.)
- [159] Alain R. P. Dirkes, Michael Maziashvili, and Zurab K. Silagadze. Black hole remnants due to Planck-length deformed QFT. *Int. J. Mod. Phys.*, D25(02):1650015, 2015. (Cited on pages 16 and 116.)
- [160] M. D. Duez, Y. T. Liu, S. L. Shapiro, and B. C. Stephens. General relativistic hydrodynamics with viscosity: Contraction, catastrophic collapse, and disk formation in hypermassive neutron stars. *Phys. Rev. D*, 69(10):104030, May 2004. (Cited on page 15.)
- [161] M. D. Duez, Y. T. Liu, S. L. Shapiro, and B. C. Stephens. Relativistic magnetohydrodynamics in dynamical spacetimes: Numerical methods and tests. *Phys. Rev. D*, 72(2):024028, July 2005. (Cited on page 14.)
- [162] M. Dumbser. *Arbitrary High Order Schemes for the Solution of Hyperbolic Conservation Laws in Complex Domains*. Shaker Verlag, Aachen, 2005. (Cited on page 33.)
- [163] M. Dumbser. Arbitrary high order PNPM schemes on unstructured meshes for the compressible Navier–Stokes equations. *Computers & Fluids*, 39:60–76, 2010. (Cited on pages 30 and 128.)
- [164] M. Dumbser. Arbitrary high order PNPM schemes on unstructured meshes for the compressible Navier–Stokes equations. *Computers & Fluids*, 39:60–76, 2010. (Cited on page 30.)
- [165] M. Dumbser and D. S. Balsara. A new efficient formulation of the HLLEM riemann solver for general conservative and non-conservative hyperbolic systems. *Journal of Computational Physics*, 304:275–319, 2016. (Cited on page 33.)
- [166] M. Dumbser, M. Castro, C. Parés, and E.F. Toro. ADER schemes on unstructured meshes for non-conservative hyperbolic systems: Applications to geophysical flows. *Computers and Fluids*, 38:1731–1748, 2009. (Cited on pages 13, 31, 34, and 121.)
- [167] M. Dumbser, C. Enaux, and E.F. Toro. Finite volume schemes of very high order of accuracy for stiff hyperbolic balance laws. *Journal of Computational Physics*, 227:3971–4001, 2008. (Cited on pages 28, 29, 33, 34, 127, and 128.)
- [168] M. Dumbser, F. Guercilena, S. Köppel, L. Rezzolla, and O. Zanotti. Conformal and covariant Z4 formulation of the Einstein equations: Strongly hyperbolic first-order reduction and solution with discontinuous Galerkin schemes. *Phys. Rev. D*, 97(8):084053, April 2018. (Cited on pages 3, 12, 14, 17, 35, 43, 52, 59, 60, 61, 133, 136, 137, 138, 139, and 169.)
- [169] M. Dumbser, A. Hidalgo, M. Castro, C. Parés, and E.F. Toro. FORCE schemes on unstructured meshes II: Non-conservative hyperbolic systems. *Computer Methods in Applied Mechanics and Engineering*, 199:625–647, 2010. (Cited on pages 13, 31, and 121.)
- [170] M. Dumbser, A. Hidalgo, and O. Zanotti. High Order Space-Time Adaptive ADER-WENO Finite Volume Schemes for Non-Conservative Hyperbolic Systems. *Computer Methods in Applied Mechanics and Engineering*, 268:359–387, 2014. (Cited on pages 34, 35, 36, 69, and 136.)
- [171] M. Dumbser and M. Kaeser. Arbitrary high order non-oscillatory finite volume schemes on unstructured meshes for linear hyperbolic systems. *Journal of Computational Physics*, 221:693–723, February 2007. (Cited on page 29.)
- [172] M. Dumbser, M. Kaeser, V. A. Titarev, and E. F. Toro. Quadrature-free non-oscillatory finite volume schemes on unstructured meshes for nonlinear hyperbolic systems. *Journal of Computational Physics*, 226:204–243, September 2007. (Cited on page 33.)

- [173] M. Dumbser, T. Schwartzkopff, and C.D. Munz. Arbitrary high order finite volume schemes for linear wave propagation. In *Computational Science and High Performance Computing II*, Notes on Numerical Fluid Mechanics and Multidisciplinary Design (NNFM), pages 129–144. Springer, 2006. (Cited on page 36.)
- [174] M. Dumbser and E. F. Toro. A simple extension of the Osher Riemann solver to non-conservative hyperbolic systems. *Journal of Scientific Computing*, 48:70–88, 2011. (Cited on pages 13, 32, and 33.)
- [175] M. Dumbser and O. Zanotti. Very high order PNPM schemes on unstructured meshes for the resistive relativistic MHD equations. *Journal of Computational Physics*, 228:6991–7006, October 2009. (Cited on pages 14 and 30.)
- [176] M. Dumbser, O. Zanotti, A. Hidalgo, and D. S. Balsara. ADER-WENO finite volume schemes with space-time adaptive mesh refinement. *Journal of Computational Physics*, 248:257–286, September 2013. (Cited on page 28.)
- [177] M. Dumbser, O. Zanotti, A. Hidalgo, and D.S. Balsara. ADER-WENO Finite Volume Schemes with Space-Time Adaptive Mesh Refinement. *Journal of Computational Physics*, 248:257–286, 2013. (Cited on pages 39, 40, and 127.)
- [178] G. Dvali, S. Folkerts, and C. Germani. Physics of Trans-Planckian Gravity. *Phys.Rev.*, D84:024039, 2011. (Cited on pages 16 and 120.)
- [179] G. Dvali, G. F. Giudice, C. Gomez, and A. Kehagias. UV-completion by classicalization. *JHEP*, 1108:108, 2011. (Cited on page 16.)
- [180] G. Dvali and C. Gomez. Self-Completeness of Einstein Gravity. 2010. (Cited on page 16.)
- [181] G. Dvali, C. Gomez, R. S. Isermann, D. Lüst, and S. Stieberger. Black hole formation and classicalization in ultra-Planckian $2 \rightarrow N$ scattering. *Nucl. Phys.*, B893:187–235, 2015. (Cited on page 16.)
- [182] Gia Dvali, Andre Franca, and Cesar Gomez. Road Signs for UV-Completion. 2012. (Cited on pages 16 and 120.)
- [183] Gia Dvali and Cesar Gomez. Ultra-High Energy Probes of Classicalization. *JCAP*, 1207:015, 2012. (Cited on page 16.)
- [184] Gia Dvali, Stefan Hofmann, and Justin Khoury. Degravitation of the cosmological constant and graviton width. *Phys. Rev.*, D76:084006, 2007. (Cited on pages 16 and 108.)
- [185] James Edholm, Alexey S. Koshelev, and Anupam Mazumdar. Behavior of the Newtonian potential for ghost-free gravity and singularity-free gravity. *Phys. Rev.*, D94(10):104033, 2016. (Cited on page 119.)
- [186] D. Eichler, M. Livio, T. Piran, and D. N. Schramm. Nucleosynthesis, neutrino bursts and gamma-rays from coalescing neutron stars. *Nature*, 340:126–128, July 1989. (Cited on page 15.)
- [187] B. Einfeldt, P. L. Roe, C. D. Munz, and B. Sjogreen. On Godunov-type methods near low densities. *Journal of Computational Physics*, 92:273–295, February 1991. (Cited on page 33.)
- [188] Albert Einstein. Die Feldgleichungen der Gravitation. *Preuss. Akad. Wiss. Berlin, Sitzungsber.*, pages 844–847, 1915. (Cited on page 43.)
- [189] Albert Einstein. Zur Allgemeinen Relativitätstheorie. *Preuss. Akad. Wiss. Berlin, Sitzungsber.*, pages 778–786, 1915. (Cited on page 43.)
- [190] Einstein Toolkit: Open Software for Relativistic Astrophysics. <http://einstein toolkit.org>. (Cited on page 96.)
- [191] Roberto Emparan and Harvey S. Reall. Black Holes in Higher Dimensions. *Living Rev. Rel.*, 11:6, 2008. (Cited on page 107.)

- [192] Z. B. Etienne, Y. T. Liu, and S. L. Shapiro. Relativistic magnetohydrodynamics in dynamical spacetimes: A new adaptive mesh refinement implementation. *Phys. Rev. D*, 82(8):084031, October 2010. (Cited on page 85.)
- [193] F. Fambri and M. Dumbser. Spectral semi-implicit and space-time discontinuous Galerkin methods for the incompressible Navier-Stokes equations on staggered Cartesian grids. *Applied Numerical Mathematics*, 110:41–74, 2016. (Cited on page 30.)
- [194] F. Fambri, M. Dumbser, S. Köppel, L. Rezzolla, and O. Zanotti. ADER discontinuous Galerkin schemes for general-relativistic ideal magnetohydrodynamics. *Mon. Not. R. Astron. Soc.*, 477:4543–4564, July 2018. (Cited on pages 3, 12, 14, 17, 35, 72, 77, 80, 85, 87, 88, 89, 90, 91, 127, 137, and 169.)
- [195] F. Fambri, M. Dumbser, and O. Zanotti. Space-time adaptive ADER-DG schemes for dissipative flows: Compressible Navier-Stokes and resistive MHD equations. *Computer Physics Communications*, 220:297–318, 2017. (Cited on pages 36 and 39.)
- [196] F. Fambri, M. Dumbser, and O. Zanotti. Space-time adaptive ADER-DG schemes for dissipative flows: Compressible Navier-Stokes and resistive MHD equations. *Computer Physics Communications*, 220:297–318, 2017. (Cited on pages 38, 39, 40, 80, 136, 137, and 139.)
- [197] Valerio Faraoni. Matter instability in modified gravity. *Phys. Rev.*, D74:104017, 2006. (Cited on page 119.)
- [198] S. Fechter and C.-D. Munz. A discontinuous Galerkin-based sharp-interface method to simulate three-dimensional compressible two-phase flow. *International Journal for Numerical Methods in Fluids*, 78(7):413–435, 2015. (Cited on page 35.)
- [199] E. Fehlberg. Klassische Runge–Kutta–Formeln fünfter und siebenter Ordnung mit Schrittweiten–Kontrolle. *Computing*, 4(2):93–106, 1969. (Cited on page 128.)
- [200] S. E. Field, J. S. Hesthaven, S. R. Lau, and A. H. Mroue. Discontinuous Galerkin method for the spherically reduced Baumgarte-Shapiro-Shibata-Nakamura system with second-order operators. *Phys. Rev. D*, 82(10):104051, November 2010. (Cited on pages 13 and 69.)
- [201] J. A. Font. Numerical hydrodynamics in general relativity. *Living Rev. Relativ.*, 3:2, 2000. (Cited on page 76.)
- [202] J. A. Font. Numerical hydrodynamics and magnetohydrodynamics in general relativity. *Living Rev. Relativ.*, 6:4; <http://www.livingreviews.org/lrr-2008-7>, 2008. (Cited on pages 14, 26, and 75.)
- [203] José A. Font and Frederic Daigne. The runaway instability of thick discs around black holes – I. the constant angular momentum case. *Mon. Not. R. Astron. Soc.*, 334:383–400, 2002. (Cited on pages 83, 84, and 137.)
- [204] Antonia M. Frassino, Sven Köppel, and Piero Nicolini. Geometric model of black hole quantum N -portrait, extradimensions and thermodynamics. *Entropy*, 18:181, 2016. (Cited on pages 3, 16, 108, 109, 110, 137, and 169.)
- [205] K O Friedrichs. Symmetric hyperbolic linear differential equations. *Communications on Pure and Applied Mathematics*, 7(2):345–392, 1954. (Cited on page 121.)
- [206] Valeri P. Frolov, W. Israel, and W. G. Unruh. Gravitational Fields of Straight and Circular Cosmic Strings: Relation Between Gravitational Mass, Angular Deficit, and Internal Structure. *Phys. Rev.*, D39:1084–1096, 1989. (Cited on page 113.)
- [207] Valeri P. Frolov and Andrei Zelnikov. Head-on collision of ultrarelativistic particles in ghost-free theories of gravity. *Phys. Rev.*, D93(6):064048, 2016. (Cited on page 119.)
- [208] E. Gaburro, M. Castro, and M. Dumbser. Well balanced Arbitrary-Lagrangian-Eulerian finite volume schemes on moving nonconforming meshes for the Euler equations of gasdynamics with gravity. *Mon. Not. R. Astron. Soc.*, 2018. in press. <https://arxiv.org/abs/1712.07765>. (Cited on page 28.)

- [209] E. Gaburro, M. Dumbser, and M. Castro. Direct Arbitrary-Lagrangian-Eulerian finite volume schemes on moving nonconforming unstructured meshes. *Computers and Fluids*, 159:254–275, 2017. (Cited on page 28.)
- [210] P. Gaete, J. A. Helayel-Neto, and E. Spallucci. Un-graviton corrections to the Schwarzschild black hole. *Phys. Lett.*, B693:155–158, 2010. (Cited on pages 16 and 108.)
- [211] B. G. Galerkin. On electrical circuits for the approximate solution of the laplace equation. *Vestnik Inzhenerov i Tekhnikov*, 19:897–908, 1915. (Cited on page 25.)
- [212] Charles F. Gammie, Jonathan C. McKinney, and G. Tóth. Harm: A numerical scheme for general relativistic magnetohydrodynamics. *Astrophys. J.*, 589:458, 2003. (Cited on page 79.)
- [213] G. Gassner, M. Dumbser, F. Hindenlang, and C.D. Munz. Explicit one-step time discretizations for discontinuous Galerkin and finite volume schemes based on local predictors. *Journal of Computational Physics*, 230(11):4232–4247, 2011. (Cited on page 34.)
- [214] B. Giacomazzo and L. Rezzolla. WhiskyMHD: a new numerical code for general relativistic magnetohydrodynamics. *Class. Quantum Grav.*, 24:235, June 2007. (Cited on page 14.)
- [215] Bruno Giacomazzo and Luciano Rezzolla. The Exact Solution of the Riemann Problem in Relativistic MHD. *Journal of Fluid Mechanics*, 562:223–259, 2006. (Cited on pages 21 and 87.)
- [216] Steven B. Giddings and Scott D. Thomas. High-energy colliders as black hole factories: The End of short distance physics. *Phys.Rev.*, D65:056010, 2002. (Cited on page 107.)
- [217] Mike Giles, Endre László, I.Z. Reguly, Jeremy Appleyard, and Julien Demouth. GPU Implementation of Finite Difference Solvers. 11 2014. (Cited on pages 25 and 136.)
- [218] S. K. Godunov. A difference method for numerical calculations of discontinuous solutions of the equations of hydrodynamics. *Mat. Sb.*, 47:271, 1959. in Russian. (Cited on pages 26 and 34.)
- [219] Hubert F. M. Goenner. On the history of unified field theories. *Living Reviews in Relativity*, 7(2), 2004. (Cited on page 108.)
- [220] T. Goodale, G. Allen, G. Lanfermann, J. Massó, T. Radke, E. Seidel, and J. Shalf. The Cactus framework and toolkit: Design and applications. In *Vector and Parallel Processing – VECPAR’2002, 5th International Conference, Lecture Notes in Computer Science*, Berlin, 2003. Springer. (Cited on pages 96 and 138.)
- [221] E. Gourgoulhon, P. Grandclément, K. Taniguchi, J. A. Marck, and S. Bonazzola. Quasiequilibrium sequences of synchronized and irrotational binary neutron stars in general relativity: Method and tests. *Phys. Rev. D*, 63:064029, 2001. (Cited on page 99.)
- [222] Eric Gourgoulhon. *3+1 Formalism in General Relativity*, volume 846 of *Lecture Notes in Physics*, Berlin Springer Verlag. 2012. (Cited on pages 44, 45, 46, 48, 49, and 78.)
- [223] Eric Gourgoulhon, Michal Bejger, and Marco Mancini. Tensor calculus with open-source software: the Sage-Manifolds project. *J. Phys. Conf. Ser.*, 600(1):012002, 2015. (Cited on page 22.)
- [224] Éric Gourgoulhon and Marco Mancini. Symbolic tensor calculus on manifolds: a SageMath implementation. 2018. (Cited on page 22.)
- [225] David J. Gross and Paul F. Mende. The High-Energy Behavior of String Scattering Amplitudes. *Phys. Lett.*, B197:129–134, 1987. (Cited on page 119.)
- [226] David J. Gross and Paul F. Mende. String Theory Beyond the Planck Scale. *Nucl. Phys.*, B303:407, 1988. (Cited on page 119.)

- [227] Federico Guercilena. *Dynamics of binary compact objects: from novel numerical approaches to the creation of heavy elements*. PhD thesis, 2018. (Cited on page 126.)
- [228] C. Gundlach. Critical phenomena in gravitational collapse. *Physics Reports*, 376:339–405, March 2003. (Cited on page 101.)
- [229] Carsten Gundlach and Jose M. Martin-Garcia. Hyperbolicity of second-order in space systems of evolution equations. *Class. Quantum Grav.*, 23:S387–S404, 2006. (Cited on pages 53 and 55.)
- [230] Ning Guo. *Investigation of Energy-Efficient Hybrid Analog/Digital Approximate Computation in Continuous Time*. PhD thesis, 2017. (Cited on pages 22 and 136.)
- [231] M. Hanuske, J. Steinheimer, L. Bovard, A. Mukherjee, S. Schramm, K. Takami, J. Papenfort, N. Wechselberger, L. Rezzolla, and H. Stöcker. Concluding Remarks: Connecting Relativistic Heavy Ion Collisions and Neutron Star Mergers by the Equation of State of Dense Hadron- and Quark Matter as signalled by Gravitational Waves. In *Journal of Physics Conference Series*, volume 878 of *Journal of Physics Conference Series*, page 012031, July 2017. (Cited on page 96.)
- [232] M. Hanuske, K. Takami, L. Bovard, L. Rezzolla, J. A. Font, F. Galeazzi, and H. Stöcker. Rotational properties of hypermassive neutron stars from binary mergers. *Phys. Rev. D*, 96(4):043004, August 2017. (Cited on page 15.)
- [233] M. Hannam, S. Husa, F. Ohme, B. Brügmann, and N. Ó Murchadha. Wormholes and trumpets: Schwarzschild spacetime for the moving-puncture generation. *Phys. Rev. D*, 78(6):064020, September 2008. (Cited on page 12.)
- [234] A. Harten, B. Engquist, S. Osher, and S. R. Chakravarthy. Uniformly High Order Accurate Essentially Non-oscillatory Schemes III. *Journal of Computational Physics*, 71:231–303, August 1987. (Cited on pages 13 and 33.)
- [235] A. Harten, P. D. Lax, and B. van Leer. On upstream differencing and godunov-type schemes for hyperbolic conservation laws. *SIAM Rev.*, 25:35, 1983. (Cited on pages 33 and 96.)
- [236] R. Hartmann and P. Houston. Adaptive discontinuous Galerkin finite element methods for the compressible Euler equations. *J. Comp. Phys.*, 183(2):508–532, 2002. (Cited on page 34.)
- [237] S. W. Hawking and Thomas Hertog. Living with ghosts. *Phys. Rev.*, D65:103515, 2002. (Cited on page 119.)
- [238] S.W. Hawking. Particle creation by black holes. *Commun. Math. Phys.*, 43:199–220, 1975. (Cited on page 15.)
- [239] M. Hempel, T. Fischer, J. Schaffner-Bielich, and M. Liebendörfer. New Equations of State in Simulations of Core-collapse Supernovae. *Astrophys. J.*, 748:70, March 2012. (Cited on page 96.)
- [240] M. Hempel and J. Schaffner-Bielich. A statistical model for a complete supernova equation of state. *Nuclear Physics A*, 837:210–254, June 2010. (Cited on pages 96 and 99.)
- [241] Jan S. Hesthaven, Sigal Gottlieb, and David Gottlieb. *Spectral methods for time-dependent problems*. Cambridge monographs on applied and computational mathematics. Cambridge university press, Cambridge, 2007. (Cited on pages 24 and 30.)
- [242] J.S. Hesthaven and T. Warburton. *Nodal Discontinuous Galerkin Methods: Algorithms, Analysis, and Applications*. Texts in Applied Mathematics. Springer, 2007. (Cited on page 30.)
- [243] Arturo Hidalgo and Michael Dumbser. Ader schemes for nonlinear systems of stiff advection-diffusion-reaction equations. *Journal of Scientific Computing*, 48:173–189, 2011. 10.1007/s10915-010-9426-6. (Cited on page 34.)
- [244] D. Hilditch, S. Bernuzzi, M. Thierfelder, Z. Cao, W. Tichy, and B. Brügmann. Compact binary evolutions with the Z4c formulation. *Phys. Rev. D*, 88(8):084057, October 2013. (Cited on pages 49 and 51.)

- [245] David Hilditch and Ronny Richter. Hyperbolicity of high-order systems of evolution equations. *Journal of Hyperbolic Differential Equations*, 12(01):1–35, 2015. (Cited on page 53.)
- [246] H.Luo, J.D.Baum, and R.Löhner. A hermite WENO-based limiter for discontinuous Galerkin method on unstructured grids. *J. Comput. Phys.*, 225(1):686–713, 2007. (Cited on page 34.)
- [247] Sabine Hossenfelder. What black holes can teach us. 2004. (Cited on pages 107 and 137.)
- [248] Sabine Hossenfelder. What black holes can teach us, 2004. (Not cited.)
- [249] Sabine Hossenfelder. Minimal Length Scale Scenarios for Quantum Gravity. *Living Rev. Rel.*, 16:2, 2013. (Cited on page 16.)
- [250] X. Y. Hu, N. A. Adams, and C.-W. Shu. Positivity-preserving method for high-order conservative schemes solving compressible Euler equations. *Journal of Computational Physics*, 242:169–180, June 2013. (Cited on page 96.)
- [251] John D. Hunter. Matplotlib: A 2D Graphics Environment. *Computing in Science & Engineering*, 9(3):90–95, 2007. (Cited on page 168.)
- [252] Sascha Husa, Ian Hinder, and Christiane Lechner. Kranc: a Mathematica application to generate numerical codes for tensorial evolution equations. *Comput. Phys. Comm.*, 174:983–1004, 2006. (Cited on page 22.)
- [253] J.M. Ibáñez, M.A. Aloy, J.A. Font, J.M. Martí, J.A. Miralles, and J.A. Pons. Riemann solvers in general relativistic hydrodynamics. In E.F. Toro, editor, *Godunov methods: theory and applications*, New York, 2001. Kluwer Academic/Plenum Publishers. (Cited on page 75.)
- [254] M. Isi, J. Mureika, and P. Nicolini. Self-Completeness and the Generalized Uncertainty Principle. *JHEP*, 1311:139, 2013. (Cited on pages 16, 108, 109, 111, and 116.)
- [255] C.W. Shu J. Zhu, X. Zhong and J. Qiu. Runge-Kutta discontinuous Galerkin method using a new type of WENO limiters on unstructured meshes. *J. Comp. Phys.*, 248:200–220, 2013. (Cited on page 34.)
- [256] H.-Th. Janka, T. Zwerger, and R. Mönchmeyer. Does artificial viscosity destroy prompt type-II supernova explosions? *Astron. Astrophys.*, 268:360–368, February 1993. (Cited on page 95.)
- [257] G. S. Jiang and C.-W. Shu. On a cell entropy inequality for discontinuous Galerkin methods. *Mathematics of Computation*, 62:531–538, 1994. (Cited on page 12.)
- [258] Guang-Shan Jiang and Chi-Wang Shu. Efficient implementation of weighted eno schemes. *J. Comput. Phys.*, 126:202–228, 1996. (Cited on pages 13, 28, and 29.)
- [259] Eric Jones, Travis Oliphant, Pearu Peterson, et al. SciPy: Open source scientific tools for Python, 2001–. (Cited on page 168.)
- [260] P. Kanti. Black holes in theories with large extra dimensions: A Review. *Int.J.Mod.Phys.*, A19:4899–4951, 2004. (Cited on page 107.)
- [261] Panagiota Kanti and Elizabeth Winstanley. Hawking Radiation from Higher-Dimensional Black Holes. *Fundam. Theor. Phys.*, 178:229–265, 2015. (Cited on page 107.)
- [262] W. Kastaun, R. Ciolfi, and B. Giacomazzo. Structure of stable binary neutron star merger remnants: A case study. *Phys. Rev. D*, 94(4):044060, August 2016. (Cited on page 15.)
- [263] Wolfgang Kastaun. *Developing a code for general relativistic hydrodynamics with application to neutron star oscillations*. PhD thesis, University of Tübingen, 2007. (Cited on page 99.)

- [264] T. Kawamura, B. Giacomazzo, W. Kastaun, R. Ciolfi, A. Endrizzi, L. Baiotti, and R. Perna. Binary neutron star mergers and short gamma-ray bursts: Effects of magnetic field orientation, equation of state, and mass ratio. *Phys. Rev. D*, 94(6):064012, September 2016. (Cited on page 15.)
- [265] Alex Kehagias and Michele Maggiore. Spherically symmetric static solutions in a nonlocal infrared modification of General Relativity. *JHEP*, 08:029, 2014. (Cited on page 119.)
- [266] A. Kempf, G. Mangano, and R. B. Mann. Hilbert space representation of the minimal length uncertainty relation. *Phys. Rev.*, D52:1108–1118, 1995. (Cited on pages 16, 109, 110, 111, and 114.)
- [267] A.M Khokhlov. Fully threaded tree algorithms for adaptive refinement fluid dynamics simulations. *Journal of Computational Physics*, 143(2):519 – 543, 1998. (Cited on pages 30, 37, and 39.)
- [268] L.E. Kidder, S.E. Field, F. Foucart, E. Schnetter, S.A. Teukolsky, A. Bohn, N. Deppe, P. Diener, F. Hébert, J. Lipnuner, J. Miller, C. D. Ott, M.A. Scheel, and T. Vincent. Spectre: A task-based discontinuous galerkin code for relativistic astrophysics. *Journal of Computational Physics*, 335:84–114, 2017. (Cited on pages 13 and 14.)
- [269] K. Kiuchi, P. Cerdá-Durán, K. Kyutoku, Y. Sekiguchi, and M. Shibata. Efficient magnetic-field amplification due to the Kelvin-Helmholtz instability in binary neutron star mergers. *Phys. Rev. D*, 92(12):124034, December 2015. (Cited on page 15.)
- [270] K. Kiuchi, Y. Sekiguchi, M. Shibata, and K. Taniguchi. Long-term general relativistic simulation of binary neutron stars collapsing to a black hole. *Phys. Rev. D*, 80(6):064037, September 2009. (Cited on page 14.)
- [271] Marco Knipfer. Generalized uncertainty principle inspired schwarzchild black holes in extra dimensions. Master’s thesis, Goethe University, Frankfurt, Germany, 2014. (Cited on pages 111 and 114.)
- [272] S. S. Komissarov. A Godunov-type scheme for relativistic magnetohydrodynamics. *Mon. Not. R. Astron. Soc.*, 303:343–366, February 1999. (Cited on page 14.)
- [273] S. S. Komissarov. General relativistic mhd simulations of monopole magnetospheres of black holes. *Mon. Not. R. Astron. Soc.*, 350:1431, 2004. (Cited on page 82.)
- [274] S. Köppel. Towards an exascale code for GRMHD on dynamical spacetimes. *arXiv:1711.08221*, November 2017. (Cited on pages 3, 14, 17, 43, 72, 138, and 169.)
- [275] S. Köppel, L. Bovard, and L. Rezzolla. General-relativistic measurement of the threshold mass to prompt collapse. *Astrophys. J. Lett.*, January 2019. (Cited on pages 3, 15, 95, 99, 100, 102, 104, 137, 139, and 169.)
- [276] S. Köppel, M. Knipfer, and P. Nicolini. Generalized Uncertainty Principle and Black Holes in Higher Dimensional Self Complete Gravity. in preparation. (Cited on pages 3, 16, 107, 137, and 169.)
- [277] S. Köppel and L. Rezzolla. Towards an exascale code for mhd on dynamical spacetimes. in preparation, 2018. (Cited on page 14.)
- [278] Sven Köppel. POKAL: Kollaboratives eLearning neu erfunden. In Claudia Bremer and Detlef Krömker, editors, *E-Learning zwischen Vision und Alltag*, volume 64, page 470. Waxmann, 2013. (Cited on page 170.)
- [279] Sven Köppel. Ultraviolet improved black holes. Master’s thesis, 2014. (Cited on page 137.)
- [280] Sven Köppel. Towards an exascale code for GRMHD on dynamical spacetimes. 2017. (Not cited.)
- [281] S. Koranda, N. Stergioulas, and J. L. Friedman. Upper Limits Set by Causality on the Rotation and Mass of Uniformly Rotating Relativistic Stars. *Astrophys. J.*, 488:799–806, October 1997. (Cited on pages 102 and 103.)
- [282] B. Koren. *Numerical methods for advection–diffusion problems*. Notes on numerical fluid mechanics, v. 45. Vieweg, Braunschweig, 1993. (Cited on page 28.)

- [283] M. Kozłowski, M. Jaroszynski, and M. A. Abramowicz. The analytic theory of fluid disks orbiting the Kerr black hole. *Astron. and Astrophys.*, 63:209–220, February 1978. (Cited on page 83.)
- [284] N.V. Krasnikov. Nonlocal gauge theories. *Theor.Math.Phys.*, 73:1184–1190, 1987. (Cited on pages 16 and 108.)
- [285] Heinz Otto Kreiss and Joseph Oliger. *Methods for the approximate solution of time dependent problems*. GARP publication series No. 10, Geneva, 1973. (Cited on page 25.)
- [286] L. Krivodonova. Limiters for high-order discontinuous galerkin methods. *Journal of Computational Physics*, 226(1):879, 2007. (Cited on page 34.)
- [287] S N Kružkov. FIRST ORDER QUASILINEAR EQUATIONS IN SEVERAL INDEPENDENT VARIABLES. *Mathematics of the USSR-Sbornik*, 10(2):217–243, February 1970. (Cited on page 126.)
- [288] M. Kutta. Beitrag zur näherungsweisen integration totaler differentialgleichungen. *Z. für Math. u. Phys.*, 46:435, 1901. (Cited on page 128.)
- [289] K. Kyutoku, K. Ioka, and M. Shibata. Ultrarelativistic electromagnetic counterpart to binary neutron star mergers. *Mon. Not. R. Astron.Soc.*, 437:L6–L10, January 2014. (Cited on page 15.)
- [290] Sven Köppel, Marco Knipfer, Maximiliano Isi, Jonas Mureika, and Piero Nicolini. Generalized uncertainty principle and extra dimensions. In *2nd Karl Schwarzschild Meeting on Gravitational Physics*, volume 208, pages 141–147, 2018. (Cited on pages 3, 16, 107, 111, 115, 120, 137, and 169.)
- [291] Matthew J. Lake and Bernard Carr. The Compton-Schwarzschild correspondence from extended de Broglie relations. *JHEP*, 11:105, 2015. (Cited on pages 16 and 115.)
- [292] Matthew J. Lake and Bernard Carr. The Compton-Schwarzschild relations in higher dimensions. 2016. (Cited on pages 16 and 115.)
- [293] Matthew J. Lake and Bernard Carr. Does Compton/Schwarzschild duality in higher dimensions exclude TeV quantum gravity? 2018. (Cited on pages 16 and 115.)
- [294] G. A. Lalazissis, J. Konig, and P. Ring. A New parametrization for the Lagrangian density of relativistic mean field theory. *Phys. Rev.*, C55:540–543, 1997. (Cited on pages 95 and 99.)
- [295] Chi-Chung Lam, Thomas Rauber, Gerald Baumgartner, Daniel Cociorva, and P. Sadayappan. Memory-optimal evaluation of expression trees involving large objects. *Computer Languages, Systems & Structures*, 37(2):63–75, 2011. (Cited on page 63.)
- [296] Greg L. Landsberg. Black holes at future colliders and beyond: A Review. In *Supersymmetry and unification of fundamental interactions. Proceedings, 10th International Conference, SUSY'02, Hamburg, Germany, June 17-23, 2002*, pages 562–577, 2002. (Cited on page 107.)
- [297] J. M. Lattimer, C. J. Pethick, D. G. Ravenhall, and D. Q. Lamb. Physical properties of hot, dense matter: The general case. *Nucl. Phys. A*, 432:646–742, 1985. (Cited on page 95.)
- [298] J. M. Lattimer and M. Prakash. The equation of state of hot, dense matter and neutron stars. *Physics Reports*, 621:127–164, March 2016. (Cited on pages 102 and 103.)
- [299] James M. Lattimer and F. Douglas Swesty. A generalized equation of state for hot, dense matter. *Nucl. Phys. A*, 535:331–376, 1991. (Cited on pages 95, 96, and 99.)
- [300] P. D. Lax and R. D. Richtmyer. Survey of the stability of linear finite difference equations. *Communications on Pure and Applied Mathematics*, 9(2):267–293, May 1956. (Cited on page 127.)

- [301] Christiane Lechner, Dana Alic, and Sascha Husa. From tensor equations to numerical code – computer algebra tools for numerical relativity. In *SYNASC 2004 – 6th International Symposium on Symbolic and Numeric Algorithms for Scientific Computing, Timisoara, Romania*, 2004. (Cited on page 22.)
- [302] L. Lehner, S. L. Liebling, C. Palenzuela, O. L. Caballero, E. O'Connor, M. Anderson, and D. Neilsen. Unequal mass binary neutron star mergers and multimessenger signals. *Classical and Quantum Gravity*, 33(18):184002, September 2016. (Cited on page 15.)
- [303] R. J. Leveque. *Numerical Methods for Conservation Laws*. Birkhauser Verlag, Basel, 1992. (Cited on pages 19 and 20.)
- [304] Jiajia Li, Casey Battaglino, Ioakeim Perros, Jimeng Sun, and Richard Vuduc. An Input-adaptive and In-place Approach to Dense Tensor-times-matrix Multiply. In *Proceedings of the International Conference for High Performance Computing, Networking, Storage and Analysis*, SC '15, pages 76:1–76:12, New York, NY, USA, 2015. ACM. (Cited on page 63.)
- [305] L. Lindblom, M. A. Scheel, L. E. Kidder, R. Owen, and O. Rinne. A new generalized harmonic evolution system. *Class. Quantum Grav.*, 23:447, August 2006. (Cited on page 58.)
- [306] Lee Lindblom and Mark A. Scheel. Dynamical gauge conditions for the Einstein evolution equations. *Phys. Rev. D*, 67:124005, 2003. (Cited on page 47.)
- [307] X.-D. Liu, S. Osher, and T. Chan. Weighted Essentially Non-oscillatory Schemes. *Journal of Computational Physics*, 115:200–212, November 1994. (Cited on page 13.)
- [308] F. Löffler, J. Faber, E. Bentivegna, T. Bode, P. Diener, R. Haas, I. Hinder, B. C. Mundim, C. D. Ott, E. Schnetter, G. Allen, M. Campanelli, and P. Laguna. The Einstein Toolkit: a community computational infrastructure for relativistic astrophysics. *Class. Quantum Grav.*, 29(11):115001, June 2012. (Cited on pages 69 and 96.)
- [309] Rainald Löhner. An adaptive finite element scheme for transient problems in CFD. *Computer Methods in Applied Mechanics and Engineering*, 61(3):323 – 338, 1987. (Cited on page 39.)
- [310] F. D. Lora-Clavijo, A. Cruz-Osorio, and F. S. Guzmán. CAFE: A New Relativistic MHD Code. *Astrophys. J. Suppl.*, 218(2):24, 2015. (Cited on page 14.)
- [311] Malcolm A. H. MacCallum. Computer algebra in gravity research. *Living Reviews in Relativity*, 21(1):6, Aug 2018. (Cited on page 22.)
- [312] Michele Maggiore. A Generalized uncertainty principle in quantum gravity. *Phys. Lett.*, B304:65–69, 1993. (Cited on page 16.)
- [313] R. B. Mann and P. Nicolini. Cosmological production of noncommutative black holes. *Phys. Rev.*, D84:064014, 2011. (Cited on page 119.)
- [314] R. B. Mann and S. F. Ross. Cosmological production of charged black hole pairs. *Phys. Rev.*, D52:2254–2265, 1995. (Cited on page 119.)
- [315] Robert B. Mann. Black holes of negative mass. *Class. Quant. Grav.*, 14:2927–2930, 1997. (Cited on page 118.)
- [316] B. Margalit and B. D. Metzger. Constraining the Maximum Mass of Neutron Stars from Multi-messenger Observations of GW170817. *Astrophys. J. Lett.*, 850:L19, December 2017. (Cited on page 15.)
- [317] J. M. Martí, J. M. Ibáñez, and J. A. Miralles. Numerical relativistic hydrodynamics: Local characteristic approach. *Phys. Rev. D*, 43:3794, 1991. (Cited on page 75.)
- [318] J. M. Martí and E. Müller. Numerical hydrodynamics in special relativity. *Living Rev. Relativ.*, 6:7; <http://www.livingreviews.org/lrr-2003-7>, 2003. (Cited on page 26.)

- [319] J. M. Martí and E. Müller. Grid-based Methods in Relativistic Hydrodynamics and Magnetohydrodynamics. *Living Reviews in Computational Astrophysics*, 1, December 2015. (Cited on page 14.)
- [320] Michael Maziashvili. Field propagation in a stochastic background space: The rate of light incoherence in stellar interferometry. *Phys. Rev.*, D86:104066, 2012. (Cited on pages 16 and 116.)
- [321] Michael Maziashvili. Hilbert space representation of higher-dimensional minimum-length deformed uncertainty relation and some of its implications for ADD model. *JCAP*, 1303:042, 2013. (Cited on pages 16 and 115.)
- [322] Michael Maziashvili. Extra-dimensional generalization of minimum-length deformed QM/QFT and some of its phenomenological consequences. *Phys. Rev.*, D91(6):064040, 2015. (Cited on pages 16 and 116.)
- [323] John McCarthy. Recursive functions of symbolic expressions and their computation by machine, part i. *Commun. ACM*, 3(4):184–195, April 1960. (Cited on page 21.)
- [324] D. L. Meier. Multidimensional astrophysical structural and dynamical analysis. i. development of a nonlinear finite element approach. *Astrophys. J.*, 518(2):788, 1999. (Cited on page 30.)
- [325] A. Meister and S. Ortlob. A positivity preserving and well-balanced DG scheme using finite volume subcells in almost dry regions. *Applied Mathematics and Computation*, 272:259–273, 2016. in press. (Cited on page 35.)
- [326] C. Meusburger and T. Schonfeld. Gauge fixing in (2+1)-gravity: Dirac bracket and spacetime geometry. *Class. Quant. Grav.*, 28:125008, 2011. (Cited on pages 46 and 136.)
- [327] F. C. Michel. Accretion of matter by condensed objects. *Astrophys. Spac. Sci.*, 15:153, 1972. (Cited on page 82.)
- [328] A. Mignone, P. Tzeferacos, and G. Bodo. High-order conservative finite difference glm-mhd schemes for cell-centered mhd. *Journal of Computational Physics*, 229:5896–5920, aug 2010. (Cited on page 13.)
- [329] J.M. Miller and E. Schnetter. An operator-based local discontinuous galerkin method compatible with the bssn formulation of the einstein equations. *Classical and Quantum Gravity*, 34(1):015003, March 2017. (Cited on pages 13 and 69.)
- [330] Charles W. Misner, Kip S. Thorne, and John A. Wheeler. *Gravitation*. W. H. Freeman, San Francisco, 1973. (Cited on pages 43 and 78.)
- [331] L. Modesto. Super-renormalizable Quantum Gravity. *Phys.Rev.*, D86:044005, 2012. (Cited on pages 16 and 108.)
- [332] L. Modesto, J. W. Moffat, and P. Nicolini. Black holes in an ultraviolet complete quantum gravity. *Phys. Lett.*, B695:397–400, 2011. (Cited on pages 16 and 108.)
- [333] Gloria Montana, Laura Tolos, Matthias Hanauske, and Luciano Rezzolla. Constraining twin stars with GW170817. November 2018. (Cited on page 15.)
- [334] M. S. Morris, K. S. Thorne, and U. Yurtsever. Wormholes, Time Machines, and the Weak Energy Condition. *Phys. Rev. Lett.*, 61:1446–1449, 1988. (Cited on page 118.)
- [335] E. R. Most, L. J. Papenfort, V. Dexheimer, M. Hanauske, S. Schramm, H. Stöcker, and L. Rezzolla. Signatures of quark-hadron phase transitions in general-relativistic neutron-star mergers. *arXiv:1807.03684*, July 2018. (Cited on page 99.)
- [336] E. R. Most, L. R. Weih, L. Rezzolla, and J. Schaffner-Bielich. New Constraints on Radii and Tidal Deformabilities of Neutron Stars from GW170817. *Phys. Rev. Lett.*, 120(26):261103, June 2018. (Cited on pages 15, 102, and 105.)
- [337] J. Mureika and P. Nicolini. Self-completeness and spontaneous dimensional reduction. *Eur.Phys.J.Plus*, 128:78, 2013. (Cited on pages 16 and 120.)

- [338] T. Nakamura, K. Oohara, and Y. Kojima. General Relativistic Collapse to Black Holes and Gravitational Waves from Black Holes. *Progress of Theoretical Physics Supplement*, 90:1–218, 1987. (Cited on pages 13 and 48.)
- [339] T. Nelson, A. Rivera, P. Balaprakash, M. Hall, P. D. Hovland, E. Jessup, and B. Norris. Generating Efficient Tensor Contractions for GPUs. In *2015 44th International Conference on Parallel Processing*, pages 969–978, Sept 2015. (Cited on page 63.)
- [340] Andrea Nerozzi, Christopher Beetle, Marco Bruni, Lior M. Burko, and Denis Pollney. Towards wave extraction in numerical relativity: The quasi-Kinnersley frame. *Phys. Rev. D*, 72:024014, 2005. (Cited on page 134.)
- [341] Ezra T. Newman and Roger Penrose. An approach to gravitational radiation by a method of spin coefficients. *J. Math. Phys.*, 3(3):566–578, 1962. erratum in J. Math. Phys. 4, 998 (1963). (Cited on page 134.)
- [342] P. Nicolini. Nonlocal and generalized uncertainty principle black holes. (Cited on pages 16, 108, and 110.)
- [343] P. Nicolini. Noncommutative black holes, the final appeal to quantum gravity: a review. *Int. J. Mod. Phys.*, A24:1229–1308, 2009. (Cited on pages 16, 108, and 110.)
- [344] P. Nicolini, J. Mureika, E. Spallucci, E. Winstanley, and M. Bleicher. Production and evaporation of Planck scale black holes at the LHC, . 2013. (Cited on page 107.)
- [345] P. Nicolini, A. Smailagic, and E. Spallucci. Noncommutative geometry inspired Schwarzschild black hole. *Phys. Lett.*, B632:547–551, 2006. (Cited on page 110.)
- [346] P. Nicolini and E. Spallucci. Noncommutative geometry inspired dirty black holes. *Class. Quant. Grav.*, 27:015010, 2010. (Cited on page 110.)
- [347] Piero Nicolini. Planckian charged black holes in ultraviolet self-complete quantum gravity. *Phys. Lett.*, B778:88–93, 2018. (Cited on page 120.)
- [348] Piero Nicolini and Euro Spallucci. Holographic screens in ultraviolet self-complete quantum gravity. *Adv. High Energy Phys.*, 2014:805684, 2014. (Cited on pages 16 and 110.)
- [349] Piero Nicolini, Euro Spallucci, and Michael F. Wondrak. Quantum Corrected Black Holes from String T-Duality. 2019. (Cited on page 110.)
- [350] S. C. Noble, C. F. Gammie, J. C. McKinney, and L. Del Zanna. Primitive Variable Solvers for Conservative General Relativistic Magnetohydrodynamics. *Astrophys. J.*, 641:626–637, April 2006. (Cited on page 75.)
- [351] Shin’ichi Nojiri and Sergei D. Odintsov. Modified gravity with negative and positive powers of the curvature: Unification of the inflation and of the cosmic acceleration. *Phys. Rev.*, D68:123512, 2003. (Cited on page 119.)
- [352] Shin’ichi Nojiri and Sergei D. Odintsov. Newton law corrections and instabilities in f(R) gravity with the effective cosmological constant epoch. *Phys. Lett.*, B652:343–348, 2007. (Cited on page 119.)
- [353] Gonzalo J. Olmo. Post-Newtonian constraints on f(R) cosmologies in metric and Palatini formalism. *Phys. Rev.*, D72:083505, 2005. (Cited on page 119.)
- [354] J. R. Oppenheimer and G. Volkoff. On massive neutron cores. *Phys. Rev.*, 55:374, 1939. (Cited on page 93.)
- [355] S. A. Orszag and C.-M. Tang. Small-scale structure of two-dimensional magnetohydrodynamic turbulence. *Journal of Fluid Mechanics*, 90:129–143, January 1979. (Cited on page 90.)
- [356] J. M. Overduin and P. S. Wesson. Kaluza-Klein gravity. *Phys. Rept.*, 283:303–380, 1997. (Cited on page 108.)
- [357] B. Owren and M. Zennaro. Derivation of efficient continuous explicit. *SIAM J. Sci. Stat. Comput.*, 13:1488–1501, 1992. (Cited on page 34.)

- [358] C. Palenzuela, L. Lehner, O. Reula, and L. Rezzolla. Beyond ideal MHD: towards a more realistic modelling of relativistic astrophysical plasmas. *Mon. Not. R. Astron. Soc.*, 394:1727–1740, April 2009. (Cited on pages 14 and 80.)
- [359] Carlos Pares. Numerical methods for nonconservative hyperbolic systems: a theoretical framework. *SIAM J. Numer. Anal.*, 44(1):300–321, 2006. (Cited on pages 28, 31, 32, 78, and 121.)
- [360] Seong Chan Park. Black holes and the LHC: A Review. *Prog. Part. Nucl. Phys.*, 67:617–650, 2012. (Cited on page 107.)
- [361] V. Paschalidis, K. Yagi, D. Alvarez-Castillo, D. B. Blaschke, and A. Sedrakian. Implications from GW170817 and I-Love-Q relations for relativistic hybrid stars. *arXiv:1712.00451*, December 2017. (Cited on page 15.)
- [362] Leandros Perivolaropoulos. Submillimeter spatial oscillations of Newton’s constant: Theoretical models and laboratory tests. *Phys. Rev.*, D95(8):084050, 2017. (Cited on page 119.)
- [363] P.-O. Persson and J. Peraire. Sub-cell shock capturing for discontinuous Galerkin methods. *AIAA Paper 2006-112*, 2006. (Cited on page 34.)
- [364] O. Porth, H. Olivares, Y. Mizuno, Z. Younsi, L. Rezzolla, M. Moscibrodzka, H. Falcke, and M. Kramer. The black hole accretion code. *Computational Astrophysics and Cosmology*, 4:1, May 2017. (Cited on pages 14, 80, and 91.)
- [365] Frans Pretorius. Evolution of binary black hole spacetimes. *Phys. Rev. Lett.*, 95:121101, 2005. (Cited on page 12.)
- [366] G. Puppo and M. Semplice. Numerical entropy and adaptivity for finite volume schemes. *Commun. Comput. Phys.*, 10(5):1132–1160, 2011. (Cited on page 39.)
- [367] J. Qiu, M. Dumbser, and C.W. Shu. The discontinuous Galerkin method with Lax-Wendroff type time discretizations. *Computer Methods in Applied Mechanics and Engineering*, 194:4528–4543, 2005. (Cited on pages 33 and 36.)
- [368] J. Qiu and C. Shu. Runge Kutta Discontinuous Galerkin Methods using WENO limiters. *SIAM J. Sci. Comp.*, 26:907–929, 2005. (Cited on page 34.)
- [369] Jianxian Qiu and Chi-Wang Shu. Hermite WENO schemes and their application as limiters for Runge-Kutta discontinuous Galerkin method: one-dimensional case. *Journal of Computational Physics*, 193(1):115–135, January 2004. (Cited on page 34.)
- [370] D. Radice. General-relativistic Large-eddy Simulations of Binary Neutron Star Mergers. *Astrophys. J. Lett.*, 838:L2, March 2017. (Cited on page 15.)
- [371] D. Radice, E. Abdikamalov, L. Rezzolla, and C. D. Ott. A new spherical harmonics scheme for multi-dimensional radiation transport I. Static matter configurations. *Journal of Computational Physics*, 242:648–669, June 2013. (Cited on pages 93 and 139.)
- [372] D. Radice, F. Galeazzi, J. Lippuner, L. F. Roberts, C. D. Ott, and L. Rezzolla. Dynamical Mass Ejection from Binary Neutron Star Mergers. *Mon. Not. R. Astron. Soc.*, 460:3255–3271, August 2016. (Cited on page 15.)
- [373] D. Radice, A. Perego, F. Zappa, and S. Bernuzzi. GW170817: Joint Constraint on the Neutron Star Equation of State from Multimessenger Observations. *Astrophys. J. Lett.*, 852:L29, January 2018. (Cited on pages 15 and 96.)
- [374] D. Radice and L. Rezzolla. Discontinuous Galerkin methods for general-relativistic hydrodynamics: Formulation and application to spherically symmetric spacetimes. *Phys. Rev. D*, 84(2):024010, July 2011. (Cited on pages 13, 14, 34, and 139.)

- [375] D. Radice and L. Rezzolla. THC: a new high-order finite-difference high-resolution shock-capturing code for special-relativistic hydrodynamics. *Astron. Astrophys.*, 547:A26, June 2012. (Cited on pages 13, 14, and 96.)
- [376] D. Radice and L. Rezzolla. Universality and Intermittency in Relativistic Turbulent Flows of a Hot Plasma. *Astrophys. J.*, 766:L10, March 2013. (Cited on page 27.)
- [377] D. Radice, L. Rezzolla, and F. Galeazzi. Beyond second-order convergence in simulations of binary neutron stars in full general-relativity. *Mon. Not. R. Astron. Soc. L.*, 437:L46–L50, June 2014. (Cited on pages 13, 14, and 96.)
- [378] D. Radice, L. Rezzolla, and F. Galeazzi. High-order fully general-relativistic hydrodynamics: new approaches and tests. *Class. Quantum Grav.*, 31(7):075012, April 2014. (Cited on pages 77 and 96.)
- [379] D. Radice, L. Rezzolla, and F. Galeazzi. High-Order Numerical-Relativity Simulations of Binary Neutron Stars. In N. V. Pogorelov, E. Audit, and G. P. Zank, editors, *Numerical Modeling of Space Plasma Flows ASTRONUM-2014*, volume 498 of *Astronomical Society of the Pacific Conference Series*, page 121, October 2015. (Cited on page 93.)
- [380] L. Randall and R. Sundrum. A large mass hierarchy from a small extra dimension. *Phys.Rev.Lett.*, 83:3370–3373, 1999. (Cited on page 107.)
- [381] L. Randall and R. Sundrum. An alternative to compactification. *Phys.Rev.Lett.*, 83:4690–4693, 1999. (Cited on page 107.)
- [382] C. Reisswig. *Binary Black Hole Mergers and Novel Approaches to Gravitational Wave Extraction in Numerical Relativity*. PhD thesis, Universität Hannover, Hannover, 2010. (Cited on page 42.)
- [383] C. Reisswig, C. D. Ott, U. Sperhake, and E. Schnetter. Gravitational wave extraction in simulations of rotating stellar core collapse. *Phys. Rev. D*, 83(6):064008, March 2011. (Cited on page 96.)
- [384] C. Reisswig and D. Pollney. Notes on the integration of numerical relativity waveforms. *Class. Quantum Grav.*, 28:195015, 2011. (Cited on page 134.)
- [385] L. Rezzolla, B. Giacomazzo, L. Baiotti, J. Granot, C. Kouveliotou, and M. A. Aloy. The Missing Link: Merging Neutron Stars Naturally Produce Jet-like Structures and Can Power Short Gamma-ray Bursts. *Astrophys. J. Letters*, 732:L6, May 2011. (Cited on page 15.)
- [386] L. Rezzolla, E. R. Most, and L. R. Weih. Using Gravitational-wave Observations and Quasi-universal Relations to Constrain the Maximum Mass of Neutron Stars. *Astrophys. J. Lett.*, 852:L25, January 2018. (Cited on page 15.)
- [387] L. Rezzolla and O. Zanotti. *Relativistic Hydrodynamics*. Oxford University Press, Oxford, UK, 2013. (Cited on pages 44, 60, 68, 73, 74, 82, 83, 95, 98, and 102.)
- [388] S. Rhebergen, O. Bokhove, and J.J.W. van der Vegt. Discontinuous Galerkin finite element methods for hyperbolic nonconservative partial differential equations. *Journal of Computational Physics*, 227:1887–1922, 2008. (Cited on page 31.)
- [389] Robert D. Richtmyer and K.W. Morton. *Difference Methods for Initial Value Problems*. Kreiger, Malabar, USA, 2nd edition, 1994. (Cited on page 127.)
- [390] W. Ritz. Über eine neue methode zur lösung gewisser variationsprobleme der mathematischen physik. *Journal für die Reine und Angewandte Mathematik*, 1909(135):1–61, 1909. (Cited on page 25.)
- [391] P. L. Roe. Characteristic-based schemes for the Euler equations. *Annual Review of Fluid Mechanics*, 18:337–365, 1986. (Cited on page 28.)

- [392] S. Rosswog, M. Liebendörfer, F.-K. Thielemann, M. B. Davies, W. Benz, and T. Piran. Mass ejection in neutron star mergers. *Astron. Astrophys.*, 341:499–526, January 1999. (Cited on page 15.)
- [393] Carlo Rovelli. Loop quantum gravity. *Living Reviews in Relativity*, 11(1):5, Jul 2008. (Cited on page 44.)
- [394] Ian Ruchlin, Zachariah B. Etienne, and Thomas W. Baumgarte. SENR/NRPy+: Numerical Relativity in Singular Curvilinear Coordinate Systems. *Phys. Rev.*, D97(6):064036, 2018. (Cited on pages 49, 52, and 129.)
- [395] M. Ruiz, S. L. Shapiro, and A. Tsokaros. GW170817, general relativistic magnetohydrodynamic simulations, and the neutron star maximum mass. *Phys. Rev. D*, 97(2):021501, January 2018. (Cited on page 15.)
- [396] Milton Ruiz, David Hilditch, and Sebastiano Bernuzzi. Constraint preserving boundary conditions for the Z4c formulation of general relativity. *Phys. Rev. D*, 83:024025, 2011. (Cited on page 51.)
- [397] V. V. Rusanov. Calculation of Interaction of Non-Steady Shock Waves with Obstacles. *J. Comput. Math. Phys. USSR*, 1:267–279, 1961. (Cited on pages 27 and 32.)
- [398] N. Sanchis-Gual, P. J. Montero, J. A. Font, E. Müller, and T. W. Baumgarte. Fully covariant and conformal formulation of the Z4 system in a reference-metric approach: Comparison with the BSSN formulation in spherical symmetry. *Phys. Rev. D*, 89(10):104033, May 2014. (Cited on page 13.)
- [399] Olivier Sarbach and Manuel Tiglio. Continuum and discrete initial-boundary value problems and einstein’s field equations. *Living Rev. Relativity*, 15(9), 2012. (Cited on page 60.)
- [400] Fabio Scardigli and Roberto Casadio. Generalized uncertainty principle, extra dimensions and holography. *Class. Quant. Grav.*, 20:3915–3926, 2003. (Cited on pages 16 and 115.)
- [401] Gerold Oltman Schellstede. On the Newtonian limit of metric f(R) gravity. *Gen. Rel. Grav.*, 48(9):118, 2016. (Cited on page 119.)
- [402] William E Schiesser and Graham W Griffiths. *A Compendium of Partial Differential Equation Models: Method of Lines Analysis with Matlab*. Cambridge University Press, 2009. (Cited on pages 23 and 136.)
- [403] E. Schnetter, S. H. Hawley, and I. Hawke. Evolutions in 3D numerical relativity using fixed mesh refinement. *Class. Quantum Grav.*, 21:1465–1488, March 2004. (Cited on pages 37, 96, 136, and 138.)
- [404] Erik Schnetter. Finding apparent horizons and other two-surfaces of constant expansion. *Class. Quantum Grav.*, 20(22):4719–4737, 2003. (Cited on page 97.)
- [405] Erik Schnetter, Peter Diener, Ernst Nils Dorband, and Manuel Tiglio. A multi-block infrastructure for three-dimensional time- dependent numerical relativity. *Class. Quantum Grav.*, 23:S553–S578, 2006. (Cited on pages 96 and 138.)
- [406] Angelika Schwarz, Dominic Etienne Charrier, Fabian Guera, Jean-Matthieu Gallard, Benjamin Hazelwood, Philipp Samfass, Sven Köppel, Tobias Weinzierl, and Vasco Varduhn. The ExaHyPE Guidebook. <http://www.exahype.eu>, 2018. (Cited on pages 3, 12, 14, 35, 40, 42, and 136.)
- [407] M. Semplice, A. Coco, and G. Russo. Adaptive mesh refinement for hyperbolic systems based on third-order compact weno reconstruction. *Journal of Scientific Computing*, 66(2):692–724, 2016. (Cited on pages 39 and 40.)
- [408] H. Shen, H. Toki, K. Oyamatsu, and K. Sumiyoshi. Relativistic equation of state of nuclear matter for supernova and neutron star. *Nuclear Physics A*, 637:435–450, July 1998. (Cited on page 99.)
- [409] M. Shibata. Fully General Relativistic Simulation of Merging Binary Clusters – Spatial Gauge Condition—. *Progress of Theoretical Physics*, 101:1199–1233, June 1999. (Cited on page 46.)
- [410] M. Shibata. *Numerical Relativity*. World Scientific, Singapore, 2016. (Cited on pages 44, 46, and 49.)

- [411] M. Shibata, S. Fujibayashi, K. Hotokezaka, K. Kiuchi, K. Kyutoku, Y. Sekiguchi, and M. Tanaka. Modeling GW170817 based on numerical relativity and its implications. *Phys. Rev. D*, 96(12):123012, December 2017. (Cited on page 15.)
- [412] M. Shibata and K. Kiuchi. Gravitational waves from remnant massive neutron stars of binary neutron star merger: Viscous hydrodynamics effects. *Phys. Rev. D*, 95(12):123003, June 2017. (Cited on page 15.)
- [413] M. Shibata and T. Nakamura. Evolution of three-dimensional gravitational waves: Harmonic slicing case. *Phys. Rev. D*, 52:5428–5444, November 1995. (Cited on pages 13, 48, and 96.)
- [414] C.W. Shu. High order WENO and DG methods for time-dependent convection-dominated PDEs: A brief survey of several recent developments. *Journal of Computational Physics*, 316:598–613, 2016. (Cited on page 30.)
- [415] D. M. Siegel, R. Ciolfi, A. I. Harte, and L. Rezzolla. Magnetorotational instability in relativistic hypermassive neutron stars. *Phys. Rev. D R*, 87(12):121302, June 2013. (Cited on page 15.)
- [416] Do Hoang Son. *Feynman loop integrals and their automatic computer-aided evaluation*. PhD thesis, 2003. (Cited on page 22.)
- [417] M. Sonntag and C.D. Munz. Shock capturing for discontinuous Galerkin methods using finite volume subcells. In J. Fuhrmann, M. Ohlberger, and C. Rohde, editors, *Finite Volumes for Complex Applications VII*, pages 945–953. Springer, 2014. (Cited on page 35.)
- [418] M. Sonntag and C.D. Munz. Efficient parallelization of a shock capturing for discontinuous Galerkin methods using finite volume sub-cells. *Journal of Scientific Computing*, 70:1262–1289, 2017. (Cited on page 35.)
- [419] Marco Sortino, G Totis, KULJANIC , and Goran Cukor. Simulation of Cutting Forces and Cutting Conditions in Complex Turning Operations. pages 203–207, 01 2009. (Cited on pages 37 and 136.)
- [420] E. Spallucci and S. Ansoldi. Regular black holes in UV self-complete quantum gravity. *Phys. Lett.*, B701:471–474, 2011. (Cited on pages 16 and 120.)
- [421] M. Sprenger, P. Nicolini, and M. Bleicher. Physics on the smallest scales: an introduction to minimal length phenomenology. *Eur.J.Phys.*, 33:853–862, 2012. (Cited on page 16.)
- [422] A. W. Steiner, M. Hempel, and T. Fischer. Core-collapse Supernova Equations of State Based on Neutron Star Observations. *Astrophys. J.*, 774:17, September 2013. (Cited on page 96.)
- [423] A. W. Steiner, J. M. Lattimer, and E. F. Brown. The Equation of State from Observed Masses and Radii of Neutron Stars. *Astrophys. Journ.*, 722:33–54, October 2010. (Cited on page 96.)
- [424] A.H. Stroud. *Approximate Calculation of Multiple Integrals*. Prentice-Hall Inc., Englewood Cliffs, New Jersey, 1971. (Cited on page 31.)
- [425] Y. Sugahara and H. Toki. Relativistic mean field theory for unstable nuclei with nonlinear sigma and omega terms. *Nucl. Phys.*, A579:557–572, 1994. (Cited on page 96.)
- [426] A. Suresh and H. T. Huynh. Accurate monotonicity-preserving schemes with runge-kutta time stepping. *Journal of Computational Physics*, 136(1):83–99, 1997. (Cited on page 96.)
- [427] Bela Szilagyi, Lee Lindblom, and Mark A. Scheel. Simulations of Binary Black Hole Mergers Using Spectral Methods. *Phys. Rev. D*, 80:124010, 2009. (Cited on page 13.)
- [428] R. Takahashi and M. Umemura. General relativistic radiative transfer code in rotating black hole space-time: ARTIST. *Mon. Not. R. Astron. Soc.*, 464:4567–4585, 2017. (Cited on page 14.)

- [429] K. Takami, L. Rezzolla, and L. Baiotti. Constraining the Equation of State of Neutron Stars from Binary Mergers. *Phys. Rev. Lett.*, 113(9):091104, August 2014. (Cited on pages 95 and 97.)
- [430] O. Tange. GNU Parallel - The Command-Line Power Tool. *:login: The USENIX Magazine*, 36(1):42–47, Feb 2011. (Cited on page 168.)
- [431] F. R. Tangherlini. Schwarzschild field in n dimensions and the dimensionality of space problem. *Nuovo Cim.*, 27:636–651, 1963. (Cited on page 107.)
- [432] M. Tavelli and M. Dumbser. A staggered space-time discontinuous Galerkin method for the three-dimensional incompressible Navier-Stokes equations on unstructured tetrahedral meshes. *Journal of Computational Physics*, 319:294 – 323, 2016. (Cited on page 30.)
- [433] M. Tavelli, M. Dumbser, D. E. Charrier, L. Rannabauer, T. Weinzierl, and M. Bader. A simple diffuse interface approach on adaptive Cartesian grids for the linear elastic wave equations with complex topography. *ArXiv e-prints*, April 2018. (Cited on page 133.)
- [434] Abdel Nasser Tawfik and Abdel Magied Diab. Review on Generalized Uncertainty Principle. *Rept. Prog. Phys.*, 78:126001, 2015. (Cited on page 16.)
- [435] Saul A. Teukolsky. Short note on the mass matrix for Gauss-Lobatto grid points. *Journal of Computational Physics*, 283:408–413, Feb 2015. (Cited on page 31.)
- [436] I. Tews, J. M. Lattimer, A. Ohnishi, and E. E. Kolomeitsev. Symmetry Parameter Constraints from a Lower Bound on Neutron-matter Energy. *Astrophys. J.*, 848:105, October 2017. (Cited on pages 96 and 99.)
- [437] The LIGO Scientific Collaboration and The Virgo Collaboration. Gw170817: Observation of gravitational waves from a binary neutron star inspiral. *Phys. Rev. Lett.*, 119:161101, Oct 2017. (Cited on pages 12, 15, and 103.)
- [438] V. A. Titarev and E. F. Toro. ADER: Arbitrary High Order Godunov Approach. *Journal of Scientific Computing*, 17:609, December 2002. (Cited on pages 24 and 33.)
- [439] V. A. Titarev and E. F. Toro. ADER schemes for three-dimensional non-linear hyperbolic systems. *Journal of Computational Physics*, 204:715–736, April 2005. (Cited on pages 24 and 33.)
- [440] H. Togashi, E. Hiyama, Y. Yamamoto, and M. Takano. Equation of state for neutron stars with hyperons by the variational method. *Phys. Rev.*, C93(3):035808, 2016. (Cited on pages 96 and 99.)
- [441] H. Togashi, K. Nakazato, Y. Takehara, S. Yamamuro, H. Suzuki, and M. Takano. Nuclear equation of state for core-collapse supernova simulations with realistic nuclear forces. *Nucl. Phys.*, A961:78–105, 2017. (Cited on pages 96 and 99.)
- [442] R. C. Tolman. Static solutions of Einstein’s field equations for spheres of fluids. *Phys. Rev.*, 55:364, 1939. (Cited on page 93.)
- [443] E. T. Tomboulis. Superrenormalizable gauge and gravitational theories. 1997. (Cited on pages 16 and 108.)
- [444] E. F. Toro. *Riemann Solvers and Numerical Methods for Fluid Dynamics*. Springer-Verlag, 1999. (Cited on pages 18, 19, and 20.)
- [445] E. F. Toro. *Riemann Solvers and Numerical Methods for Fluid Dynamics*. Springer-Verlag, third edition, 2009. (Cited on pages 60 and 74.)
- [446] E. F. Toro, A. Hidalgo, and M. Dumbser. FORCE schemes on unstructured meshes I: Conservative hyperbolic systems. *Journal of Computational Physics*, 228:3368–3389, May 2009. (Cited on page 34.)

- [447] E. F. Toro and V. A. Titarev. Derivative Riemann solvers for systems of conservation laws and ADER methods. *Journal of Computational Physics*, 212(1):150–165, 2006. (Cited on pages 24 and 33.)
- [448] E.F. Toro. *Riemann Solvers and Numerical Methods for Fluid Dynamics*. Springer, third edition, 2009. (Cited on pages 28 and 32.)
- [449] S. Typel. Relativistic model for nuclear matter and atomic nuclei with momentum-dependent self-energies. *Phys. Rev.*, C71:064301, 2005. (Cited on page 96.)
- [450] S. Typel, G. Röpke, T. Klähn, D. Blaschke, and H. H. Wolter. Composition and thermodynamics of nuclear matter with light clusters. *Phys. Rev. C*, 81(1):015803, January 2010. (Cited on pages 96 and 99.)
- [451] B. Ulmann. *Analog Computing*. Oldenbourg Wissenschaftsverlag, 2013. (Cited on page 22.)
- [452] W. G. Unruh. Experimental black-hole evaporation? *Phys. Rev. Lett.*, 46:1351–1353, May 1981. (Cited on page 22.)
- [453] James van Meter, John G. Baker, Michael Koppitz, and Dae-Il Choi. How to move a black hole without excision: gauge conditions for the numerical evolution of a moving puncture. *Phys. Rev. D*, 73:124011, 2006. (Cited on page 48.)
- [454] G. Veneziano. A stringy nature needs just two constants. *Europhys.Lett.*, 2:199, 1986. (Cited on page 16.)
- [455] Robert M. Wald. *General relativity*. The University of Chicago Press, Chicago, 1984. (Cited on page 43.)
- [456] Robert M. Wald. Introduction to Gravitational Self-Force. *Fundam. Theor. Phys.*, 162:253–262, 2011. [,253(2009)]. (Cited on page 43.)
- [457] L. R. Weih, E. R. Most, and L. Rezzolla. On the stability and maximum mass of differentially rotating relativistic stars. *Mon. Not. R. Astron. Soc.*, 473:L126–L130, January 2018. (Cited on page 100.)
- [458] T. Weinzierl and M. Mehl. Peano-A traversal and storage scheme for octree-like adaptive cartesian multiscale grids. *SIAM Journal on Scientific Computing*, 33:2732–2760, 2011. (Cited on pages 39 and 139.)
- [459] Tobias Weinzierl. The Peano software - parallel, automaton-based, dynamically adaptive grid traversals. *ArXiv e-prints*, page arXiv:1506.04496, June 2015. (Cited on pages 38 and 136.)
- [460] Andreas Weyhausen, Sebastiano Bernuzzi, and David Hilditch. Constraint damping for the Z4c formulation of general relativity. *Phys. Rev. D*, D85:024038, 2012. (Cited on page 51.)
- [461] C. J. White, J. M. Stone, and C. F. Gammie. An Extension of the Athena++ Code Framework for GRMHD Based on Advanced Riemann Solvers and Staggered-mesh Constrained Transport. *Astrophys. J.s*, 225:22, August 2016. (Cited on page 14.)
- [462] J. R. Wilson. Some magnetic effects in stellar collapse and accretion. In P. G. Bergman, E. J. Fenyves, and L. Motz, editors, *Seventh Texas Symposium on Relativistic Astrophysics*, volume 262 of *Annals of the New York Academy of Sciences*, pages 123–132, October 1975. (Cited on page 14.)
- [463] Elizabeth Winstanley. Hawking radiation from rotating brane black holes. In *Conference on Black Holes and Naked Singularities Milan, Italy, May 10-12, 2007*, 2007. (Cited on page 107.)
- [464] K. Yagi and N. Yunes. I-Love-Q. *Science*, 341:365, February 2013. (Cited on page 100.)
- [465] James W. York. Gravitational degrees of freedom and the initial-value problem. *Phys. Rev. Lett.*, 26:1656–1658, 1971. (Cited on page 49.)
- [466] James W. York. Role of conformal three-geometry in the dynamics of gravitation. *Phys. Rev. Lett.*, 28:1082–1085, 1972. (Cited on page 49.)

- [467] James W. York. Kinematics and dynamics of general relativity. In Larry L. Smarr, editor, *Sources of gravitational radiation*, pages 83–126. Cambridge University Press, Cambridge, UK, 1979. (Cited on pages [45](#), [46](#), and [78](#).)
- [468] O. Zanotti and M. Dumbser. A high order special relativistic hydrodynamic and magnetohydrodynamic code with space-time adaptive mesh refinement. *Computer Physics Communications*, 188:110–127, March 2015. (Cited on page [128](#).)
- [469] O. Zanotti and M. Dumbser. Efficient conservative ader schemes based on weno reconstruction and space-time predictor in primitive variables. *Computational Astrophysics and Cosmology*, 3(1):1, 2016. (Cited on page [34](#).)
- [470] O. Zanotti, F. Fambri, and M. Dumbser. Solving the relativistic magnetohydrodynamics equations with ADER discontinuous Galerkin methods, a posteriori subcell limiting and adaptive mesh refinement. *Mon. Not. R. Astron. Soc.*, 452:3010–3029, 2015. (Cited on pages [14](#), [36](#), [39](#), [90](#), and [91](#).)
- [471] O. Zanotti, F. Fambri, and M. Dumbser. Solving the relativistic magnetohydrodynamics equations with ADER discontinuous Galerkin methods, a posteriori subcell limiting and adaptive mesh refinement. *Mon. Not. R. Astron. Soc.*, 452:3010–3029, September 2015. (Cited on page [69](#).)
- [472] O. Zanotti, F. Fambri, M. Dumbser, and A. Hidalgo. Space-time adaptive ader discontinuous galerkin finite element schemes with a posteriori sub-cell finite volume limiting. *Computers and Fluids*, 118(0):204 – 224, 2015. (Cited on pages [36](#), [39](#), and [69](#).)
- [473] Weiqun Zhang and A.I. MacFadyen. RAM: A relativistic adaptive mesh refinement hydrodynamics code. *The Astrophysical Journal Supplement Series*, 164:255, 2006. (Cited on page [13](#).)
- [474] J. Zhu, J. Qiu, C.-W. Shu, and M. Dumbser. Runge-Kutta discontinuous Galerkin method using WENO limiters ii: Unstructured meshes. *J. Comput. Phys.*, 227(9):4330–4353, 2008. (Cited on page [34](#).)
- [475] M. Zilhão and F. Löffler. An Introduction to the Einstein Toolkit. *International Journal of Modern Physics A*, 28:40014, September 2013. (Cited on page [96](#).)

Acknowledgement

My gratitude goes to my supervisors for the close supervision, patience in explaining concepts, the many opportunities for traveling and exchange and meetings at any time and place. Especially I thank my primary supervisor, Luciano Rezzolla, for the one of a kind way of remote collaboration since my move-out of Frankfurt in 2017. My secondary supervisor, Piero Nicolini, is expressed my special thanks for the countless cofees in Otto-Stern-Zentrum.

I also want to thank the large group of Relativistic Astrophysics at the Institute for Theoretical Physics (ITP) in Frankfurt, especially my fellow students of the hydrodynamics subgroup, Federico Guercilena, Jens Papenfort, Elias Most and Luke Bovard for many fruitful discussions and exchange of the knowledge. I also benefited from insights provided by Filipo Galeazzi, Bruno Mundim, Matthias Hanauske and Mariafelicia De Laurentis and most of the other people in this large international, fluctuating and colorful group. Special thanks go to my collegues Alejandro Cruz Osorio and Roman Gold with which I shared my office at ITP consecutively.

Special thanks goes to the ExaHyPE consortium and in the frontline Michael Dumbser for his tireless efforts of spreading the knowledge about sophisticated numerical methods and for the various invitations to Trento University. I express my special thanks to my fellows Dominic Charrier, Jean-Mathieu Gallard, Angelika Schwarz, Ben Hazelwood and Leonard Rannabauer for their great collaboration and the many discussions. Special thanks also to Tobias Weinzierl for his relentless efforts of convincing about the power of loosing control and various invitations to Durham University. Gratitude is further owed to Olindo Zanotti, Michael Bader and Vasco Varduhn for start-up support in their research fields.

I also thank the exotic high energy physics (quantum gravity) group at Giersch Science Center/Frankfurt Institute for Advanced Studies (GSC/FIAS) in Frankfurt, especially my fellow students Marco Knipfer, Antonia Frassino and Michael Wondrak for many inspiring discussions.

Last but not least I thank FIAS and ITP for their kind hospitality, furthermore the graduate schools HGS-HiRE (HIC for FAIR/GSI) and FIGSS (FIAS) for infrastructure, travel support and softskill schooling. For running simulations within this thesis, I enjoyed access to various clusters of the of the Gauss Supercomputing Center, especially the LRZ computing center in Munich/Garching (SuperMUC and CoolMUC) and the HLHRS in Stuttgart (Hazelhen), the CSC in Frankfurt (Loewe and Fuchs), the Durham-based supercomputer (Hamilton) as well as local computing facilities in ITP and FIAS. Special thanks goes to the administrative teams of CSC, ITP and FIAS which provided personal support in any condition.

I received fundamental support from the European Union's Horizon 2020 Research and Innovation Programme (Grant 671698, call FETHPC-1-2014, project ExaHyPE) and the COST Action MP1304 "NewCompStar".

In order to appreciate the work of open source software authors, I want to cite scientific codes which ask for credits: GNU Parallel [430], scipy [259] and matplotlib [251]. Also technically this work is standing on the shoulder of giants, as I made use of the rich contemporary GNU/Linux software infrastructure and all the scientific ecosystems – primarily scientific python – available for free.

Curriculum Vitae



Personal information

Name Sven Köppel

E-Mail koeppel@fias.uni-frankfurt.de

Date of Birth January 31, 1989

Place of Birth Königstein (Taunus), Germany

Web page fias.uni-frankfurt.de/~koeppel

Place of residence Münster (Westfalen), Germany

Descendants Lola *2017

Education

2015 PhD studies, Institut für theoretische Physik, Goethe Universität Frankfurt am Main, Supervisor: Prof. L. Rezzolla.

2014 Master's thesis, Frankfurt Institute for Advanced Studies, Title: *Ultraviolet improved Black Holes*, Supervisor: Prof. P. Nicolini.

2011 Bachelor's thesis, Institut für theoretische Physik, Title: *The QCD Equation of State in the Early Universe*, Goethe Universität Frankfurt am Main, Supervisor: Prof. O. Phillipsen.

2008 Abitur, Eichendorffschule mit gymnasialer Oberstufe Immanuel-Kant, Kelkheim (Taunus).

Peer-reviewed Publications

- S. Köppel, L. Bovard, L. Rezzolla, “Universal relations for binary neutron star lifetimes”, published in *Astrophysical Journal Letters* 2019 [275]
- F. Fambri, M. Dumbser, S. Köppel, L. Rezzolla, O. Zanotti, “ADER discontinuous Galerkin schemes for general-relativistic ideal magnetohydrodynamics”, published in *Mon.Not.Roy.Astron.Soc.* 2018 [194]
- M. Dumbser, F. Guercilena, S. Köppel, L. Rezzolla, O. Zanotti, “Conformal and covariant Z4 formulation of the Einstein equations strongly hyperbolic first-order reduction and solutions with discontinuous Galerkin schemes”, published in *Phys.Rev.D.* 2018 [168]
- A. Frassino, S. Köppel, P. Nicolini, “Geometric model of black hole quantum N-portrait, extra dimensions and thermodynamics”, published in *Entropy* 2016 [204]

Upcoming Publications

- S. Köppel, M. Knipfer, P. Nicolini, “Generalized Uncertainty Principle and Black Holes in Higher Dimensional Self Complete Gravity”, to be published [276]

Peer-reviewed Conference Proceedings

- S. Köppel, “Towards an exascale code for GRMHD on dynamical spacetimes”, published in *J.Phys.Conf.Ser.* 2018 [274]
- S. Köppel, M. Knipfer, M. Isi, J. Mureika, P. Nicolini, “Generalized uncertainty principle and extra dimensions”, published in *Springer Proc.Phys.* 2018 [290]

Presentations, Invitations and Posters

- Predicting gravitational waves on computers, at When Gravitational Waves hit Durham - an ExaHyPE workshop, Durham School of Engineering and Computing Sciences, on 2017-11-30 (invited talk).
- Towards an Exascale code for MHD on dynamical space-times, at Astronum 2017, Centre de congrès des Saint-Malo, France, on 2017-06-27.
- Mini Overview, ExaHyPE: Exascale Spacetree ADER-DG, at Mini-Workshop on Preparing for PRACE Exascale Systems, Juelich Supercomputing Centre, Forschungszentrum Juelich, on 2017-06-01 (invited talk).
- Einsteins Equations in ExaHyPE, at ExaHyPE Research Council, LRZ, Technische Universität München, Garching, on 2017-04-03 (and 4 more talks there).
- Probing star collisions with Exascale computers, FIGSS seminar, FIAS, Uni Frankfurt, on 2016-12-12.
- Donuts in Space, at Palaver SS 2016, ITP Uni Frankfurt, on 2016-05-30 (and one more talk there at 2014).
- On gravity self-completeness on Anti-de Sitter background, at DPG-Frühjahrestagung 2016, Uni Hamburg, on 2016-03-01.
- ExaHyPE: Various Equations and Quick Adaption to the Users' Needs Becoming Open Source, SIAM-CSE, Atlanta (USA), on 2016-02-28 (invited poster).
- The Generalized Uncertainty Principle and Extra Dimensions, at Geometry and Physics seminar, DFT at IFIN-HH, Bucharest, on 2015-09-25 (invited talk).
- The Generalized Uncertainty Principle in extra dimensions, at Karl Schwarzschild Meeting on Gravitational Physics 2015, Frankfurt, on 2015-07-21.
- The quest for physics at shortest scales, at FIAS scientific retreat, Riezlern, on 2015-01-18.
- Quantum gravity improved black holes, at Astro Coffee, FIAS 0.101, on 2015-01-27.
- On gravity self-completeness in higher dimensions, at DPG-Frühjahrestagung 2015, TU-Berlin, on 2015-03-20.
- Quantum gravity improved black holes, at DPG Physics School General Relativity 99, DPG Zentrum Bad Honnef, Uni Bonn, on 2014-09-14 (Poster).

Publications and Invitations in eLearning-related matter

- S. Köppel, "Soziale Wissenschaft", published in USE: Universität Studieren / Studieren Erforschen, 2014 (proceeding).
- S. Köppel, "POKAL: Kollaboratives eLearning neu erfunden", published in Medien in der Wissenschaft [278].
- UNIversal 2014 Studienkongress, "Wissenschaft als soziales Netzwerk", on 2014-07-15 (invited talk).
- Hessisches eLearning-Fachforum 2014, Hochschule Rhein-Main, "eLearning von Studierenden für Studierende, Studentische Contests und eLearning-Settings an der Goethe-Universität Frankfurt" (invited talk).
- GMW 2013 (Jahrestagung der Gesellschaft für Medien in der Wissenschaft) an der Goethe-Universität Frankfurt, "POKAL – Kollaboratives eLearning neu erfunden" (invited talk).
- And 20 more talks about e-Learning at Uni Frankfurt between 2011-2015.

Relevant academic work experience

2015-2017 ERC Horizon 2020 Project: "ExaHyPE: An ExaScale Hyperbolic PDE Engine", with PIs Prof. M. Bader, Prof. M. Dumbser, Prof. L. Rezzolla, Prof. T. Weinzierl.

2010-2016 PhysikOnline: eLearning for physicists, Center for Scientific Computing, Goethe Universität Frankfurt, Prof. H. Lüdde.

2015 UniΦ, OpenScience social publication platform, Studi umdigitale, Institute for Computer Science, Goethe Universität Frankfurt, Prof. D. Krömer.

2011-2012 Psychology eLearning, Interdisciplinary College Of University Didactics (IKH), Goethe Universität Frankfurt, Prof. H. Horz.

2008-2010 BioKemika: Chief development of a biochemical search engine, Institute for biophysical chemistry and Life sciences, Goethe Universität Frankfurt, Prof. Clemens Glauert.

Relevant academic grants

- 2015, 2016 "RiedbergTV" (20k€, SeLF eLearning funds)
- 2011–2016 "PhysikOnline" (300k€, QSL funds)
- 2011, 2013 "POKAL: PhysikOnline Kollaborative Arbeits- und Lenrplattform" (25k€ in total, SeLF)